TÉCNICO LISBOA

UNIVERSIDADE DE LISBOA

INSTITUTO SUPERIOR TÉCNICO

Quantitative Evaluation of Cerebral Haemodynamics using Magnetic Resonance Imaging

Joana Carolina Sequeira Pinto

Supervisor: Doctor Patrícia Margarida Piedade Figueiredo

Co-Supervisors:

Doctor Pedro Ferro Vilela

Doctor Noam Shemesh

Thesis approved in public session to obtain the PhD Degree in Biomedical Engineering

Jury final decision: Pass with Distinction and Honour

2019

TÉCNICO LISBOA

UNIVERSIDADE DE LISBOA

INSTITUTO SUPERIOR TÉCNICO

Quantitative Evaluation of Cerebral Haemodynamics using Magnetic Resonance Imaging

Joana Carolina Sequeira Pinto

Supervisor: Doctor Patrícia Margarida Piedade Figueiredo

Co-Supervisors:

Doctor Pedro Ferro Vilela

Doctor Noam Shemesh

Thesis approved in public session to obtain the PhD Degree in Biomedical Engineering

Jury final decision: Pass with Distinction and Honour

Jury

Chairperson: Doctor João Pedro Estrela Rodrigues Conde, Instituto Superior Técnico, Universidade de Lisboa

Members of the Committee:

Doctor Matthias Van Osch, Faculty of Medicine, Leiden University, The Netherlands

Doctor António José Bastos Leite, Faculdade de Medicina, Universidade do Porto

Doctor Patrícia Margarida Piedade Figueiredo, Instituto Superior Técnico, Universidade de Lisboa

Doctor Alexandre da Rocha Freire de Andrade, Faculdade de Ciências, Universidade de Lisboa

Doctor Rita Homem de Gouveia Constanzo Nunes, Instituto Superior Técnico, Universidade de Lisboa

Funding Institutions:

Fundação para a Ciência e a Tecnologia

2019

Abstract

Small Vessel Disease (SVD) encompasses all pathological processes affecting the small vessels of the brain. To date, structural lesions and cognitive dysfunction are the hallmarks of this disease. Nevertheless, SVD is expected to affect the functional integrity of vessels at an earlier stage and, for that reason, identification of haemodynamic biomarkers might be of great interest. On that matter, magnetic resonance imaging (MRI) offers a number of non-invasive methods for assessing different aspects of cerebral haemodynamics with great potential to provide the desired biomarkers; these are however still in the research domain.

The work described in this Thesis aims to develop non-invasive and quantitative MRI techniques for fast and reliable evaluation of cerebral haemodynamics, by overcoming some of their current methodological limitations.

Firstly, the impact of calibration methods on the quantification of cerebral blood flow using arterial spin labeling (ASL) MRI was assessed. Results highlight the need for a complete description of the calibration procedure in ASL studies and demonstrate that voxelwise calibration is the least sensitive strategy to the different pipeline options.

Secondly, the methodological aspects of several non-invasive cerebrovascular reactivity (CVR) assessment techniques using blood oxygen level dependent (BOLD) functional MRI (fMRI) were introduced and discussed. Furthermore, new and improved modeling strategies for the accurate quantification of CVR were studied. A Fourier series set consisting of a sine–cosine pair at the task frequency and its two harmonics is shown to be an appropriate model for BOLD-fMRI CVR measurements based on a breath-hold task with preparatory inspiration.

Improved models were proposed to assess the contribution of physiological (cardiac and respiratory) sources to the spontaneous fluctuations to the BOLD-fMRI signal. Results demonstrate that resting-state fMRI functional connectivity measures at 7 Tesla may be improved by optimizing physiological noise correction at least at the cluster level.

Finally, we applied the previously developed techniques to the study of a group of SVD patients and showed their feasibility in delivering useful metrics of cerebral haemodynamics. In particular, our preliminary work highlights the potential of these metrics to predict cognitive decline in SVD, further supporting the hypothesis that functional metrics might provide sensitive disease biomarkers.

Overall, our results evidence that the proposed MRI methodological developments provide

promising cerebral haemodynamic measurements, with potential application as disease biomarkers.

Keywords

functional magnetic resonance imaging, cerebral haemodynamics, cerebrovascular reactivity, cerebral blood flow, small vessel disease

Resumo

A doença dos pequenos vasos (*small vessel disease*, SVD) abrange todos os processos patológicos que afectam os pequenos vasos do cérebro. Até à data, as lesões estruturais e a disfunção cognitiva são as principais características desta doença. No entanto, espera-se que a SVD afecte a integridade funcional dos vasos num estadio mais precoce da doença, de tal forma que a identificação de biomarcadores hemodinâmicos é de grande interesse. Nesse sentido, a ressonância magnética (MR) oferece uma série de métodos não invasivos para avaliar diferentes aspectos da hemodinâmica cerebral com grande potencial para fornecer os biomarcadores desejados; no entanto, estes ainda estão numa fase inicial de desenvolvimento.

O trabalho descrito nesta Tese tem como objetivo desenvolver técnicas de imagem por MR (MRI) não-invasivas e quantitativas para a avaliação rápida e fiável da hemodinâmica cerebral, superando algumas das limitações metodológicas actuais.

Primeiramente, foi avaliado o impacto dos métodos de calibração na quantificação da perfusão cerebral utilizando *arterial spin labeling* (ASL). Os resultados destacam a necessidade de uma descrição completa do procedimento de calibração em estudos de ASL e demonstram que a calibração *voxelwise* é a estratégia menos sensível às diferentes opções de processamento.

Em segundo lugar, foram apresentados e discutidos os aspectos metodológicos de várias técnicas não invasivas de avaliação da reactividade cerebrovascular (CVR), utilizando ressonância magnética funcional (fMRI) baseada no contraste *blood oxygen level dependent* (BOLD). Adicionalmente, novas estratégias de modelação para a quantificação precisa de CVR foram investigadas. Um conjunto de séries de Fourier, consistindo num par seno-cosseno com a frequência da tarefa e duas harmónicas, é um modelo apropriado para medições BOLD-fMRI de CVR baseadas numa tarefa de apneia com inspiração preparatória.

Foram ainda propostos novos modelos para avaliação da contribuição de fontes fisiológicas (cardíacas e respiratórias) para as flutuações espontâneas do sinal BOLD-fMRI. Os resultados demonstram que as medidas de conectividade funcional fMRI em estado de repouso a 7 Tesla podem ser melhoradas através da optimização da correcção do ruído fisiológico pelo menos a nível do *cluster*.

Por fim, aplicámos as técnicas previamente desenvolvidas a um grupo de pacientes com SVD e demonstrámos a sua viabilidade em fornecer métricas úteis da hemodinâmica cerebral. Em particular, o nosso trabalho preliminar destaca o potencial dessas métricas para prever o

declínio cognitivo destes doentes, corroborando a hipótese de que as métricas funcionais podem fornecer biomarcadores de doenças sensíveis. Em geral, os nossos resultados evidenciam que os desenvolvimentos metodológicos da MR propostos fornecem medidas hemodinâmicas cerebrais promissoras, com potencial aplicação como biomarcadores de doenças.

Palavras Chave

imagem por ressonância magnética funcional, hemodinâmica cerebral, reactividade cerebrovascular, fluxo sanguíneo cerebral, doença dos pequenos vasos

Acknowledgments

Firstly, I would like to take this opportunity to thank everyone who has helped and supported me during the course of my PhD studies.

In particular, I would like to express my deepest gratitude to my supervisor, Professor Patrícia Figueiredo. Her time, knowledge and guidance over the last years were invaluable. I am continually inspired by her immeasurable dedication to research and her students. Thank you, Patrícia.

Additional thanks go to my co-supervisors Dr. Pedro Vilela for the insightful discussions and guidance and Dr. Noam Shemesh for his availability and support.

For their continuously interest on my research, I would also like to acknowledge Prof. Lopes da Silva and Prof. Rita Nunes. Additionally, I would like to thank Prof. Michael Chappell and his group at IBME for all their help and support during my stay in Oxford.

I would also like to acknowledge the members of Projects NeuroPhysIm and HiFi-MRI for all their help, in particular Ana Fouto, Joana Moreira, Tânia Charrua, Carmo Moser, João Periquito, Gonçalo Gomes, Ana Graça and Sandro Nunes.

I could not forget to thank the friends who encouraged and accompanied me closely throughout this journey, particularly Rodolfo Abreu, Catarina Barata, Carlos Santiago, Nuno Fachada, Janir Ramos, João Jorge, Inês Sousa, Andreia Gaspar and Daniela Medley. A special thanks goes to Benjamin Schaper.

Finally, I must thank my family, particularly my parents, for always being so supportive: *obrigada por tudo.*

I would like to acknowledge the Portuguese Science Foundation for financial support through the Doctoral Grant PD/BD/135114/2017 and Project PTDC/BBB-IMG/2137/2012, the staff of Hospital da Luz for logistic support during data acquisition, and the Institute for Systems and Robotics for financial and administrative support.

Contents

List of Figures

List of Tables

Abbreviations

aBV	Arterial blood volume
ACA	Anterior cerebral artery
ACZ	Acetazolamide
ALFF	Amplitude of low frequency fluctuations
ANOVA	Analysis of variance
ASL	Arterial spin labeling
ATT	Arterial transit time
BET	Brain extraction tool
BH	Breath hold task
BOLD	Blood oxygen level dependent
BS	Background suppression
CAA	Cerebral amyloid angiopathy
CASL	Continuous arterial spin labeling
CBF	Cerebral blood flow
CBV	Cerebral blood volume
CDB	Cued deep breathing
cGMP	Cyclic guanosine monophosphate
$CMRO_2$	Cerebral metabolic rate of oxygen consumption
CO_2	Carbon dioxide
CPP	Cerebral perfusion pressure
CRF	Cardiac response function
CSF	Cerebrospinal fluid
CV	Coefficient of variation
CV_{inter}	Inter-subject coefficient of variation
CV_{intra}	Intra-subject coefficient of variation
CVR	Cerebrovascular reactivity

DEF	Dynamic end-tidal forcing
dHb	Deoxyhaemoglobin
DMN	Default mode network
DTI	Diffusion tensor imaging
DWI	Diffusion-weighted imaging
EEG	Electroencephalography
EPI	Echo-planar imaging
EPISTAR	Echo-planar imaging with signal targeting by alternating radiofrequency pulses
EV	Explanatory variable
FAIR	Flow-sensitive alternating inversion recovery
fALFF	Fractional amplitude of low frequency fluctuations
FAST	FSL's automated segmentation tool
FCS	Functional connectivity strength
FILM	FSL's improved linear model
FLAIR	Fluid attenuated inversion recovery
FLIRT	FSL's linear image registration tool
fMRI	Functional magnetic resonance imaging
FSL	FMRIB's software library
FWHM	Full width at half maximum
GE	Gradient echo
GLM	General linear model
GM	Gray matter
GRASE	Gradient- and spin-echo
GS	Global signal
Hb	Oxyhaemoglobin
HR	Heart rate
HRF	Hemodynamic response function
ICA	Independent component analysis
ICC	Intraclass correlation coefficient
ICP	Intracranial pressure
IPS	Intra-parietal sulcus
IRF	Impulse response function
$\mathbf{M}_{0t}$	Equilibrium magnetization of tissue
$\mathbf{M}_{0b}$	Equilibrium magnetization of arterial blood
MAP	Mean arterial blood pressure

MCA	Middle cerebral artery
MCFLIRT	FSL's motion correction tool
MEG	Magnetoencephalography
MNI	Montreal neurological institute
MRI	Magnetic resonance imaging
MT	Magnetization transfer
NIRS	Near-infrared spectroscopy
NO	Nitrous oxide
O_2	Oxygen
OEF	Oxygen extraction fraction
OLS	Ordinary least squares
PaO_2	Arterial partial pressure of oxygen
$PaCO_2$	Arterial partial pressure of carbon dioxide
PASL	Pulsed arterial spin labeling
PCA	Posterior cerebral artery
pCASL	Pseudo-continuous arterial spin labeling
PCC	Posterior cingulate cortex
PET	Positron emission tomography
$PETCO_2$	End-tidal pressure of oxygen
$PETCO_2$	End-tidal pressure of carbon dioxide
PF	Physiological fluctuations
PICORE	Proximal inversion with control for off-resonance effects
PLD	Post-labeling delay
PSC	Percent signal change
PVE	Partial volume estimate
PWV	Pulse wave velocity
Q2TIPS	Quantitative imaging of perfusion using a simple subtraction version II with thin-slice TI1 periodic saturation
QUIPSS-II	Quantitative imaging of perfusion using a simple subtraction version II
RETROICOR	Retrospective image-based correction
RF	Radio frequency
ROI	Region of interest
RRF	Respiratory response function
RSFA	Resting-state fluctuations amplitude
RSN	Resting-state network

RT	Reference tissue
RV	Respiratory volume
RVT	Respiratory volume per unit time
SGD	Sequential gas delivery
SMA	Supplementary motor area
SMS	Simultaneous multi-slice
SNR	Signal-to-noise ratio
SPECT	Single-photon emission computed tomography
STD	Standard deviation
SVD	Small vessel disease
TDU	Transcranial Doppler ultrasound
TE	Echo time
TI	Inversion time
TOF	Time-of-flight angiography
TR	Repetition time
TTP	Time-to-peak
VASO	Vascular-space occupancy
VE	Variance explained
VSASL	Velocity-selective arterial spin labeling
WM	White matter
Xe-CT	Xenon computed tomography
λ	Brain-blood water partition coefficient

1

Introduction

Contents

1.1 Motivation

Nowadays, age-related functional decline and associated diseases are a primary concern in our society. In particular, in recent years there has been an increased interest in the pathological condition Small Vessel Disease (SVD), as it is the cause of 20% of strokes worldwide and a major source of vascular dementia and cognitive decline, particularly in the elderly. This pathology includes all processes affecting the small vessels of the brain, and because damage in these cannot be readily visualized *in vivo*, consequences of SVD such as structural lesions and cognitive dysfunction remain the hallmarks of the disease. Nevertheless, SVD is expected to affect the functional integrity of vessels at an earlier stage and, for that reason, identification of functional biomarkers that support early diagnosis, monitoring progression and evaluation of new therapies, might be of great interest and potential. In particular, alterations in cerebral haemodynamics might hold great promise in providing new insights into the pathophysiology of SVD, as these complex but coordinated physiological mechanisms supplying the brain with the necessary oxygen and energy substrates might be impaired or even abolished. Therefore, characterizing haemodynamics across the brain is crucial to infer its health state. Magnetic resonance imaging (MRI) techniques hold great promise in providing accessible, non-invasive mapping of these cerebral haemodynamics, leading to potentialy sensitive SVD biomarkers. However, the predominantly indirect and non-quantitative nature of MRI to assess these parameters has hampered its translation into routine clinical applicability.

The work developed in the scope of this Thesis is centered on overcoming some of these methodological limitations, aiming to develop non-invasive and quantitative MRI techniques for fast and reliable evaluation of cerebral haemodynamics. The main focus was on the following MRI techniques: arterial spin labeling (ASL) for imaging baseline cerebral blood flow (CBF); blood oxygen level dependent (BOLD) functional MRI (fMRI) to image cerebrovascular reactivity in response to a vasoactive challenge; and resting-state BOLD-fMRI to image spontaneous haemodynamic fluctuations. Firstly, a systematic comparison of different calibration procedures for absolute quantification of baseline perfusion measurements using two of the most commonly used ASL sequences in healthy subjects was performed. Then, non-invasive cerebrovascular reactivity assessment protocol and analysis method for better understanding of the BOLD response to a breath-holding task were optimized. Finally, the problem of modeling cardiac and respiratory effects at high-field in BOLD fMRI and assessment of their impact on functional connectivity were addressed. Some of the methodologies previously optimized were then applied to a group of SVD patients, in order to assess their role and impact as possible disease biomarkers. Expectantly, the results obtained in this Thesis will evidence that non-invasive fMRI methodologies can be successfully used to obtain cerebral haemodynamic metrics of interest, providing novel insights into the brain's physiological mechanisms, that might be impaired or abolished in pathological states.

1.2 Objectives

The main objective of the Thesis is the development of non-invasive and quantitative MRI techniques for fast and reliable evaluation of cerebral haemodynamics, with application as potential biomarkers in SVD.

For this purpose, the following specific objectives were considered:

1. To assess the impact of calibration methods in the quantification of regional CBF using ASL MRI;

2. To investigate methods for the quantification of cerebrovascular reactivity, based on modeling the BOLD-fMRI response to a breath hold task;

3. To investigate the contribution of physiological (cardiac and respiratory) sources to the spontaneous fluctuations of BOLD-fMRI, based on modeling their contributions to resting-state BOLD-fMRI data;

4. To apply the proposed methodologies to a group of SVD patients in order to demonstrate their applicability and investigate their potential as disease biomarkers.

1.3 Thesis Outline

Figure 1.1: Thesis outline overview, highlighting the steps that will be addressed individually.

Figure 1.1 depicts the Thesis outline, highlighting the several steps that will be addressed individually. Firstly, the motivation underlying the development of this work, including the objectives, the outline and contributions is highlighted in this Chapter. Subsequently, this Thesis is divided into three main parts.

The first part comprises the theoretical background, presented in **Chapters 2** and **3**. **Chapter 2** will provide a brief introduction of the anatomical and physiological basis of brain haemodynamics. Key concepts, such as cerebral blood flow and cerebrovascular reactivity, will be introduced and discussed more extensively. **Chapter 3** will give an overview of the imaging methods commonly used to measure cerebral haemodynamics. The primary focus will be on MRI methods, in particular, the two most important functional MRI contrasts, BOLD and ASL.

The second main part includes **Chapters 4**, **5**, **6** and **7**, focusing on the methodological work developed in the scope of this Thesis. **Chapter 4** assesses the impact of calibration strategies on ASL-derived CBF measurements during resting-state. This chapter was developed in collaboration with the Institute of Biomedical Engineering (IBME), Wellcome Centre for Integrative Neuroimaging (FMRIB) and the Nuffield Department of Clinical Neuroscience, at the University of Oxford. **Chapter 5** gives an overview of the several non-invasive methodologies currently used to map changes in cerebral haemodynamics, particularly cerebrovascular reactivity. **Chapter 6** further develops on fMRI cerebrovascular reactivity assessment, introducing a novel modeling strategy and assessing its reproducibility. **Chapter 7** optimizes physiological noise modeling and correction methods in resting-state BOLD fMRI. This last chapter was developed under the scope of Project HiFi-MRI, "Whole Brain Functional Connectivity Analysis of Ultra-High Field fMRI", a joint collaboration between *Instituto de Sistemas e Robótica* (ISR-Lisboa), *Instituto de Engenharia de Sistemas e Computadores, Investigação e Desenvolvimento* (INESC-ID) and the Athinoula A. Martinos Center for Biomedical Imaging (MGH/MIT/HMS).

The last section consists on the application of the methods developed in the previous chapters to a group of Small Vessel Disease patients (**Chapter 8**). This Chapter was developed under the scope of Project NeuroPhysIm, "Non-Invasive Quantitative Imaging of Cerebral Physiology", a joint collaboration between *Instituto de Sistemas e Robótica* (ISR-Lisboa), *Hospital da Luz* and *CEDOC - Chronic Diseases Research Center* (FCM/UNL). Finally, **Chapter 9** summarizes the main findings of this thesis, assesses its impact and describes possible future directions.

1.4 Contributions arising from the Thesis

1.4.1 Publications

The work in the scope of this Thesis resulted in nine communications at international conferences (as 1^{st} author) and four manuscripts accepted, under revision or in preparation for peer-reviewed international journals (as 1^{st} author).

Journal Articles

1. **Joana Pinto**, João Jorge, Inês Sousa, Pedro Vilela, Patrícia Figueiredo. "Fourier modelling of the BOLD response to a breath-hold task: optimization and reproducibility." (*NeuroImage, 135 (2016) 223-231*)

2. **Joana Pinto**, Sandro Nunes, Marta Bianciardi, Afonso Dias, L Miguel Silveira, Lawrence L Wald, Patrícia Figueiredo."Improved 7 Tesla resting-state fMRI connectivity measurements by cluster-based modeling of respiratory volume and heart rate effects." (*NeuroImage, 153 (2017) 262-272*)

3. **Joana Pinto**, Michael A. Chappell, Thomas W. Okell, Melvin Mezue, Andrew R Segerdahl, Irene Tracey, Pedro Vilela, Patrícia Figueiredo. "Calibration of arterial spin labeling data

- potential pitfalls in post-processing." (*accepted, Magnetic Resonance in Medicine, 2019*)

4. **Joana Pinto**, Patrícia Figueiredo. "Non-invasive mapping of cerebrovascular reactivity using MRI: methodological aspects." (*in preparation*)

Conference Communications

1. **Joana Pinto**, Inês Sousa, Pedro Vilela, Patrícia Figueiredo. "Dynamics of the BOLD response to breath-holding and paced deep breathing." *Human Brain Mapping (HBM) Congress*, 2014.

2. **Joana Pinto**, João Periquito, Pedro Vilela, Patrícia Figueiredo. "Characterization of the BOLD response across the brain to different breath-holding tasks." *Human Brain Mapping (HBM) Congress*, 2015.

3. **Joana Pinto**, Pedro Vilela, Michael A. Chappell, Patrícia Figueiredo. "Impact of calibration method on the reproducibility of CBF mapping using multiple post-labeling-delay PASL." *24th Annual Meeting of the International Society of Magnetic Resonance in Medicine (ISMRM)*, 2016. Oral Presentation.

4. **Joana Pinto**, Michael A. Chappell, Patrícia Figueiredo. "Impact of calibration method on CBF multi-session reproducibility using multiple post-labeling-delay pCASL." *33rd Annual Meeting of the European Society of Magnetic Resonance in Medicine and Biology (ESMRMB)*, 2016, Oral Presentation (Lightning Talk).

5. **Joana Pinto**, Sandro Nunes, Marta Bianciardi, Afonso Diasm Luís M. Silveira, Lawrence L. Wald, Patrícia Figueiredo. "Region-specific modeling of heart rate and respiratory volume signal contributions in whole-brain high-spatial resolution resting-state fMRI at 7 Tesla." *25th Annual Meeting of the International Society of Magnetic Resonance in Medicine (ISMRM)*, 2017.

6. **Joana Pinto**, Sandro Nunes, Marta Bianciardi, Afonso Diasm Luís M. Silveira, Lawrence L. Wald, Patrícia Figueiredo. "Impact of physiological noise optimization on functional connectivity measures in rs-fMRI at 7T." *Human Brain Mapping (HBM) Congress*, 2017.

7. **Joana Pinto**, Pedro Vilela, Michael A. Chappell, Patrícia Figueiredo. "Impact of calibration method on CBF quantification using multiple post-labeling-delay PASL." *Joint Annual Meeting of the International Society of Magnetic Resonance in Medicine (ISMRM) and European Society of Magnetic Resonance in Medicine and Biology (ESMRMB)*, 2018.

8. **Joana Pinto**, Michael A. Chappell, Thomas W. Okell, Melvin Mezue, Andrew R. Segerdahl, Irene Tracey, Pedro Vilela, Patrícia Figueiredo. "Impact of calibration methods and processing options on CBF quantification using ASL." *University of Michigan ASL MRI Workshop*, 2019.

9. **Joana Pinto**, Tânia Charrua, Ana Fouto, Rita G. Nunes, Luisa Alves, Sofia Calado, Carina Gonçalves, Margarida Rebolo, Pedro Vilela, Miguel Viana-Baptista, Patrícia Figueiredo. "Breath-hold BOLD-fMRI cerebrovascular reactivity metrics predict cognitive impairment in cerebral small vessel disease" *27th Annual Meeting of the International Society of Magnetic Resonance in Medicine (ISMRM)*, 2019.

1.4.2 Awards

Additionaly, two communications were awarded with prizes:

- **Honorable Mention**: Joana Pinto, Inês Sousa, Pedro Vilela, Patrícia Figueiredo. "Reproducibility of vasoreactivity measurements using breath-hold in combination with BOLD fMRI." *2013 2nd Joint Meeting of the Portuguese Society of Neuroradiology (SPNR) and of the Spanish Society of Neuroradiology (SENR).* 2013.

- **Magna Cum Laude**: Joana Pinto, Pedro Vilela, Michael A. Chappell, Patrícia Figueiredo. "Impact of calibration method on the reproducibility of CBF mapping using multiple post-labeling-delay PASL." *24th Annual Meeting of the International Society of Magnetic Resonance in Medicine (ISMRM)*, 2016.

1.4.3 Invited Talks

- Berlin Ultrahigh Field Facility, Max Delbrück Center, December 2017, *"Human fMRI: an overview of acquisition and analysis methods"*

1.4.4 Internships

- Institute of Biomedical Engineering (IBME), University of Oxford, United Kingdom.

Short Term Scientific Mission in the scope of COST Action AID ("ASL in Dementia"), at the Institute of Biomedical Engineering (IBME), University of Oxford, under supervision of Prof. Michael A. Chappell. September-December 2015.

2

Basics of Cerebral Haemodynamics

Contents

This chapter contains a brief overview of the anatomy and physiology of cerebrovasculature. Key haemodynamic concepts, including *cerebral blood flow* and *cerebrovascular reactivity*, will be discussed further. This chapter will provide the anatomical and physiological background for the following chapter, where methods for cerebral haemodynamics imaging will be illustrated in more detail (Chapter 3).

2.1 Anatomy and Structure of Cerebrovasculature

The human brain is a key organ of the nervous system. Despite only contributing 2% to the total body mass, it receives an extraordinary amount of resources even at rest: 12-15% of the cardiac output, 20% of total body oxygen consumption, and 25% of total body glucose utilization (Tameem and Krovvidi, 2013; Villien et al., 2014). Nevertheless, the human brain has a limited capacity for storage, making the precise regulation of cerebral haemodynamics crucial for the maintenance of a steady supply (Ainslie and Brassard, 2014).

Blood is supplied to the brain through two major artery sets:

- two internal carotid arteries;
- two vertebral arteries.

The internal carotid arteries branch from the common carotid arteries and supply blood to most of the cerebrum (80% of all brain blood (Nolte, 2009)). Their most important branches are the anterior and middle cerebral arteries (ACA and MCA, respectively). The vertebral arteries supply the remaining 20% of brain blood, perfusing the brainstem and cerebellum as well as some parts of the spinal cord, diencephalon, temporal, and occipital lobes (Nolte, 2009). These arteries branch into the posterior inferior cerebellar artery, the anterior spinal artery and the basilar artery. The latter branches into anterior inferior cerebellar artery, pontine arteries, superior cerebellar artery, and also ascends along the inferior surface of the brainstem forming two posterior cerebral arteries (PCA).

The ACA and MCA are connected to the PCA through the posterior communicating artery, forming the cerebral arterial circle, commonly known as Circle of Willis (Figure 2.1). When a supplying artery is compromised, the Circle of Willis allows redistribution of blood. Nevertheless, the anatomic structure of the circle of Willis varies substantially between individuals (Papantchev et al., 2013) and frequently the arterial circle is incomplete.

Each of the major cerebral arteries (ACA, MCA and PCA) supplies blood to specific regions of the brain (Nolte, 2009). The ACA mainly supplies the medial and inferior frontal lobe, medial parietal lobe, cingulate gyrus in the limbic lobe, and the corpus collosum. This artery can be divided into five segments, from A1 to A5. The left and right ACA are connected by the anterior communicating artery. Regarding MCA, the four main branches, M1 to M4, supply parts of the lateral cerebral cortex as well as the inferior frontal lobe, the temporal pole of the temporal lobe and the insular cortices. Finally, the PCA supplies the medial inferior part of the temporal lobe,

the medial inferior occipital lobe, the parahippocampal gyrus, the hippocampus, parts of the corpus callosum, and parts of the brainstem. Regions supplied simultaneously by two separate group of arteries are called watershed areas (Momjian-Mayor and Baron, 2005).

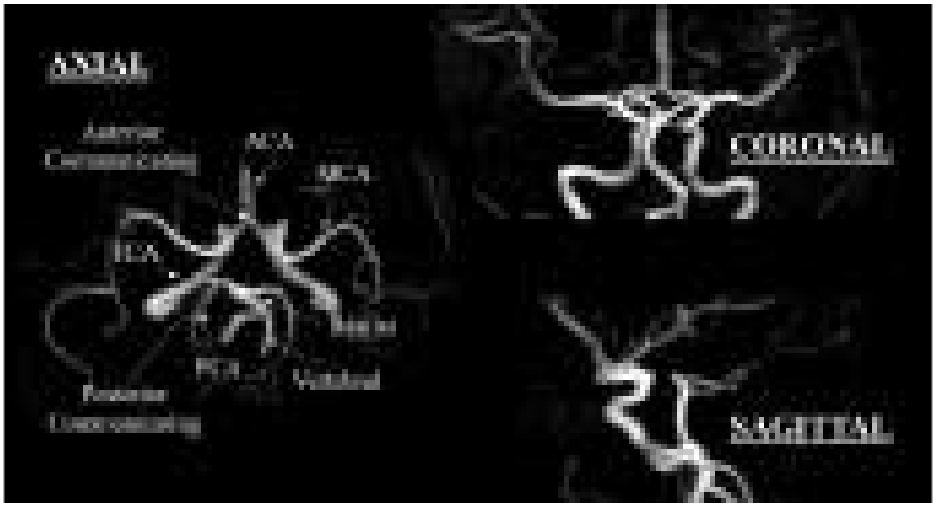

Figure 2.1: Illustrative example of an MR time-of-flight image in the three anatomical planes (axial, coronal and sagittal), displaying the major cerebral arteries and the Circle of Willis.

The main cerebral arteries also give rise to smaller branches: the superficial/pial and the deep perforating arteries (Cipolla, 2009). The latter are small branches that supply deep cerebral structures such as the basal ganglia or the internal capsule and are the terminal vessels of medium-sized arteries or the Circle of Willis. The pial arteries are usually located on the surface of the brain and emerge directly from medium-sized vessels (Pantoni, 2010). The walls of small arteries can be surrounded by fluid-filled cavities know as perivascular spaces or Virchow-Robin spaces (Kwee and Kwee, 2007). There are three types of perivascular spaces, depending on their location: (i) located along the lenticulostriate arteries entering the basal ganglia; (ii) located along the area supplied by the perforating arteries as they enter the cortical gray matter and extend into the white matter; and (iii) located in the midbrain (Kwee and Kwee, 2007). These spaces are thought to be part of a brain fluid transport system that facilitates interstitial fluid exchange and clearance of waste products from the brain (Brown et al., 2018).

As arteries dive down into the brain tissue, they transition into penetrating arteries and parenchymal arterioles and the perivascular spaces disappear (Jessen et al., 2015). Subsequently, the capillary bed is comprised of a dense network of cells and other entities. This network, that includes endothelial cells, pericytes, smooth muscle cells, astrocytes, microglia, oligodendrocytes and neurons, is collectively known as *the neurovascular unit* (Iadecola, 2017; Jessen et al., 2015). The neurovascular unit is important for disease processes and is thought to be one of the primary sites of dysfunction for some disease states (Cipolla, 2009).

The different types of cerebral vessels can also be differentiated in terms of their structure (Figure 2.2). Arteries are thick-walled vessels, comprised of three concentric layers: tunica intima

(endothelium and internal elastic lamina), tunica media (smooth muscle, elastin and collagen fibers) and, tunica adventitia (collagen fibers, fibroblasts and others specific cells including perivascular nerves) (Cipolla, 2009). Bigger arteries can be subdivided into elastic and muscular vessels. The elastic arteries receive blood directly from the heart (e.g. aorta and its branches) and their elastic mechanism is used to store and dissipate energy originated from the contraction of the heart. Their tunica media is broad and contains elastin and collagen but only few smooth muscle fibers. Due to this characteristic, elastic arteries are able to expand and recoil intensely, maintaining a relatively constant pressure in the arteries despite blood flow pulsation. Then, the muscular arteries draw blood from the elastic arteries and branch into the resistance vessels: small arteries and arterioles. In contrast to elastic arteries, the level of elastin in muscular arteries is now reduced and blood pulsation begins to decline. Their tunica media is composed mainly of smooth muscle, with some elastin and collagen. Arterioles tend to have less elastic but more smooth muscle cells than arteries, having greater flexibility to control their diameter. Nevertheless, blood no longer pulses as it gets through this type of vessel. Finally, the capillaries are the narrowest of blood vessels and they form a dense mesh, also know as capillary bed. This is where the gases and nutrients are exchanged between the blood and the tissues (Cipolla, 2009). The absence of smooth muscle and connective tissue layers allows a more rapid exchange of materials between the blood and the tissues (Julian Seifter et al., 2005).

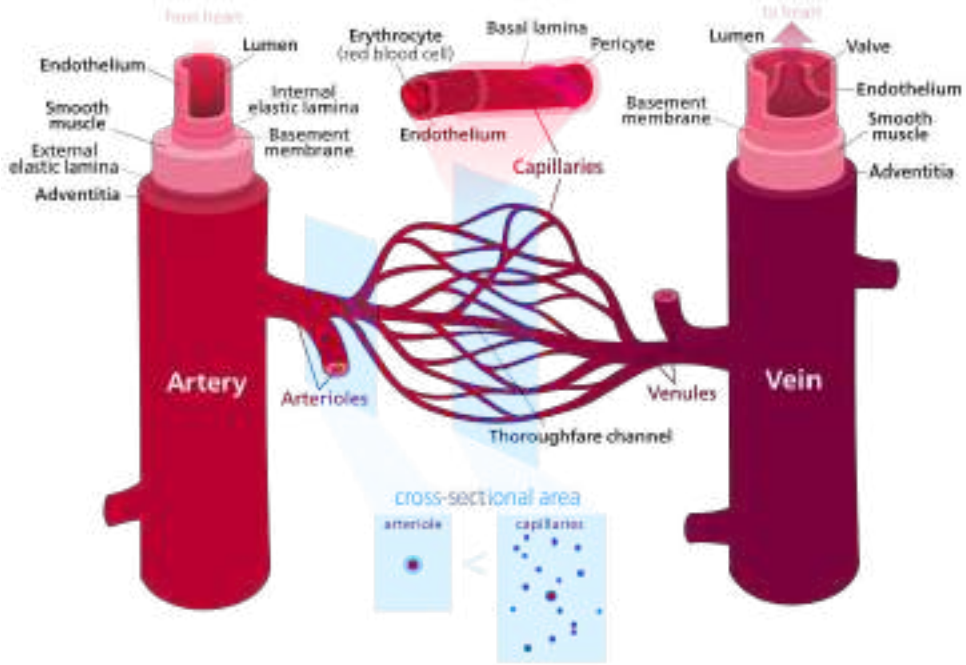

Figure 2.2: Illustrative scheme of the different blood vessels (arteries, arterioles, capillaries, venules and veins) and their structure. This figure is licensed under version 3.0 of the Creative Commons CC-BY-SA license (author: Kelvinsong).

2.2 Cerebrovascular Haemodynamics Concepts

One of the major breakthroughs in cerebral haemodynamics research occurred in 1881, when italian physiologist Angelo Mosso showed stronger brain and forearm pulsations during cognitive events, suggesting a close relationship between cerebral blood flow (CBF) and brain function (Sandrone et al., 2014). Roy and Sherrington further characterized this relationship by attributing vasodilation and an increase in CBF to an increased demand for cerebral metabolism in response to neuronal activity (Roy and Sherrington, 1890). CBF and metabolism were first measured quantitatively in monkeys in 1942 by Dumke and Schmidt and six years later, another breakthrough occurred when Kety and Schmidt observed in humans that, when inhaling nitrous oxide (NO), CBF is dramatically increased by elevation of arterial partial pressure of carbon dioxide ($PaCO_2$) (Kety and Schmidt, 1945). This method led to global acceptance of the hypothesis that cerebral activity, blood flow and metabolism are all linked and laid the foundations for modern functional imaging of cerebral haemodynamics.

Key Parameters

Some key concepts are commonly used to characterize haemodynamics (Table 2.1). It is important to distinguish global from regional haemodynamic parameters. In this Thesis, the regional parameters are considered. For example, CBF is used to refer to regional CBF (or perfusion) rather than global CBF.

Cerebral blood volume (CBV) is defined as the fraction of blood vessels volume per unit of brain tissue volume. At rest, CBV average values are approximately 4 ml of blood vessels/100 ml of tissue (Rostrup et al., 2005). The arterial fraction of CBV (aBV) is approximately 30%, yielding an aBV of about 1 ml of arterial blood vessels per 100 ml of tissue (Ito et al., 2001). Another parameter of interest is the cerebral metabolic rate of O_2, $CMRO_2$. This parameter can be defined as the consumed oxygen per unit of tissue volume per unit of time. $CMRO_2$ depends on the oxygen extraction fraction (e.g. fraction of delivered O_2 that is extracted from the blood), CBF and arterial concentration of O_2 (Buxton, 2010). The brain has the highest metabolic requirements of any organ in the body, consuming 20% of basal oxygen at rest and relying almost completely on oxygen-dependent metabolism of glucose for energy production (Tameem and Krovvidi, 2013). Typical cortical rest values of $CMRO_2$ are 3.5 ml of O_2 per 100 g of brain tissue per min (Ainslie and Duffin, 2009). Finally, CBF, also know as cerebral perfusion, is defined as the volume of blood that reaches a defined mass of brain tissue in a given period of time, most commonly, milliliters of blood per minute per 100g of brain tissue (ml/100g/min). Average CBF values in humans are believed to be in the 40-60 ml/100g/min range (Ito et al., 2004; Rostrup et al., 2005) and approximately three times lower in white matter than in gray matter (approximate average values: 20 mL/100g/min and 70 mL/100g/min, respectively) (Taccone et al., 2013).

Table 2.1: Main Cerebral Haemodynamics Parameters.

Metric	Acronym	Definition	Units
Cerebral Blood Volume	CBV	Volume of blood present in 100g of tissue	ml/100g
Cerebral Metabolic Rate of Oxygen Consumption	$CMRO_2$	Amount of oxygen metabolized by the brain per unit time	μmol/min
Cerebral Blood Flow	CBF	Volume of arterial blood that is delivered to 100 g of brain tissue per unit time	ml/100g/min

2.2.1 Cerebral Blood Flow

Since Kety and Schimdt's groundbreaking finding, CBF is found to be a key parameter in the adequate provision of nutrients and oxygen to the brain, being therefore essential to brain functioning. In steady state, CBF can be described mathematically by:

$$CBF = \frac{CPP}{Resistance} \tag{2.1}$$

where $Resistance$ is the resistance to flow and CPP is the cerebral perfusion pressure, given by Equation 2.2.

$$CPP = MAP - ICP \tag{2.2}$$

where MAP corresponds to the mean arterial blood pressure and ICP to the intracranial pressure. The corresponding equation for a single vessel states that the resistance of a vessel can be described by the Poiseuille equation of fluid dynamics, given by:

$$Resistance = \frac{8\mu L}{\pi r^4} \tag{2.3}$$

where μ is the viscosity of blood, L the length of the vessel and r the radius (Payne, 2016). As depicted in Equation 2.3, the resistance of a blood vessel is dependent upon radius, length and haematocrit. Assuming the last two are largely invariant in time, blood flow is mainly controlled through changes in vessel radius. Furthermore, Equation 2.3 also shows that vessel resistance is inversely proportional to the radius to the fourth power, meaning that even small changes in vessel radius can yield large changes in blood flow (Payne, 2016).

2.2.1.A Regulation of Cerebral Blood Flow

CBF regulation is achieved through the combination of several physiological effectors that work together to ensure optimal delivery of oxygen and nutrients. To date, these mechanisms remain quite poorly understood, in part due to the difficult brain vascular assessment *in vivo* and the complex nature of cerebral vasculature and its corresponding dynamics. Nevertheless,

several hypothesis for CBF regulatory mechanisms have been proposed throughout literature, including an integrative view described by Ainslie et al. that states that the principal regulators of CBF are (Ainslie and Duffin, 2009; Willie et al., 2014):

- **arterial blood gases** (chemical regulation);
- **mean arterial pressure** (autoregulation);
- **autonomic nervous system** (neurogenic regulation);
- **nerve cell activity** (metabolic regulation);
- **systemic factors** (systemic regulation).

CBF regulation via arterial blood gases changes is the basis for the work of this Thesis. Nevertheless, the other regulators may concurrently affect the vascular tone, so they will also be addressed.

Arterial blood gases

CBF is most sensitive to changes in arterial blood gas levels. It is consensual that an increase in $PaCO_2$ relative to normal values, also known as hypercapnia, results in relaxation of the vascular smooth muscle of vessels, leading to vasodilation (Wei et al., 1980). This change is normally credited to occur at the level of the arterioles and capillaries (Ainslie and Duffin, 2009). The opposite condition, know as hypocapnia, where there is a decrease in $PaCO_2$ levels, leads to a vasoconstrictor effect but this seems to be dependent on vessel size (Wei et al., 1980).

As mentioned previously, the effect of carbon dioxide (CO_2) level on CBF was already observed in 1948 by Kety and Schmidt. In 1964, Reivich et al. further worked on this interaction, proposing a CBF-$PaCO_2$ relationship (Equation 2.4), based on animal models (Reivich, 1964)

$$CBF = 20.9 + \frac{92.8}{1 + 10570e^{-5.251log(PaCO_2)}} \tag{2.4}$$

The mechanism behind these CO_2-driven CBF changes remain to be fully understood, although it is widely considered that CO_2 does not act directly on the smooth muscle of vessels but instead determines local pH levels. After CO_2 enters the blood stream, this molecule reacts with water forming carbonic acid, H_2CO_3. This process is accelerated by the enzyme carbonic anhydrase, which leads to the rapid dissociation of the carbonic acid into bicarbonate ions and a free proton, that are easily dissolved in the plasma for removal (Equation 2.5). These end products affect the local pH, that causes a range of signaling pathways to be initiated, ultimately leading to changes in vascular tone.

$$[CO_2] + [H_2O] \iff [H_2CO_3] \iff [H^+] + [HCO_3^-] \tag{2.5}$$

Increased CO_2 content and, consequently, decreased pH level, results in the opening of potassium (K^+) channels on smooth muscle cells. This will lead to endothelial cell hyperpolarization that decreases the activity of voltage-dependent calcium (Ca^{2+}) channels, diminishing intracellular Ca^{2+} and ultimately leading to direct relaxation of the smooth muscle and vasodilation (Ainslie and Duffin, 2009; Jackson, 2005).

Other alternative or complementary hypothesis is the CO_2/pH-induced alterations in vasodilating factors, including shear stress-mediated release of nitric oxide (NO) and prostaglandins as well as adrenomedullin and C-natriuretic peptide (Ainslie and Duffin, 2009). NO is created from an aminoacid, L-arginine, through the action of a number of NO synthase enzymes, within the endothelial cells. It stimulates the production of cyclic guanosine monophosphate (cGMP), which in turn activates protein kinase G, resulting in the uptake of Ca^{2+} and the opening of calcium-activated K^+ channels, leading to a reduction in vessel tone (Payne, 2016).

Regarding PaO_2, over the normal physiological ranges, CBF is known to be less sensitive to changes in its tension level. However, it has been observed that hyperoxia causes vasoconstriction, while hypoxia causes vasodilation. Nevertheless, it is not straightforward to separate the effects of PaO_2 and $PaCO_2$ levels, with hypoxia-induced activation of peripheral chemoreceptor activity leading to hyperventilation-induced lowering of $PaCO_2$ and subsequent cerebral vasoconstriction (Ainslie and Duffin, 2009).

Mean arterial pressure

The term cerebral autoregulation was first used in 1959 by Lassen (Lassen, 1959). In his review work, he extracted measurements from seven studies, plotting mean values of CBF against MAP, describing a plateau region where CBF is relatively stable across a significant range of arterial blood pressures (50-150 mmHg) (Lassen, 1959; Payne, 2016; Taccone et al., 2013).

In normal conditions, in order to maintain CBF stable within that range, a raise in MAP will lead to vasoconstriction, whereas a decrease induces vasodilation (Taccone et al., 2013). Interestingly, recent analyses observed that in fact, the CBF-MAP relationship does not remain constant through a broad range of pressures, as previously described and commonly cited in literature, and that, although the autoregulatory mechanisms do indeed exist, they are dependent on the degree and direction of the change (Willie et al., 2014).

The mechanisms behind autoregulation still remain to be fully understood, although there is evidence for a combination of several effectors such as the sympathetic nerve activity, neuronal and myogenic mechanisms (Willie et al., 2014). Already in 1902, Bayliss et al. proposed that the autoregulation mechanism would be essentially myogenic (Bayliss, 1902), although more recent studies have demonstrated a potentially greater role of larger arteries and their anatomy (Schubert et al., 2011), of pericytes at the capillary scale (Hall et al., 2014; Payne, 2016) and of the activation of specific receptors and second messengers, including cGMP (previously introduced). There have also been a number of reports on the influence of CO_2 on cerebral autoregulation:

mild hypercapnia has been shown to impair autoregulation, whereas hypocapnia may lead to variable effects (Ainslie and Duffin, 2009).

Autonomic nervous system

Cerebral circulation is richly innervated with sympathetic nerve fibers. However, the role of the sympathetic nerve activity in CBF regulation remains controversial and seems to be minor in rest, most likely because it is masked by other more powerful regulators (Ainslie and Duffin, 2009; Payne, 2016).

Nevertheless, the sympathetic nerve activity can release neurotransmitters into the perivascular space that influence vascular tone (mainly vasoconstriction), such as norepinephrine and neuropeptide-Y. Most intrinsic nerves also connect to astrocyte foot processes, indirectly altering vascular tone (more details will be provided in the next subsection, *nerve cell activity*). Some reports suggest that sympathetic nerve activity serves a protective function for the cerebral microcirculation (Ainslie and Duffin, 2009). Another hypothesis is that sympathetic nerve activity influences the reactivity of CBF to CO_2, through the control of the vascular smooth muscle of arterioles via sympathetic innervation, in particular from the brainstem control center.

Nerve cell activity

This regulator corresponds to increases in CBF in response to neuronal activation so that increases in the metabolic demand may be met. This coupling is thought to be mediated during synaptic transmission through various molecules, including CO_2, O_2, K^+, Ca^{2+}, H^+ and adenosine (Zauner and Muizelaar, 1997). Adenosine, which is formed from adenosine triphosphate breakdown during energy consumption, appears to play a significant role in glutamate-induced dilation of pial arterioles (Peterson et al., 2011). Astrocytes are also a possible mediator in this hypothesis. These cells are highly connected with each other and are known to release vasoactive factors upon changes in Ca^{2+} level at their end-feet, caused by electrical neuronal activity or increased glutamate, inducing vasodilation (Ko et al., 2008). Furthermore, hyperpolarization of pericytes has been shown to lead to their relaxation and capillary dilation (Hall et al., 2014)

Systemic factors

It has been recently established that CBF can be also dependent on cardiac output (Secher et al., 2008). These mechanisms have not been clearly delineated although some reports suggest a direct effect. For example, it has been observed that an increase in cardiac output with volume expansion and decrease with lower body negative pressure, linearly alters CBF velocity without changes in blood pressure and $PaCO_2$ (Ainslie and Duffin, 2009). The mechanisms behind this interaction are not fully understood, although flow-mediated mechanisms have been suggested. For instance, increased pulsatile pressure and/or blood flow leads to release of sheer stress

response of endothelial cells, which in turn results in a decrease in the resistance of arterioles and an increase in CBF (Ainslie and Duffin, 2009). Nevertheless, this mechanism may also interact with others. For example, during CO_2 reactivity testing, autonomic nervous system and heart rate levels change, subsequently also altering cardiac output (Ainslie and Duffin, 2009).

2.2.2 Cerebral Vascular Reactivity

Vessels have an intrinsic reactive mechanism that alters their calibre in response to changes in the arterial level of gases. This mechanism is known as cerebrovascular reactivity (CVR). CVR can be seen as potential biomarker for understanding how the cerebral vasculature controls the distribution of CBF but also for detection of cerebrovascular pathophysiology, since disease states of the brain may impair or abolish this CBF reactivity. In fact, impaired CVR has been shown to be associated with several pathological conditions, such as arterial stenosis/occlusion, Moyamoya disease or Small Vessel Disease (Heyn et al., 2010; Mandell et al., 2008a).

Nevertheless, the use of advanced imaging techniques has revealed that even in healthy subjects, there are differences in CVR spatiotemporal dynamics, reflecting regional differences in cerebral vascular tone and response (Kastrup et al., 1998; Leoni et al., 2008; Thomason et al., 2005). For example, CVR amplitude is higher in gray matter than in white matter. Additionally, in terms of timing, gray matter regions tend to react faster than white matter regions. Nonetheless, even within each tissue there are regional differences in the vascular response, rendering the need to study voxelwise dynamics (Figure 2.3).

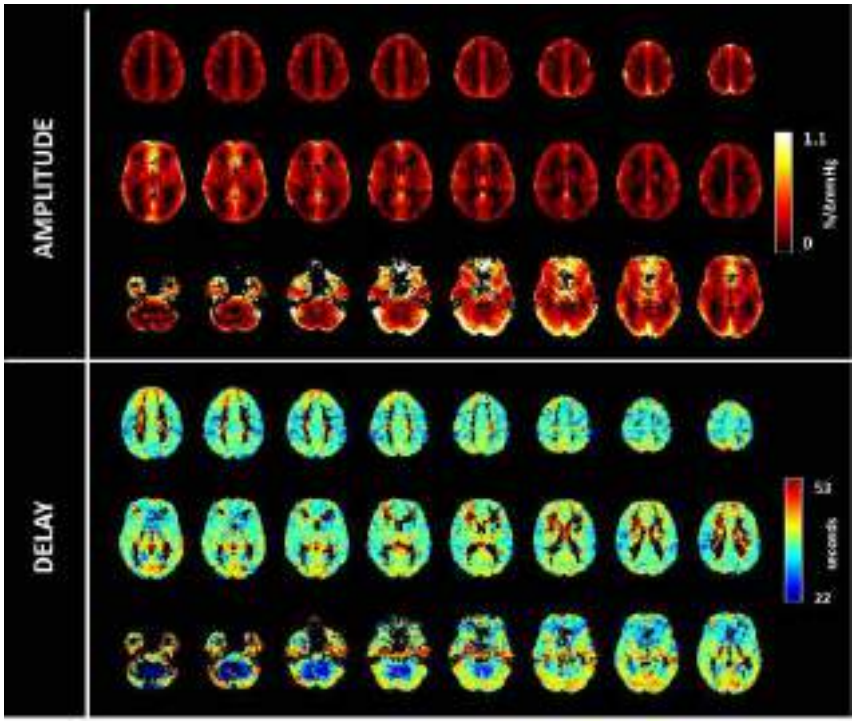

Figure 2.3: Illustrative examples of average CVR amplitude and delay maps across 10 healthy subjects.

Mapping those differences across the brain is not only important for the investigation of CBF regulation mechanisms and dynamics in a healthy brain, but also to detect any pathology-related deviations. Furthermore, negative CVR values can be observed when a vasoactive stimulus results in the redistribution of CBF from regions of exhausted CVR to areas with preserved CVR capacity (Conklin et al., 2010). It has also been shown that CO_2 reactivity is influenced by the degree of wakefulness. Studies have reported reduced CVR during sleep and elevated CVR during exercise (Ainslie et al., 2007; Meadows et al., 2003; Rasmussen et al., 2005). CVR mapping can also be used for other purposes, such as a normalizing factor in task-induced fMRI studies, in order to reduce inter- and intrasubject variability (Handwerker et al., 2007; Thomason et al., 2007).

CVR evaluation is usually performed through the application of a vasoactive stimulus and a subsequent measurement of the vascular response. The ideal challenge for CVR assessment should be safe, non-invasive and should produce a CBF change that is measurable in a reproducible way using an appropriate imaging method. Most of the existing reports suggest that $CMRO_2$ is not significantly altered by changes in $PaCO_2$ (Mandell et al., 2008b; Novack et al., 1953). For quantitative interpretation of results, i.e, to express CVR as percent signal change in CBF per mmHg change in $PaCO_2$, it is critical to quantify $PaCO_2$ during CVR assessment. However, direct measurement of this pressure requires blood sampling, making it highly invasive and, for that reason, the end-tidal pressure of gases generally acts as non-invasive surrogate ($PETCO_2$ and $PETO_2$).

A brief overview of the methods that induce a variation in CBF, allowing CVR mapping, can be found in Appendix A, although the non-invasive methods will be discussed more thoroughly in Chapter 5. The imaging techniques being used to evaluate cerebral haemodynamics, including CVR, will be discussed in the next chapter (Chapter 3).

3

Imaging Cerebral Haemodynamics

Contents

This chapter will begin with a brief introduction of some of the most important imaging techniques being used to evaluate cerebral haemodynamics, followed by an introduction of the basics of the two most common contrasts for functional magnetic resonance imaging (fMRI), namely Blood Oxygen Level Dependent (BOLD) and Arterial Spin Labeling (ASL).

3.1 Overview of Imaging Methods

Since its introduction in 1989 by Aaslid et al. (Aaslid et al., 1989), Transcranial Doppler Ultrasound (TDU) has become one of the most commonly used techniques for measuring blood flow velocities in cerebral vessels with large caliber (Haussen et al., 2012; Markus et al., 2000; Müller et al., 1995; Petrica et al., 2007; Schwertfeger et al., 2006; Silvestrini et al., 1999). The mean flow velocities assessed by TDU can then be used as an indirect estimation of global cerebral blood flow (CBF). TDU is a widely available and inexpensive technique that does not require exposure to ionizing radiation, making it completely non-invasive. TDU's main disadvantage still remains its poor spatial resolution, with only a few windows for ultrasound transmission existing across the skull (Markus et al., 2000). Consequently, this method cannot evaluate regional CBF, limiting brain haemodynamics mapping.

A number of other imaging methods are based on the Fick principle, measuring the concentration of a tracer that is administered in the circulation and diluted in the blood, hence acting as a CBF tracer. By application of the appropriate tracer kinetic theory, it is then possible to quantify CBF based on the tracer concentration-time curve. One of these techniques is the Xenon computed tomography (Xe-CT). Xe-CT is based on the inhalation of ^{133}Xe gas, which is a radioactive, diffusible CBF tracer. However, it requires the use of ionizing radiation and radioactive gas, making it invasive and expensive (Pindzola et al., 2001). Another CT based technique is the Perfusion Contrast Tomography, which is based on the intravenous injection of a nondiffusible iodinated contrast (Wintermark et al., 2005). The major disadvantages of this method are the use of ionizing radiation and the adverse effects of iodinated contrasts.

Using the same tracer kinetics principles, CBF can in principle also be measured by Positron Emission Tomography (PET) through the administration of ^{15}O-labeled water ($^{15}H_2O$). However, the requirement of an onsite cyclotron, extremely high costs and use of ionizing radiation severely limit the clinical applicability of this technique (Carroll et al., 2002). Single-photon emission computed tomography (SPECT) is probably the nuclear medicine technique most widely available for cerebral haemodynamics assessment (Aso et al., 2009; Kim et al., 2000; Sato et al., 2011). However, like PET, it involves the administration of a radioactive tracer, is expensive and provides poor spatial resolution.

More recently, it has become possible to evaluate cerebral haemodynamics non-invasively and with relatively high spatial and temporal resolution by magnetic resonance imaging (MRI). For regional haemodynamic assessment, approaches based on the use of exogenous agents can be applied. In principle, dynamic susceptibility contrast (DSC) allows estimation of several

haemodynamic parameters, including CBF, cerebral blood volume (CBV) and mean transit time, by making use of an intravascular CBF tracer, usually gadolinium-based, that causes local changes in susceptibility and therefore in the transverse relaxation time mechanisms (T_2/T_2^*). Dynamic contrast enhanced (DCE) is another method relying on relaxivity mechanisms, i.e., longitudinal relaxation time mechanisms (T_1) which, in the brain, are however only observable when blood-brain barrier leakage occurs. In this case, DCE allows estimation of other tissue specific parameters, such as transfer constant (K^{trans}), volume fraction of the extravascular extracellular space (v_e), the volume fraction of plasma (v_p) and the flux rate constant (k_{ep}) (Shin et al., 2014).

Truly quantitative measurements of CBF can only be obtained by MRI using ASL (Alsop et al., 2015; Golay et al., 2007). However, the BOLD contrast is still the most commonly used functional MRI (fMRI) contrast. Nevertheless, BOLD is qualitative and represents the combined effect of several haemodynamic parameters including CBF, CBV and blood oxygenation. More recently, the vascular-space occupancy (VASO) contrast has also been developed to non-invasively quantify CBV (Lu et al., 2003).

Throughout this Thesis, the focus will be on BOLD and ASL fMRI contrasts. Hence, more detailed descriptions of these contrasts will be provided in the next sections.

3.2 Blood Oxygen Level Dependent Contrast

3.2.1 Basis of BOLD Contrast

In 1990, Ogawa and colleagues verified that changes in blood oxygenation can lead to changes in MRI signal and called this the BOLD contrast. This was achieved by observing an MRI signal loss around blood vessels of cat brains under hypoxia and this effect was reversed with normoxia (Ogawa et al., 1990). In fact, back in 1936, Pauling and Coryell had already observed that haemoglobin (Hb), a protein of red blood cells, can behave as a diamagnetic substance when bound to oxygen or paramagnetic substance when deoxygenated (deoxyhaemoglobin, dHb) (Pauling and Coryell, 1936), thus affecting the local magnetic susceptibility of blood. Consequently, these changes in local magnetic susceptibility will produce distortions in the applied magnetic field, altering transverse relaxation mechanisms. In particular, the time constant T_2 describes the relaxation along the plane perpendicular (transverse) to the main/static magnetic field, B_0, and arises from the loss of phase coherence caused by interactions with neighboring nuclei (spin-spin interactions). Additionally, transverse relaxation is also affected by different sources of off-resonance including inhomogeneities in the main magnetic field, caused by both the intrinsic defects in the magnet itself or the different magnetic susceptibilities produced by the tissue and/or other materials, such as the dHb in the blood. The combination of this effect and T_2 relaxation is characterized by the time constant T_2^*. In 1982, decreases in the T_2 (and also T_2^*) of blood were observed as a function of decreases in blood oxygenation (Thulborn et al.,

1982).

The BOLD contrast may be obtained using either spin-echo (T_2-weighted) or gradient-echo (T_2^*-weighted) acquisition sequences. In both cases, the BOLD effect depends on a wide range of physiological factors, including not only the local amount of blood volume (CBV) and blood oxygen saturation, but also the size of blood vessels. During the time scale of an echo time (TE), water molecules undergo some degree of diffusion inside and across the blood vessels; if the blood is somehow paramagnetic, namely in the capillaries and venules, then diffusion across the associated magnetic field gradients will induce the accumulation of phase offsets. These T_2 effects are most pronounced for the smallest vessels, i.e. the capillaries, for which the field gradients seen by the diffusing molecules are steepest. In the larger venules, diffusion across a relatively shallow field gradient produces only negligible T_2 effects. In contrast, T_2^* effects produced by off-resonance protons along the field gradient are relatively insensitive to vessel size. The vessel sensitivity of T_2 effects render them more specific than T_2^* effects to oxygenation changes in the capillaries, which is often desired. However, because T_2^* effects are generally larger than T_2 effects, gradient-echo sequences are most commonly used to measure the BOLD signal in order to achieve sufficient SNR. In this Thesis gradient-echo sequences will be used to achieve BOLD contrast.

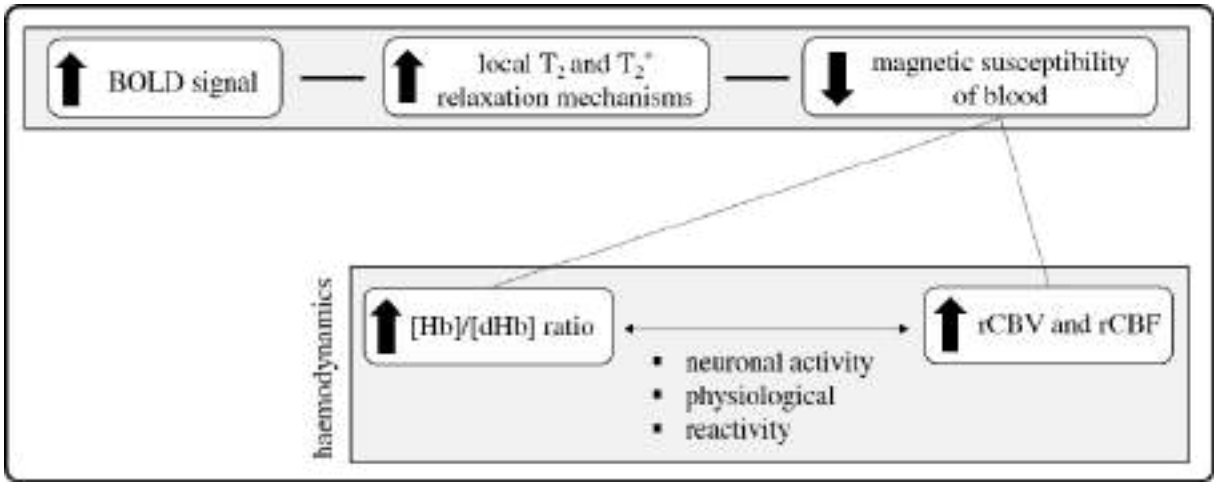

Figure 3.1: Schematic illustration of the relationship between BOLD-fMRI signal and haemodynamics.

Overall, the BOLD signal is a complex function of several underlying physical and physiological factors (Figure 3.1). Nevertheless, it can be assumed that the BOLD signal depends on the level of blood oxygen saturation (and hence also variations in CBV, i.e., CBF), and that any changes in these parameters will lead to a BOLD signal change, regardless of their origin. In particular, neurovascular coupling mechanisms lead to BOLD signal changes associated with neuronal activity. This type of activity relies on the availability of oxygen and glucose, which must be supplied by the vascular system through the blood. Overall, a local increase in neuronal activity will lead to an increase in the O_2 consumption, which transiently decreases the Hb/dHb ratio concentration. Nevertheless, vasodilation is also triggered in the capillary bed leading to

a regional CBF increase and resulting in a net increase of the concentration of Hb relative to the concentration of dHb, resulting in a positive BOLD response, that occurs 5 – 8 s after the stimulus onset (Buxton, 2009). Then the BOLD response decreases over a few seconds, dipping below the initial baseline, often coined post-stimulus undershoot. Stabilization at its equilibrium occurs after a slow 12-18 s recovery. A negative inflection of the BOLD response after the stimulus onset, known as initial dip, is also described in a number of studies, possibly reflecting the decrease in oxygen saturation before the increase in CBF occurs. This dynamic BOLD response generated from a brief neuronal stimulus is usually referred to as the haemodynamic response function (HRF).

The HRF function is commonly used as a transfer function between a mathematical representation of the stimulus time-course and the associated BOLD response. By assuming a linear system, the BOLD response can be estimated by convolving a representative of the neuronal activation, such as stimuli/task time-course, with an HRF (Worsley and Friston, 1995). Usually a canonical HRF, defined as a double gamma function, is considered (Friston et al., 1998). Nevertheless, different brain regions, subjects, and conditions may lead to different haemodynamic responses, making the assumption of an unique HRF to some extent inappropriate. This issue is partially averted by adding the temporal derivative to the canonical HRF when modeling the BOLD signal time course, accounting for variations in both time-to-peak and onset time. Other strategies include the use of a Fourier basis set or a set of temporally optimized gamma-based HRFs.

Other contributors to BOLD signal contrast include spontaneous physiological changes not directly related to neuronal activity as well as changes induced by other stimuli such as CO_2 (CVR). The latter assumes that BOLD signal contrast is mainly elicited by CBF changes rather than metabolic demands. These mechanisms are fundamental to the work of this Thesis.

3.2.1.A High-field BOLD Imaging

MRI signal-to-noise ratio (SNR) is found to be approximately proportional to the applied field B_0, with thermal noise increasing linearly with B_0 and signal intensity increasing with its square (Edelstein et al., 1986). Additionally, the BOLD signal is also enhanced by other field strength-dependent factors, including an increase in effects due to magnetic susceptibility differences between blood containing dHb and surrounding tissues (Turner et al., 1993; van der Zwaag et al., 2009), shortening of T_2 and T_2^* of venous blood, resulting in higher GM spatial specificity at typical BOLD TEs (Gati et al., 1997; Yacoub et al., 2001).

Nevertheless, despite earlier studies characterizing the dominant aspect of thermal noise, recent studies have verified that at higher fields, there is also a significant increase in the contribution of non-thermal noise components, which include subject motion and physiological processes (Krüger and Glover, 2001; Krüger et al., 2001; Triantafyllou et al., 2005). Kruger et al. formally demonstrated that the total noise of an image, as measured by its standard deviation σ, is composed of two main components (Krüger and Glover, 2001):

$$\sigma = \sqrt{\sigma_0^2 + \sigma_p^2} \tag{3.1}$$

where σ_0^2 corresponds to the square-law sum of thermal noise and systematic noise components (e.g. scanner drift, technical imperfections) and σ_p^2 corresponds to fluctuations in the signal over time due to motion and physiological contributions, in particular associated with cardiac and respiratory functions. This component is thought to be dependent on the image signal S, $\sigma_p = \lambda S$, with λ being a constant that expresses the degree of degradation on the image signal by non-thermal processes, expected to be roughly independent of field strength (Krüger and Glover, 2001). Since SNR can be defined by $\frac{S}{\sigma}$ and assuming only purely thermal noise, $SNR_0 = \frac{S}{\sigma_0}$, the total SNR can be defined as:

$$SNR = \frac{SNR_0}{\sqrt{1 + \lambda^2 SNR_0^2}} \tag{3.2}$$

According to this relationship as SNR_0 increases, SNR approaches the asymptotic limit of $1/\lambda$, meaning that further increases in field strength yield only small increases in SNR (Triantafyllou et al., 2005).

3.2.2 Sources of the BOLD Signal

BOLD fMRI experiments are typically designed to detect changes caused by task-evoked stimuli contrasting against a baseline condition. These are the so-called *task-based* fMRI experiments. Then, using an appropriate statistical analysis method, it is possible to determine the brain regions that are significantly responsive to the stimuli applied. Nevertheless, BOLD signal can also be acquired in combination with task-free conditions, so-called *Resting State* fMRI. This modality is commonly used to assess *functional connectivity*, i.e., to infer temporal dependence between signal fluctuations of different brain regions. In contrast with the traditional task-based BOLD fMRI, the resting-state approach has the advantage of not requiring the performance of a task, being more easily integrated into clinical protocols (Liu, 2013).

Nevertheless, and as previously described, BOLD signal fluctuations result from several sources. For that reason, when using BOLD contrast for fMRI studies of brain activity, it is crucial to characterize and remove components of no interest in order to ensure that BOLD measures reflect changes related to the contributor of interest exclusively. In the specific case of neuronal activity, these non-neuronal processes are commonly referred as physiological noise. In task-evoked BOLD fMRI, since the timing and amplitude of the task are known *a priori*, it is in principle simpler to separate and remove non-neuronal components of BOLD signal, increasing statistical significance. However, resting-state fMRI analyses are not based on a previously defined task and/or model, instead searching for correlations in the BOLD signal, thus being more prone to contamination from other sources. These confounds can increase the apparent functional connectivity by introducing spurious similarities between the time series, but can also reduce it by introducing different confounds across regions (Murphy et al., 2013).

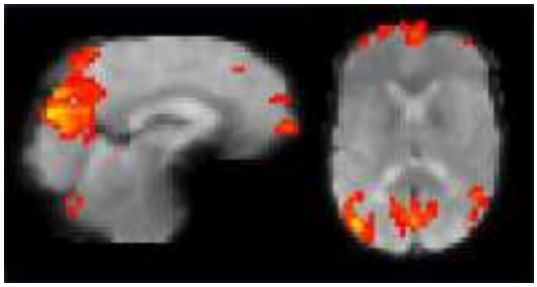

Figure 3.2: Illustrative example of a independent component depicting the Default Mode Network. The voxels significantly associated with the independent component are depicted in color (representing the Z statistic) overlaid on the EPI BOLD image, for one representative sagittal slice and one representative axial slice.

Nevertheless, these non-neuronal fluctuations might contain valuable information about cerebral haemodynamics, hence should not be disregarded. For that reason, both neuronal and non-neuronal contributions of BOLD-fMRI signals will be briefly described in the next subsections.

3.2.2.A Neuronal Activity

Even in the absence of a task, BOLD signal has intrinsic fluctuations that are thought to be of neuronal origin. Resting-state low-frequency fluctuations were first observed using fMRI by Bharat Biswal, when studying how different regions of the brain communicate when not engaging in any active task (Biswal et al., 1995). Interestingly, a few years later, a PET study demonstrated that the activity of a set of brain regions, as measured by OEF using ^{15}O, was ongoing when a person was not focused on a specific task and this activity was suspended during performance of an active task (Raichle et al., 2001). This finding reinforced the hypothesis that these regions constitute a network supporting a default mode of brain function, coined as the *default mode network* (DMN) (Figure 3.2). To date, the DMN is still the most notable and easily detectable network in resting-state fMRI (Greicius et al., 2003; Raichle et al., 2001) and, despite some researchers arguing that the DMN is the result of vascular coupling of large vessels, studies using other modalities (e.g. PET and electroencephalography (EEG)) have also observed these patterns, contradicting this vascular hypothesis (Buckner et al., 2008)

Resting-state fMRI studies have consistently identified a number of other so-called resting state networks (RSNs) in healthy subjects. In contrast to the DMN, these are task-positive networks decreasing their activity during rest compared to task and they include visual, auditory, and attention networks (Smith et al., 2009). These RSNs are identified as networks of functionally connected brain regions as assessed by the temporal correlation of their BOLD signals and represent well known functional networks also observed in task-based fMRI (Smith et al., 2009).

3.2.2.B Other Contributors

As mentioned previously, BOLD fMRI signal changes result from contributions of both neuronal and non-neuronal origins. The latter include head motion, cardiac (≈ 1 Hz) and respiratory (≈ 0.3 Hz) sources (Brooks et al., 2013; Cordes et al., 2001), which are commonly referred to as physiological noise. This component, if left uncorrected, may compromise the analysis of fMRI data, especially when studying spontaneous brain activity.

Head Motion Head motion is one of the most common and critical artifacts in fMRI (Van Dijk et al., 2012). The most evident impact of this BOLD modulator is the alteration of the content of a voxel. Head motion also modifies the uniformity of the magnetic field applied, and the locations of geometric distortions and signal dropout boundaries (Friston et al., 1996; Murphy et al., 2013). The use of head constraints and careful subject preparation prior to acquisition are commonly used methods to minimize the impact of this component on BOLD fMRI.

Cardiac and respiratory modulations Cardiac function leads to arterial pulsatility that results in deformation of brain tissue and originates small displacements as well as changes in CBV and CBF across the cardiac cycle (Dagli et al., 1999; Greitz et al., 1993; Krüger and Glover, 2001; Murphy et al., 2013). Regarding respiration, the thoracic modulation within each respiratory cycle produces head and chest motion as well as changes in the static magnetic field B_0 (Raj et al., 2001). Both the cardiac and respiratory-related signal changes induce quasi-periodic BOLD fluctuations, mainly near and within large blood vessels, in the former, and distributed across the brain, in the latter (Birn, 2012). Additionally, CSF flow is also modulated by both physiological cycles, resulting in further signal changes in or close to areas with high CSF content (Kao et al., 2008). Non-periodic BOLD signal fluctuations can also be induced, mainly due to changes in cardiac rate as well as minute ventilation (i.e. breathing depth and rate) (Birn et al., 2006; Shmueli et al., 2007). Bulk motion originated from the cardiac and respiration cycles will lead to similar confound effects as head motion (Murphy et al., 2013).

The recording and monitoring of additional physiological measurements during fMRI acquisition using pulse oximetry, electrocardiogram or respiratory belts can be quite useful to identify frequencies of interest. Nevertheless, due to the intrinsic long TR of common BOLD EPI acquisitions ($> 2s$) the associated BOLD fluctuations can be aliased into the low-frequency range, being mistaken as neuronal fluctuations. Models have been developed to predict BOLD fluctuations from concurrent cardiac and respiratory recordings (as will be discussed in Section 3.2.3.D). Furthermore, it has been shown that other BOLD fluctuations in the low-frequency range are significantly correlated with changes in cardiac and respiratory rates ($\approx$0.04 Hz for cardiac and $\approx$0.03Hz for respiration (Murphy et al., 2013), although these fluctuations are thought to be related to changes in arterial CO_2 concentration and blood pressure.

Arterial CO_2 Several studies based on respiratory manipulations, including hypercapnia and hypocapnia conditions, have described a very tight relationship between BOLD signal and end-tidal CO_2 ($PETCO_2$) fluctuations. Wise and colleagues demonstrated that 16% of spontaneous BOLD variance in gray matter can be explained by $PETCO_2$ fluctuations (Wise et al., 2004). Chang et al. compared the effect of respiratory volume and $PETCO_2$ levels, reporting a high correlation between these components, yielding similar performance in terms of spatial and temporal BOLD signal variance (Chang and Glover, 2009a). Nevertheless, more recently, Golestani and colleagues demonstrated that $PETCO_2$ fluctuations explain a unique portion of the BOLD fMRI signal variance compared to cardiac and respiratory components (Golestani et al., 2015).

Other contributors Arterial blood pressure fluctuates over time mainly due to autoregulatory mechanisms, maintaining a steady-state CBF. In animal models, increases in the amplitude of low-frequency BOLD fluctuations have been demonstrated with a decrease in mean arterial pressure (Biswal and Kannurpatti, 2009). It has also been shown that the heart rate and blood pressure contribute to about 10% of low-frequency oscillations in the Hb concentration (measured by Optical Topography), with the latter explaining approximately 5% (Katura et al., 2006). Pulse wave velocity measurements, a surrogate of arterial blood pressure, obtained using partially inflated pressure cuffs, also demonstrated that these metrics can explain between 3% and 14% of the variance in the global signal across subjects and that this relationship is almost instantaneous with the delay being less than a 3 s (Murphy et al., 2011a). Mitsis and colleagues demonstrated that blood pressure fluctuations explain most of the high-frequency CBF velocity variations detected by TDU (> 0.04 Hz), whereas CO_2 fluctuations and nonlinear interactions between pressure and CO_2 have a considerable effect in the lower frequency range (<0.04 Hz). Furthermore, they also observed that blood pressure accounts for 60% of the CBF fluctuations prediction power and the CO_2 only accounts for an additional 17% (Mitsis et al., 2004).

Even in the absence of a stimulus, the tone of cerebral blood vessels oscillates spontaneously in the low-frequency range (0.05 - 0.2 Hz) (Aalkjaer et al., 2011; Aalkjaer and Nilsson, 2005). This mechanism called vasomotion was first reported in 1853 (Jones, 1853) and to date is still controversial in terms of its association with other physiological confounds, although some reports suggest that this mechanism is independent of fluctuations in cardiac, respiratory, arterial CO_2 concentration and blood pressure fluctuations, and might stem from myogenic mechanisms (Hudetz et al., 1998; Nilsson and Aalkjaer, 2003; Pradhan and Chakravarthy, 2011). In fact, an ultra-fast fMRI study in humans observed that central nervous system fluid pulsations were detected in the very low (0.001 - 0.023 Hz) and low frequency (0.023 - 0.073 Hz) range, modifying the perivascular spaces volume (Kiviniemi et al., 2016). While pulsations generated from the R-wave of the cardiac cycle drove fluid movement in the peri-arterial regions ($\approx$ 1 Hz), pulsations generated from respiratory cycle drove fluid movement in the perivenous spaces ($\approx$ 0.3 Hz). A third type of fluctuations was also observed within even lower frequency range (0.001 - 0.73 Hz), displaying unique spatiotemporal dynamics (Kiviniemi et al., 2016).

3.2.3 BOLD Signal Analysis

Analysis of BOLD-fMRI data is most commonly performed on a voxel-by-voxel basis using univariate time series analysis methods, usually under the framework of general linear models. Multivariate data-driven methods can also be used, usually by employing independent component analysis (ICA).

3.2.3.A Model-Based Methods

The first method to ever be applied to resting-state fMRI data was the seed-based correlation analysis. Back in 1995, Biswal and colleagues used this method to compare the signal time-course of a previously defined region of interest, called the seed region, with all the other time-courses through a GLM analysis (Biswal et al., 1995).

General Linear Model The GLM is the most commonly used model-based method in fMRI data analysis. GLM can be seen as a generalization of a multiple linear regression model that, by using an univariate model of the BOLD signal over time, analysis each voxel's time series independently and describes the observed data as a linear combination of explanatory variables (EV) or regressors and a noise term. These EVs can be related to effects of interest, but can also be confounds that are not related to the experimental hypothesis (Smith et al., 2004). In fMRI studies, it is common to convolve the temporal waveform defined by the task onsets and durations with a canonical HRF, resulting in the quantification of an estimate of the BOLD signal for the condition of interest. Confounding factors can also be added on the GLM as additional EVs. The GLM can be formulate in matrix notation as it follows:

$$y = \beta \mathbf{X} + e \tag{3.3}$$

where y is a vector (N) corresponding to the signal measured at a specific voxel (N is the number of time points), matrix $\mathbf{X}$, often referred to as the design matrix, groups together all of the EVs (N $\times$ P, P is the number of EVs), and β is a vector (P) of the parameters that are estimated by fitting the model to the data and indicates how much the model effect contributes to the observed data. The higher it is, the better the fit. The error term vector (N), e, accounts for the residual error between the fitted model and the experimental data and it is generally modeled as an independently and identically distributed Gaussian random variable (Friston et al., 1995; Worsley et al., 2002). So the main goal is to find the β values that minimize the sum of squared residuals and this can be achieved by an Ordinary Least Squares (OLS) approach. The OLS solution for the estimate β is given by:

$$\hat{\beta} = (\mathbf{X}^T\mathbf{X})^{-1}(\mathbf{X}^T y) \tag{3.4}$$

To evaluate the statistical significance of a model effect for a given voxel, it is necessary to convert the β into a statistic. For the simple case of a GLM with a single regressor of interest t-statistic can be derived using (Friston et al., 1995)

$$t = \frac{\hat{\beta}}{std(\hat{\beta})} \tag{3.5}$$

In order to compare several contrasts at the same time, for example, to see whether any of them (or any combination of them) is significantly non-zero, it is also possible to use a F-test. Finally, the resulting statistical parameter map obtained in all voxels for each EV is then transformed into a Z-statistic image using standard statistical transformations. A thresholding procedure can then be applied according to a pre-defined level of statistical confidence in order to identify voxels exhibiting statistically significant effects. Different techniques can be used in order to account for the multiple comparisons arising from the massively univariate model fit performed across voxels. The most conservative approach is the Bonferroni correction, or voxelwise correction, but most commonly a less conservative correction can be achieved based on the theory of Gaussian random fields to take into account a certain degree of dependence between voxels, which is the case of the cluster thresholding method, where a threshold is used to define continuous clusters and then each cluster's estimated significance level is compared with the cluster probability threshold.

3.2.3.B Data-Driven Methods

In contrast to the GLM approach, independent component analysis (ICA) is an exploratory data-driven approach that does not require any prior information or predefined model (Comon, 1994; Hyvärinen and Oja, 2000). This strategy performs decomposition of a dataset into a number of underlying sources or independent components, by imposing their independence spatially or temporally (Brooks et al., 2013). When using spatial ICA, this method generates a spatial map and corresponding time-course for each component. It is common to apply this technique as an exploratory approach prior to any modeling or statistical inference in order to identify certain components. This step is usually performed by visual inspection or correlation with predefined RSN templates, although more robust and complex methods have been applied to overcome this issue, including automatic classification methods (Griffanti et al., 2014; Salimi-Khorshidi et al., 2014). ICA has also been shown to be capable to differentiate between instrumentation artifacts, neuronal-induced fluctuations or physiological sources, such as cardiac or respiratory (Beckmann and Smith, 2004).

3.2.3.C Other Analysis Methods

Retrieving information directly from spontaneous BOLD fluctuations can also be performed. The resting-state fluctuation amplitude (RSFA), computed as the temporal standard deviation of the time-series, has been used as a resting-state fMRI metric, yielding information about

signal variability. Subsequently, other metrics based on RSFA have also been derived, including the coefficient of variation (CV) (Jahanian et al., 2014, 2016) or the physiological fluctuation metric (PF) (Makedonov et al., 2013).

One aspect that all these resting state metrics have in common is the use of the whole signal frequency spectrum, not differentiating between frequency bands. Nonetheless, it has been demonstrated that neuronal-related BOLD activity is usually in the lower frequency band (<0.1 Hz). For that reason, other approaches have taken that information into account by separating the BOLD signal into its several frequency components. These approaches include the amplitude of low frequency fluctuations (ALFF) and fractional ALFF (fALFF) (Zuo et al., 2010). Metrics based on the amplitude of spontaneous BOLD fluctuations will be described in more detail in Chapter 5.

3.2.3.D Physiological Noise Modeling and Correction

One of the first attempts to remove the contribution of physiological BOLD fluctuations of no interest in BOLD-fMRI was to apply temporal filtering. However, since typical fMRI acquisition schemes use relatively long TRs (2 - 3 s), aliasing of both cardiac ($\approx$ 1 Hz) and respiratory ($\approx$ 0.3 Hz) components limits the ability to effectively use this approach (Bhattacharyya and Lowe, 2004). For this reason, other alternatives have been proposed, including model-based approaches, that require recording of external physiological measurements or BOLD fMRI itself, and data-driven methods.

Model-based approaches rely on the recording of external cardiac and respiratory signal measurements during MRI acquisition. Back in 2000, the retrospective image correction technique (RETROspective Image CORrection, RETROICOR) was proposed by Glover et al. (Glover et al., 2000) in order to model and correct contributions of cardiac and respiratory processes. This strategy is based on the retrospective correction method previously developed by Hu et al. (RETROKCOR) (Hu et al., 1995), that performs correction in k-space, prior to image reconstruction. In RETROICOR this correction is performed in image space by describing the cardiac and respiratory contributions to the BOLD signal and then regressing them out in a GLM framework. The quasi-periodic contributions of physiological processes are described by a low-order Fourier expansion based on the phases of the respiratory and cardiac cycles acquired externally (Equations 3.6 and 3.7).

$$y_c(t) = \sum_{m_c=1}^{M_c} \left(\beta_{1,m_c} \cos\left(m_c \phi_c(t)\right) + \beta_{2,m_c} \sin\left(m_c \phi_c(t)\right)\right) \tag{3.6}$$

$$y_r(t) = \sum_{m_r=1}^{M_r} \left(\beta_{1,m_r} \cos\left(m_r \phi_r(t)\right) + \beta_{2,m_r} \sin\left(m_r \phi_r(t)\right)\right) \tag{3.7}$$

where $y_c(t)$ and $y_r(t)$ are the estimated cardiac and respiratory contributions at a specific time point t, β_{1,m_c} and β_{1,m_r} denote the coefficients to be estimated by the GLM approach, m_r

and m_c are the order of the model and $\phi_r(t)$ and $\phi_c(t)$ are the cardiac and respiratory phases computed as:

$$\phi_c(t) = 2\pi \frac{t - t_1}{t_2 - t_1} \tag{3.8}$$

where t_1 and t_2 are the R peak times in the cardiac cycles, preceding and succeeding t, and

$$\phi_r(t) = \text{sign}\left(\frac{dx}{dt}(t)\right) \pi \frac{\sum_{b=1}^{round} (100x(t)/x_{\max})}{\sum_{b=1}^{100} H(b)} \tag{3.9}$$

where $H(b)$ represents a 100-bin histogram of the respiratory amplitude signal x. The use of $H(b)$ is motivated by head motion being additionally dependent on the depth of breathing within each cycle. The original work by Glover and colleagues proposed a Fourier expansion until second order, as higher terms did not add any significant information to the model (Glover et al., 2000).

Non-periodic fluctuations arising from cardiac and respiratory processes may also be retrieved and modeled using physiological traces, including the respiratory volume per unit time (RVT), proposed by Birn et al. (Birn et al., 2006). RVT models respiratory non-periodic fluctuations based on the timing and amplitude of the respiratory peaks. Birn et al. also proposed a respiratory haemodynamic function, the respiration response function (RRF) (Birn et al., 2008) (Equation 3.10), based on the deconvolution of the average response to a series of deep breaths and obtaining the double gamma parameters that best fit the deconvolved response.

$$RRF(t) = 0.6t^{2.1}e^{-t/1.6} - 0.0023t^{3.54}e^{-t/4.25} \tag{3.10}$$

A simpler metric, the respiratory volume (RV), also based on the respiratory waveform, was proposed by Chang et al. (Chang and Glover, 2009b). The RV was defined as the standard deviation of the respiratory trace on a sliding window of 3 TRs centered at each TR.

Regarding non-periodic fluctuations from cardiac processes, Shmueli et al. introduced a new cardiac regressor, taking into account changes in heart rate, and computed as follows (Shmueli et al., 2007):

$$HR\,(t_n) = \frac{1}{t_{n+1} - t_n} \tag{3.11}$$

where t_n are to the time instants corresponding to maximum peaks. After estimation of HR, the signal is usually subjected to removal of spurious time points. This is performed by replacing time points more than 1.96 standard deviation away from the local median by linear interpolation. The waveform is then smoothed using a Gaussian filter, followed by resampling to match the fMRI acquisition rate (Shmueli et al., 2007).

Subsequent work by Chang et al. yielded a cardiac response function (CRF) (Equation 3.12), the counterpart of the RRF, by deconvolution of the global BOLD fMRI signal using a Gaussian process (Chang et al., 2009).

$$CRF(t) = 0.6t^{2.7}e^{-t/1.6} - 16\frac{1}{\sqrt{2\pi(9)}}\exp\left(-\frac{1}{2}\frac{(t-12)^2}{9}\right) \tag{3.12}$$

These functions aim to characterize how physiological fluctuations are reflected on the measured BOLD signal. Nevertheless, the exact timing and shape of these effects are still unclear and variations between subjects can be observed. In order to overcome this issue, Bianciardi et al. developed a lag-based optimization approach, shifting the original non-periodic respiratory and cardiac regressors in a range of [-20 ; 20] s, in steps of 1 s. The optimal lag is then chosen by selecting the lag with the highest variance explained (Bianciardi et al., 2009a). Another approach that takes into account variations in the effects of physiological fluctuations on fMRI signal across subjects was proposed by Falahpour et al., employing subject-specific RRF and CRF response functions obtained by deconvolution of the global BOLD signal (Falahpour et al., 2013). Additionally, Wise and colleagues measured $PETCO_2$ level using a capnograph and included its waveform as confounding regressor in a GLM analysis (Wise et al., 2004) and, more recently, response functions to $PETCO_2$ were estimated voxelwise by Golestani and colleagues, using the same methodology as Chang et al. (Chang and Glover, 2009a; Golestani et al., 2015).

Techniques based on BOLD fMRI data itself and not requiring any additional physiological recordings can also be used to estimate and correct for physiological noise. In particular, components related to head motion are usually minimized by regressing out estimated head motion parameters. More abrupt approaches include outlier detection and subsequent removal. ICA-based methods are also commonly used to detect components of no interest including motion. Other approaches use tissue-specific or global signal averaged BOLD fMRI time-courses, to be regressed out from BOLD signal. These waveforms are commonly used as regressors since their signal fluctuations are unlikely to show any neuronal activity (Birn et al., 2009; Weissenbacher et al., 2009). Global signal regression has been widely used in resting-state fMRI connectivity studies, although this strategy has raised some concerns, since this signal might also include widespread neuronal contributions and removing these might undermine the purpose of this approach. Furthermore, it has been shown that global signal regression introduces anti-correlations between brain regions (Murphy et al., 2009; Weissenbacher et al., 2009), and can even generate correlation among regions that had no correlation prior to regression (Saad et al., 2012).

Despite the plethora of physiological noise removal methods, these different approaches likely reveal complementary insights into the brain's functional organization and connection. Nevertheless, the complex nature of BOLD signal limits the extent to which we can fully understand all these mechanisms. More direct metrics of cerebral haemodynamics, including ASL derived parameters, might provide useful information, hasting this process.

3.3 Arterial Spin Labeling Contrast

ASL MRI is an extremely appealing non-invasive tool that evaluates CBF in a potentially quantitative manner. ASL takes advantage of the high abundance of water molecules in the human body and cleverly uses blood water protons as an endogenous non-invasive CBF tracer. The underlying principle of ASL is that the arterial water molecules of blood in the neck region can be *labeled* or *tagged*. This labeling can be performed by applying radiofrequency (RF) pulses to saturate or invert the longitudinal magnetization of the water molecules. As blood flows into the region of interest, the magnetization relaxes towards equilibrium with T_1 of the blood and after a delay, generally known as inversion time (TI) or post-labeling delay (PLD), allowing for inflow of labelled blood, an image is acquired in the region of interest (Figure 3.3). This image is referred to as the *tag image* or *label image* and reflects signal from inverted magnetization of the inflowing blood and from the static tissue magnetization.

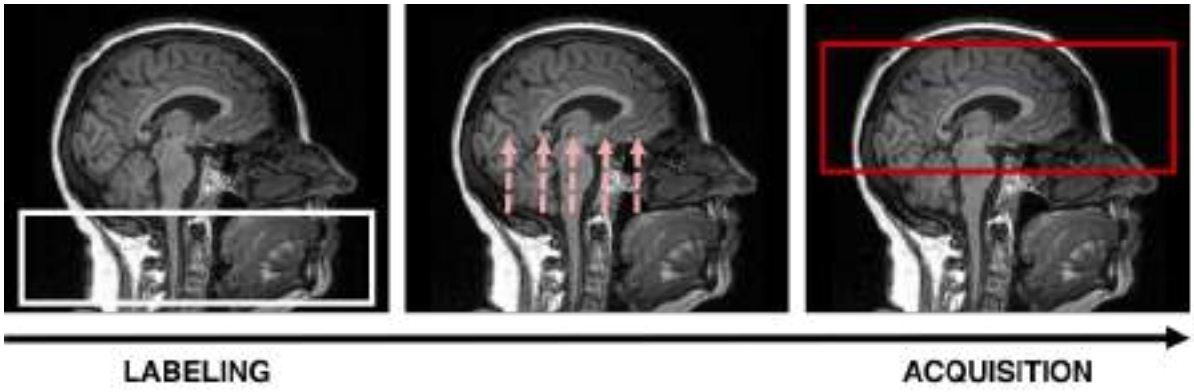

Figure 3.3: Schematic diagram of imaging and labeling regions for ASL imaging.

A second image in the same region is also acquired in a similar way but without the labeling process. In this case the blood is fully relaxed and reflects only the static tissue signal. This image is known as the *control image*. In the ideal case, the label and control images would be acquired at precisely the same time but since that can not be achieved, tag and control images are typically acquired in a temporally interleaved way. The subtraction of the control and tag images allows the removal of the contribution of the static tissue to the label image, yielding a magnetization difference image that is approximately proportional to CBF.

The greatest limitation of the ASL technique lies in its intrinsically very low SNR. For example, in the normal human brain at 3T, the signal produced by the delivery of blood is just about 1 - 2 % of the total signal (Golay et al., 2004). In order to obtain sufficient SNR, the acquisition of the label-control images is repeated multiple times and averaged. Furthermore, the short lifetime of the label and the fact that blood requires some time to travel from the labeling band to the region of interest will possibly confound results. In fact, in some cerebrovascular diseases the delay of the inflowing blood might be so great that there is no signal left by the time the blood reaches the tissue. Another issue is the possibility of the region of interest imaged

containing large vessels that are destined to perfuse more distal capillary vessels, leading to an overestimation of local CBF.

3.3.1 ASL Acquisition

Regarding the labeling of the arterial blood, a large number of techniques have been proposed over time (for a review see (Alsop et al., 2015), and for an update on recent advances see (van Osch et al., 2018)). Here we describe the four main ASL techniques that are currently available: pulsed ASL (PASL), continuous ASL (CASL), pseudo-continuous ASL (pCASL) (Figure 3.4), and velocity-selective ASL (VSASL) .

Continuous ASL

The first implementation of ASL was the CASL technique proposed initially by Detre et al. using multiple saturation pulses (Detre et al., 1992) and later by Williams et al. using inversion pulses (Williams et al., 1992). This scheme makes use of flow-driven adiabatic inversion to continuously invert the magnetization of the arterial blood water flowing through the labeling plane over a long period of time (typically 1–3 s) (Alsop et al., 2015). The labeling plane is positioned orthogonally to the carotid and vertebral arteries in the neck. Some disadvantages of this scheme are the significant saturation of brain tissue through magnetization transfer (MT) effects or the high RF power deposition, that most RF amplifiers cannot provide without modification. Solutions for the MT effects have been proposed, including the use of separate labeling and imaging coils (double-coil CASL) or the implementation of advanced labeling schemes to produce identical magnetization transfer effects in the volume of interest (Silva and Kim, 2003). Nevertheless, because of specific absorption rate limitations and additional hardware requirements, CASL is currently only rarely used.

Pseudo-continuous ASL

pCASL has been more recently proposed to overcome some of the CASL disadvantages, but still yielding a high SNR (Dai et al., 2008). pCASL uses a train of discrete RF pulses instead of a long and effective continuous RF pulse. This labeling scheme has higher inversion efficiency (85-95%) and lower RF power deposition than CASL. Variations of this technique include vessel-encoded pCASL, combining vascular territory imaging with pCASL by modifying the train of labeling pulses using transverse gradients and phase cycling to selectively tag the chosen arteries (Wong, 2007), yielding good reproducibility (Gevers et al., 2011). Currently, pCASL is the most often used and recommended ASL sequence (Alsop et al., 2015).

Pulsed ASL

A number of PASL techniques were proposed soon after CASL. In PASL schemes, a thick slab of tissue is inverted proximal to the imaging slice, using a single RF pulse or a short train of

pulses, with a total duration of typically 10–20 ms. PASL techniques can be divided into those that label spins asymmetrically or symmetrically with respect to the imaging plane.

The symmetrical PASL sequences are referred to as Flow-sensitive Alternating Inversion Recovery (FAIR) sequences (Kim, 1995). In this particular scheme, when performing labeling, a global inversion pulse is employed, labeling inside and outside the readout region (non-selective). For the control image, the inversion pulse is employed but with a slice-selection gradient aimed only at the readout slab (slice selective).

Asymmetrical PASL techniques are based on an original sequence called echo-planar imaging with signal targeting by alternating radiofrequency pulses (EPISTAR) (Edelman et al., 1994). In this scheme, the labeling slab is positioned at the same distance to the volume of interest as the control slab but proximally to it rather than distally. Subtracting label from control images yields a perfusion-weighted image where MT effects have been minimized. Another asymmetrical PASL scheme, derivative of EPISTAR, is the proximal inversion with control for off-resonance effects (PICORE) (Wong et al., 1997). The labelling is identical to EPISTAR with imaging slice saturation and proximal inversion pulses. The main difference is that the control image is acquired with off-resonance inversion pulse without the spatial encoding gradient.

One of the major drawbacks of PASL techniques is the uncertainty in the duration of the labeling bolus, i.e, the time that arterial blood takes to travel across the labeling slab. One way to control for this issue is improving the definition of the bolus. This can be achieved by introducing the Quantitative imaging of perfusion using a simple subtraction version II (QUIPSS-II) modification (Wong et al., 1998), in which a slab-selective saturation pulse is used in the same position as the labeling bolus to remove the tail end of the labeled bolus. The efficacy of this scheme was improved by introducing the quantitative imaging of perfusion using a simple subtraction version II with thin-slice TI1 periodic saturation (Q2TIPS) (Luh et al., 1999).

Compared to the CASL schemes, the SNR of the PASL approach is fundamentally lower due to the fixed width of the labeling slab, yielding smaller amount of labeled water. In contrast, the inversion efficiency of PASL (approximately 95%) is higher and the RF power deposition is lower.

Velocity-selective SASL

In VSASL the labeling is based on velocity rather than spatial location (Wong et al., 2006). Velocity selective pulses are used to label the blood inflowing above a preset cutoff velocity value. Then after a delay to allow inflow of labeled blood into the tissue, an image is acquired with velocity less than the preset cutoff velocity. The hypothesis is that spins surviving the velocity thresholds should be arterial spins decelerating into tissues, since static spins do not survive the first threshold and venous spins generally increase their velocity, flowing above the velocity threshold. With this approach an uniform transit time is guaranteed, being less sensitive to long transit delay times; however, the choice of appropriate cutoff velocity is critical (Wong et al., 2006) and, because the labeling is done using saturation pulses, the SNR is lower than

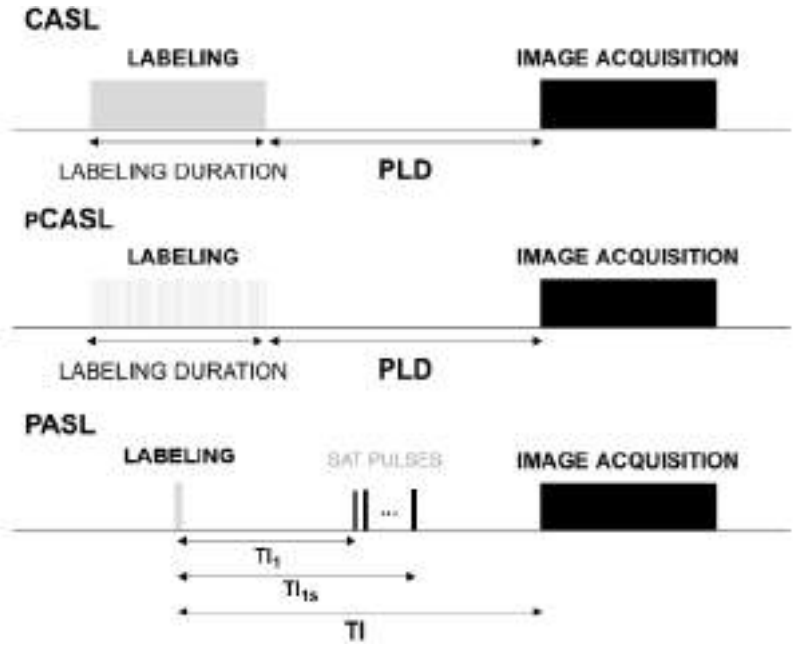

Figure 3.4: Illustrative timing diagram for the main ASL techniques (CASL, pCASL and PASL). For PASL the Q2TIPS technique is illustrated, where periodic saturation pulses are applied from TI_1 to TI_{1s}. Based on (Alsop et al., 2015; Luh et al., 1999).

in the other schemes. In general VSASL is still being considered to be in stage of development and is less available than others. Nevertheless, VSASL may be particularly beneficial in clinical situations where slow or collateral flow is encountered.

Background Suppression

The idea of background suppression (BS) is to attempt to null any static tissues contribution while preserving the ASL signal. This is commonly achieved through a combination of spatially selective saturation and inversion pulses. BS can markedly improve temporal SNR, although there is a tradeoff between the number of labeling pulses used, the amount of static tissue suppressed, and the reduction in the ASL signal. Usually two pulses are considered a good trade-off (Alsop et al., 2015).

Readout Methods

Regarding readout methods, both multi-slice 2D and 3D segmented methods are commonly used, including EPI as well SPIRAL and 3D GRASE (Vidorreta et al., 2013). Despite 2D image acquisition methods being less sensitive to head motion and being more widely available, they result in slice-to-slice variations in signal due to transit time and relaxation effects and background suppression is only optimal for one slice, being progressively less efficient for other slices (Alsop et al., 2015). In contrast, 3D segmented sequences (Fernández-Seara et al., 2005; Vidorreta et al., 2013), offer higher SNR, better spatial resolution, better background suppression,

and are relatively insensitive to off-resonance effects. When comparing 3D acquisitions with and without background suppression, the former yields a 3-fold increment in temporal SNR (Vidorreta et al., 2013).

Single and Multiple Time Delay

The time delay after labeling and before image acquisition is called the PLD or TI, depending on the ASL labeling scheme. This delay allows for the labeled arterial water to flow into the imaging region. PLD refers to the delay between the time at which the labeled blood leaves the labeling plane (in pCASL) and image acquisition; TI can be seen as the delay between the time at which the labeled bolus passes through the distal end of the labeling slab and image acquisition (Alsop et al., 2015). With the PASL QUIPSS II modification, the temporal width of the labeled bolus can be controlled and is referred to as TI1.

In single PLD/TI ASL imaging, the PLD/TI value is usually set just longer than the longest value of arterial transit time (ATT) expected to be present in the subject, in order to guarantee that the entire labeled bolus has reached the imaging region. However, the labeled ASL signal decays with time constant T_1, and ATTs depend on labeling location and other factors, also varying greatly across the brain, being usually between 500 and 1500 ms (Alsop et al., 2015), although in cerebrovascular disease these values can be even higher. Therefore, when using single PLD/TI imaging the choice of PLD/TI should be made carefully in order to achieve a good compromise between acceptable SNR and an accurate CBF quantification. However, if there is a pathological condition where the ATT is abnormally long, the single PLD/TI approach might not be effective in providing accurate CBF values. In those cases it is possible to circumvent this issue altogether by collecting images at multiple-PLD/TI points. By fitting a mathematical kinetic model to the multiple data points it is possible to estimate CBF more precisely, while also estimating ATT as well as other perfusion-related parameters.

3.3.2 ASL Modeling

The magnetization difference between the label image and the control image, ΔM, can be mathematically described by a kinetic model as a function of the PLD/TI, assuming ΔM as the concentration of a CBF tracer (Buxton et al., 1998).

To date, the general kinetic model proposed by Buxton remains one of the most common models used to fit ASL data (Buxton et al., 1998). It describes the magnetization differences between control and label images in the brain tissue, according to the following equations in the cases of PASL and pCASL, respectively:

PASL

$$\Delta M_{tiss}(t) = \alpha M_{0a} \frac{2f}{k} \begin{cases} 0 & \text{if } t < ATT \\ e^{\frac{-t}{T_{1a}}}(e^{k(t-ATT)} - 1) & \text{if } ATT \leq t < ATT + \tau \\ e^{\frac{-t}{T_{1a}}}(e^{k(t-ATT)} - e^{k(t-ATT-\tau)}) & \text{if } t \geq ATT + \tau \end{cases} \tag{3.13}$$

pCASL

$$\Delta M_{tiss}(t) = \alpha M_{0a} 2f T_1^{'} \begin{cases} 0 & \text{if } t < ATT \\ e^{\frac{-ATT}{T_{1a}}}(1 - e^{\frac{(t-ATT)}{T_1^{'}}}) & \text{if } ATT \leq t < ATT + \tau \\ e^{\frac{-ATT}{T_{1a}}}(e^{\frac{-(t-\tau-ATT)}{T_1^{'}}} - e^{\frac{-(t-ATT)}{T_1^{'}}}) & \text{if } t \geq ATT + \tau \end{cases} \tag{3.14}$$

with $k = \frac{1}{T_{1a}} - \frac{1}{T_1^{'}}$,$\frac{1}{T_1^{'}} = \frac{1}{T_1} + \frac{f}{\lambda}$, where ΔM_{tissue} is the control-label magnetization difference measured from the tissue compartment; M_{0a} is the equilibrium magnetization of the arterial blood; τ is the label bolus duration; T_{1a} is the longitudinal relaxation time of arterial blood; $T_1^{'}$ is the longitudinal relaxation time of brain tissue; λ is the blood-brain water partition coefficient, scaling the signal intensity of tissue to that of blood; α is the labeling (inversion) efficiency; and t corresponds to TI for PASL and $\tau + PLD$ for pCASL.

A potential source of error in ASL measurements is signal arising from intravascular blood that is destined for more distal tissue. In particular, in multiple-PLD/TI acquisitions the intravascular arterial signal contribution is mainly present at short PLD values and usually can be visualized in the magnetization difference images as bright foci in macrovascular locations. One way to overcome this issue is to use an extended kinetic model that incorporates the intravascular component, arterial blood volume (aBV), in addition to the tissue component, which is described by the following equations in the cases of PASL and pCASL, respectively (Chappell et al., 2010):

PASL

$$\Delta M_{art}(t) = \alpha M_{0a} 2aBV \begin{cases} 0 & \text{if } t < ATTa \\ e^{\frac{-t}{T_{1a}}} & \text{if } ATTa \leq t < ATTa + \tau \\ 0 & \text{if } t \geq ATTa + \tau \end{cases} \tag{3.15}$$

pCASL

$$\Delta M_{art}(t) = \alpha M_{0a} 2aBV \begin{cases} 0 & \text{if } t < ATTa \\ e^{\frac{-AATa}{T_{1a}}} & \text{if } ATTa \leq t < ATTa + \tau \\ 0 & \text{if } t \geq ATTa + \tau \end{cases} \tag{3.16}$$

where $ATTa$ is the intravascular arterial transit time; and τ_a is the intravascular bolus duration (Chappell et al., 2010, 2009).

Finally, the total magnetization difference measured in each voxel is then given by:

PASL

$$\Delta M_{total}(TI) = \Delta M_{tiss}(TI) + \Delta M_{art}(TI) \tag{3.17}$$

pCASL

$$\Delta M_{total}(PLD) = \Delta M_{tiss}(PLD) + \Delta M_{art}(PLD) \tag{3.18}$$

3.3.3 ASL Data Analysis

For single-PLD/TI ASL, CBF quantification follows several assumptions, including, that the entire labeled bolus has been delivered to the target tissue (in the case of PASL, this is achieved using the QUIPSS II or Q2TIPS sequences, in which τ = TI1), there is no outflow of labeled blood water and relaxation of the labeled spins is governed by T_1 of blood (Alsop et al., 2015). Under these assumptions, CBF can be computed at each voxel using the following equations (in ml/100g/min):

PASL (QUIPSS II or Q2TIPS)

$$CBF = \frac{6000\lambda\Delta M e^{\frac{TI}{T_{1a}}}}{2\alpha TI_1 M_{0a}} \tag{3.19}$$

pCASL

$$CBF = \frac{6000\lambda\Delta M e^{\frac{PLD}{T_{1a}}}}{2\alpha T_{1a} M_{0a}(1 - e^{-\frac{\tau}{T_{1a}}})} \tag{3.20}$$

The factor of 6000 converts the units from ml/g/s to ml/100g/min.

For multiple delay acquisitions the model in Equations 3.19 and 3.20 should be fitted to the data in order to obtain the perfusion parameters (CBF, ATT and potentially aBV). A popular model fitting approach is based on Bayesian statistics and assumes prior distributions of the different parameters in the model (Chappell et al., 2009). Spatial priors may also be used in order to constrain the spatial variations in the estimated parameters. This approach helps to deal with the limited SNR of the data, combined with the high number of parameters in the model.

This method has been compared with other model fitting techniques, namely nonlinear least squares based on the trust region reflective optimization algorithm (Coleman and Li, 2006), with the Bayesian model estimation procedure providing the best compromise between reliability and reproducibility when using a Q2TIPS PASL sequence in a multiple-PLD scheme (Sousa et al., 2014a)

Partial volume effects (PVEs) are also commonly considered in the analysis of ASL data, and a number of PVE estimation and correction techniques have been proposed (Asllani et al., 2008; Chappell et al., 2011).

The final step in ASL data analysis is usually the calibration step, which converts relative CBF (and aBV) measurements into absolute measures. M_{0a} can be estimated using several approaches including the acquisition of a separate proton density image, averaging of the control images at a specific PLD/TI or by fitting a saturation recovery curve to the multiple-TI control images. The different calibration methods and respective pipeline options will be described and investigated in detail in the next chapter (Chapter 4).

4

Impact of the calibration strategy on the quantification of ASL perfusion imaging

Contents

This Chapter corresponds to the article (accepted in Magnetic Resonance in Medicine): **Joana Pinto**, Michael A. Chappell, Thomas W. Okell, Melvin Mezue, Andrew R Segerdahl, Irene Tracey, Pedro Vilela, Patrícia Figueiredo, "Calibration of arterial spin labeling data - potential pitfalls in post-processing".

The work was developed through a collaboration with the Institute of Biomedical Engineering (IBME) (Prof. Michael Chappell), Wellcome Centre for Integrative Neuroimaging (FMRIB) and the Nuffield Department of Clinical Neuroscience at the University of Oxford (Short Term Scientific Mission in the scope of European COST Action "ASL in Dementia" - BM1103).

4.1 Abstract

Purpose: To assess the impact of the different ASL calibration methods and the corresponding processing pipeline options on ASL perfusion quantification.

Theory and Methods: Absolute quantification of perfusion measurements is one of the promises of arterial spin labeling (ASL) techniques. However, it is highly dependent on a calibration procedure that involves a complex processing pipeline for which no standardized procedure has been fully established. In this work, we systematically compare the main ASL calibration methods, as well as various calibration options, using two datasets acquired with the most common sequences, pulsed ASL and pseudo-continuous ASL.

Results: We found generally small differences across the main calibration methods, when using a set of carefully chosen pipeline options. However, we observed significant and sometimes large variations in perfusion values when we changed these away from their default values, particularly regarding correction for incomplete T_1 relaxation and for radiofrequency field inhomogeneities.

Conclusion: Overall, the voxelwise calibration method was the least sensitive to the processing options, further supporting the approach proposed by the ASL white paper. Regardless of the method chosen, our findings highlight the need for a complete description of the calibration procedure in ASL studies, including a number of options that are often overlooked.

4.2 Introduction

Arterial spin labeling (ASL) is a non-invasive magnetic resonance imaging (MRI) technique that provides quantitative images of tissue perfusion, by using magnetically labeled blood water protons as an endogenous blood flow tracer (Alsop and Detre, 1996; Detre et al., 1992; Williams et al., 1992). ASL is acknowledged to have great potential as a completely non-invasive quantitative perfusion imaging technique, but its implementation has been challenging due to the intrinsically low signal-to-noise ratio (SNR). This has motivated the development of a multitude of signal acquisition and processing strategies that aim to overcome this limitation as well as the

publication of a ASL implementation consensus paper (Alsop et al., 2015). Although pseudo-continuous ASL (pCASL) is the recommended labeling strategy, pulsed ASL (PASL) is still a commonly used technique (Gevers et al., 2011; Gil-Gouveia et al., 2017; Mutsaerts et al., 2015; Pimentel et al., 2013; Wang et al., 2011).

In principle, cerebral blood flow (CBF) can be quantified based on a single time delay measurement – the post-labeling delay (PLD) in pCASL; and the inversion time (TI) in PASL – provided that it is long enough relative to the transit time of the label bolus between the arteries and the capillaries, the so-called arterial transit time (ATT). However, if this condition cannot be assumed, which is the case in pathologies presenting delayed arterial transit times, multiple-PLD/TI measurements are necessary (Figueiredo et al., 2005; Gonzalez-At et al., 2000; MacIntosh et al., 2010). Furthermore, if an appropriate kinetic model is fitted to the data, the multiple-PLD/TI strategy allows the assessment of not only CBF but also ATT (Buxton et al., 1998) and potentially arterial blood volume (aBV) (Chappell et al., 2010; Sousa et al., 2014b), which may be parameters of interest in their own right. In any case, in order to obtain CBF measures in absolute units it is necessary that the relative CBF (CBF_{rel}) images should be normalized by the equilibrium magnetization of arterial blood (M_{0a}), which is usually achieved by extrapolation from the value of the equilibrium magnetization measured in tissue (M_{0t}). Critically, it has been demonstrated through theoretical analysis that the two factors that CBF quantification using ASL is most sensitive to are M_{0a} estimation and labeling efficiency (Wu et al., 2010).

The current recommendation for ASL calibration involves the acquisition of a separate proton-density weighted image followed by the extraction of M_{0t} by extrapolation as a function of the repetition time (TR). This is subsequently converted to an M_{0a} image by dividing the image by the brain average brain-blood water partition coefficient (λ) (Alsop et al., 2015) and then applying spatial smoothing. If no background suppression is employed (e.g. PICORE (Luh et al., 1999)), it is also possible to obtain M_{0t} directly from the ASL data by averaging the control images at a particular PLD/TI. In the specific case of multiple-TI PASL, it is possible to obtain M_{0t} by fitting a saturation-recovery curve to the multiple-TI control images. Additionally to the selection of a calibration image, it is necessary to decide whether to compute a voxelwise M_{0a} value, or a single average value across a homogeneous reference region, usually gray matter (GM), white-matter (WM) or cerebral spinal fluid (CSF) (Cavuşoğlu et al., 2009; Chen et al., 2011). For the practical implementation of the calibration pipeline, a number of subtler choices must also be made; however, these are rarely discussed or even reported in ASL studies. Although some calibration method comparisons have been reported (Cavuşoğlu et al., 2009; Chen et al., 2011; Fazlollahi et al., 2015; Wu et al., 2010), the impact of the corresponding processing options has yet to be investigated.

Here, we systematically compare the impact of using different calibration pipelines on the quantification of perfusion and its reproducibility, using both PASL and pCASL acquisitions, in order to obtain a set of recommendations regarding the preferred pipeline options and the need

to report them.

4.3 Methods

4.3.1 Data Acquisition

Test-retest multiple-PLD/TI pCASL and PASL datasets were previously acquired (Mezue et al., 2014; Sousa et al., 2014b). The PASL study was approved by the Hospital da Luz Ethics Committee, and all subjects gave written informed consent in accordance with the Declaration of Helsinki. The pCASL study was performed under an agreed technical development protocol approved by the Oxford University Clinical Trials and Research Governance office, in accordance with International Electrotechnical Commission and United Kingdom Health Protection Agency guidelines.

In the PASL study, a group of 9 healthy volunteers (22.9 ± 5.6 years, 4 males) was studied on a 3T Siemens Verio whole-body MRI system (Erlangen, Germany) using a 12-channel-receive head radiofrequency (RF) coil, on two sessions separated by approximately 1 week (Sousa et al., 2014b). In the pCASL study, a group of 8 healthy volunteers (28.3 ± 2.5 years, 6 males) was studied on a 3T Siemens Verio whole-body MRI system (Erlangen, Germany) using a 32-channel receive head RF coil, on three occasions separated by 1 week and 1 month (Mezue et al., 2014). A reference image with no labeling or background suppression, TR=6s, and all other parameters identical to the pCASL scan, was collected for calibration. In both datasets, T_1-weighted structural images were acquired from each subject for tissue segmentation and registration purposes. Acquisition details for both datasets are summarized in Table 4.1.

Table 4.1: Summary of the main acquisition parameters for the PASL and pCASL datasets.

	PASL (PICORE-Q2TIPS (Luh et al., 1999))	**pCASL**
Readout	2D multi-slice GE-EPI	2D multi-slice GE-EPI
Background suppression	No	Yes
TR	2500 ms	4000 ms
TE	19 ms	13 ms
Number of slices	9	24
Slice time	50.0 ms	45.2 ms
Voxel size	3.5×3.5×5.0 mm^3	3.5×3.5×5.0 mm^3
Labeling parameters	Labeling slab thickness = 100 mm	Labeling duration = 1400 ms
	Labeling bolus duration = 750 ms*	
	Labeling slab gap = 18.8 mm	
TI/PLD values	400–2400 ms, in steps of 200 ms (11 values)	250-1500 ms, in steps of 250 ms (6 values)
Control-label pairs	8 for each TI	8 for each PLD

* The Q2TIPS module allowed limiting the labeling to a maximum of 750 ms by adjusting TI1 and TI1s for each TI: for TI2 <1000 ms, TI1 = TI1s = TI - 25 ms; and for TI >1000 ms, TI1 = 750 ms and TI1s = 900 ms.

4.3.2 Data Analysis

Image analysis was conducted using FSL (FSL 5.0.1, http://fsl.fmrib.ox.ac.uk/fsl/fslwiki/FSL) and MATLAB (2013a, http://mathworks.com). The multiple-PLD/TI ASL images in each dataset were aligned with each other by motion correction using MCFLIRT (Jenkinson et al., 2002). For each dataset, at each PLD/TI, the control images and the pairwise differences between control and label images were averaged across repetitions, yielding time series of mean control images ($M_{control}$(PLD/TI)) and mean magnetization difference images (ΔM_{diff}(PLD/TI)) as a function of PLD/TI, respectively. Additionally, for the PASL dataset, off-resonance effects caused by imperfect inversion slice profile in 2D multi-slice imaging were corrected (Figueiredo et al., 2005).

The structural images were segmented using FAST (Zhang et al., 2001) in order to estimate tissue masks, and corresponding partial volume estimate (PVE) maps. Both types of image were co-registered to the ASL space of each subject/session using a linear transformation (FLIRT (Jenkinson et al., 2002)) (supplementary information can be found in Appendix B). For the PASL datasets, the T_1 map derived from the saturation recovery approach was used as reference image, instead of the ASL data, since it provided more tissue contrast.

An extended kinetic model including a tissue contribution and an intravascular arterial compartment was fitted to ΔM_{diff}(PLD/TI), yielding maps of relative CBF and aBV, and ATT (Chappell et al., 2010) (supplementary information can be found in Appendix B).

4.3.2.A Calibration Methods

Calibration is required in order to obtain CBF (ml/100g/min) in absolute units, through normalization by M_{0a} (and α, the labeling/inversion efficiency):

$$CBF = \frac{CBF_{rel}}{\alpha M_{0a}} \times 6000 \tag{4.1}$$

Calibration therefore entails estimation of M_{0a} and it is achieved in two main steps:

1. Generation of M_{0t} map
2. Extrapolation of M_{0a} from M_{0t} map

Generation of M_{0t} Map

The method used for generating the M_{0t} map depends on the acquisition scheme and options chosen.

Long TR calibration scan (LongTR) For the pCASL study, the common long TR calibration scan strategy (LongTR) was used, whereby a corrected M_{0t} map, $M_{0t,corr}$(i), is obtained from a separately acquired long TR scan, M_{0t}(i), by correcting for the amount of T_1 relaxation at that TR at each voxel, according to:

$$M_{0t,corr}(i) = \frac{M_{0t}(i)}{1 - e^{\frac{TR_{long}}{T_{1,t}}}} \tag{4.2}$$

where $T_{1,t}$ corresponds to the tissue-specific T_1 in each voxel i ($T_{1,GM} = 1.3$ s, $T_{1,WM} = 1.0$ s, and $T_{1,CSF} = 4.3$ s). This correction was performed based on the corresponding tissue segmentation obtained previously.

ASL control averaging (CtrAvg) and control saturation recovery (SatRec) For PASL, because no background suppression was applied, it was also possible to estimate M_{0t} based on the ASL control images. This can be performed either by averaging control images at a fixed TI (CtrAvg), or by fitting a saturation-recovery curve to M_{ctrl}(TI) (SatRec) if multiple TIs are sampled and the acquisition sequence includes presaturation, which is the case of Q2TIPS PASL (Luh et al., 1999). This strategy also allows estimation of M_{0t}, T_{1t} and saturation efficiency (A) (asl_calib, `https://fsl.fmrib.ox.ac.uk/fsl/fslwiki/BASIL/`).

Extrapolation of M_{0a} from the M_{0t} Map

Once an M_{0t} map is derived, the next step is the extrapolation of M_{0a}. Two types of methods are commonly used for that purpose: the reference tissue (RT) and the voxelwise (Voxel) methods.

Reference tissue method (RT-CSF, RT-WM and RT-GM) In this approach, in order to compensate for spatial variations in image intensity due to RF receive coil sensitivity and RF transmit inhomogeneities, a bias image is estimated from the original ASL datasets using FAST (Evans et al., 1993); this is then applied to the ASL data prior to kinetic model fitting, and also to the M_{0t} maps obtained in the previous section, prior to any corrections.

The RT approach consists in computing a single M_{0a} value based on a homogeneous tissue region, within GM, WM or CSF. For this purpose, a restrictive tissue mask was obtained from the respective PVE map in ASL space, through the application of a stringent threshold ($PVE_{tissue} \geq 0.9$). Additionally, the CSF mask was further intersected with a mask of the lateral ventricles derived from the MNI atlas (Evans et al., 1993).

Finally, the M_{0a} value was computed by normalizing the reference tissue-averaged M_{0t},corr with the respective λ, while correcting for the difference in T_2^* relaxation between the reference tissue and arterial blood (associated with the M_{0t} measurement using GE EPI), yielding:

$$M_{0a} = \frac{< M_{0t,corr} >_{rt} e^{TE(\frac{1}{T^*_{2,rt}} - \frac{1}{T^*_{2,a}})}}{\lambda_{rt}} \tag{4.3}$$

where $T^*_{2,a}$=50 ms is the transverse relaxation time of arterial blood, $T^*_{2,rt}$ is the transverse relaxation time of the reference tissue $T^*_{2,CSF} = 400$ ms, $T^*_{2,WM} = 50$ ms, $T^*_{2,GM} = 60$ ms), and λ_{rt} is blood/brain water partition coefficient of the reference tissue ($\lambda_{CSF} = 1.15$, $\lambda_{WM} = 0.82$, $\lambda_{GM} = 0.98$).

Voxelwise method (Voxel) The $M_{0t,corr}$ map was first smoothed using a 2D median filter with FWHM = 10.5 mm, in order to minimize noise contributions. Then, an M_{0a} map was obtained through direct extrapolation from the $M_{0t,corr}$ value in each voxel, by normalizing with the respective tissue λ, while correcting for the difference in T_2^* relaxation between the respective tissue and arterial blood, according to:

$$M_{0a}(i) = \frac{M_{0t,corr}(i) e^{TE(\frac{1}{T^*_{2,t}} - \frac{1}{T^*_{2,a}})}}{\lambda_t} \tag{4.4}$$

where $T^*_{2,t}$ and λ_t are the transverse relaxation time and the blood/brain water partition coefficient, respectively, of the tissue in each voxel. Regarding λ_t, an average brain value of 0.9 was chosen by default.

4.3.2.B Calibration Pipeline Options

The various options that must be made in the pipeline of each calibration method are summarized in Table 4.2. These were tested by fixing the other options at their default values, on the data acquired in the first session of each subject. For the extrapolation of M_{0a}, the alternative options were tested only in the case of SatRec (assuming the effects would be similar in the other cases). For illustration, a summary of the Voxel method pipeline and options is displayed in Figure 4.1.

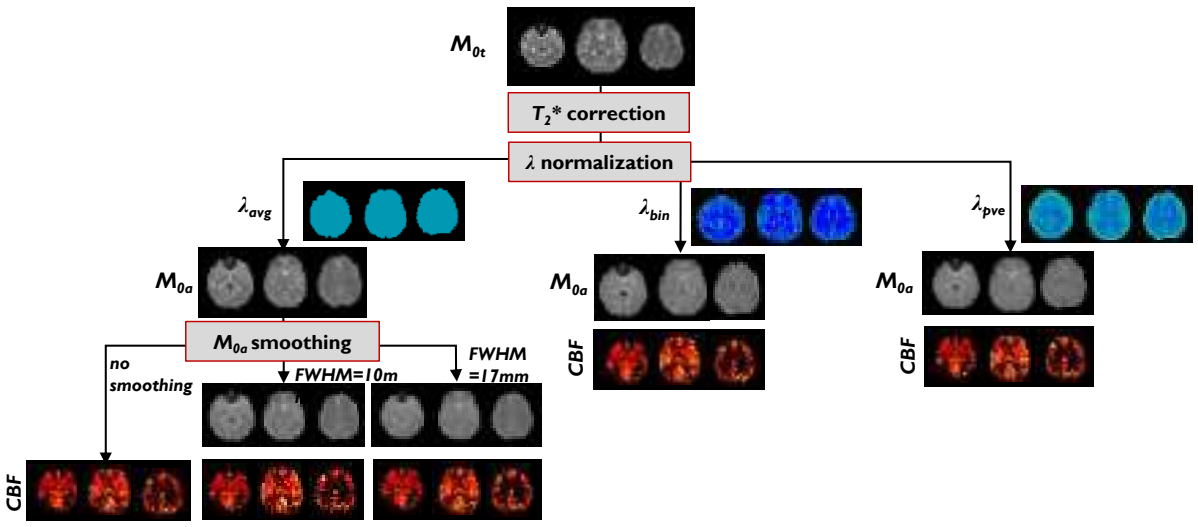

Figure 4.1: Illustrative individual example of the voxel M_{0a} extrapolation method pipeline options.

Generation of M_{0t} Map

T_1 correction Correction for incomplete T_1 relaxation was performed when using the CtrAvg and LongTR methods to obtain the M_{0t} map. The current recommendation indicates that this step should only be performed if TR<5 s (Alsop et al., 2015), making it not mandatory for

Table 4.2: Summary of calibration methods and pipeline options tested.

Method		**Options**	
Generation of M_{0t} map			
PASL - SatRec	Presaturation efficiency	**A estimated (default)**	
		A=100%	
PASL - CtrAvg	TI value	**long TI∼2400 ms (default)**	
		short TI∼800 ms	
	T_1 correction	**yes (default)**	
		no	
	Presaturation efficiency	**A=90% (default)**	
		A=100%	
pCASL - LongTR	T_1 correction	**Yes (default)**	
		No	
Extrapolation of M_{0a} from M_{0t} map			
Reference Tissue CSF	RT mask	**restrictive (default)**	restricted threshold (PVE_{CSF} ≥0.9) intersected with MNI atlas ventricles mask
		intermediate	less restricted threshold (PVE_{CSF} ≥0.6) intersected with MNI atlas ventricles mask
		extensive	less restricted threshold (PVE_{CSF} ≥0.6)
	Bias correction	yes (default)	
		no	
Reference Tissue WM	RT mask	restrictive (default)	restricted threshold (PVE_{WM} ≥0.9)
		extensive	less restricted threshold (PVE_{WM} ≥0.6)
	Bias correction	**yes (default)**	
		no	
Reference Tissue GM	RT mask	**restrictive (default)**	restricted threshold (PVE_{GM} ≥0.9)
		extensive	less restricted threshold (PVE_{GM} ≥0.6)
	Bias correction	**yes (default)**	
		no	
Voxel	Smoothing	none	
		FWHM=10.5 mm (default)	
		FWHM=17.5 mm	
	λ value	**Brain average (λ_{avg}=0.9) (default)**	$\lambda_{avg} = \lambda_{GM} PVE_{GM} + \lambda_{WM} PVE_{WM}$
		PVE-weighted average (λ_{wgt})	$\lambda_{wgt}(i) = \lambda_{GM} PVE_{GM} + \lambda_{WM} PVE_{WM} + \lambda_{CSF} PVE_{CSF}$
		Tissue-specific (λ_{ts})	$\lambda_{ts} = \begin{cases} \lambda_{GM} = 0.98 & \text{if } GM \\ \lambda_{WM} = 0.82 & \text{if } WM \\ \lambda_{CSF} = 1.15 & \text{if } CSF \end{cases}$

the LongTR method (TR = 6 s). However, the consensus paper also recommends the use of a voxelwise approach, in which case this may not have a significant impact (as we will show). We therefore tested the impact of correcting the M_{0t} images for T_1 relaxation in all M_{0a} extrapolation methods (Default), with the option of no correction.

Fixed TI value One of the crucial points when using the CtrAvg approach in PASL is the selection of the fixed TI value to be used for averaging the control images. We compared CBF results obtained using two TI values: the longest, 2400 ms (Default), and a shorter value, 800 ms.

Presaturation efficiency When acquisition sequences include presaturation pulses, such as Q2TIPS PASL, quantification of the presaturation efficiency, A, might be an important factor. In the SatRec approach it is also possible to estimate presaturation efficiency (A) as part of model fitting (Default); for this approach, we compared estimation of A with having a fixed A = 100 %. For the CtrAvg approach, since it is not possible obtain an estimate, we compared A = 90 % (the approximate average value of A estimated in SatRec) (Default) with A = 100 %.

Extrapolation of M_{0a} from the M_{0t} Map

RT mask Whenever using the RT method, the choice of a tissue region of interest may range between being very restrictive (Default) or more inclusive, resulting in considerably different PVEs and potentially very different calibrations. Here, we explored the impact of using less restricted tissue masks.

Bias correction When using the RT method, by default, M_{0t} and CBF maps were normalized using the smoothed estimated bias image (Default). We compared this with the option of no bias correction. This was only tested in reference tissue methods, since the Voxel method intrinsically corrects for such spatial variations in image intensity.

Partition coefficient In principle, a different λ value exists in each voxel since water partition differs as a function of tissue type and hence the voxel's PVEs. For simplicity, a single brain average value is usually used for all voxels: most commonly, the average of GM and WM values is chosen (Default). Here we tested this as well as two other alternatives, a tissue-specific and a PVE-weighted average λ.

Smoothing Spatial smoothing of the M_{0t} image is performed in order to avoid amplification of noise contributions upon division of CBF by it, in the Voxel method. In this study, a median filter with FWHM = 10.5 mm (3×3) was applied to the M_{0t} map (Default). This was compared with using FWHM = 17.5 mm (5×5), as well as with the option of no smoothing.

4.3.2.C Impact on CBF Quantification and Reproducibility

In order to evaluate the impact of the different calibration methods and respective pipeline options, the average CBF value was computed across GM for each dataset. For this purpose, a GM mask was derived for each subject and session using the GM mask obtained from segmentation, co-registered to ASL space. Statistically significant differences between methods and options were tested using repeated-measures one-way analysis of variance (ANOVA). When significant effects were found, post-hoc analysis using pairwise T-test were performed ($p<0.05$).The reproducibility of the GM average CBF measurements was also assessed, by computing the inter- and intra-subject coefficients of variation (CV_{inter} and CV_{intra}) for the median CBF values across GM (supplementary information can be found in Appendix B) (Mezue et al., 2014; Pinto et al., 2016; Sousa et al., 2014b; Tjandra et al., 2005). Significant differences in CV across M_{0a} estimation methods, for each M_{0t} map generation method, were assessed using jackknife resampling, followed by 1-way ANOVA and posthoc pairwise T-tests between methods (significant effects for $p<0.05$).

4.4 Results

We firstly present the quantification and reproducibility results obtained for the main calibration methods using the default pipeline options. Secondly, the impact of variations in the pipeline options is assessed.

4.4.1 Comparison Between Calibration Methods

Figure 4.2 shows illustrative examples of individual CBF maps obtained using the main M_{0a} extrapolation methods (RT-CSF/RT-WM/RT-GM/Voxel), using the SatRec and CtrAvg M_{0t} generation methods in PASL and the LongTR M_{0t} generation method in pCASL, with the corresponding default pipeline options. Minor differences can be observed in the Voxel compared to the RT methods, particularly in the borders of CBF maps. This can be explained by the amplification of noise that occurs upon the voxelwise division by the M_{0t} map performed in the Voxel method.

The group results for the average GM CBF values, obtained using the different calibration methods with the respective default options, for the first session of each dataset, are presented in Figure 4.3. For PASL, both M_{0t} generation methods yielded similar CBF values across the four M_{0a} extrapolation methods. For PASL CtrAvg and pCASL approaches, CBF values were significantly different across methods except between RT-WM and RT-GM methods and RT-CSF and Voxel methods.

Finally, the reproducibility metrics (CV_{inter} and CV_{intra}) of the average GM CBF values for the main calibration methods, using the default pipeline options, are presented in Figure 4.4. All methods were found to exhibit good reproducibility, with pCASL being superior to

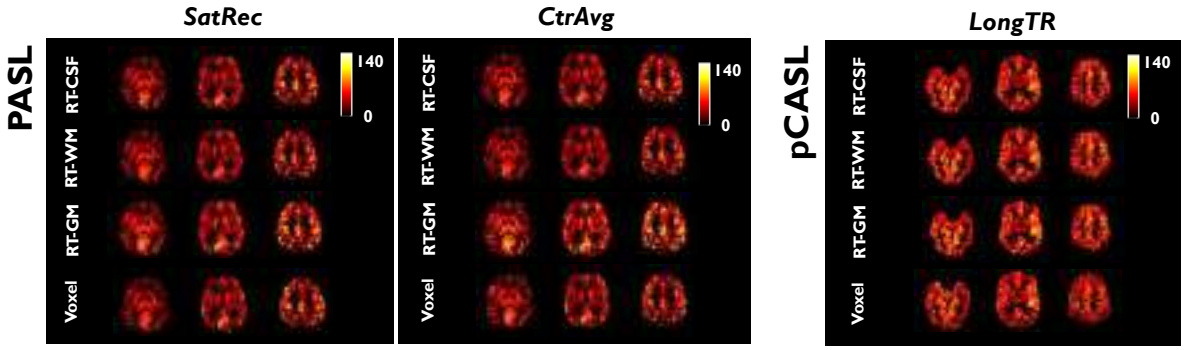

Figure 4.2: Illustrative examples of individual CBF maps obtained using the four M_{0a} extrapolation methods (RT-CSF/RT-WM/RT-GM/Voxel), using the SatRec and CtrAvg M_{0t} generation methods in PASL and the LongTR M_{0t} generation method in pCASL, with the respective default pipeline options.

PASL, and the RT-WM method generally yielding the worst values. A significant main effect of calibration method was found across M_{0a} estimation methods, for each M_{0t} map generation method. Subsequent post-hoc analysis yielded significant differences between several M_{0a} estimation methods. The Voxel and RT-CSF methods yielded the lowest CV_{intra} values, while the RT-GM method yielded the lowest CV_{inter} values, with significant differences in several cases. The RT-WM method systematically performed worst for both CV_{intra} and CV_{inter}, often with significant differences.

4.4.2 Impact of Calibration Pipeline Options

The group results for the GM average CBF values obtained when varying the calibration pipeline options are presented in Figure 4.5, for each of the main calibration methods tested on session 1 of each dataset. For each method there was a significant main effect of the pipeline option; subsequent pairwise comparisons revealed significant differences between some options, as indicated in the plots.

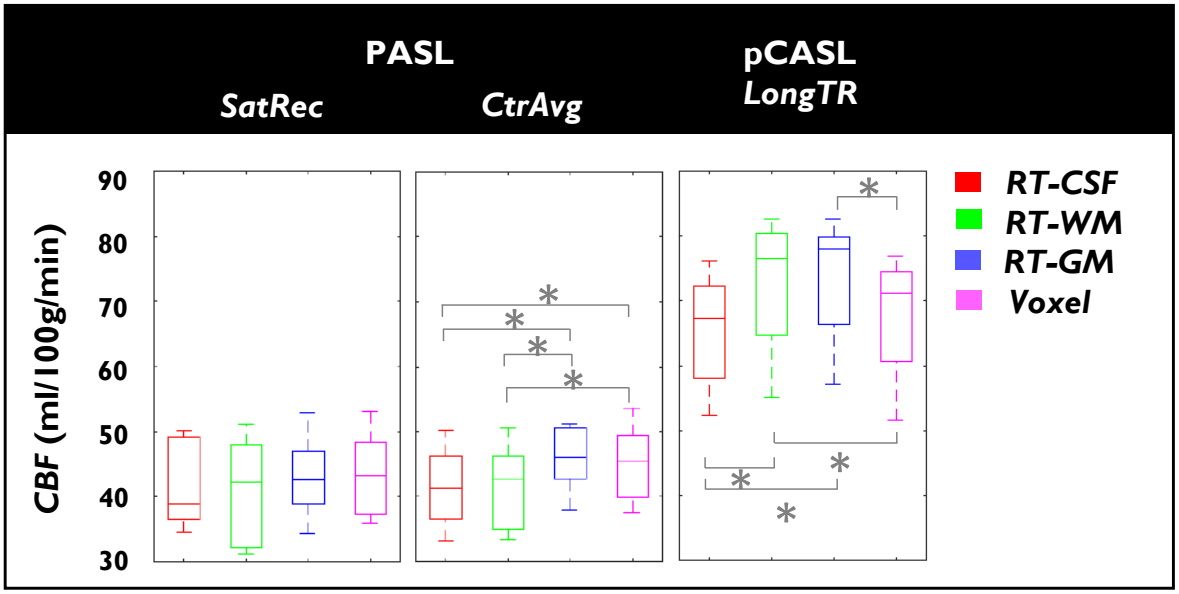

Figure 4.3: Group results for the GM average CBF values obtained using the different calibration methods for session 1 of the PASL and pCASL datasets, with the respective default options. Bottom and top edges of box plots represent the 25^{th} and 75^{th} percentiles, respectively. Significant differences as assessed by pairwise T-tests ($p<0.05$) are indicated with *.

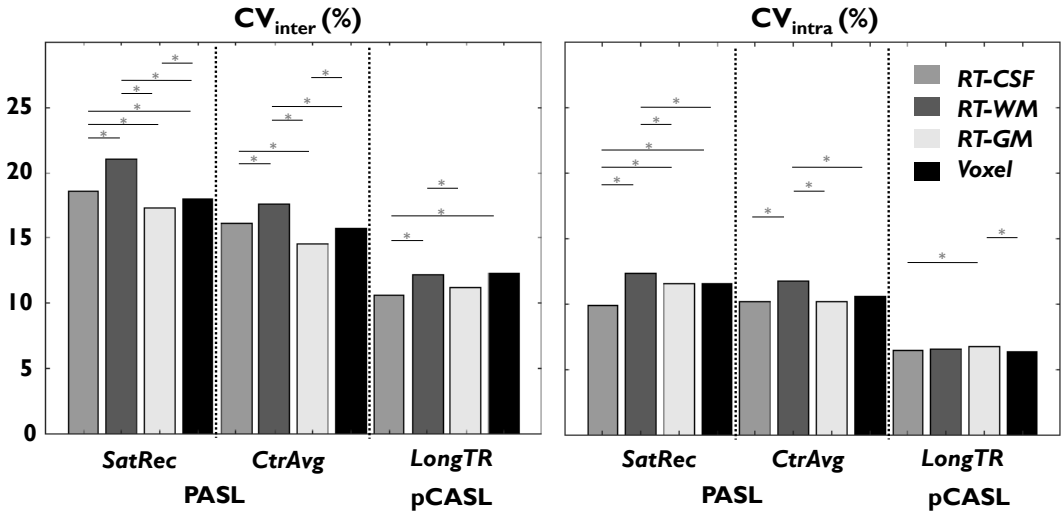

Figure 4.4: Reproducibility metrics (CV_{inter}, CV_{intra}) of GM average CBF values, obtained for each data set, and each of the main calibration methods, using their default pipeline options. Significant pairwise differences assessed by pairwise T-tests ($p<0.05$) are indicated with *.

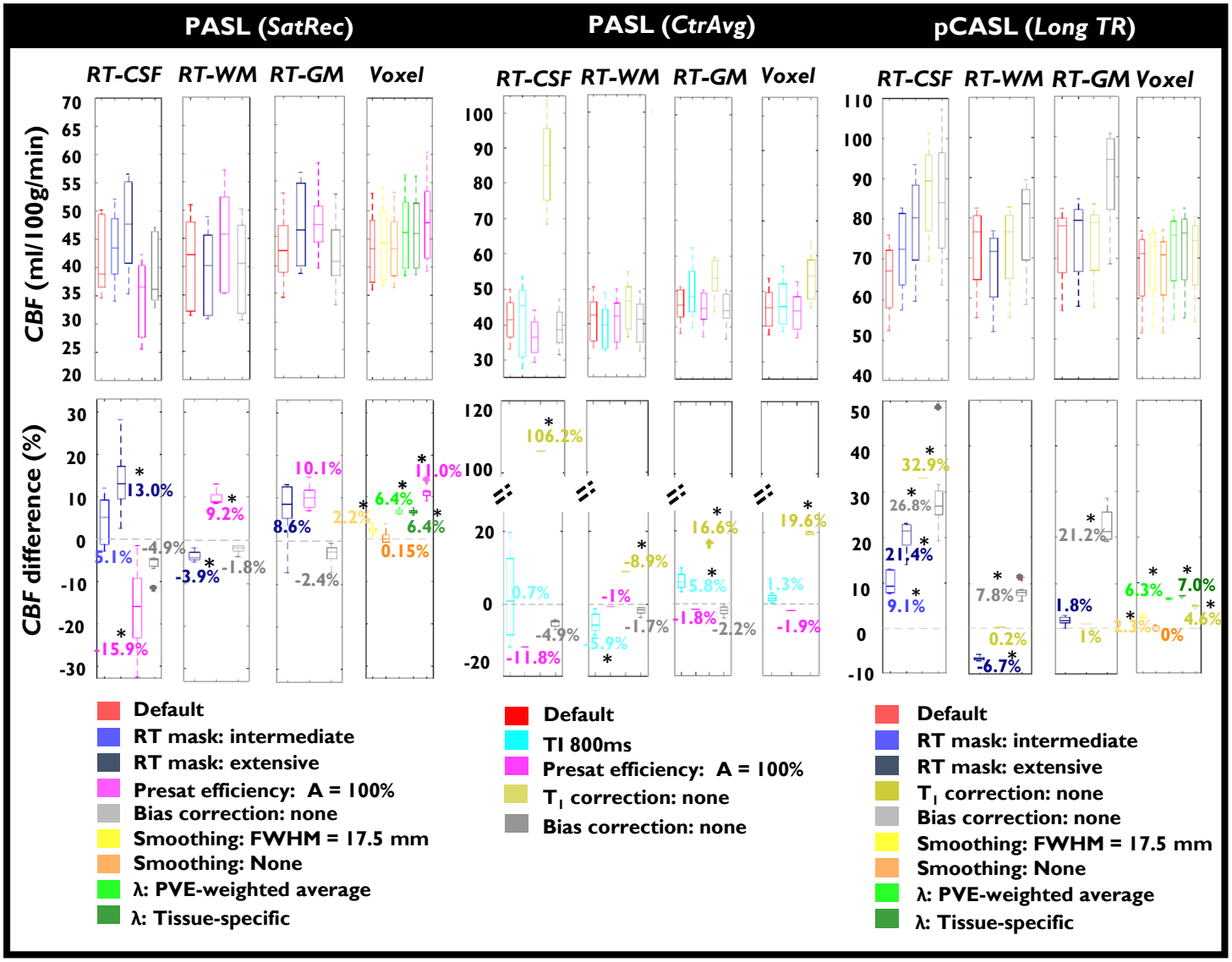

Figure 4.5: Group results for the GM average CBF values (top) and differences relative to default options (bottom), obtained when varying the calibration pipeline options, for each of the main calibration methods tested, in session 1 of PASL – SatRec (left), PASL – CtrAvg (middle) and pCASL – LongTR (right). Box plots represent the 25^{th} and 75^{th} percentiles, respectively. Significant differences as assessed by pairwise T-tests ($p<0.05$) are indicated with *.

When applying the SatRec method for M_{0t} generation, the RT-CSF approach yielded the highest CBF differences across methods, with the extensive mask producing significantly greater CBF values relative to the default option that uses a much more restricted mask. WM masking options resulted in a significant CBF decrease, but of only $\sim$ 5 % relative to the default value. Fixing A = 100% instead of allowing its estimation (A $\sim$ 90 %), yielded significant CBF differences relative to default option, for all methods except for RT-GM. Not correcting for field inhomogeneities using bias correction had small and non-significant impact on CBF quantification, although higher when using the RT-CSF approach compared with the other RT approaches. For the Voxel approach, an increase in kernel size for spatial smoothing led to significant but small effects on CBF. Not applying any smoothing at all yielded non-significant differences. Finally, different options for the value of λ also resulted in significant but small CBF differences.

In contrast with the SatRec approach, the CtrAvg approach revealed great sensitivity to some pipeline options, particularly the T_1 correction, and more so when using the RT-CSF method. Significant increases in CBF as high as $\sim$100% were found when using the RT-CSF method, if no T_1 correction was performed. When using TI = 800 ms, significant CBF differences were found for RT-WM and RT-GM methods compared to the default option.

When applying the pCASL LongTR method for M_{0t} generation, differences in CBF values were obtained with the different options, particularly when using the RT-CSF method. When not performing T_1 correction, the RT-CSF method yielded a significantly greater difference compared with the default options, with the Voxel method yielding a significant but smaller difference. Consistently with the PASL SatRec results, less restrictive masks led to important and significant CBF differences, except for the RT-GM method, particularly in the case of the extensive CSF mask. Also, similarly with PASL SatRec but to a higher extent, bias correction had greater and always significant impact on all RT-methods, particularly on RT-CSF and RT-GM. When using the Voxel method, results were similar to the PASL SatRec case, with different spatial smoothing options and the value of λ yielding minor differences relative to the default option. In fact, not applying any smoothing at all yielded non-significant differences in CBF quantification.

4.5 Discussion

We systematically compared the main ASL calibration methods as well as associated processing options, in terms of perfusion values and corresponding test-retest reproducibility.

4.5.1 Comparison Between Calibration Methods

When comparing the different calibration methods using the default processing pipeline options, minimal differences were observed in CBF within each dataset (Figure 4.2). When

focusing on the GM average CBF values (Fig. 4.3), relatively small differences were found, despite being significant in some cases.

For PASL, significant differences in CBF across methods were only found when using control averaging for calibration, while fitting a saturation recovery across control images was robust to varying the calibration method. This finding is consistent with the observation that the CtrAvg approach is indeed considerably more sensitive to variations in the calibration pipeline than the SatRec approach.

For pCASL, significantly lower CBF values were obtained when using the CSF as a reference region, compared with other strategies for extrapolating M_{0a} from M_{0t}. This finding may be explained by the fact that our pCASL dataset, obtained using a 32-channel head coil, suffered from B_1 field inhomogeneities that were not fully accounted for by correction using an estimated bias image. In fact, this interpretation is corroborated by the observation that, in the case of pCASL, when using less restrictive CSF masks (including the whole lateral ventricles rather than just a few central voxels where coil sensitivity is much lower), the CBF values increased considerably and became comparable to the ones obtained using the Voxel approach.

To be noted that the bias field correction approach used here is not the ideal method for accounting for RF inhomogeneity. Nevertheless, this strategy serves the purpose of evaluating the relative differences between calibration methods and pipeline options. In fact, it clearly emphasizes the impact of sensitivity correction on CBF, particularly when using the RT-CSF approach. Furthermore, the values obtained with RT methods, when corrected for the bias field, become closer to the ones obtained with the Voxel method, which intrinsically corrects for this issue. Nevertheless, when using RT methods, we recommend the use of more accurate RF sensitivity mapping such as the acquisition of a receive RF coil sensitivity map in one or more separate scans (usually by comparing a head coil with a body coil image) (Okell et al., 2013).

It is possible to circumvent RF field inhomogeneity issues altogether by employing the voxelwise M_{0a} extrapolation method for calibration. In this case, a value of M_{0a} is computed at each voxel based on the measured M_{0t} in that voxel, which is therefore affected by the same RF coil sensitivity as the ASL measurements themselves. Normalization of the estimated CBF map by the M_{0a} map therefore intrinsically corrects for coil sensitivity variations. This well-known effect has been explicitly reported (Fazlollahi et al., 2015), with observed signal loss in anterior regions on both proton-density and perfusion-weighted ASL images being successfully restored in the final perfusion maps by calibration using a Voxel approach. Nevertheless, the voxelwise division intrinsic to this approach might lead to increased variability in CBF quantification due to noise amplification, and also to edge and/or partial volume effects (Chappell et al., 2011).

4.5.2 Relation With Previous Comparisons Between Calibration Methods

For the extrapolation of M_{0a} from M_{0t}, since in theory M_{0a} is a single value, the RT methods should be more suitable to perform calibration. Furthermore, within these methods, the composition of CSF is more similar to that of arterial blood (in comparison to GM or WM),

thus RT-CSF should be the method chosen. For the generation of M_{0t} map, one can argue that the least appropriate method theoretically is CtrAvg, mainly because it strongly depends on the assumed value of T_1. In the case of LongTR, if CSF is the chosen reference tissue, then an even longer TR than previously recommended must be used to comply with theory. Nevertheless, very few studies have investigated the impact of different calibration strategies and, critically, they are not in agreement. One study compared the three M_{0a} extrapolation schemes that we also tested here (RT-CSF, RT-WM and Voxel) using data collected with three single-TI (1400 ms) PASL sequences (including PICORE-Q2TIPS), and found $\sim$ 35% higher CBF values for the RT-CSF relative to the Voxel method (Cavuşoğlu et al., 2009). Another study also observed a discrepancy in CBF quantification when using different calibration methods based on single–PLD pCASL data, with RT-WM yielding the lowest CBF values and Voxel the highest ($\sim$20% difference) (Fazlollahi et al., 2015). A third study compared different calibration methods on CASL and pCASL data, and found only minor differences. However, they reported slightly lower CBF values using RT-CSF compared with RT-WM, possibly due to not correcting for the uneven sensitivity profile of the head coil (Chen et al., 2011).

4.5.3 Impact of Calibration Pipeline Options

We observed that some of the processing options had great impact on the final results while others were relatively unimportant. One of the processing options with greatest impact was the correction of the M_{0t} map for incomplete T_1 relaxation in each tissue based on the TR of the respective image acquisition, particularly when using the CSF as a reference tissue. In the current guidelines, this correction is only recommended when TR<5s (Alsop et al., 2015). However, this recommendation is coupled with the use of the Voxel method for extrapolating M_{0a}, in which case we do not observe large effects of T_1 correction. In fact, the impact of T_1 correction is much greater if the RT-CSF extrapolation method is used, because CSF has a much longer T_1 than GM or WM. In this case, a TR longer than 16 s would be required for an almost full recovery of the longitudinal magnetisation. Therefore, we believe that this correction should be applied even if TR is longer than 5s, when the RT-CSF calibration method is used. A related option with high impact is the value of PLD/TI used to extract M_{0t}. In the case of the CtrAvg approach in PASL, using a lower TI leads to greater sensitivity in CBF quantification. For PASL, the presaturation efficiency value was also important. Because this is sequence-specific and therefore should be chosen accordingly. Interestingly, the impact of bias correction is highly dependent, not only on the M_{0t} extrapolation method, but also on the type of ASL dataset and the RF coil sensitivity of the acquisition. In contrast with the 12-channel RF coil used for the PASL dataset, the 32-channel RF coil used for the pCASL dataset displayed a relatively heterogeneous sensitivity profile, leading to significant impact of bias correction, particularly when using RT-CSF and RT-GM methods.

Overall, our results indicate that, when acquiring multiple-TI PASL data, the SatRec approach is preferable to the CtrAvg approach since the latter strongly depends on the choice

of PLD/TI value and on T_1 correction. In terms of M_{0a} extrapolation, overall the RT-CSF approach was the most sensitive to variations in the processing options, making this approach more prone to CBF discrepancies. In addition, variability in the CBF differences across subjects was also greater than with other M_{0t} extrapolation methods. In particular, the RT-CSF method is highly dependent, not only on T_1 correction as discussed before, but also on the tissue mask and whether or not bias correction is performed. The RT-WM and RT-GM methods are also dependent on these parameters but to a lesser extent. Notwithstanding, the RT-WM approach might not be feasible whenever WM lesions are present, such as in multiple sclerosis or small vessel disease. On the other hand, the RT-GM approach is highly influenced by PVE, rendering the use of restrictive GM masks mandatory. Nevertheless, approaches for PVE correction most often target only the relative CBF images and not M_0 measures (Asllani et al., 2008; Chappell et al., 2011). Therefore, we believe that this correction should not affect our results concerning the comparison of calibration methods. Similarly to the RT-WM and RT-GM methods, the Voxel method yielded relatively small CBF differences across different processing options. In fact, some options had negligible impact on CBF quantification, namely the degree of smoothing and the values of the water partition coefficient. A summary scheme of recommended calibration procedures, as well as the corresponding options that should applied/reported, is depicted in Figure 4.6.

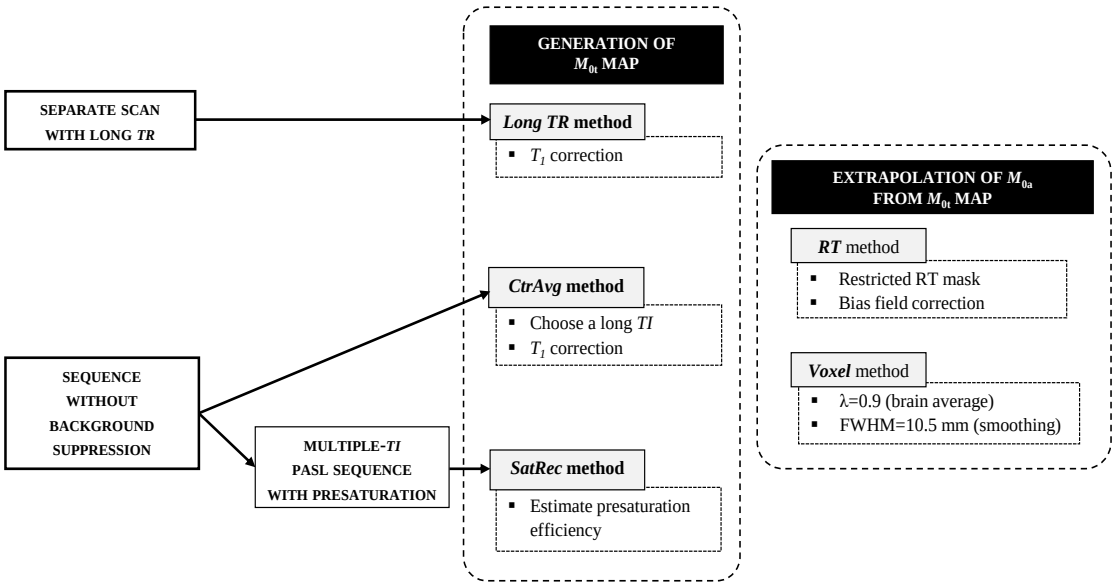

Figure 4.6: Summary of the main calibration methods, according to the data acquisition procedure (left), and with indication of the corresponding recommended options, for the generation of the M_{0t} map (middle), and the extrapolation of M_{0a} from the M_{0t} map (right).

4.5.4 CBF Values, Spatial Distributions and Reproducibility

The maps obtained in our study exhibit spatial distributions that are consistent with the expected variations across tissues and brain regions (Mutsaerts et al., 2015; Sousa et al., 2014b; Wang et al., 2011). All average GM CBF values found in our study were within the wide range of values reported in the literature. However, the PASL dataset systematically produced lower CBF values than the pCASL dataset. Surprisingly, in a study using five different commonly used ASL sequences, the opposite pattern was seen between single-PLD pCASL and multiple-TI PASL using the RT-CSF calibration method (25/40ml/100g/min for pCASL/PASL)6. In another study, similar values were found for both PASL and pCASL single-PLD/TI sequences (62/60ml/100g/min for PASL/pCASL), using different calibrations strategies (extra calibration scan strategy for PASL and control averaging strategy for pCASL) (Chen et al., 2011). Nevertheless, the differences between pCASL and PASL observed here could be explained partially by other factors not being taken into account such as labeling efficieny or SNR. We therefore further recommend that ASL studies should not attempt to compare CBF values obtained with different labeling schemes.

The inter- and intra-subject coefficients of variation obtained in our study for GM average CBF values are all within intervals of good reproducibility. For PASL, CV_{intra} of ∼10-12 % is in agreement with the literature. A multiple-TI QUASAR ASL study using a model-free approach reported a within-week CV_{intra} of 10 % (Petersen et al., 2010), whereas a study from our group achieved within-week CV_{intra} values in the range of 10-21 % depending on the type of fitting strategy and acquisition sequence (Sousa et al., 2011). A single-TI PASL study, using a PASL sequence similar to the one employed in our study, found a within-week CV_{intra} of ∼6% (Wang et al., 2011). Regarding pCASL, our results of ∼ 6-7 % are also in accordance with the literature. A single-PLD pCASL study using two different PLD values yielded CV_{intra} values of ∼5-10 %, which increased with PLD (Wu et al., 2014). Also consistently, a multiple-PLD pCASL study obtained a CV_{intra} of ∼5 % for average week-repeat GM CBF value (Mezue et al., 2014).

4.5.5 Limitations and Future Work

Although our approach aimed to systematically and comprehensively test all relevant processing options in the calibration methods used, options regarding relatively less important parameters could also be tested, in particular the tissue-specific T_2^* used to correct for T_2^* decay when deriving the M_{0t} maps. Another option that could be tested is the use of the subject-specific or voxelwise T_1 values, which could be estimated directly when using the SatRec approach in PASL, or acquired separately. Importantly, some of the calibration methods may not be appropriate to use in certain clinical populations. For example, in patients with WM abnormalities, such as in multiple sclerosis or small vessel disease, the RT-CSF or RT-GM methods may be preferable to the RT-WM. Furthermore, we acknowledge that some options could not be tested due to the lack of data availability. In particular, the LongTR approach should be also

compared using PASL, in order to determine the best method for M_{0t} generation. Additionally, a more precise approach for correction of B_1 field inhomogeneities, namely by normalization the data using a receive RF coil sensitivity map, should be performed and compared across calibration approaches. Finally, a prospective study assessing the impact of calibration strategies by acquiring both PASL and pCASL on the same subjects should be conducted in order to further validate our results.

4.6 Conclusion

In conclusion, we found that considerable discrepancies in CBF values can be obtained when using different options in the calibration pipeline of pCASL and PASL data. In general, the greatest sensitivity was found for correction for incomplete T_1 relaxation when using proton density reference images for calibration. Correction for RF field inhomogeneities also had great impact, as did the value of presaturation efficiency, while the mask used for the reference tissue had moderate impact. In contrast, the degree of spatial smoothing applied to the calibration images or the values of brain-blood water partition coefficient had only negligible effects. Our findings further support the use of a voxelwise approach as proposed in the ASL white paper given its relatively low sensitivity to these options. Calibration methods based on CSF or WM as reference tissue tend to be more sensitive to such options and less reproducible, respectively, and should therefore be avoided. Nevertheless, our results emphasize the need for consistent processing pipelines across studies as well as the need for a complete description of the various calibration options, so that absolute CBF quantification is effectively achieved. Failure to take the impact of these fine calibration options into account would seriously compromise the utility and applicability of ASL perfusion imaging.

Acknowledgements

This work was supported by the Portuguese Foundation for Science and Technology (FCT) grants PTDC/BBB-IMG/2137/2012, PD/BD/135114/2017 and UID/EEA/50009/2013; the Engineering and Physical Sciences Research Council UK (EP/P012361/1) and the Wellcome Trust (203139/Z/16/Z). The authors wish to express their gratitude to the European Cooperation in Science and Technology – Arterial spin labelling Initiative in Dementia (COST – AID Action BM1103).

5

Noninvasive Mapping of Cerebrovascular Reactivity using MRI: Methodological Aspects

Contents

This Chapter corresponds to the article (currently *in preparation*): Joana Pinto, Patrícia Figueiredo. "Non-invasive mapping of cerebrovascular reactivity using MRI: methodological aspects".

5.1 Abstract

Cerebrovascular reactivity (CVR) is defined as the ability of vessels to alter their calibre in response to vasoactive factors by means of dilating or constricting in order to increase or decrease regional cerebral blood flow (CBF). Importantly, CVR may provide a sensitive biomarker for pathologies where vasculature is compromised. Moreover, the spatiotemporal dynamics of CVR observed in healthy subjects, reflecting regional differences in cerebral vascular tone and response, may also be important in functional magnetic resonance imaging (fMRI) studies based on neurovascular coupling mechanisms.

Assessment of CVR is usually based on the use of a vasoactive stimulus combined with a CBF measurement technique. Although Transcranial Doppler Ultrasound has been frequently used to obtained global flow velocity measurements, magnetic resonance imaging (MRI) techniques are increasingly employed for obtaining CBF maps, particularly using non-invasive methods such as the blood oxygen level dependent (BOLD) contrast or arterial spin labeling (ASL). For the vasoactive stimulus, vasodilatory hypercapnia is usually induced through the manipulation of respiratory gases, including the inhalation of increased concentration of carbon dioxide. However, these methods are somehow invasive and may not be well-tolerated by some populations. Furthermore, they require complex experimental setups that may not be widely available. For these reasons, noninvasive methods such as hypercapnia-inducing breath-holding have become increasingly sought-after. Most recently, a new generation of noninvasive methods for CVR assessment has been proposed, based on the spontaneous respiratory fluctuations occurring during resting-state.

In this work, we systematically review noninvasive techniques for mapping CVR, focusing on the methodological aspects of the vasoactive modulation and the respective imaging using MRI. Hopefully, this review will motivate the wider use of non-invasive CVR assessment techniques and, in this way, allow a deeper exploration of the potential of CVR, not only as a disease biomarker, but also as an important variable in common resting-state functional MRI studies.

5.2 Introduction

CVR is an intrinsic regulatory mechanism of the brain whereby blood vessels adjust their calibre in response to vasoactive stimuli, in order to increase or decrease the regional cerebral blood flow (CBF). Importantly, CVR is thought to be a sensitive biomarker for the brain's vascular health in a wide range of conditions and pathologies, including stroke (Geranmayeh et al., 2015; Krainik et al., 2005; Markus and Cullinane, 2001; Zhao et al., 2009), cerebral stenosis

(Chang and Glover, 2009a; Ziyeh et al., 2005), glioma (Fierstra et al., 2016; Hsu et al., 2004; Iranmahboob et al., 2016; Pillai and Zacá, 2011; Zacà et al., 2014), small vessel disease (Hund-Georgiadis et al., 2003; Sam et al., 2016c) and Moyamoya disease (Donahue et al., 2013; Heyn et al., 2010; Mandell et al., 2008b). Moreover, even in an healthy brain, CVR mapping has revealed spatiotemporal patterns possibly reflecting regional variations in cerebral vasculature (Kastrup et al., 1998; Leoni et al., 2008; Thomason et al., 2005). Importantly, CVR directly impacts commonly used haemodynamic measures of brain activity, namely using blood oxygen level dependent (BOLD) functional MRI (fMRI) (Ogawa et al., 1990). CVR mapping has therefore been used as a normalizing factor in fMRI studies in order to reduce inter- and intrasubject variability (Handwerker et al., 2007; Thomason et al., 2007; Tsvetanov et al., 2015).

In order to evaluate CVR, a challenge to the vasculature is usually applied while the associated CBF changes are measured. Transcranial Doppler Ultrasound (TDU) has been commonly used to measure mean blood flow velocities in major cerebral arteries (most notably the middle cerebral arteries which are accessible through an acoustic window on the skull), providing an indirect index of global CBF, and hence of CVR (Haussen et al., 2012; Müller et al., 1995). To obtain a map of CBF, and hence CVR, Positron Emission Tomography (PET) and Single-Photon Emission Computed Tomography (SPECT) (Aso et al., 2009; Choi et al., 2013) can be used in combination with appropriate CBF radiotracers. While TDU allows only global and indirect CVR evaluation, PET and SPECT involve the administration of radiotracers. By overcoming both limitations, and further allowing improved spatial and temporal resolution, MRI techniques have become increasingly popular for CVR assessment. The blood oxygen level dependent (BOLD) contrast commonly used in functional MRI (fMRI) studies has been particularly useful in this context. Although the BOLD signal results from a complex combination of several physiological parameters, including not only CBF but also cerebral blood volume (CBV) and blood oxygenation, it is nevertheless thought to reflect predominantly CBF changes (Mandell et al., 2008b). For truly quantitative measurements of CBF, the non-invasive Arterial Spin Labeling (ASL) perfusion imaging method can be used. Unfortunately, due to ASL's intrinsic low signal-to-noise ratio and relatively poor temporal resolution, only a few studies have employed this measurement technique for evaluating CVR (Kastrup et al., 1999; Leoni et al., 2012; Li et al., 1999; Noth et al., 2008; Tancredi et al., 2012).

Regarding the vascular challenge, the most common approach involves the induction of hypercapnia, whereby the arterial blood partial pressure of carbon dioxide (CO_2) is increased, leading to vasodilation and increased CBF. In clinical settings, acetazolamide, a drug also known as Diamox, is often used for this purpose: a selective inhibitor of the enzyme carbonic anhydrase, it decreases the conversion rate of CO_2 to bicarbonate, hence causing hypercapnia (Aso et al., 2009; Müller et al., 1995; Vorstrup et al., 1984). The injection of acetazolamide is however an invasive procedure that leads to variable responses between subjects (Fierstra et al., 2013), and may result in adverse reactions, including dizziness, nausea, vomiting, headache (Dahl et al., 1995; Saito et al., 2011). Another relatively common method of inducing hypercapnia is the

inhalation of air with an increased CO_2 concentration. In fact, it is possible to induce blood gas changes by manipulating the respiratory gases. In general, these methods are based on the inhalation of a gas mixture with altered concentration in relation to normal breathing air, although the composition of those mixtures will depend on the main goal of the study. Different techniques have been developed and improved along the years in order to control precisely gas levels, including: Fixed Inspiratory Challenge (Bandettini and Wong, 1997; Cantin et al., 2011; Yezhuvath et al., 2009); Dynamic End-Tidal Forcing (Robbins et al., 1982; Wise et al., 2007); Sequential Gas Delivery (Kassner et al., 2010; Mandell et al., 2008b; van der Zande et al., 2005; Vesely et al., 2001); and Prospective End-Tidal Targeting (Mark et al., 2010; Prisman et al., 2008; Slessarev et al., 2007; Spano et al., 2013). In particular, a specific level of end-tidal CO_2 partial pressure is usually targeted as this is thought to be a proxy/surrogate of arterial CO_2 partial pressure.

Some of these respiratory gas manipulation techniques allow the precise targeting of specific end-tidal gas concentrations, despite variable ventilatory responses, hence providing extremely reliable methods for CVR assessment (Mark et al., 2010; Spano et al., 2013). Nevertheless, the required experimental setups are quite complex, including uncomfortable breathing masks, and may be associated with low tolerance by some clinical populations or cause ethical concerns for studies of healthy volunteers. Together with the limited availability of the required gas modulation devices, these factors may hinder the wider applicability of these methods. Alternatively, completely noninvasive strategies have also been proposed, based on respiratory tasks such as breath holding or paced deep breathing. Because of their total noninvasiveness and relatively simple and inexpensive implementation, these strategies might offer a new opportunity for the application of CVR assessment as a useful clinical and research tool. In fact, they rely solely on the subject's intrinsic ventilatory response and have been shown to be well tolerated by healthy volunteers as well as patients and to yield results comparable to those obtained with invasive methods (Golestani et al., 2016; Kastrup et al., 2001; Magon et al., 2009).

The aim of this work is to review noninvasive CVR mapping techniques using MRI. For this purpose, we will focus on the BOLD contrast for the MRI assessment of CBF changes, and we will consider the different noninvasive methods that can be used to elicit a vascular response, including: task-based methods that induce changes in arterial pressure of blood gases and consequently vasodilation/vasoconstriction and measurable changes in CBF; and resting-state approaches that rely simply on the spontaneous fluctuations of respiration during resting state. In each case, we first describe the details of experimental design and data acquisition for the respective vasoactive modulation approach and we then discuss data analysis and modeling methodologies to derive CVR maps from the associated MRI measurements. It should be noted that a summary of some of the stimuli commonly used to evaluate CVR, with the exception of resting-state CVR methods, can be found in (Fierstra et al., 2013) and a description of practical aspects when using only invasive respiratory challenges in combination with MR techniques is provided in (Moreton et al., 2016). Our review differs from these previous ones by focusing only

on noninvasive methodologies and their corresponding processing strategies.

5.3 Task-Based Methods

5.3.1 Data Acquisition

5.3.1.A Breath-Holding

The use of the breath-hold (BH) task for CVR measurement was first described by Ratnatunga and Adiseshiah using TDU (Ratnatunga and Adiseshiah, 1990) and since then the BH task has been the most common non-invasive challenge chosen to elicit a cerebrovascular response. Despite being performed mostly by healthy adults, studies of children and elderly populations confirm that this type of task can be effectively used to measure CVR even in populations that are generally considered less cooperative (Handwerker et al., 2007; Kannurpatti et al., 2010; Raut et al., 2016; Riecker et al., 2003; Thomas et al., 2013; Thomason et al., 2005). Furthermore, this task has also been successfully applied in patients with pathologies such as stroke (Raut et al., 2016; Shiino et al., 2003), obstructive sleep apnea (Buterbaugh et al., 2015; Ponsaing et al., 2018; Prilipko et al., 2014), schizophrenia (Friedman et al., 2008) and glioma (Hsu et al., 2004; Iranmahboob et al., 2016). Other works have investigated the relationship between BH-CVR measurements and factors such as vascular risk/hypertension (Haight et al., 2015; Tchistiakova et al., 2015), smoking (Friedman et al., 2008), altitude/diving (Vestergaard and Larsson, 2017; Yan et al., 2011) and physical activity (Gonzales et al., 2014; Svaldi et al., 2015). Furthermore, some studies have reported high correlations between CVR mapping results obtained using BH compared with methods based on CO_2 inhalation (Biswal et al., 2007; Kannurpatti and Biswal, 2008; Kastrup et al., 2001; Tancredi and Hoge, 2013). A systematic review of CVR mapping only using the BH task can be found in (Urback et al., 2017).

Task Design

BH Period Duration

The BH paradigms usually follow a standard block design, with alternating periods of breath holding and normal breathing. In the literature, the duration of the BH blocks has ranged from 3 s (Liu et al., 2002) to over one minute (Li et al., 1999; Nakada et al., 2001; Vestergaard and Larsson, 2017), but with most studies using periods between 10 and 30 s. Significant hypercapnia states have been reported with BH periods as short as 6 s (Abbott et al., 2005), with no significant changes being observed when using 3 or 5 s BH durations (Liu et al., 2002). Nevertheless, the amplitude of the response increases with BH duration, with longer durations yielding more significantly responsive voxels as well as more reproducible results (Andrade et al., 2006; Bright and Murphy, 2013; Kastrup et al., 1999; Magon et al., 2009). Liu et al. have observed that the responding brain volume reaches a plateau approximately at a BH length of 20 s (Liu et al.,

2002), hence 6 - 20 s might be an appropriate interval for CVR assessment. Nevertheless, smaller BH durations will be less susceptible to correlate with head motion and will be easier to tolerate, particularly in clinical settings (van Oers et al., 2018). Several studies have successfully applied BH with durations around 15 s, hence this values might be a good compromise for BH CVR assessment (Bright et al., 2011; Donahue et al., 2009; Friedman et al., 2008; Geranmayeh et al., 2015; Haight et al., 2015; Iranmahboob et al., 2016; Leoni et al., 2008; Lipp et al., 2014, 2015; Tchistiakova et al., 2014; van Oers et al., 2018).

Resting Period Duration

Regarding the normal breathing periods alternating with the BH periods, these usually have a long duration in order to allow blood gas levels to return to baseline. The values are usually dependent on the BH period chosen for the same task, but these have ranged from 13.5 s (Prilipko et al., 2014; Thomason and Glover, 2008) to 90 s (Nakada et al., 2001). Another aspect is the breathing rhythm, which may be self-paced or computer-paced. The latter may help minimize variability inherent to the variable breathing rates within and between subjects, resulting in a more consistent baseline condition (Scouten and Schwarzbauer, 2008). On the other hand, computer-paced breathing methods require the choice of an appropriate respiratory frequency for achieving a normocapnic baseline state, and this is highly dependent on physiological variations in lung function and breathing depth, within and across subjects. Breathing rates between 1/2.5 Hz and 1/6 Hz have been reported in literature (Birn et al., 2008; Bright and Murphy, 2013; Chang et al., 2008; Handwerker et al., 2007; Lipp et al., 2014, 2015; Scouten and Schwarzbauer, 2008; Wu et al., 2015). However, Bright and Murphy observed mild hypocapnia compared to resting-state levels when using a 1/6 Hz rate. Using a higher respiratory rate (1/3.75 Hz), Tancredi and Hoge also observed lower CO_2 values in comparison to self-paced baseline values (Tancredi and Hoge, 2013). Targeting the respiratory frequency to match the participant's spontaneous breathing rate might minimize these hypocapnic effects of computer-paced breathing. Residual effects after controlling for breathing rate may be related to the fact that breathing automatically becomes deeper when paced, which could also lead to hypocapnia (Bright and Murphy, 2013).

Number of cycles

The number of BH cycles differs between studies, ranging from 1 (Li et al., 1999; Nakada et al., 2001) to 12 (Tancredi et al., 2012). In principle, the more cycles are acquired the more averaging can be done and thus the higher signal-to-noise ratio can be achieved. However, more cycles also lead to longer protocol durations and hence to greater susceptibility to motion and exhaustion. Most of the BH-CVR studies use between 3 and 7 cycles. Lipp and colleagues assessed the reproducibility of CVR measurements using different numbers of cycles and recommended at least 3 cycles to guarantee reproducible maps, when a breath-hold duration of 15 s is used with 18 s of rest (Lipp et al., 2015).

End-expiration or end-inspiration BH

The BH task may be performed following either an inspiration or an expiration. Studies comparing end-expiration and end-inspiration BH protocols obtained slightly different results in terms of timing and amplitude, with end-expiration based protocols achieving faster responses. However, when taking into account only the maximum amplitude despite timing differences, both BH tasks yield comparable results (Kastrup et al., 2001; Leoni et al., 2012; Li et al., 1999). When using an end-inspiration BH task, the amplitude of the BOLD response also depends on the depth of the preparatory inspiration; to overcome this issue, a feedback mechanism has been proposed (Thomason and Glover, 2008). Moreover, end-inspiration and end-expiration BH protocols have been found to produce BOLD responses with markedly different shapes (Hsu et al., 2004; Liu et al., 2002). In one study, the end-inspiration BH protocols yielded a biphasic response while the end-expiration protocols only induced an increase in the BOLD signal following the BH onset. However, some other studies observed more complex responses, with end-expiration BH protocols yielding a biphasic shape, while end-inspiration BH protocols yielded a triphasic shape (Magon et al., 2009). The authors suggest that the additional initial short positive peak of end-inspiration BH responses may result from the combination of several physiological mechanisms associated with the respiratory act itself, such as variation of heart rate, reduction of pulmonary vascular tension and resistance and autonomic modulation of neuronal responses (Magon et al., 2009; Nakada et al., 2001; Thomason et al., 2005). End-expiration tasks may also induce additional head motion due to the urge to inspire towards the end of the task (Thomason et al., 2007).

Despite the relatively greater complexity of the response, end-inspiration approaches may nevertheless be more suitable for potentially less cooperative patients, since they are easier to perform (Pillai and Mikulis, 2014; Roberts et al., 2009). One possible physiological explanation for this relative ease is that an increased lung volume inhibits the respiratory centres through the Hering-Breuer reflex, thus lengthening the BH breaking point and associated CO_2 change (Chapin, 1955; Muxworthy, 1951; Skow et al., 2015). Alternatively to an explicit end-inspiration or end-expiration BH protocol, in some studies, subjects are instructed to cease breathing wherever they were in their natural respiratory cycle (Hsu et al., 2004; Liu et al., 2002).

Task Instructions

Task instructions are usually provided using the visual modality, but auditory cues can also be used (Chang et al., 2008; Kannurpatti and Biswal, 2008; Riecker et al., 2003; Tancredi and Hoge, 2013). Visual tasks have ranged from simple verbal instructions displayed on a screen (Birn et al., 2008; Bright and Murphy, 2013; Haight et al., 2015; Handwerker et al., 2007; Magon et al., 2009; Svaldi et al., 2015), to color-coded or symbolic cues (Friedman et al., 2008; Kannurpatti et al., 2010; Prilipko et al., 2014; Thomason and Glover, 2008; Van Oers et al., 2010). Furthermore, some studies have included some feedback cues such as decreasing size circles/squares or numerical countdowns displaying the time left until the next cue (Prilipko

et al., 2014; Thomason et al., 2005). A study from Thomason and Glover used additional, simultaneous respiratory measurements, e.g. through a respiratory belt, to retrieve information to be used as feedback cue for targeting inspiration levels (Thomason and Glover, 2008). Another important aspect of task-based methods is the neuronal activation possibly induced by the instructions. In order to minimize this type of confound, similar brightness levels should be used for the instructions during both the periods of BH and normal breathing (Kastrup et al., 1999). Additionally, a supplementary task-based acquisition, with similar (visual/auditory) stimulation but no breath-holding can be performed in order to detect task-based areas of neuronal activity and remove them for subsequent analysis.

Monitoring

Monitoring of task performance can be achieved through monitoring or acquisition of other physiological measurements during acquisition, including $PETCO_2$ levels. This can be achieved through the use of external devices such as a capnograph in combination with a nasal cannula, measuring the CO_2 levels at each expiration. Sampling should be performed as close to the subject's expired air flow as possible in order to reduce the time delay between sampling and recording (Chu et al., 2011; Moreton et al., 2016; Peacock et al., 2016).

Furthermore, pre-scan training is also highly recommended when using task-based methods in order to ensure that the patient understands and performs the task correctly (Kannurpatti and Biswal, 2008; Kannurpatti et al., 2010; MacIntosh et al., 2003; Magon et al., 2009; Pillai and Mikulis, 2014). Additionally, it also makes the patient more familiar and less anxious about the task itself, improving compliance.

5.3.1.B Other Breathing Tasks

Despite the BH task being a valuable method to induce hypercapnia and vasodilation non-invasively, techniques to induce vasoconstriction might be useful whenever cerebral vessels are already dilated and further vasodilation is not possible (Bright et al., 2011; Zhao et al., 2009). In that case, hyperventilation might provide a valuable alternative to the BH task, yielding the opposite effect: an increase in respiration rate/depth induces hypocapnia, which in turn causes vasoconstriction and decreased CBF.

A number of studies have used this approach in combination with fMRI in healthy and patient groups (Cohen et al., 2002; Hajjar et al., 2010; Krainik et al., 2005; Naganawa et al., 2002; Posse et al., 1997; Tancredi and Hoge, 2013; Weckesser et al., 1999). The hyperventilation periods are usually long, ranging from 1 minute (Weckesser et al., 1999) to 10 minutes (Posse et al., 1997). While some studies only instruct subjects to hyperventilate with no fixed rate or depth, others opt to specify a certain rate/depth (Krainik et al., 2005). In some studies, subjects are trained outside the scanner, verifying $PETCO_2$ levels in order to assess subject compliance (Posse et al., 1997; Zhao et al., 2009) or to determine the subject-wise rate that best yields the required hypocapnic effect to be used in the final protocol (Cohen et al., 2002). Nevertheless, prolonged

hyperventilation periods may cause undesired effects such as light-headedness, dizziness, visual disturbance, numbness and paresthesia, palpitations, tachycardia, shakiness, tension or anxiety, panic attacks and weakness or exhaustion (Posse et al., 1997). Moreover, hyperventilation paradigms usually induce high levels of head motion associated with the inspiration/expiration cycle.

In order to overcome such limitations, paced breathing methods inducing mild hypocapnia have been proposed. Bright et al. (Bright et al., 2009) introduced a Cued Deep Breathing (CDB) paradigm consisting in a controlled and mild increase of respiration rate (1/4 Hz) in blocks of only a few breaths (2 or 3) (Figure 5.1) (Bright et al., 2009, 2011). This method, which has subsequently also been referred to as paced deep breathing, was compared with more standard approaches, such as BH or CO_2 inhalation, yielding similar results (Bright et al., 2009). In another study, Sousa et al. showed that a similar CDB protocol yielded CVR measurements with good within- and between-subject reproducibility (Sousa et al., 2014a). Additionally, Bright et al. compared CDB and BH tasks after CO_2 inhalation, mimicking cases where further basal vasodilation is not possible, and observed that CDB-derived CVR values were greater than those obtained using BH (Bright et al., 2011). Vogt and colleagues studied the impact of faster (1/2.5 Hz) and deeper paced respiration for longer periods and found that the combination of rapid and deep breathes yielded the lowest $PETCO_2$ value. Furthermore, they also observed that $PETCO_2$ decreases were higher when using cued normal breathing rather than non-cued normal breathing (Vogt et al., 2011).

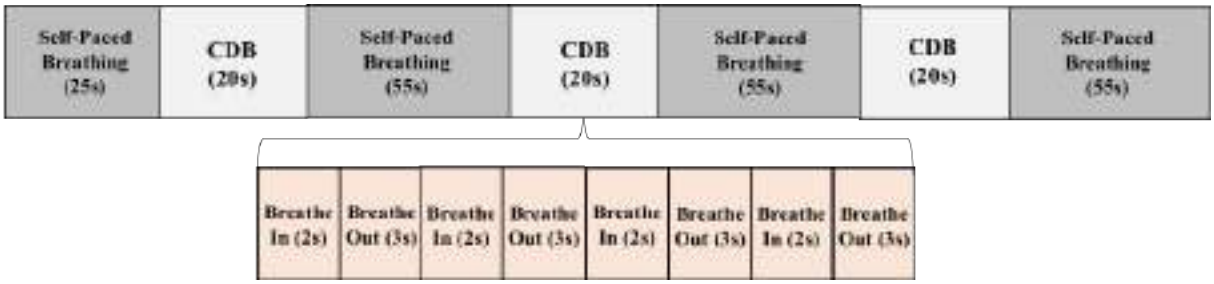

Figure 5.1: Example of a Cued Deep Breathing (CDB) protocol, with 20 s of CDB and 25 s of self-paced breathing.

Responses to neuronal activation have also been used as a surrogate of CVR (Dumas et al., 2012; Switzer et al., 2016; van Opstal et al., 2017). Both visual and motor tasks have been used as vasoactive stimuli, due to the robustness of their elicited fMRI response. Nevertheless, a major limitation is the fact that this strategy only allows mapping of specific brain regions.

A summary of the most common non-invasive respiratory methodologies to induce a vascular response and their acquisition options can be seen in Table 5.1.

Table 5.1: Summary of the most common non-invasive methodologies to induce a vascular response, their impact on arterial CO_2 levels, cerebral vessels resistance and BOLD-fMRI signal, as well as the acquisition parameters and options of each method.

Task		**Effect on CO_2 levels**	**Effect on cerebral vessels**	**Impact on BOLD-fMRI signal**
BH		↑	vasodilation	↑
Other Breathing Tasks	**Hyperventilation**	↓	vasoconstriction	↓
	CDB	↓	vasoconstriction	↓
Acquisition				
Cycles	number		**Task-dependent**	**Options**
Instructions	visual/auditory/mixed		**BH**	duration
Resting Period	duration			inspiration/expiration
			CDB	duration
				frequency

5.3.2 Data Analysis

Several strategies have been proposed to model fMRI responses to a vasoactive task, with focus on model-driven approaches, ranging from simple correlation to the general linear model (GLM) analysis. Regardless of the method chosen and the task performed, one of the most important steps when using this type of approach is undoubtedly the choice of model used in the analysis. Since task paradigms usually consist of alternate periods of task and baseline, a simple box-car function describing this block design paradigm may provide a suitable model of the fMRI response, assuming a constant time-response relation throughout the experiment (Biswal et al., 2007; Kastrup et al., 1999). In order to account for the temporal dynamics of the vascular response to the respiratory task, the box-car should be convolved with an appropriate impulse response function. Some studies have used the canonic haemodynamic response function (HRF) commonly used to describe the BOLD response to an impulse of neuronal activity; in this case, adding the dispersion derivative to the model may be important to allow for the longer delays observed in the case of the respiratory tasks (Bright and Murphy, 2013; Bulte et al., 2009; Haight et al., 2015; Magon et al., 2009; Thomason et al., 2005). Other approaches include the use of ramp functions, assuming a linear increase in the BOLD response with time when using a BH task (Bright and Murphy, 2013).

In order to specifically model the impulsive response function associated with respiratory tasks, Birn and colleagues have derived a new function to model the BOLD response to variations in the respiration volume per time (RVT) based on the measurement of single deep breaths. This new function was called Respiration Response Function (RRF) and was shown to provide a significantly better fit to the signal changes induced by breath-holding and cued breathing

than typically used neuronal HRFs (Birn et al., 2008). In a later study, Vogt et al. derived a transfer function based on $PETCO_2$ variations for paced hyperventilation and compared this with an optimized version of the RRF (Vogt et al., 2011). Some studies have used individual $PETCO_2$ time-courses as regressors in the model, intrinsically accounting for variations between subjects as well as within a single acquisition, but requiring collection of extra physiological measurements. In particular, it has been demonstrated that the use of $PETCO_2$ models convolved with a standard HRF can cope with incorrect task performance, which is particularly relevant in non-compliant participants and thus has potentially great impact on patient studies (Bright and Murphy, 2013).

Nonetheless, one aspect these modeling strategies have in common is the assumption that a single, fixed time course is sufficient to explain variations across the brain. However, it has been suggested that the response to vasoactive stimuli may exhibit different delays across brain regions, not only in healthy subjects but also in cerebrovascular disease patients. Some studies have attempted to overcome this limitation by incorporating voxelwise delay maps into the analysis (Andrade et al., 2006; Bright et al., 2011; Chang et al., 2008; Geranmayeh et al., 2015; Magon et al., 2009; Tong et al., 2011). The most common approach to obtain these maps is by simply shifting the model and determining the time shift that provides the highest cross-correlation with the BOLD signal voxelwise. Other approaches aim to estimate response delay-related parameters (onset, time-to-peak, full width at half maximum) as well as its amplitude voxelwise. This has been achieved by using the Hilbert transform (Raut et al., 2016), auto-regressive methods based on pseudo-trapezoidal fitting (Leoni et al., 2008) or a Fourier basis model as response model (Pinto et al., 2016). The latter exploits the essential biphasic shape of the response and the overall periodicity of the signal variations at the paradigm frequency, allowing for variable phase delays across the brain (Blockley et al., 2011). It has been reported that a sine–cosine pair at the task frequency and its two harmonics is a suitable model for end-inspiration BH CVR measurements, yielding robust and reproducible estimates (Pinto et al., 2016) (Figure 5.2).

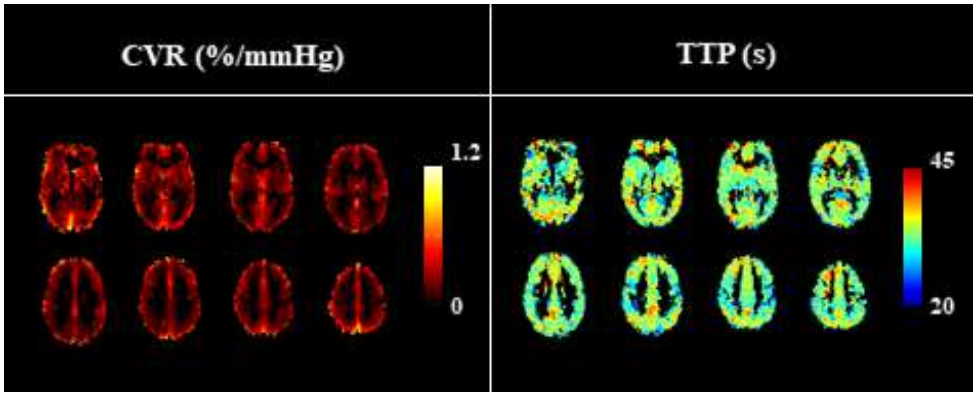

Figure 5.2: CVR amplitude (right) and time-to-peak, TTP (left) maps obtained in a BH BOLD-fMRI experiment using a Fourier basis model with two harmonics: average of a group of subjects.

Murphy et al. evaluated some of these different strategies when modeling the BOLD response to a BH task, including $PETCO_2$ and the sine-cosine approach. They observed that variance in the BOLD response is best explained by fitting either a sine wave at the task frequency or the $PETCO_2$ trace convolved with a standard HRF and including its temporal derivative (Murphy et al., 2011b). A more recent study showed that a sine-cosine model yielded similar or higher values of repeatability than the ones based on $PETCO_2$ (Lipp et al., 2015). The authors explain their results by stating that the use of the $PETCO_2$ trace may induce additional variability, by introducing the experimental errors of the capnograph's measurement into the computation of CVR. Moreover, other potential confounding factors are inaccuracies in the synchronization between $PETCO_2$ and fMRI recordings. Additionally, in the specific case of the BH task, since there is no $PETCO_2$ information during the BH period, interpolation must be performed. Surprisingly, although the sine-cosine model does not account for deviations in task performance, which could be a relative disadvantage compared with $PETCO_2$-based models, its performance was highly repeatable across subjects (Lipp et al., 2015).

A sinusoidal approach was also investigated by van Niftrik and colleagues, by comparing several sine-based modeling strategies for the BOLD response to a BH task in patients with unilateral hemispheric impaired perfusion. The voxelwise optimal delay, obtained through phase-shift, yielded significantly higher CVR values and better differentiation between affected and unaffected brain tissues. Additionally, two sine waves with different frequencies were used in order to accommodate the fact that the BH and resting periods had considerably different durations (van Niftrik et al., 2016). In the same work, stimulus independent models, which were based on the BOLD signal time-course averaged across a representative ROI, produced similar results to the sine-based strategies ones. In the case of patients with unilateral lesions they also considered a model based on a ROI of the unnafected brain area (van Niftrik et al., 2016). Despite the added benefit of not requiring any external measurements and avoiding timing confounds and measurement errors previously described, models based on the fMRI data itself are only applicable for within-patient comparisons and can be highly dependent on the ROI chosen (Geranmayeh et al., 2015). A new iterative method called Regressor Interpolation at Progressive Time Delays (RIPTiDe), also based on a predefined model, has been applied in CVR studies in order to optimize more robustly timing differences across the brain (Donahue et al., 2016; Tong et al., 2011).

5.4 Resting State Methods

The last years have seen an increasing interest in the study of the brain's intrinsic functional connectivity, based on time synchronous fluctuations in the BOLD signal across different brain regions (Biswal et al., 1995). The hemodynamically-driven changes in tissue and vessel oxygenation underlying the BOLD signal are, however, caused by a combination of neuronal activity and non-neuronal mechanisms, including respiration variations or blood pulsation. This non-

neuronal information is usually called physiological noise in the context of conventional fMRI studies of brain activity since it is of no interest in those cases. In resting state fMRI (rs-fMRI) studies, the common approach is to model and eliminate this type of information (Birn, 2012; Greicius et al., 2003; Pinto et al., 2017). However, these physiological fluctuations could also potentially contain information of interest about the cerebral haemodynamics, including CVR mechanisms. In particular, metrics quantifying low frequency oscillations are commonly used in rs-fMRI studies to infer about spontaneous neuronal activity, since it is assumed this information is within this frequency range. Nevertheless, other mechanisms might contribute to these fluctuations, including different physiological processes and even non-physiological components (Caballero-Gaudes and Reynolds, 2017; Murphy et al., 2013). In fact, it is well known that the aliasing of higher frequency fluctuations (respiratory and cardiac) into the low frequency range, due to the typically low temporal resolution of fMRI data, plays a significant role in spontaneous BOLD fluctuations. Other issues include bulk motion of certain brain regions due to cardiac and respiratory pulsations (Harvey et al., 2008), head motion and breathing-induced B_0 field fluctuations or spin history artefacts introduced by breathing-related head movements (Friston et al., 1996). Nevertheless, it has been observed that some of these processes affect distinct areas. For example, cardiac-related artifacts primarily affect areas with high arterial density while respiration-induced signal changes mostly occur in highly vascular regions, such as gray matter and large vessels (Birn et al., 2006).

Physiological fluctuations occurring within the low-frequency band are thought to be mainly governed by the autonomic nervous system. In fact, heart rate variability is a metric commonly used as a marker of autonomic nervous system activity; it has two components, a higher frequency one thought to be related to respiration-induced parasympathetic heart rate modulation (0.15 - 0.4 Hz) and a lower frequency one at around 0.05 - 0.15 Hz (Chang et al., 2013). The latter component appears to occur in synchrony with oscillations of the arterial blood vessels' sympathetic vasomotor tone, also known as Mayer waves of blood pressure (0.03 - 0.15 Hz) (Draghici and Taylor, 2016; Julien, 2006). Another mechanism in the low-frequency range are the vasomotion fluctuations ($\sim$0.1 Hz) caused by contraction of the smooth muscle of the arterioles as a consequence of an increase in blood volume, which are thought to be independent of cardiac and respiratory cycles (Murphy et al., 2013). More recently, low and very low-frequency pulsations (0.023 - 0.73 Hz and 0.001 - 0.023 Hz, respectively) have also been described as a mechanism for CSF pulsations (Glymphatic system) (Mäkiranta et al., 2004).

Other physiological mechanisms, that induce low-frequency BOLD oscillations and might be more closely related to CVR and the physiology underlying the task-based mechanisms previously described, are the changes in the arterial concentration of blood gases. Back in 1997, Biswal et al. showed that the amplitude of BOLD low-frequency fluctuations was reversibly sensitive to hypercapnia, diminishing the fluctuations observed in the sensorimotor cortex (Biswal et al., 1997). These results were further supported by a functional near-infrared spectroscopy (NIRS) study that demonstrated that slow spontaneous oscillations in cerebral oxygenation in

the human could be detected with or without visual stimuli and that they were attenuated by hypercapnia (Obrig et al., 2000). In 2004, Wise et al. further demonstrated that low frequency BOLD signal is correlated with spontaneous CO_2 fluctuations across the human brain (Wise et al., 2004). Additional investigation confirmed that low frequency fluctuations are also correlated in amplitude and spatially with hypercapnic responses, including the BH-challenge (Biswal et al., 2007), in both younger and older populations (Kannurpatti and Biswal, 2008; Kannurpatti et al., 2011).

Simultaneous multimodal studies have provided useful insights into the origin of low-frequency oscillations of BOLD fMRI data. In particular, the concurrent collection of fMRI and NIRS (high temporal resolution) demonstrated that spatiotemporal patterns of low-frequency oscillations evolve similarly to the circulatory system in the brain rather than from local variations in neuronal activation (Tong and deB. Frederick, 2010). Further investigation determined that this pattern can also be seen when using BH BOLD fMRI in combination with fNIRS (Tong et al., 2011) or even when acquiring NIRS in peripheral sites (fingertip and toes) after delay corrections (Tong and deB. Frederick, 2010).

Having in mind all these physiological mechanisms, a new set of methods simply relying on the intrinsic variations of respiration during resting state have been successfully used to assess CVR using MRI. These methods have the additional advantage of not requiring any task to induce a vasoactive response (Golestani et al., 2016; Kannurpatti et al., 2011), being less demanding in terms of instrumentation and more easily implemented. This might be advantageous and more suitable for CVR mapping in certain populations such as patients with language–comprehension problems or with visual/auditory impairment.

5.4.1 Data Analysis

To date, several metrics have been proposed to derive CVR information from rs-fMRI and they can be subdivided in two main types:

1. Data-driven: fMRI Signal variation
2. Model-driven: Signal regression using fMRI temporal series/external recordings

Signal Variation The resting-state fluctuation amplitude (RSFA) is a relatively simple metric commonly used in rs-fMRI studies, being computed as the temporal standard deviation of the BOLD time series (Kannurpatti and Biswal, 2008). Studies comparing RSFA with CO_2 manipulations and BH tasks have reported similar results between the approaches (Kannurpatti and Biswal, 2008; Kannurpatti et al., 2014; Wang et al., 2016). Furthermore, it was also observed that rs-fMRI methods were less dependent on patient performance. Nevertheless, recent studies state that RSFA may not provide the best representation of CVR, demonstrated by the lower repeatability and variance explained when compared with the BH task (Lipp et al., 2015). Interestingly, a magnetoencephalography-fMRI study confirmed that, in fact, RSFA is

modulated by measures of vascular function and not driven solely by changes in the variance of neural activity (Tsvetanov et al., 2015).

Several other metrics based on the spontaneous BOLD fluctuations in rs-fMRI have been proposed. Makedonov et al. proposed a physiological fluctuations (PF) metric, which consists of the subtraction of temporal variance in signal attributed to thermal noise from the total temporal variance at a particular voxel. The thermal component was determined as the average variance in a region placed outside the brain. With this metric, the authors demonstrated that PF in white matter correlates with cardiac pulsatility in that same tissue and is increased in Alzheimer's disease (Makedonov et al., 2013, 2016). The coefficient of variation (CV) is another metric related to RSFA, which is simply computed as the signal temporal standard deviation normalized by the mean signal intensity (Jahanian et al., 2014, 2016). Jahanian et al. performed a thorough study comparing young healthy volunteers with hypertensive elderly subjects with chronic kidney disease, obtaining significantly higher CVs in the latter group. Within groups, higher CVs in GM were also observed relative to WM. Interestingly, CV differences mainly arose from very low frequency components of the BOLD signal fluctuations (<0.025 Hz), after a comparison using 3 different frequency bands (0.01 - 0.014, 0.014 - 0.025, and 0.25 - 1 Hz). Jahanian et al. also assessed the impact of different tissue segmentation methods on CV, finding no significant differences. CVs dissimilarities also became more significant after removal of physiological motion effects using the retrospective image-based correction (RETROICOR) method (Jahanian et al., 2014). In another work from the same group with older adults, the authors compared this approach with BH-CVR, showing strong linear correlation between the two methods. Furthermore, they also showed that using only the standard deviation (RSFA) instead of the normalized version (CV) yielded a weaker correlation to BH-CV, assuming that the normalization step eliminates the influence of baseline BOLD signal (Jahanian et al., 2016). Golestani et al also used a similar approach with normalized RSFA, and despite not outranking the CO_2 and frequency-based methods in terms of within-subject accuracy, this method was best at representing whole-brain CVR variations across subjects. Nevertheless, at individual-subject level it only yielded moderate correlation with CO_2-based CVR measurements, being outperformed by regression methods ($PETCO_2$ parametric-deconvolution) (Golestani et al., 2016). Liu et al. compared different physiological modulators of fMRI signal, obtaining a marginal correlation between CO_2-CVR and resting state CV CVR. The authors attributed this weak relationship with CV to factors such as bulk motion, spontaneous neural activity and also to some extent breathing variations (Liu, 2013).

Taking into account that some physiological processes fluctuations can be well defined within a frequency range, some authors have restricted their analysis to a low frequency band. Usually, a frequency band of the 0.01 - 0.1 or 0.01 – 0.08 Hz is chosen in order to restrict the signal to its frequency components of interest, while also removing high-frequency components possibly mostly contaminated by noise. The amplitude of low-frequency fluctuations (ALFF) metric was first described in 2007 and is computed as the square root of the power spectrum across a specific

low-frequency band of the preprocessed rs-fMRI BOLD signal (Yu-Feng et al., 2007). Recently, this metric has been used to rescale the amplitude of task-related fMRI in order to account for vascular differences, calling this the VasA method (Kazan et al., 2016).

Nevertheless, the low-frequency band is quite broad and specific bands within this range may have different contributions from diverse mechanisms. For that reason several studies have sub-divided this band into different *oscillation classes*. Buzsaki and colleagues proposed a subdivision into four different slow frequency ranges (slow-1: 1.4 - 0.5 Hz, slow-2: 0.5 – 0.2 Hz, slow-3: 0.066 - 0.2 and slow-4: 0.025 – 0.066 Hz) (Buzsaki, 2004). Subsequently, Zuo et al demonstrated differences in the spatial distributions of ALFF in four frequency bands including some of the ones previously defined by Buzsaki et al.: slow-2 (0.198 – 0.25 Hz), slow-3 (0.073 – 0.198 Hz), slow-4 (0.027 – 0.073 Hz) and slow-5 (0.01 – 0.027 Hz) (Zuo et al., 2010).

Another metric derived from ALFF is the fractional ALFF (fALFF). This metric represents the relative contribution of specific low frequency oscillations to the whole frequency range and is computed as power within the low-frequency range normalized by the power of the whole spectrum (Zou et al., 2008). Both ALFF and fALFF have been shown to yield moderate to high test-retest reliability in gray matter regions, although the former yields higher reliability than the latter (Zuo et al., 2010). Nevertheless, it has also been demonstrated that ALFF is more prone to physiological noise sources in comparison to fALFF, in particular near the ventricles and large blood vessels (Zou et al., 2008; Zuo et al., 2010). Both metrics might provide important information and there is a tradeoff between reliability/specificity so some authors recommend reporting both measures (Zuo et al., 2010). Kalcher and colleagues introduced a correction method that computes a voxelwise scaling factor based on fALFF in order to correct for variance from vascular effects, significantly reducing inter-subject variability of task-based activation maps (Kalcher et al., 2013). Golestani et al. also decided to use this methodology assuming that fALFF would likely reduce vascular contribution, compromising its vascular link. However their results showed that this metric was outperformed by the others, including CV. Recently, de Vis and colleagues compared ALFF and fALFF metrics of rs-fMRI with hypercapnia and hypoxia CVR fMRI measurements. While hypercapnia fMRI BOLD led to very large effect sizes, rs-fMRI ALFF / fALFF metrics only showed moderate effect sizes in the control group, which were further decreased in patients. Furthermore, the latter metrics were found to be confounded by resting CBV, which explained 53% of variance in the ALFF metric and 29% in fALFF (healthy controls) (De Vis et al., 2018).

Both rs-fMRI ALFF and BH fMRI CVR metrics have been compared with other rs-fMRI metrics namely the regional heterogeneity (ReHo). ReHo is a measure of the local synchronization of the fMRI BOLD time series, for a given voxel relative to the nearest neighboring voxels. rs-fMRI ReHo has been found to be moderately correlated with BH fMRI responses and strongly correlated with ALFF (Yuan et al., 2013).

It should be noted that these metrics are merely qualitative since they are not normalized against a common scale, usually the levels of $PETCO_2$. Nevertheless, they can be sensitive to

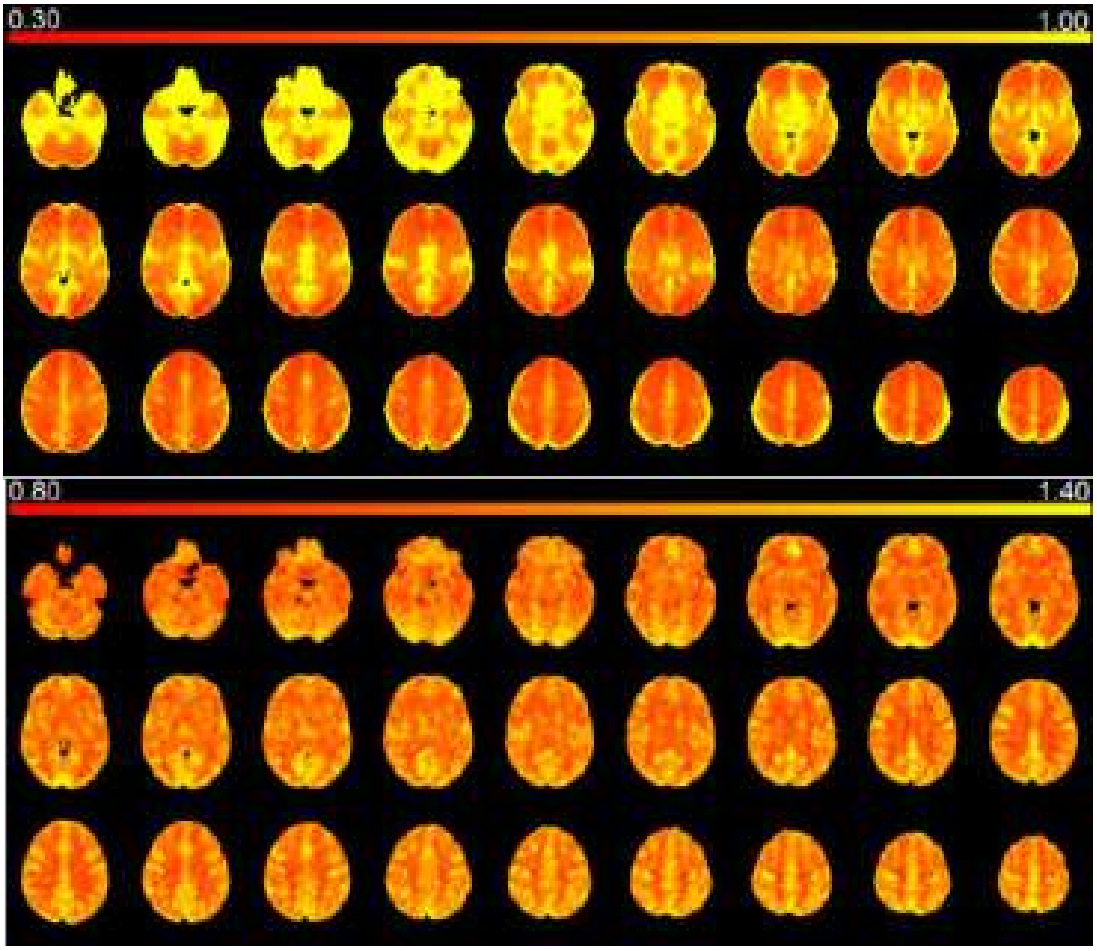

Figure 5.3: Illustrative example of maps of ALFF (top) and fALFF computed in the 0.01 - 0.023 Hz frequency band (bottom) – average across 12 healthy individuals in MNI space.

spatial differences since they are computed for each voxel separately.

Signal Regression Given that $PETCO_2$ is a well-established surrogate of arterial CO_2, regression of the spontaneous BOLD signal by the spontaneous variations in this metric can also be used in order to estimate CVR in rs-fMRI (Wise et al., 2004). In 2009, Chang et al. verified that $PETCO_2$ and RVT have a significant linear relationship and account for similar patterns of spatial and temporal variations. However, the authors also observed differences between the two metrics and variance explained of BOLD signal was higher when using a combination of the two metrics (Chang and Glover, 2009a). Resting state studies have reported the use of $PETCO_2$ as a regressor to map CVR in healthy volunteers (Golestani et al., 2016; Lipp et al., 2015) as well as in patients with cerebrovascular diseases (Liu et al., 2017). Golestani and colleagues investigated the impact of using $PETCO_2$ in rs-fMRI quantitative mapping of CVR (Golestani et al., 2016). They assume that rs-fMRI signal can be mainly described as a combination of cardiac, respiratory, and $PETCO_2$ changes. Their previous work had demonstrated that these changes are not entirely independent (Golestani et al., 2015), so they decided to first remove the cardiac and respiration contributions and then estimate the relationship between resting

state BOLD and $PETCO_2$ fluctuations. For the latter, $PETCO_2$ fluctuations were fitted voxel-wise to the rs-fMRI BOLD time course through two different strategies, including a parametric deconvolution method. This approach was applied, using cardiac, respiratory, and $PETCO_2$ information, deriving a $PETCO_2$-based response function ($HRFCO_2$), constructed from variants of a canonical HRF. This new response was then convolved with the $PETCO_2$ time course and regressed against the rs-BOLD signal, obtaining a rs-CVR metric (Golestani et al., 2016). The parametric deconvolution rs-CVR measurements yielded significant within-subject agreement with a standard CO_2 challenge. Nevertheless, it has also been reported that rs-fMRI response to intrinsic $PETCO_2$ fluctuations in healthy subjects may not be a reproducible metric, with lower intra-class correlation values than BH-CVR metrics (Lipp et al., 2015).

In 2015, Liu et al. described the use of rs-fMRI global-signal regression to derive CVR (Liu et al., 2015). They hypothesized that the average rs-fMRI BOLD signal across the whole brain reflects spontaneous CO_2 fluctuations and can therefore also serve as a reliable regressor for CVR estimation. They validated their rs-fMRI CVR maps through comparison with CO_2-inhalation CVR maps and obtained identical contrasts, although with different absolute values, since the latter is normalized by the CO_2 change. Finally, Liu et al. applied their new method in Moyamoya disease patients, obtaining reduced CVR in the diseased territories. The patient rs-fMRI CVR maps were comparable to those derived from CO_2-inhalation (Liu et al., 2015). The group further developed this work recently, integrating $PETCO_2$ information to identify the rs-BOLD signal frequency band that is most related to this metric. They tested five different low frequency bands from 0 to 0.2 Hz. Using cross-correlation between the rs-fMRI BOLD time course and $PETCO_2$ time course, they observed that correlation is highest when the time course is filtered at the 0.02 – 0.04 Hz frequency range (Liu et al., 2017). Using global BOLD signal within this frequency range, CVR measurements obtained are highly reproducible and are spatially correlated with maps obtained using the conventional CO_2-CVR measurements. This strategy was also applied to a group of Moyamoya disease patients and identified vasodilatory deficits, demonstrating the clinical feasibility of the method. Despite their findings, Liu et al. admit that, even when using a specific frequency range, the signal might contain some contributions from non-CO_2 related sources, such as neural activity, motion and heart rate changes (Liu et al., 2017). Liu et al also observed that global BOLD signal regression methods provide significantly better CVR maps (in terms of Z-score) comparatively to $PETCO_2$ methods and speculated that this is because $PETCO_2$ had a low sampling frequency contrarily to the BOLD signal, which was acquired with high temporal resolution (Liu et al., 2017).

Golestani and colleagues observed a good within-subject agreement between rs-fMRI global-signal regression and standard CO_2 manipulation CVR assessment. Nevertheless, the BOLD global-signal regression was much less reproducible and more variable than other rs-fMRI metrics, RSFA and ALFF. The authors state that one possible reason for this is the close relationship between global signal regression CVR estimates and frame-wise motion (Golestani et al., 2016).

Table 5.2: Summary of the most common rs-fMRI methodologies used to derive CVR-based metrics.

			Metric	Computation
rs-fMRI signal fluctuations	Data-driven	Whole spectrum	RSFA	σ_{EPI}
			CV	$\frac{\sigma_{EPI}}{\mu_{EPI}}$
			PF	$\frac{\sqrt{\sigma^2_{EPI}-\sigma^2_{thermal}}}{\mu_{EPI}}$
		Low frequencies	ALFF	$\frac{\sum_{k:f_k\in[f_{min};f_{max}]}\sqrt{\frac{\lvert FFT\rvert^2_{f_k}}{N}}}{n_k}$
			fALFF	$\frac{ALFF_{k:f_k\in[f_{min};f_{max}]}}{ALFF_{m:f_m\in[0;f_{max}]}}$
	Model- driven	Linear regression	$PETCO_2$	Regression against fMRI signal
			Global signal	
			Tissue signal	

σ_{EPI} - temporal standard deviation; μ_{EPI} - temporal mean; $\sigma^2_{thermal}$ - temporal variance due to thermal noise; FFT - Fast Fourier transform; f - frequency range; k - number of bins within a specific frequency range; m - number of bins of the entire frequency range; f_{min} - minimum frequency; f_{max} - maximum frequency; N - number of time points; n_k - number of frequency bins

Regression using rs-fMRI signal averaged across a specific tissue mask has also been proposed recently by Jahanian et al. in a cohort of older adults. In particular, the CSF signal was chosen since it can be seen as a good representation of internal physiological fluctuations, which is essentially free from fluctuations of neuronal origin. This approach yielded significant correlations with BH-derived CVR, but lower than the RSFA (CV) method. Global GM and WM mean signals were also considered as separate regressors but results showed clear biases in those measurements and their use either separately or in combination is therefore not recommended for CVR assessment (Jahanian et al., 2016).

A summary of the most common rs-fMRI methodologies used to derive CVR-based metrics can be seen in Table 5.2.

5.5 Other Considerations

$PETCO_2$ as surrogate Estimation of the arterial gas pressures $PaCO_2$ during CVR assessment is a critical requirement for quantitative interpretation of results. However, direct measurement of $PaCO_2$ requires blood sampling, making it highly invasive and, for that reason, $PETCO_2$ generally acts as a non-invasive surrogate. $PETCO_2$ is assumed to be representative of alveolar gas pressure of CO_2 and since $PaCO_2$ and alveolar gas pressure of CO_2 values are taken to be identical due to the rapid diffusion of oxygen and carbon dioxide between the alveoli and the blood in the pulmonary capillaries, it is assumed that $PETCO_2$ is representative of $PaCO_2$ (Ito et al., 2008). This assumption, however, only applies to a healthy person and in patients with diminished cardiopulmonary function there can be a difference between alveolar

gas pressure of CO_2 and $PaCO_2$ caused by different ventilation-to-perfusion matching (Jones et al., 1979; Peebles et al., 2007). In addition, methods also assume a linear relation between BOLD signal changes and $PETCO_2$ levels. However, this relation can be described by a sigmoidal shape model (Reivich, 1964) which does in fact have a linear part, but also a non-linear portion, mainly on the lower range of $PETCO_2$ values, so conclusions derived from hypocapnic states require more caution (Tancredi and Hoge, 2013).

Role of O_2 The role of arterial O_2 pressure in regulation of CBF seems to be minor (Ainslie and Duffin, 2009), with CO_2 cerebral reactivity being 60/150 times larger than to O_2 (Prisman et al., 2008). Bulte et al. estimated that the O_2 flow changes would be too small to even influence the BOLD-weighted signal (Bulte et al., 2007) and Mark and colleagues observed no change in CBF, assess by ASL, during a isocapnic hyperoxia stimulus (Mark et al., 2011). Tancredi and colleagues also verified that when using BH the level of $PETO_2$ decreased, causing mild hypoxia that could contribute a slight vasodilatory input, which would tend to exaggerate CVR measures. While the latter effect could explain the tendency of BH measures of CVR to be higher than those for CO_2 inspiration, the difference is fairly small and not statistically significant (Tancredi and Hoge, 2013).

Basal $PETCO_2$ level The impact of baseline vascular tension on CVR, through the influence of basal carbon dioxide, has been investigated in a number of CVR CO_2 studies (Golestani et al., 2016; Halani et al., 2015), as well as non-invasive methods including BH (Bright et al., 2011), demonstrating great dependence and high inter-subject variability in the relationship (Golestani et al., 2016; van Niftrik et al., 2018). However, Tancredi and colleagues observed that the impact of baseline CO_2 is negligible when considering relative measures comparatively with absolute quantification (Tancredi and Hoge, 2013).

CVR – quantitative or qualitative measure? CVR can be a relative metric, computed as percentage signal change of fMRI response normalized by the signal averaged over normal breathing periods. Other strategies for CVR computation include the use of $PETCO_2$ information, introduced as an amplitude measurement normalization factor, in an attempt to minimize variability due to respiratory and task compliance differences across sessions and subjects, yielding a quantitative measure of CVR. Murphy demonstrated that the spatial extent of stimulus-evoked activation is further improved when using this approach (Murphy et al., 2011b). However, Goode et al. found contradictory results in the use of $PETCO_2$ normalization. Absolute BOLD signal intensity changes after an hypercapnic challenge showed better reproducibility and lower between-subject variability than BOLD ratios normalized by $PETCO_2$ (Goode et al., 2009). When comparing BH-CVR with CO_2-inhalation CVR, Kastrup observed higher correlation when normalizing data with individual $PETCO_2$ changes (Kastrup et al., 2001). However, in some cases, the $PETCO_2$ normalization step is not mandatory and may not be useful, for example, when using a representative ROI (e.g. lesion) time-series to compare with their contralateral

locations, in order to assess regional CVR assessment. Additionally, CVR normalized against whole brain or reference tissue can be a more sensitive biomarker than absolute CVR in clinical application as it minimizes inter-subject variations (Yezhuvath et al., 2009).

5.6 Future Work

In real life, exact control of arterial CO_2 levels and the concomitant fMRI signal acquisition might not be exact. Additionally, the multitude of aspects and parameters that influence the measured BOLD response and their relation are too complex and are not yet fully understood and interpreted. Multimodality imaging techniques might be beneficial for this purpose, allowing a better interpretation of the mechanisms and their relations. In particular, the use of methodologies that measure the neuronal activation directly (e.g. EEG or magnetoencephalography (MEG)). Nevertheless, investigating the spatiotemporal dynamics of BOLD response in different regions or even within the whole brain might elucidate the mechanisms that contribute to those responses (e.g. vascular vs neuronal). The use of high temporal resolution acquisitions (e.g. simultaneous multi-slice or parallel imaging) might also be advantageous to clearly separate contributions, avoiding aliasing of faster responses.

5.7 Conclusions

In this review, we overviewed the most common methodological approaches used to evaluate CVR using MRI, with special focus on non-invasive methods. The motivation underlying the use of the non-invasive methodologies was first highlighted, comparing these approaches with more common, invasive ones. Then the different non-invasive methods that elicit a vascular response were described more thoroughly, subdiving then in two groups, task-based methods and resting-state approaches. In each one of these groups, data acquisition and modeling strategies for CVR assessment were presented and discussed. To date, there is still a multitude of acquisition methods and analysis strategies for non-invasive CVR assessment using MRI, hindering the applicability of these methods in routine clinical settings. Furthermore, due to the complexity of the physiological mechanisms behind the haemodynamic responses, a deeper understanding is still required in order to draw plausible inferences between different mechanisms. In the future, validation studies are needed in order to standardized the methodological approaches and reach a consensus on the most suitable acquisition method and analysis strategy to derive a vascular health biomarker.

Acknowledgements

This work was supported by the Portuguese Foundation for Science and Technology (FCT) grants PTDC/BBB-IMG/2137/2012, PTDC/EEI-ELC/3246/2012, SFRH/BD/51449/2011, UID/EEA/50009/2013 and PD/BD/135114/2017.

6

Fourier Modeling of the BOLD Response to a Breath-Hold Task: Optimization and Reproducibility

Contents

This Chapter corresponds to the article published in **NeuroImage**, 135 (2016) 223-231: **Joana Pinto**, João Jorge, Inês Sousa, Pedro Vilela, Patrícia Figueiredo, "Fourier modeling of the BOLD response to a breath-hold task: optimization and reproducibility".

6.1 Abstract

Cerebrovascular reactivity (CVR) reflects the capacity of blood vessels to adjust their caliber in order to maintain a steady supply of brain perfusion, and it may provide a sensitive disease biomarker. Measurement of the blood oxygen level dependent (BOLD) response to a hypercapnia-inducing breath-hold (BH) task has been frequently used to map CVR noninvasively using functional magnetic resonance imaging (fMRI). However, the best modeling approach for the accurate quantification of CVR maps remains an open issue. Here, we compare and optimize Fourier models of the BOLD response to a BH task with a preparatory inspiration, and assess the test-retest reproducibility of the associated CVR measurements, in a group of 10 healthy volunteers studied over two fMRI sessions. Linear combinations of sine-cosine pairs at the BH task frequency and its successive harmonics were added sequentially in a nested models approach, and were compared in terms of the adjusted coefficient of determination and corresponding variance explained (VE) of the BOLD signal, as well as the number of voxels exhibiting significant BOLD responses, the estimated CVR values, and their test-retest reproducibility. The brain average VE increased significantly with the Fourier model order, up to the 3^{rd} order. However, the number of responsive voxels increased significantly only up to the 2^{nd} order, and started to decrease from the 3^{rd} order onwards. Moreover, no significant relative underestimation of CVR values was observed beyond the 2^{nd} order. Hence, the 2^{nd} order model was concluded to be the optimal choice for the studied paradigm. This model also yielded the best test-retest reproducibility results, with intra-subject coefficients of variation of 12 and 16% and an intra-class correlation coefficient of 0.74. In conclusion, our results indicate that a Fourier series set consisting of a sine-cosine pair at the BH task frequency and its two harmonics is a suitable model for BOLD-fMRI CVR measurements based on a BH task with preparatory inspiration, yielding robust estimates of this important physiological parameter.

6.2 Introduction

Cerebrovascular reactivity (CVR) mechanisms allow the adjustment of the regional cerebral blood flow (CBF), through changes in local vasculature calibre, in order to maintain a constant supply of oxygen (O_2) and nutrients to the tissues despite fluctuations in perfusion pressure and blood gas concentrations. These mechanisms may be compromised in pathological conditions, which makes them a potential disease biomarker (Cantin et al., 2011; Leoni et al., 2012; Pillai and Zacá, 2011; Spano et al., 2013). CVR can be evaluated by combining a challenge to the vasculature with the measurement of the associated CBF changes using an appropriate

technique.

The blood oxygen level dependent (BOLD) contrast commonly used in functional magnetic resonance imaging (fMRI) offers a completely non-invasive technique for CVR assessment. It results from a complex combination of several haemodynamic parameters, and is generally thought to reflect the balance between CBF and O_2 consumption (Mark et al., 2015). If the hypercapnia condition is isometabolic relative to the normocapnia condition, it can then be assumed that the associated BOLD response predominantly reflects changes in CBF (Mandell et al., 2008b). Its wide availability and ease of implementation have favored the use of the BOLD contrast for CVR assessment, relative to more direct but also more difficult methods of CBF measurement such as Arterial Spin Labeling (ASL).

The most commonly used cerebrovascular challenges involve the administration of vasodilating drugs (i.e. acetazolamide) or the manipulation of respiratory gases (i.e. carbon dioxide (CO_2), O_2) inducing hypercapnia (Fierstra et al., 2013). Different techniques have been developed for the controlled manipulation of the end-tidal pressure of respiratory gases, including end-tidal forcing (Robbins et al., 1982; Wise et al., 2007) and more recently, computer-controlled prospective end-tidal targeting (Mark et al., 2010; Prisman et al., 2008; Slessarev et al., 2007; Spano et al., 2013). These techniques allow the targeting of specific CO_2 and O_2 end-tidal concentrations and in this way the achievement of precise hypercapnia levels with no hypoxia, despite variable ventilatory responses, hence providing more reliable methods for CVR assessment. However, noninvasive respiratory tasks have also been proposed, which present the important advantages of not requiring complex experimental setups including uncomfortable breathing masks and being well tolerated by healthy volunteers as well as patients. Most notably, breath-hold (BH) tasks are commonly used in both clinical and research settings, leading to mild hypercapnia and vasodilation and inducing measurable CBF and BOLD signal increases (Bright and Murphy, 2013; Kastrup et al., 1999, 2001; Lipp et al., 2015; Magon et al., 2009; Pillai and Mikulis, 2014; Scouten and Schwarzbauer, 2008; Thomason and Glover, 2008). In contrast to techniques based on the controlled manipulations of respiratory gases, the use of BH tasks does not allow for precise control of end-tidal CO_2 pressure ($PETCO_2$) levels and hence hypercapnia levels. Nevertheless, it has been shown that CVR measurements obtained using BH are comparable to those obtained upon CO_2 inhalation (Kastrup et al., 2001). Moreover, it has also been shown that the mild hypoxia that may be associated with a BH task does not significantly influence CVR results when compared with methods that target and maintain O_2 levels (Tancredi and Hoge, 2013).

Characterizing the CBF spatiotemporal dynamics may provide important additional insights into CVR. In fact, the haemodynamic response delays associated with CVR can be of great interest for the characterization of vascular latencies across the brain, in resting-state or stimulus-evoked fMRI studies as well as in disease (Bright et al., 2009; Chang et al., 2008). The dynamics of CVR have been previously studied using a sinusoidal modulated CO_2 stimulus (Blockley et al., 2011) and more recently by transfer function analysis using controlled respiratory gas

manipulations performed in a block design alternating different levels of $PETCO_2$ (Duffin et al., 2015). In BH tasks, BH periods are naturally alternated with normal breathing, therefore intrinsically yielding a block design paradigm. This means that, in this case, it is not only interesting but also necessary to model the dynamics of the BOLD response to BH appropriately, in order to be able to capture the associated CBF changes (Birn et al., 2008; Bright and Murphy, 2013; Murphy et al., 2011b; Vogt et al., 2011). However, modeling the BOLD response to BH remains a challenge (Birn et al., 2008; Bright and Murphy, 2013; Murphy et al., 2011b; Vogt et al., 2011).

One limitation is that most analysis approaches do not implicitly account for a time-to-peak in the BOLD response; this is often introduced as a time lag or an additional dispersion of the impulse response function to the task, and most often a single delay is fixed, or pre-optimized, and then used for the whole brain (Bright and Murphy, 2013; Bright et al., 2009, 2011; Magon et al., 2009; Murphy et al., 2011b; Scouten and Schwarzbauer, 2008). Although including the time derivative of the response in a general linear model may partially account for a variable time-to-peak across the brain, this would probably not be sufficient to accommodate the observed large variations. Some studies have attempted to overcome this limitation by employing cross-correlation analysis to optimize the delay voxelwise (Chang et al., 2008). A sinusoidal model exploits the essentially biphasic shape of the BH BOLD response and the overall periodicity of the BOLD signal variations at the paradigm frequency, allowing for variable phase delays across the brain.

In a recent BH study, this model was compared with a number of alternative models based on either a block design of the task or the measured trace of the $PETCO_2$ (Murphy et al., 2011b). Even though convolution with a haemodynamic response function (HRF), lagging by an optimized time-to-peak and with the addition of the time derivative, were considered for the task and $PETCO_2$ models, the sinusoidal model, which assumes only the BH task frequency and requires no further parameters or inputs, was nevertheless the best at explaining BOLD signal variations, comparable only with the $PETCO_2$ convolution model (Murphy et al., 2011b). Another more recent work (Lipp et al., 2015) compared three BH-based analysis approaches, and found that a sine-cosine model yielded similar or higher values of repeatability than the ones based on the $PETCO_2$. The authors explain their results by admitting that the use of the $PETCO_2$ trace recorded during each session may induce additional variability, by introducing the capnograph's measurement errors into the computation of the CVR values. Moreover, it may also be confounded by other factors such as inaccuracies in the synchronization between $PETCO_2$ and fMRI recordings. Surprisingly, although the sine-cosine and task models do not account for deviations in task performance, which could be a relative disadvantage, their performance was highly repeatable across subjects.

Most of these modeling efforts have been aimed at the BOLD response to BH tasks performed at the end of an expiration (Bright and Murphy, 2013; Lipp et al., 2015). However, it has been shown that BH tasks can be more easily performed following a preparatory inspiration (Pillai

and Mikulis, 2014; Roberts et al., 2009; Thomason et al., 2007), which is especially critical in patient populations. One possible physiological explanation is that an increased lung volume will inhibit the respiratory centers through the Hering-Breuer reflex, increasing the breath-hold breaking point and $PETCO_2$ change (Chapin, 1955; Muxworthy, 1951; Skow et al., 2015). In this case, the BOLD response to BH becomes even more complex, and it often assumes a triphasic shape, being the additional peak probably a result of the combination of several physiological mechanisms induced by the respiratory act itself, such as heart rate variation, the reduction of pulmonary vascular tension and resistance, and autonomic modulation of cerebral responses (Magon et al., 2009; Nakada et al., 2001; Thomason et al., 2005).

Here, we propose to model the BOLD response to an end-inspiration BH task through a Fourier basis set, including a sine-cosine pair at the task frequency as well as a number of harmonics (Josephs et al., 1997). We compare different order models in a nested models approach, in terms of the adjusted coefficient of determination (R^2_{adj}) and the VE, as well as the number of voxels exhibiting a significant BOLD response, and the values of the CVR measurements derived from each model. The inter- and intra-subject reproducibility of CVR measurements were also estimated, and compared across models.

6.3 Materials and Methods

6.3.1 Data Acquisition

A group of 10 healthy volunteers (5M, age: 22.9 ± 5.3 yrs) was studied on a 3T Siemens Verio MRI system using a 12-channel-receive radio-frequency coil, on two different sessions, separated by approximately one week. The study was approved by the local ethics committee and all subjects provided informed consent. One subject did not performed the task correctly, and thus was excluded from further analysis. In each session, the volunteers performed a BH task following visual instructions. The BH protocol comprised two 25 s periods of self-paced breathing (baseline), at the beginning and end of the protocol, and three 75 s cycles of alternating periods of 20 s apnea (BH) preceded by a preparatory inspiration, and followed by 55 s of self-paced breathing.

BOLD images were obtained using a gradient echo-echo planar imaging (GE-EPI) sequence (TR/TE=2500/50 ms), from 18 contiguous axial slices, with voxel resolution of 3.5 x 3.5 x 7.0 mm^3. Each BOLD-fMRI dataset was composed of 110 volumes (approximately 4.5 min). Throughout the experiment, $PETCO_2$ was monitored using a capnograph (PN 8050. Drager, Lubeck, Germany), by sampling each exhalation using an oral and nasal cannula. A T1-weighted structural image was also collected using an MPRAGE sequence with TR/TE = 2250/2.26 ms, and 1 mm^3 resolution.

6.3.2 Data Analysis

Image analysis was conducted using the FMRIB Software Library FSL 5.0.1 (http://fsl.fmrib.ox.ac.uk/fsl/fslwiki/FSL) and MATLAB routines (version 2011a, http://mathworks.com) developed in-house. Functional data were corrected for head motion using a rigid body transformation with 6 degrees-of-freedom (3 translations and 3 rotations) (Jenkinson et al., 2002), brain-extracted (Smith, 2002), spatially smoothed (Gaussian kernel, 5 mm FWHM) and temporally high-pass filtered (100 s cutoff). Functional images were co-registered using FLIRT (Jenkinson et al., 2002) to the subject's structural image and using FNIRT (Andersson et al., 2007) to the Montreal Neurological Institute (MNI) space.

A general linear model (GLM) including up to five Fourier basis sets was defined to model the BOLD response to the BH task; each set consisted of a sine-cosine pair with the paradigm period ($\omega = 75$ s) or one of its harmonics, and was sequentially added to the GLM in a nested model approach, yielding the following five models of increasing order (0^{th} to 4^{th}):

$$\begin{aligned}
M_0 &: Y(t) = a_0 \sin(\omega t) + b_0 \cos(\omega t) \\
M_1 &: Y(t) = \left[M_0 + a_1 \sin(2\omega t) + b_1 \cos(2\omega t)\right] \\
M_2 &: Y(t) = \left[M_1 + a_2 \sin(3\omega t) + b_2 \cos(3\omega t)\right] \\
M_3 &: Y(t) = \left[M_2 + a_3 \sin(4\omega t) + b_3 \cos(4\omega t)\right] \\
M_4 &: Y(t) = \left[M_3 + a_4 \sin(5\omega t) + b_4 \cos(5\omega t)\right]
\end{aligned} \tag{6.1}$$

where Y is the BOLD signal, t is time, and a_i and bi are the parameter estimates for the Fourier term of ith order. Each GLM was fit to the data in each voxel using FILM, and cluster thresholding (cluster $p < 0.05$ and voxel $Z > 2.3$) was then performed on the maps of the F test across the GLM estimated coefficients.

BOLD percentage signal changes (PSC) were computed in each voxel as the amplitude of the model's maximum relative to the average signal during the baseline periods multiplied by 100. In order to remove outliers, PSC values 2 standard deviations above the mean were removed from further analysis. Average $\Delta PETCO_2$ values were calculated for each subject and session, by computing the average difference between the $PETCO_2$ value of the first expiration following the BH periods and the mean of the $PETCO_2$ values during baseline. CVR values in units of %BOLD/ΔmmHg were then obtained in each voxel by normalizing the PSC values by the average $\Delta PETCO_2$ in each dataset. Time-to-peak (TTP) values were also computed in each voxel as the time of the model curve maximum relative to the onset of the BH.

Gray matter (GM) masks were obtained individually by tissue segmentation of the structural images using the FAST tool (Zhang et al., 2001) and co-registered to the functional images in each subject/session. The CVR and TTP maps were then analyzed within GM.

6.3.2.A Model Fitting Comparison

The nested models were compared by computing their coefficients of determination adjusted for the degrees of freedom, R^2_{adj} (Bianciardi et al., 2009a; Jorge et al., 2013), as:

$$R^2_{adj} = 1 - \frac{N-1}{N-P-1}\frac{\sum_{i=1}^{N}(y_i - y'_i)^2}{\sum_{i=1}^{N}(y-\bar{y})^2} \tag{6.2}$$

where N is the number of volumes in the dataset; P is the number of regressors; y_i and y are respectively the i-th value of y (the BOLD-fMRI data) and y' (the estimation of y by the model), and $\bar{y}$ is the temporal mean of y. The VE by each model, M_{n+1}, in relation to the previous one, M_n, is then computed as the difference between the respective R^2_{adj} values:

$$VE_{n+1,n} = \left[R^2_{adj}(M_{n+1}) - R^2_{adj}(M_n)\right] \times 100 \tag{6.3}$$

A T-test on VE_{n+1}, n was used to test whether M_{n+1} explains significantly more variance than M_n ($p<0.05$). The number of voxels exhibiting significant BOLD changes, as well as the median GM CVR measurements, were also computed for each model, and compared between successive models using T-tests .

6.3.2.B Test-Retest Reproducibility Analysis

To quantify reproducibility of the CVR measurements obtained with each model, the following metrics were computed for the median value across GM voxels: the inter- and intra-subject coefficients of variation (CV_{inter} and CV_{intra}), and the intraclass correlation coefficients (ICC) (Sousa et al., 2014a). The CV_{inter} metric measures the variability across subjects, reflecting the inter-individual variability in the population studied. The CV_{inter} was first computed for each session as (Bland and Altman, 1996):

$$CV_{inter} = \frac{SD}{\mu} \times 100[\%] \tag{6.4}$$

where μ and SD are the mean and standard deviation of the parameter across subjects. The final CV_{inter} was computed as the mean of the CV_{inter} of the two sessions. The CV_{intra} metric measures the variability between sessions of the same subject, which reflects mainly naturally occurring physiological variations within each subject as well as possible measurement errors. Since the literature is not systematic in terms of reproducibility metrics, for the purpose of comparison with previous reports, we decide to include the two most common variants of CV_{intra}. CV_{intra1} was computed as (Bland and Altman, 1996):

$$CV_{intra1} = \frac{SD_{ws}}{\mu} \times 100[\%] \tag{6.5}$$

where μ is the mean value of the parameter across subjects and sessions and SD_{ws} is the SD of repeated measurements, in this case the within-subject SD. Since we only have two

measurements per subject, estimation of SD_{ws} can be simplified to:

$$SD_{ws} = \sqrt{\frac{\sum_{i=1}^{k} (a_{R_iS_1} - a_{R_iS_2})^2}{2 \times k}} \tag{6.6}$$

where k is the number of subjects and $a_{R_iS_1}$ and $a_{R_iS_2}$ are the measurements of subject i on session 1 and 2, respectively (Bland and Altman, 1996). CV_{intra2} was computed by dividing the standard deviation of the CVR measurements by their mean for each subject (similar to CV_{inter}) (Lipp et al., 2015). A CV value of 33 % is usually recognized as the upper fiducial limit for acceptable variability in a normal distribution (Magon et al., 2009). The ICC metric reflects both intra- and inter-subject variability; it evaluates how reproducible measurements of the same subject are across sessions, taking into account their inter-subject variability. A two-way mixed ICC, single measure, was chosen to assess the reproducibility of CVR measurements, according to (Shrout and Fleiss, 1979):

$$ICC(3,1) = \frac{BMS - EMS}{BMS + (k-1)EMS} \tag{6.7}$$

where BMS is the between-subjects mean of squares, EMS is the error mean square and k is the number of sessions. ICC levels can be grouped in terms of their reliability using Cicchetti et al. recommendations: poor (< 0.4), fair (0.41 – 0.59), good (0.60 – 0.74) and excellent (> 0.75) reliability (Cicchetti, 2010). ICC of 0.4 is usually considered the acceptability limit in fMRI studies (Aron et al., 2006; Eaton et al., 2008).

6.4 Results

Nine out of the ten volunteers successfully performed the BH task, as assessed by $PETCO_2$ monitoring, with no major difficulties reported. The mean Δ $PETCO_2$ achieved with the BH task, across cycles, subjects and sessions, was 7.1 ± 0.9 mmHg. The average absolute mean head displacement, estimated by motion correction of the BH BOLD data, was 0.16 ± 0.07 mm across all subjects and sessions. The absolute mean of the degrees of rotation about the x, y and z axes were 0.06 ± 0.03, 0.04 ± 0.02 and 0.04 ± 0.02, while the absolute mean of the translations along x, y and z were 0.02 ± 0.01, 0.05 ± 0.02, 0.11 ± 0.07 mm, respectively. Rotations about the x axis, and translations along z, are generally greatest, which is consistent with head motion associated with the execution of the BH task, and the preparatory inspiration in particular.

An illustrative example of the five tested models (M_0 to M_4) adjusted to the BOLD time course of a representative voxel is shown in Figure 6.1. For this specific voxel, the R^2_{adj} coefficients of the five models M_0 to M_4 were, respectively, 0.28, 0.34, 0.43, 0.42 and 0.41. These values are consistent with the observation that model M_1 explains the data better than M_0, and that models M_2, M_3 and M_4 explain the BOLD time course better than M_1, but are not considerably different from each other. This finding can also be appreciated at both the individual and group levels, through the VE maps obtained for each pair of models, as shown in Figure 6.2. While

an overall improvement is observed across the brain from model M_0 to M_1 and from model M_1 to M_2, only a few voxels exhibit an improvement from model M_2 to M_3.

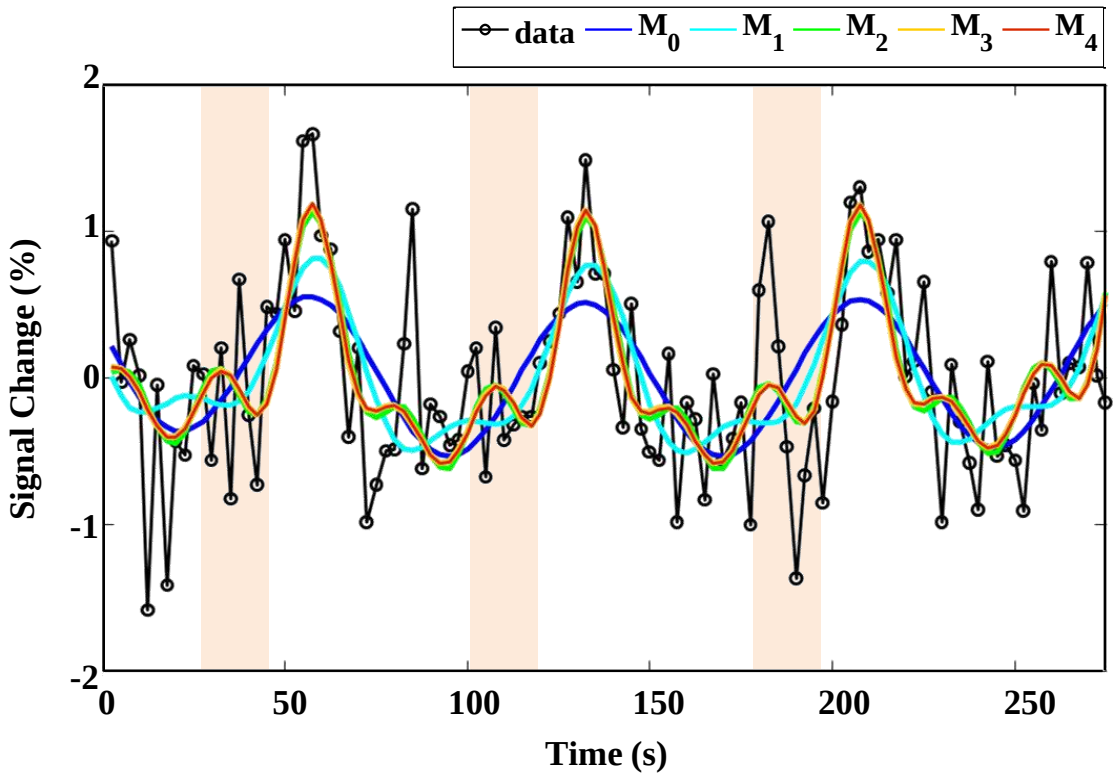

Figure 6.1: Model time courses: Illustrative example of the five tested models (M_0 to M_4) adjusted to the BOLD time course of a representative voxel (data). In accordance to our results, M_2, M_3 and M_4 explain the BOLD time course better than M_0 and M_1, but are not considerably different from each other.

The overall model fit comparison analysis is summarized in Figure 6.3, showing for each model/pair of models the GM median values, averaged across subjects and sessions, of: R^2_{adj}/VE; number of responsive voxels/corresponding difference between models; and CVR/corresponding CVR difference between models. Statistically significant differences were found for all CVR values across models. All models explained additionally more variance than the respective model of immediately lower order up to M_3. In terms of the total number of voxels exhibiting significant BOLD responses, models M_2 and M_3 outperformed both lower order models M_0 and M_1 as well as the higher order model M_4, with no significant differences between them. As expected, we also found that higher order models produced increasing CVR values, suggesting that relative underestimation occurs due to the relatively poorer fit for lower order models; however, the relative underestimation obtained with M_2 relative to M_3 (4%) and M_3 relative to M_4 (6%) were both well within the observed intra- and inter-subject variability of CVR measurements. The reproducibility metrics (CV_{inter}, CV_{intra1}, CV_{intra2}, and ICC) of the GM median CVR values for all models are presented in Table 6.1. Models M_2 and M_3 produced

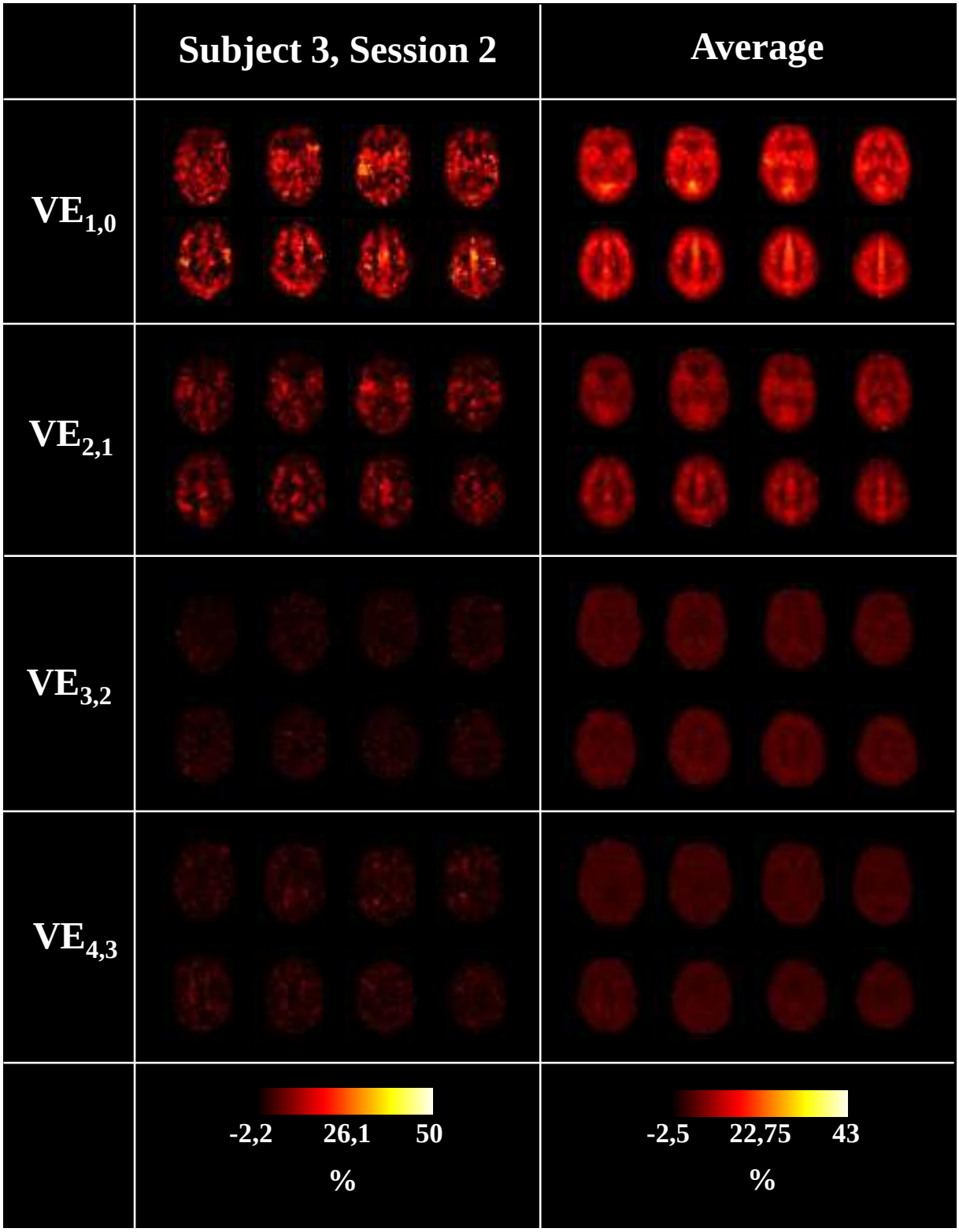

Figure 6.2: Model comparison VE maps: Illustrative example from one representative dataset (left) and group average (right) VE maps obtained for each pair of compared models. $VE_{a,b}$ represents the additional variance explained by model M_a relative to model M_b.

higher ICC values and lower within-subject variability than all other models, again with no considerable differences between them.

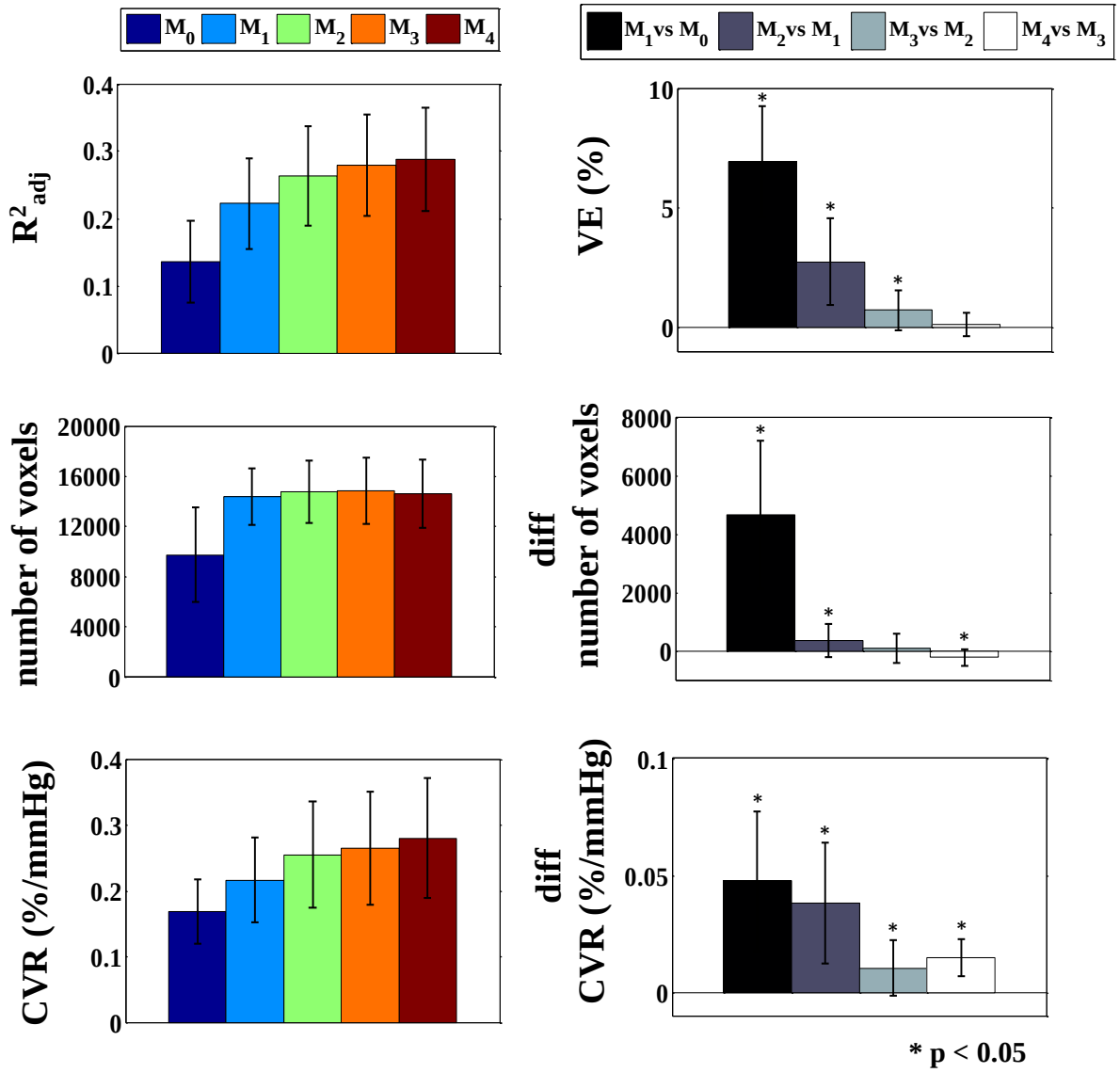

Figure 6.3: Model comparison: Values for each model on the left and for each model pair comparison on the right. (Top panel) Median GM R^2_{adj} (left) and VE values (right). (Middle panel) Total number of voxels exhibiting a significant BOLD response (left) and respective differences (right). (Bottom panel) Median GM CVR measurements(left) and respective differences(right). Bars represent group average values across subjects and sessions and error bars represent the respective standard deviation of the mean. * represents T-test significant differences ($p < 0.05$).

Since no important differences in terms of performance (number of responsive voxels, CVR estimation and reproducibility) were found between models M_2 and M_3, M_2 was chosen as the optimal model given its relatively greater simplicity (compared to M_3, which still yielded greater VE). The average CVR and TTP maps across subjects and sessions, obtained using the M_2 model, are shown in Figure 6.4. The two session maps of the 9 subjects were analyzed, but only voxels that exhibited a significant response in at least 12 of the 18 maps were included to

Table 6.1: Reproducibility metrics: CV_{inter}, CV_{intra1}, CV_{intra2}, and ICC of the median CVR values across GM for all models.

Models	**CV_{inter}**	**CV_{intra1}**	**CV_{intra2}**	**ICC**
$\mathbf{M_0}$	29.7	19.1	14.3	0.54
$\mathbf{M_1}$	30.1	19.7	14.8	0.53
$\mathbf{M_2}$	32.2	15.8	11.7	0.74
$\mathbf{M_3}$	32.9	16.0	11.0	0.75
$\mathbf{M_4}$	33.1	17.5	11.4	0.70

create the average images presented. The corresponding GM median values of CVR are shown in Figure 6.5, for each subject and session, as well as their overall average.

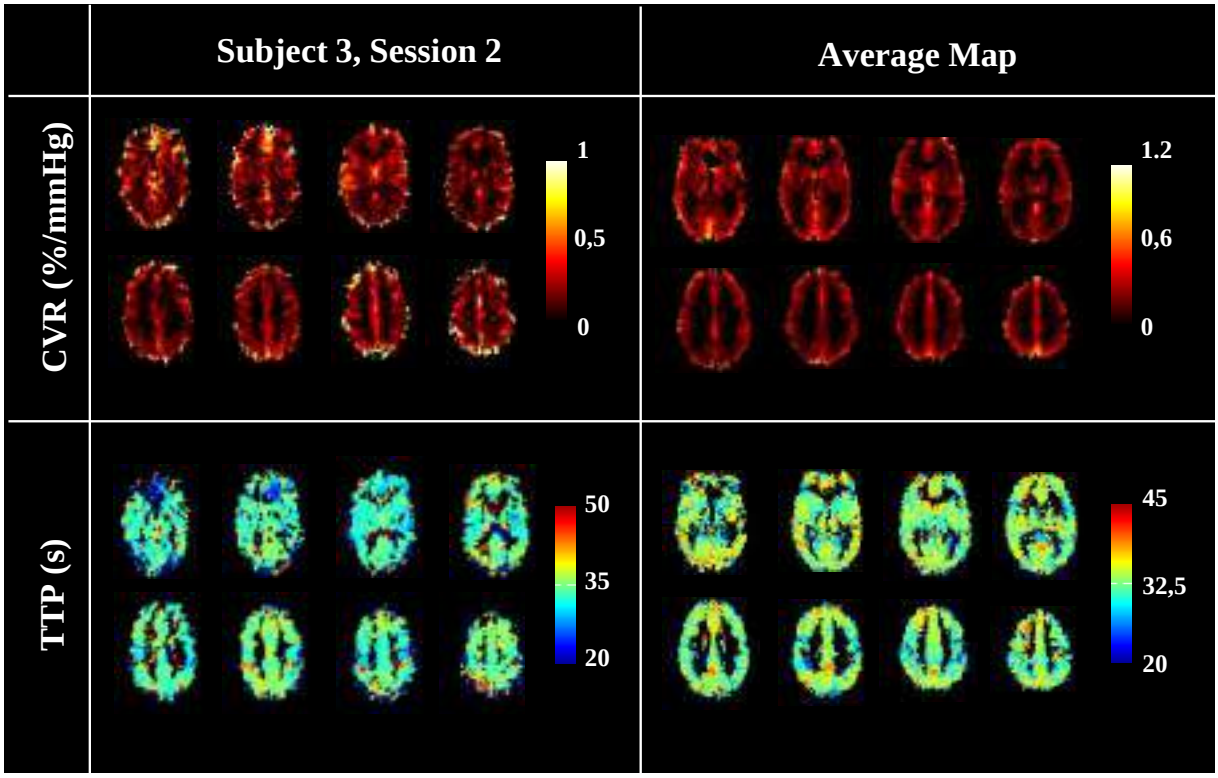

Figure 6.4: CVR and TTP maps:Illustrative example from one representative dataset (left). Group average (right), obtained using the M_2 model (only voxels exhibiting a response in at least 12 maps out of the 18 are presented.

6.5 Discussion

In this study, we investigated the capability of Fourier series up to the 4^{th} order to model the BOLD response to a BH task with a preparatory inspiration. We found that a sine-cosine linear combination at the task frequency with its first two harmonics explained significantly more

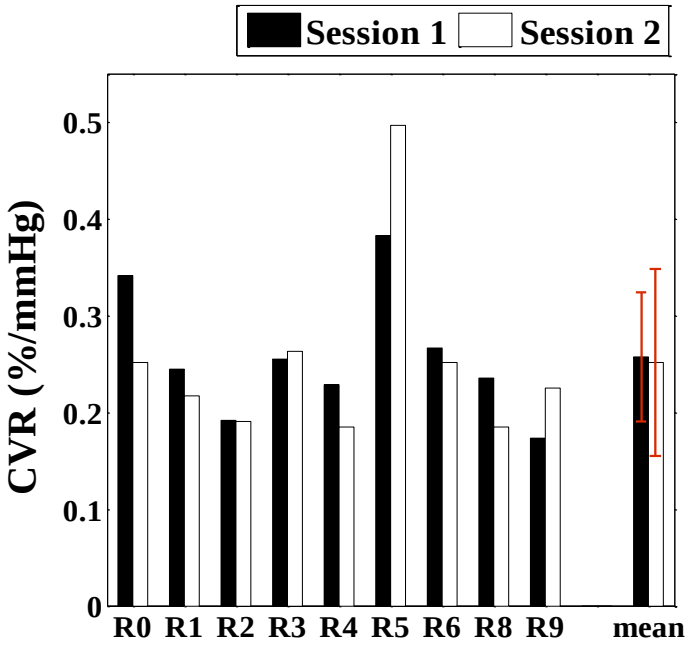

Figure 6.5: CVR GM values: Median GM CVR for each subject (R0 to R9) and session, as well as their overall group mean. Error bars represent standard deviation of the mean.

variance than lower order models, while producing a greater number of responsive voxels, no significant relative underestimation of the CVR amplitude, and better test-retest reproducibility when compared with lower-order models as well as models above the 2^{nd} order, with no significant differences relative to the 3^{th} order model.

6.5.1 Model Fitting Comparison

6.5.1.A Sinusoidal Modeling - Why?

A sinusoid composed of the linear combination of a sine and a cosine has been previously proposed to model the BOLD response to a BH task, by exploiting the periodic nature of the task and associated signal variations (Handwerker et al., 2007; Lipp et al., 2015; Murphy et al., 2011b; Thomason and Glover, 2008; Thomason et al., 2005). In one study, the sine-cosine model was found to explain the BOLD data better than models based on the task timing convolved with a haemodynamic response function, and it was comparable to models based on the recorded $PETCO_2$ time courses (Murphy et al., 2011b). Although $PETCO_2$ models did not explain more variance than the sinusoidal model in healthy volunteers, they do have the advantage that they can cope with incorrect task performance, which is particularly relevant in non-compliant participants and thus has potentially great impact in patient studies. This was shown in a recent study where incorrect task performance was mimicked by BH periods of variable durations (Bright and Murphy, 2013).

Nevertheless, as was emphasized in a recent study that also compares sinusoidal and $PETCO_2$

models and reports no significant differences between these two models in terms of model fit, the $PETCO_2$ model may be confounded by various experimental and physiological factors affecting the $PETCO_2$ recordings, which would reduce their relative advantage (Lipp et al., 2015). In particular, there may be inaccuracies in the synchronisation between $PETCO_2$ and fMRI recordings, namely in the estimation of the time that the exhaled air takes to pass through the tube connecting the mask/nasal cannula to the CO_2 monitor, or paradigm-related factors such as the ventilatory pace and depth (Sousa et al., 2014a). Besides the $PETCO_2$ recording errors, the sine-cosine model is also insensitive to the HRF assumptions required for both $PETCO_2$ and task-based models. Moreover, the sine-cosine model allows the voxelwise phase mapping of the response delay by fitting a single GLM (with only one input, the paradigm frequency) to the data, hence avoiding time lag assumptions or separate optimizations. Even if a Fourier model is used, it is still possible to cope with potentially non-cooperative patients by using the $PETCO_2$ trace as an indicator of poorly executed trials, which would then be removed from subsequent analysis.

6.5.1.B Harmonics - Are They Needed?

It is known that the BOLD BH response may have a complex shape, especially when a preparatory inspiration is performed in order to facilitate task performance (Pillai and Mikulis, 2014; Roberts et al., 2009; Thomason et al., 2007). In fact, in agreement with our results, Magon and colleagues verified that the BOLD response to BH protocols with preparatory inspiration exhibit a triphasic shape (Magon et al., 2009). Therefore, we hypothesized that the inclusion of higher order Fourier basis sets could improve the sine-cosine modeling of the BH BOLD response, by adding more flexibility to the amplitude, phase and shape parameters of the response. We did indeed find that adding higher order Fourier basis sets increased significantly the BOLD signal VE by the model up to the 3rd order. Although adding more regressors to the model may incur in overfitting, the use of the R^2_{adj} metric aims to overcome this issue by taking into account the increased number of effective degrees of freedom and in this way penalizing models with more regressors . Despite the improved model fitting and the possible risk of overfitting, the number of voxels exhibiting a significant BOLD response across the brain did however not increase significantly beyond the 2nd order, and in fact started to decrease beyond the 3rd order. This probably indicates that, although a better model fit is obtained in some voxels at such high orders, other voxels in fact do not benefit from the additional degrees of freedom. Nevertheless, our results clearly indicate that adding two harmonics to a sine-cosine significantly improves modeling of the BOLD response to a BH task with a preparatory inspiration. Although Fourier basis sets have previously been used to model BH BOLD responses (Handwerker et al., 2007; Thomason and Glover, 2008; Thomason et al., 2005), to our knowledge, the impact of adding higher order terms to a sinusoidal model of BH BOLD signal has not been previously systematically investigated. This is highly important since one of the consequences of the poorer model fit obtained with lower order models, most notably the sine-cosine model (M_0), was the

relative underestimation of CVR measurements.

6.5.2 Test-Retest Reproducibility Analysis

Although models M_2 and M_3 yielded the best test-retest reproducibility results for the CVR measurements, all models were found to exhibit generally good reproducibility. The CV_{intra} values obtained in this work (15.8 - 19.7 % for CV_{intra1} and 11.0 – 14.8 % for CV_{intra2}) were under the 33 % fiducial limit (Johnson and Welch, 1940). As expected and consistently with the literature, variability between subjects (29.7 - 33.1 %, CV_{inter}) was higher than between sessions, probably because most variability derives from physiological differences among subjects (Leontiev and Buxton, 2007; Lipp et al., 2015; Magon et al., 2009). ICC values (0.53 - 0.75) were above 0.4 which is usually considered the acceptability minimum in fMRI studies (Aron et al., 2006; Eaton et al., 2008).

In a previous study using an end-inspiration task similar to ours, lower values of CV_{intra1}(6%) were reported for BOLD PSC (Magon et al., 2009); however, several methodological differences may explain this apparent discrepancy, most notably the fact that PSC values were not normalized by the respective $\Delta PETCO_2$. In fact, it has been shown that such normalization may indeed introduce additional intra-subject variability in CVR measurements (Goode et al., 2009). Probably for the same reason, an even lower CV_{inter} value of 20 % was also observed in this study (Magon et al., 2009).

The value of CV_{intra2} = 11.7% achieved by the optimal model, M_2, is comparable with values reported when using sine-cosine models of BOLD responses to BH without preparatory inspiration, CV_{intra2} = 12% (Lipp et al., 2015). In this recent study, comparable albeit slightly lower CV_{intra2} values were obtained using other models, namely 8 % when using $PETCO_2$ as regressor, and 11% when using a block design (Lipp et al., 2015). Our CV_{inter} values were slightly higher than the ones reported in this same study for the sine–cosine modeling (26%). However, when using other models such as block design the values we obtained are similar: 31%. The ICC value of 0.74 achieved by the optimal model, M_2, is also similar to the ones reported in this same study: 0.74. Other models also yielded comparable results, namely when using $PETCO_2$ as regressor (0.62) or when using a block design (0.71) (Lipp et al., 2015).

In another study, Bright and colleagues evaluated the quantification of CVR using BOLD-fMRI despite poor BH performance (Bright and Murphy, 2013). Patient data were simulated in healthy volunteers by mimicking poor BH performance through varying BH consistency and ability levels using 3 different BH challenges, of 10, 15 or 20 s durations. A $PETCO_2$ model resulted in good repeatability of GM median CVR (ICC = 0.82), despite variability in BH performance, while uniform and time-scaled ramp models yielded unacceptable repeatability (0.43 and 0.45, respectively). However, it should be noted that in the latter cases CVR values were not normalised by $PETCO_2$ variations. It should also be noted that an end-expiration BH task was performed and normal breathing was externally paced (in contrast to end-inspiration BH and self-paced breathing, respectively, in our case). Also, the phase was optimised using

cross-correlation between the regressor and the corresponding time-series. Although the use of $PETCO_2$ trace can be extremely informative particularly when task compliance is variable, if subjects perform the task correctly then the information provided by the task time-course should not be less reliable than the $PETCO_2$ trace (Sousa et al., 2014a).

Another study showed that, when an end-inspiration BH task is performed, the amplitude of the BOLD response depends on the depth of the preparatory inspiration (Thomason and Glover, 2008). A feedback mechanism was proposed to overcome the issue of variability in inspiration depth; however, this increases the degree of complexity of implementation of the BH task, and a BH with preparatory inspiration remains easier to perform across a broad spectrum of populations (Thomason et al., 2007).

Nevertheless, the proposed approach is generalizable to other paradigms, and it would in particular be equally applicable to the analysis of the BOLD response to an end-expiration BH task. We expect that, in this case, a smaller number of harmonics would be required due to the decreased complexity of the BOLD response. In fact, in contrast to the triphasic shape observed for end-inspiration BH, a biphasic shape is expected for this type of data (Kastrup et al., 1998). Most critically, the initial BOLD increase introduces a higher variability of the response shape across the brain, which is present in the triphasic but not the biphasic response, may have determined the need for the higher harmonics.

6.5.3 CVR and TTP mapping

The proposed sine-cosine modeling approach allows a fast assessment of both the amplitude (CVR) and dynamics (TTP) of the BOLD response to a BH task on a voxelwise basis, based on a single GLM fit across the brain (Blockley et al., 2011). The group average GM CVR value of 0.25 ± 0.08 % mmHg obtained in our study for M_2 are in accordance with the literature (Bright and Murphy, 2013; Lipp et al., 2015), and the CVR maps show the expected contrast between GM and white matter (Kastrup et al., 1999). Average TTP results (32.6 ± 2.34 s) are also in accordance with values reported in the literature for similar BH tasks. A similar BH protocol yielded comparable TTP values: for 15 and 21 s BH, average TTP were 31 and 34 s, respectively (Magon et al., 2009). For a 20 s BH with expiration a TTP of approximately 30 s was obtained (Birn et al., 2008). Andrade et al obtained TTP of approximately 37 s for a 27 s BH with inspiration (Andrade et al., 2006). Moreover, and consistently with previous reports, we also found considerable variations in the BOLD response TTP across the brain, which further supports the use of modeling strategies that include the temporal aspect of the response (Bright et al., 2009; Leoni et al., 2008).

6.5.4 Limitations and Future Work

One pitfall of our study is that the BOLD contrast does not provide a direct measure of CBF, but rather measures a complex combination of vascular and metabolic parameters including O_2

metabolism and CBV as well as CBF. Although it is assumed that mild hypercapnia does not significantly change cerebral metabolic rate of oxygen ($CMRO_2$) and BOLD changes therefore represent mainly CBF changes (Mandell et al., 2008b), it would nevertheless be desirable to use a true perfusion imaging technique such as ASL (Leoni et al., 2012; Tancredi and Hoge, 2013; Tancredi et al., 2012). The intrinsically low signal-to-noise ratio, together with additional technical difficulty, have limited the applicability of ASL to studies of CVR. Nonetheless, a recent report found that regional and global CVR are similar when using pseudo-continuous ASL (pCASL) and BOLD contrasts, suggesting that the two techniques can provide consistent information and be suitable for studying disease processes with vascular dysfunction (Zhou et al., 2015). Furthermore, a linear relationship between BOLD- and CBF-derived CVR values had already been observed during hypercapnia in healthy volunteers (Mark et al., 2010) and patients (Mandell et al., 2008b). Nevertheless, care should be taken when assessing CVR using the BOLD contrast, particularly if variations in the basal vascular tension or oxygenation level are expected (Bright et al., 2011; Halani et al., 2015).

Since the preparatory inspiration in a BH task leads to a more complex BOLD response, BH without inspiration may be a more simple protocol to be used when trying to understand the impact of hypercapnia. It has also been shown that the end-expiration BH technique with computer-paced breathing offers superior repeatability (Scouten and Schwarzbauer, 2008). However, when dealing with potentially less cooperative patients, end-inspiration protocols tend to be easier to perform (Pillai and Mikulis, 2014; Roberts et al., 2009). Moreover, BH without preparatory inspiration tasks may induce additional head motion associated with the urge to breath towards the end of task (Thomason et al., 2007). More studies are needed in order to establish the relative advantages and disadvantages of the two types of BH tasks. In the future, a study comparing end-inspiration with end-expiration BH in terms of the impact of the proposed method would be of added value . In BH tasks, CBF changes due to alterations in $PaCO_2$ may vary due to differences in subject's minute ventilation (breathing rate and depth) and physiological variations in lung function. Using computer-paced normal breathing instead of self-paced breathing could reduce differences between subjects and between- and within-sessions (Scouten and Schwarzbauer, 2008). Nevertheless, we employed a self-paced breathing baseline period, because it minimizes deep breathing and associated hypocapnia and was found to be better accepted by the volunteers. We then attempted to minimize variability due to respiratory and task compliance differences across sessions and subjects, by normalizing the BOLD amplitude measurements by the respective $PETCO_2$ changes. It should be noted, however, that the BH task does not allow lung gas to be monitored during the BH period, as no gas is exhaled at that time, so there is no $PETCO_2$ information during those periods and an interpolation assuming some variation must be performed.

Regarding O_2 changes that might compromise the results, more recent and complex methods allow the targeting and maintenance of O_2 levels constant despite variations in $PETCO_2$, which yields improved stability and predictability of the BOLD signal (Mark et al., 2010). Nevertheless,

a recent study has shown that mild hypoxia occurred during a 20 s BH task with paced breathing but this did not significantly influence the CVR results relative to gas inhalation methods that target and maintain O_2 levels (Tancredi and Hoge, 2013). The same study tackled the issue of the shape of the CVR response to CO_2, observing significant effects of baseline CO_2 on absolute CVR measures, particularly when a hypocapnic baseline is present (Tancredi and Hoge, 2013). In our case, since no pacing was employed, $PETCO_2$ values in the normocapnic range should be achieved. Nevertheless, in the same study the impact of baseline CO_2 was found to be negligible when considering relative measures, which is also our case (Tancredi and Hoge, 2013).

6.6 Conclusions

In summary, our results indicate that Fourier series are suitable for modeling the BOLD responses to BH tasks in CVR studies, even when a preparatory inspiration is employed to facilitate task performance. Specifically, a sine-cosine model with two harmonics was found to explain significantly more variance than lower-order models and produced greater number of responsive voxels and better test-retest reproducibility when compared with both lower- and higher order models (with no significant differences relative to the 3^{rd} order model). All models were found to exhibit generally good reproducibility, consistent with the literature and within the acceptable limits in fMRI studies.

Acknowledgments

We acknowledge the Portuguese Foundation for Science and Technology (FCT) through grants PTDC/BBB-IMG/2137/2012, SFRH/BD/51449/2011 and UID/EEA/50009/2013. We acknowledge logistic support from Hospital da Luz and the technicians Ana Cristina Santos, Fernando Gonçalves and Cidália Martins for their assistance with scanning.

7

Improved 7 Tesla Resting-State fMRI Connectivity Measurements by Cluster-based Modeling of Respiratory Volume and Heart Rate Effects

Contents

This Chapter corresponds to the article published in **NeuroImage**, 153 (2017) 262-272: **Joana Pinto**, Sandro Nunes, Marta Bianciardi, Afonso Dias, L. Miguel Silveira, Lawrence L. Wald, Patrícia Figueiredo, "Improved 7 Tesla resting-state fMRI connectivity measurements by cluster-based modeling of respiratory volume and heart rate effects".

The work was developed under the scope of FCT Project HiFi-MRI, "Whole Brain Functional Connectivity Analysis of Ultra-High Field fMRI", (PTDC/EEI-ELC/3246/ 2012, 2013-2015), a joint collaboration between the Evolutionary Systems and Biomedical Engineering Laboratory (LaSEEB) at ISR-Lisboa, ALGOS - Algorithms for Optimization and Simulation and KDBIO - Knowledge Discovery and Bioinformatics research groups at INESC-ID, and the Athinoula A. Martinos Center for Biomedical Imaging at Massachusetts General Hospital/Massachusetts Institute of Technology/Harvard Medical School.

7.1 Abstract

Several strategies have been proposed to model and remove physiological noise from resting-state functional magnetic resonance imaging (rs-fMRI) data, particularly at ultrahigh fields (7 Tesla), including contributions from respiratory volume (RV) and heart rate (HR) signal fluctuations. Recent studies suggest that these contributions are highly variable across subjects and that physiological noise correction may thus benefit from optimization at the subject or even voxel level. Here, we systematically investigated the impact of the degree of spatial specificity (group, subject, newly proposed cluster, and voxel levels) on the optimization of RV and HR models. For each degree of spatial specificity, we measured the fMRI signal variance explained (VE) by each model, as well as the functional connectivity underlying three well-known resting-state networks (RSNs) obtained from the fMRI data after removal of RV+HR contributions. Whole-brain, high-resolution rs-fMRI data were acquired from twelve healthy volunteers at 7 Tesla (7T), while simultaneously recording their cardiac and respiratory signals. Although VE increased with spatial specificity up to the voxel level, the accuracy of functional connectivity measurements improved only up to the cluster level, and subsequently decreased at the voxel level. This suggests that voxelwise modeling over-fits to local fluctuations with no physiological meaning. In conclusion, our results indicate that 7T rs-fMRI connectivity measurements improve if a cluster-based physiological noise correction approach is employed in order to take into account the individual spatial variability in the HR and RV contributions.

7.2 Introduction

The last years have seen an increasing interest in the study of the brain's intrinsic functional connectivity, based on non-invasive, whole-brain measurements performed during rs-fMRI. Functional connections are inferred from time synchronous fluctuations in the blood-oxygen level

dependent (BOLD) signal across different brain regions (Biswal et al., 1995; Kwong et al., 1992; Ogawa et al., 1992). The hemodynamically-driven changes in tissue and vessel oxygenation underlying the BOLD signal are, however, caused by a combination of neuronal activity and non-neuronal mechanisms, the latter usually referred to as physiological noise (Birn, 2012; Fox et al., 2005; Greicius et al., 2003). Being able to unequivocally identify and eliminate the synchronous activity arising from sources of no interest is thus crucial to obtain accurate measurements of functional connectivity. A significant fraction of the spurious BOLD fluctuations is caused by cardiac and respiration mechanisms (Biswal et al., 1997; Cordes et al., 2001; Dagli et al., 1999; de Munck et al., 2008), inducing changes in cerebral blood flow (CBF), cerebral blood volume (CBV), arterial pulsatility and arterial CO_2 partial pressure (Dagli et al., 1999; Greitz et al., 1993; Krüger et al., 2001; Murphy et al., 2013; Purdon and Weisskoff, 1998); as well as in the static magnetic field (Abhishek Raj et al., 2011). Various methods have been proposed in the literature to account for these effects, ranging from simply band-pass filtering the signal (Zhang et al., 2011) in the frequency band of interest (typically 0.01 - 0.1 Hz) to modeling and regressing out spurious signals (inferred directly from the fMRI data or from externally acquired physiological data) in a general linear modeling (GLM) framework (Harvey et al., 2008; Jo et al., 2010; Kong et al., 2012; Murphy et al., 2009).

Techniques based on externally acquired cardiac and respiratory signals have been shown to explain significant variance of the BOLD signal and improve the accuracy of the resulting functional connectivity measurements (Bianciardi et al., 2009a; Birn et al., 2014; Chang and Glover, 2009a). Periodic fluctuations arising from the cardiac and respiratory cycles are commonly modeled by RETROICOR, a well-established technique that fits a low-order Fourier series of the phase of each cycle to the BOLD signal (Glover et al., 2000). In addition, the respiratory volume (RV) per unit time is typically used to model non-periodic low-frequency respiratory fluctuations, which are associated with slow changes in the end-tidal CO_2 pressure, a surrogate marker of the arterial CO_2 partial pressure (Birn et al., 2006). Similarly, non-periodic cardiac fluctuations are usually modeled by the heart rate (HR) temporal variation (Shmueli et al., 2007). However, the relationship between the BOLD signal and these subtle changes in the respiration depth and frequency, as well as in the cardiac rate, is still not fully understood. Respiratory and cardiac response functions have been empirically determined and proposed to describe these relations. Specifically, their contributions to the BOLD signal are modeled by convolving the RV and HR time courses with a respiratory response function (RRF) (Birn et al., 2008) and a cardiac response function (CRF) (Chang and Glover, 2009a), respectively. Another strategy has also been proposed, which follows a finite impulse response (FIR) filtering approach whereby a number of temporally lagged versions of the RV and HR time courses are included in the model (Bianciardi et al., 2009a; Shmueli et al., 2007). Both approaches have been shown to significantly explain BOLD signal variance in addition to RETROICOR.

Most critically, in both cases a high degree of variability across subjects and brain regions has been reported in the RV and HR models that best explain BOLD signal fluctuations (Birn

et al., 2014; Falahpour et al., 2013; Golestani et al., 2015; Nunes et al., 2015). Birn and colleagues hypothesized that physiological noise contributions modeled using different approaches were in general more variable across subjects than within subjects, by observing that their removal reduced the within-subject variability more than the between-subjects variability in the ensuing functional connectivity measurements (Birn et al., 2014). Such variability is supported by the findings of Falahpour and colleagues, where the derivation of subject-specific RV and HR response functions improved physiological noise correction (Falahpour et al., 2013). More recently, Golestani and colleagues reported high spatial and inter-subject variability in the timing of the estimated RV, HR and $PETCO_2$ response functions, especially when using a long repetition time (2500 ms) (Golestani et al., 2015).

Optimization at the voxel level, either by maximizing the BOLD signal variance explained (VE) through temporal lagging of the HR and RV signals, or by maximizing a cost function in a response function deconvolution method, has also been employed in some studies (Birn et al., 2006; Chang and Glover, 2009a; Golestani et al., 2015). Although significantly explaining more variance in the data, it is not clear whether the apparent improved performance of voxelwise models is due to truly increased model sensitivity or to overfitting to very localized effects with no physiological meaning. This issue is particularly problematic for higher spatial resolution fMRI data collected at high field strengths, where thermal noise dominates over physiological noise (Krüger and Glover, 2001; Krüger et al., 2001; Triantafyllou et al., 2005). Thus, being able to identify the level of spatial specificity of the physiological noise model that optimizes, not only the VE of spurious signal fluctuations but also the accuracy of the resulting functional connectivity measurements becomes a necessity.

In this paper, we compared a large set of physiological noise modeling approaches based on externally acquired cardiac and respiratory data, optimized at different levels of spatial specificity (group, subject, newly proposed cluster and voxel). This comparison was performed on whole-brain high spatial resolution rs-fMRI data collected at 7T, both in terms of the VE in the BOLD data and of the ensuing improvements in the accuracy of the functional connectivity measurements obtained in three well-known resting-state networks (RSNs).

7.3 Methods

7.3.1 Data Acquisition

A group of 12 healthy subjects (6M/6F, 28 $\pm$ 1 years old) was studied on a 7T Siemens whole-body scanner equipped with a custom-built 32-channel radiofrequency loop coil head array for signal reception, and a detunable band-pass birdcage coil for radiofrequency transmission. A rs-fMRI dataset with a duration of approximately 5 minutes, was collected using a simultaneous-multi-slice (SMS) echo-planar-imaging (EPI) sequence, with echo time (TE) = 32 ms, repetition time (TR) = 2500 ms, flip angle = 75^{o}, field of view=264 x 198 mm2. A total of

123 sagittal slices, covering the whole brain with 1.1 mm isotropic resolution, were acquired in an interleaved order with a GRAPPA acceleration factor of 3 (Griswold et al., 2002), echo-spacing = 0.82 ms, and SMS factor = 3. A whole-brain T1-weighted structural image was also collected using a multi-echo MPRAGE sequence with 1 mm isotropic resolution (van der Kouwe et al., 2008). Cardiac and respiratory data were simultaneously recorded using a pulse transducer (TN1012/ST, ADInstruments) placed on the subject's left index finger, and a pneumatic belt (UFI Model 1132 Pneumotrace II, UFI) strapped around the subjects' upper abdomen, respectively. Both cardiac and respiratory recordings were acquired with a sampling rate of 1000 Hz, simultaneously with a tag signaling the fMRI volume triggers.

7.3.2 Data Pre-Processing

Data analysis was performed using FSL 5.0 (Jenkinson et al., 2012; Smith et al., 2004) tools and in-house software implemented in MATLAB2013a. For the fMRI data, quasi-periodic cardiac and respiratory fluctuations were first regressed out using RETROICOR (up to the 2^{nd} order), synchronized in time with each acquisition slice. The following pre-processing steps were then applied: correction for slice acquisition timings by interpolation to the center of each TR interval; head motion correction by volume-to-volume re-alignment; removal of slow drifts by regressing out using a set of polynomials (up to the 3^{rd} order); and spatial smoothing by low-pass filtering using a Gaussian kernel with FWHM = 3 mm. A second analysis was also performed using a larger smoothing kernel (FWHM = 5 mm), in order to test the impact of spatial smoothing on the effects of physiological noise modeling at different levels of spatial specificity.

Linear registration between the functional and structural images was performed using Boundary - Based Registration (BBR), and the structural images were normalized to the MNI standard space by non-linear registration (FLIRT and FNIRT tools from FSL) (Greve and Fischl, 2009; Jenkinson and Smith, 2001; Jenkinson et al., 2002). Gray matter (GM), white matter (WM) and cerebral spinal fluid (CSF) masks were obtained by segmentation of the T1-weighted structural image (FAST tool from FSL), and subsequently adding the brainstem from the MNI atlas to the GM mask (Collins et al., 1995; Mazziotta et al., 2001). Both masks were then eroded using a 3 mm spherical kernel as recommended in (Jo et al., 2010), so that partial volume effects were minimized. Additionally, the eroded CSF mask was intersected with a large ventricle's mask extracted from the MNI space, following the rationale described in (Chang and Glover, 2009a). The concurrently acquired respiratory and cardiac signals were low-pass filtered at 0.5 Hz and 1.6 Hz, respectively, and peak detection was performed on the filtered cardiac signal for posterior construction of the physiological regressors.

7.3.3 Physiological Noise Models

A set of competing models was tested for the physiological noise contributions from non-periodic fluctuations of cardiac and respiratory signals based on HR and RV, respectively. RV was defined as the standard deviation of the respiratory waveform in a 5 s sliding window (corresponding to 2 TRs) centered at each time point (Chang and Glover, 2009a). HR was defined as the inverse of the peak-to-peak interval of the filtered cardiac signal; HR values more than 1.96 standard deviations away from the median were considered spurious, and were replaced by linear interpolation (Bianciardi et al., 2009a; Shmueli et al., 2007).

Variability in the timings and shape of the BOLD response to HR and RV fluctuations was taken into account through a time-lagging optimization procedure, whereby the RV and HR regressors were time-lagged in a [-20 20] s interval in 1 s steps; for each lagged time course, a GLM analysis was carried out and the VE was computed (Bianciardi et al., 2009a; Jorge et al., 2013);. Two models were then built: 1) a *Single-Lag* model based on the lagged time course yielding the maximum VE value; and 2) a *Dual-Lag* model comprising the two lagged time courses yielding the two greatest VE values corresponding to a positive and a negative fMRI signal change (the purpose of selecting one lag yielding a positive and another one yielding a negative signal change is to taken into account the commonly observed biphasic shape of the VE vs lag curves). The same process was repeated after convolving RV and HR with the previously proposed impulse response functions (IRF), RRF (Birn et al., 2008) and CRF (Chang and Glover, 2009a), respectively, yielding the *Standard IRF Convolution* model. Subject-specific IRF's were also derived by simultaneously deconvolving RV and HR from the GM global signal (GS) using a Gaussian process (Chang and Glover, 2009a; Falahpour et al., 2013), yielding the *GS-derived IRF Convolution* model. No lag optimization was performed in this case, as the deconvolution process intrinsically adapts the response for temporal differences.

7.3.4 Lag Optimization at Different Levels of Spatial Specificity

The lag optimization methodology based on maximizing the VE was applied to both RV and HR, at each of the four different levels of spatial specificity tested here (*group*, *subject*, newly proposed *cluster*, and *voxel*), as described next. VE averages were solely computed across GM voxels, where BOLD fluctuations of neuronal origin are expected to occur.

1. *Group*: The GM average VE vs lag curves were averaged across all subjects in the group, and the resulting group average VE vs lag curves were then used to obtain a unique model of each type (*Single-Lag, Dual-Lag, Standard IRF Convolution*) for the whole group. Group IRF's were computed as the group average of the IRF's obtained for each subject from the GM average fMRI GS, and used to generate the *GS-derived IRF Convolution* models. This level of specificity assumes a homogeneous behavior of RV and HR responses across subjects, as well as across the brain.

2. *Subject*: The GM average VE vs lag curves were used to obtain a unique model of each type (*Single-Lag, Dual-Lag, Standard IRF Convolution*) for each subject. Subject-specific IRF's were derived from the GM average fMRI GS and used to generate the *GS-derived IRF Convolution* models. In contrast with the group level of specificity, this level of specificity takes into account differences across subjects, but it still assumes a homogenous behavior across the brain.

3. *Cluster*: In order to account for the spatial variability of RV and HR contributions within across the brain, a novel approach was proposed to obtain clusters of voxels with temporally distinct responses to RV and HR fluctuations by clustering the VE vs lag curves of all GM voxels in each dataset using a *k-means* algorithm with $k = \{2,3,4,5,6\}$ clusters (the squared Euclidean distance was used as the distance metric; and local minima were minimized by performing 10 replicates using different initial cluster centroid positions chosen at random (`https://www.mathworks.com/help/stats/kmeans.html`). The optimal lags were then extracted from the average VE vs. lag curve of each cluster. Because some clusters obtained in this way present a monophasic behavior (purely positive or negative responses), defining a *Dual-Lag* model is not always possible; in such clusters, a *Single-Lag* model was chosen. Cluster-specific IRF's were derived from the cluster average fMRI GS's and used to generate the *GS-derived IRF Convolution* models.

4. *Voxel*: The VE vs lag curve measured in each voxel was used to determine the optimal lags for the model applied to that voxel. The *Dual-Lag* model was not tested at this level because it is not possible to clearly identify the second peak corresponding to a biphasic curve consistently in all voxels due to noise. This level of specificity takes into account differences in the RV and HR responses across subjects and voxels.

7.3.5 Variance Explained in the fMRI Data

Model performance was first evaluated by computing the VE by each competing physiological model. Functional connectivity fluctuations are usually evaluated in GM, thus, for optimization purposes, average VE results were restricted to the whole GM. The percentage fMRI signal VE was defined as the adjusted coefficient of determination (R^2_{adj}) multiplied by 100. R^2_{adj} increases only if the addition of a regressor explains more information that what would be expected by chance, penalizing the unnecessary loss of degrees of freedom. This is an important requirement in our comparison since models with different levels of complexity, i.e. with a variable number of regressors, were compared against each other. For each level of spatial specificity, the model explaining the highest percentage of variance in the GM was subsequently used for the functional connectivity analysis. In order to further inform the choice of the optimal number of clusters in addition to the model's VE, we also used a silhouette clustering evaluation criterion. The silhouette value is computed for each point in a cluster, and it measures how similar that point is to points within the same cluster when compared to points in other clusters (Kaufman and

Rousseeuw, 1990). If most points have a high silhouette value, then the clustering solution is appropriate.

7.3.6 Impact on Functional Connectivity Measurements

To assess the impact of the physiological noise correction methods on the accuracy of functional connectivity measurements, three commonly identified RSNs were analyzed based on the following seeds: posterior cingulate cortex (PCC) (MNI coordinates: -6 -58 28), supplementary motor area (SMA) (MNI coordinates: -2 10 48) and intra-parietal sulcus (IPS) (MNI coordinates: 26 -58 48) (Toro et al., 2008). For each dataset, and for each physiological noise correction method tested (*Group-, Subject-, Cluster-*, and *Voxel*-level correction), the average time course in each seed (5 mm sphere centered at the specified MNI coordinates) was extracted and orthogonalized against each other, by removing from each one the variability shared with the other two, as implemented in the FEAT tool in FSL (`fsl.fmrib.ox.ac.uk/fsl`). For comparison purposes, data pre-processed but without any physiological noise correction (*Uncorrected*) was also included in the analysis. A multiple regression analysis was then performed, in a GLM framework, in order to obtain a map of the correlations with each seed, expressed by the respective GLM parameter estimates (PE), or coefficients of fit. Group-level RSNs were obtained by entering each of the three PE maps from each subject, and for each physiological noise correction tested, into a higher-level statistical analysis using a mixed-effects model (as implemented in FSL's FLAME), and correcting for multiple comparisons at the cluster level using Gaussian random field theory (voxel $Z > 2.3$ and cluster $p < 0.05$) (Margulies et al., 2007; Shehzad et al., 2009).

For each dataset, and for each model specificity tested, the functional connectivity strength (FCS) of a given RSN (how strongly the voxels are correlated with the corresponding seed) was computed as the average across the respective group-level thresholded Z-statistic map of the percent signal change (PSC) associated with the respective seed (fit coefficient normalized by the mean signal amplitude over time). In order to assess the specificity of these functional connectivity measurements, we computed the ratio between the FCS of a given RSN and the average PSC across the whole gray matter for the different physiological noise correction methods. The rationale is that an accurate functional connectivity measurement should reflect fluctuations of neuronal origin that are specific to the RSN, and hence this ratio should increase as generic fluctuations of non-neuronal origin are better removed from the data, while RSN-specific fluctuations are preserved. Besides this outcome measure, we also computed the average PSC across a region where no fluctuations of neuronal origin are expected, consisting of the WM and CSF masks obtained by image segmentation.

7.4 Results

The results obtained for the lag optimization of the contributions of HR and RV fluctuations to the fMRI signal, in terms of the VE values obtained across subjects and brain regions, are first presented. These motivate the exploration of the different levels of spatial specificity tested for physiological noise modeling and correction. Their impact on the accuracy of functional connectivity measurements of three RSNs is then presented.

7.4.1 Physiological Noise Modeling Lag Optimization

The variation as a function of time-lag of the fMRI signal VE associated with the RV and HR physiological noise model contributions, is shown in Figure 7.1 (top), averaged across GM for each individual subject as well as across subjects. The individual optimal time-lags, yielding the maxima VE values, vary significantly across subjects for both RV and HR, as evidenced by the wide error bounds defined by the mean and the standard errors of the mean (7.9 $\pm$ 2.5 s and 5.3 $\pm$ 1.9 s, respectively). Although the shape of the individual VE vs lag curves is also quite variable across subjects, a biphasic behavior emerges at the group level, with a major peak at approximately +11 / +9 s and a minor peak at approximately -7 / -3 s, for RV / HR, respectively. Individual HR curves are in general noisier: while a large positive peak is consistently observed, inter-individual differences dilute the position of the average negative peak. Furthermore, the biphasic behavior is also less clear at the subject level, with more than two peaks being observed in some subjects. The RRF and CRF estimated for each subject based on their global GM signal, using a *Subject-specific* optimization, are also shown in Figure 7.1 (bottom), together with the standard RRF and CRF (Birn et al., 2008; Chang and Glover, 2009a). We found that both responses are highly variable across subjects. Nevertheless, overall, we obtained faster responses than previously reported, presenting earlier 1^{st} and 2^{nd} peaks for both RV and HR ($\sim$ 2 and 8 s).

The optimal time-lag maps, for both RV and HR regressors, are shown in Figure 7.2, for the group average with the respective standard error (SE). Although some inter-subject variability is apparent from the SE maps, time-lags significantly different from zero are nevertheless found in different brain regions, with consistent patterns across subjects. For RV, large positive time-lags are found in the occipital cortex and along the interhemispheric fissure. For HR, positive time-lags are found in posterior regions adjacent to the sinus rectus. For both RV and HR, predominantly negative time-lags are observed in WM, in contrast with mainly positive time-lags in GM.

7.4.2 Clustering Based on VE vs Lag Curves

The newly proposed spatial clustering of GM voxels based on the shape of the VE vs lag curves is illustrated in Figure 7.3, for k = 3 (the optimal number of clusters found in this study, as described in the next sub-section). The spatial distribution and average VE curves of the

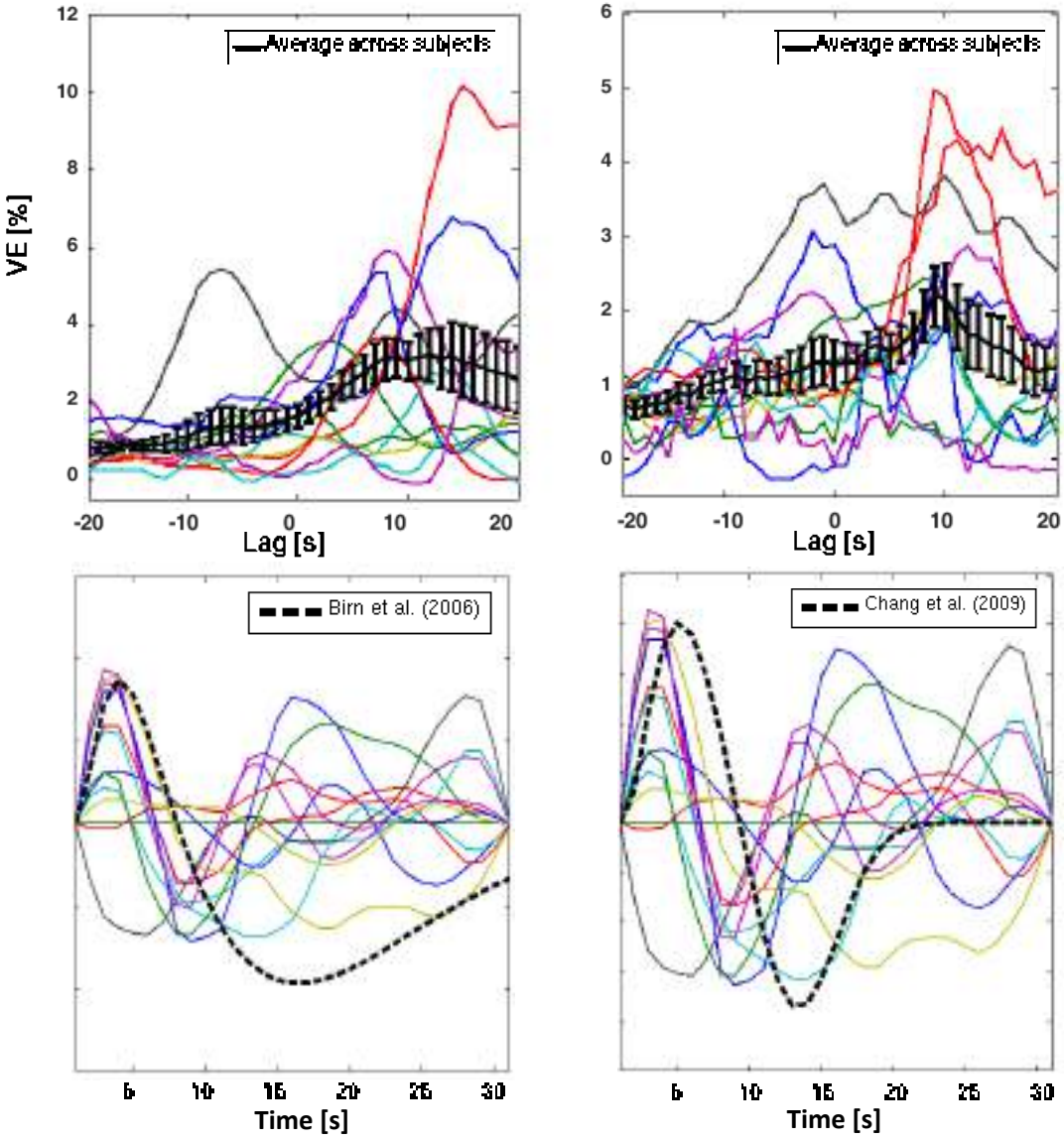

Figure 7.1: Top: Curves of the GM-averaged VE by RV (left) and HR (right) regressors, for each individual subject (color) and on average across subjects (black), as a function of the time-lag that was applied to the RV and HR regressors. Error bars represent the standard error of the mean. Bottom: RRF and CRF curves derived from the GM global signal for each subject(color), overlayed with the standard RRF and CRF curves reported in (Birn et al., 2006) and (Chang and Glover, 2009a), respectively (black, dashed).

three clusters obtained for a representative subject, for both RV and HR, are shown. In both cases, the biphasic behavior (one negative and one positive VE peak) is present in two of the three clusters, while the third cluster reveals a monophasic behavior, with the VE peak centered close to 0 s. Biphasic curves are, however, very asymmetric with respect to the peaks amplitude,

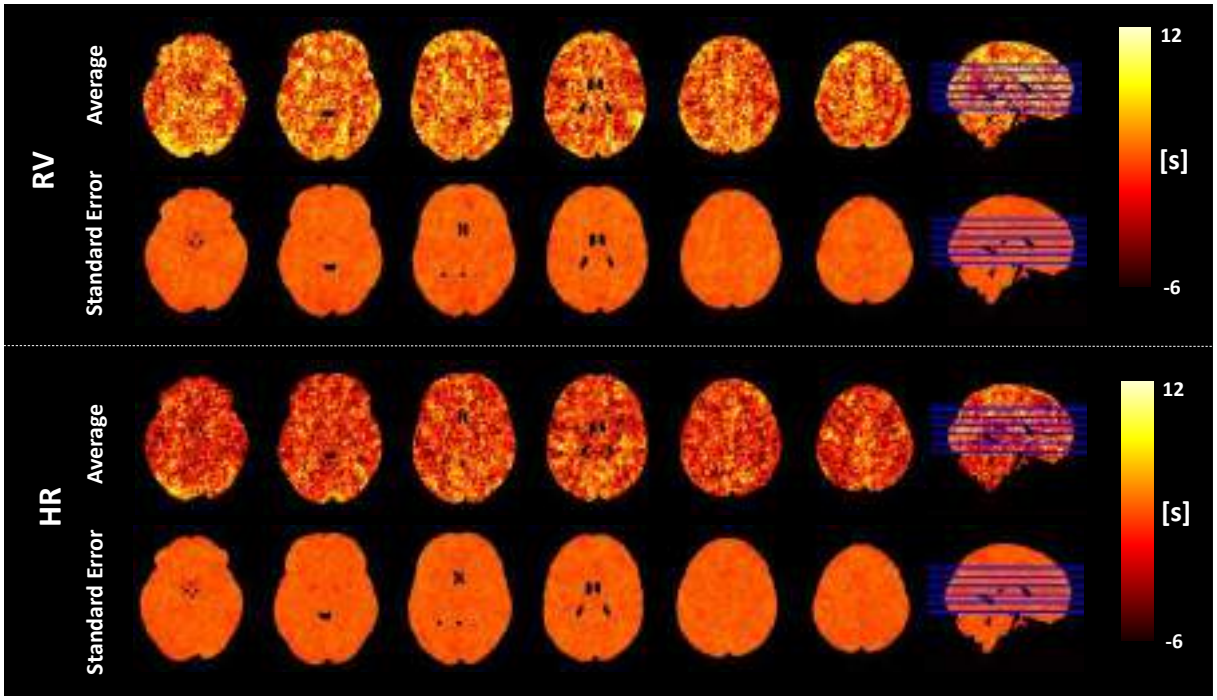

Figure 7.2: Group average and associated standard error maps of the 1^{st} optimal time-lag value, obtained for both RV and HR physiological noise models in 6 representative axial slices (MNI coordinates Z = 56, 68, 80, 92, 104, 116).

exhibiting a clearly dominating negative or positive peak. In general, three clusters with clear structural differences were found for every dataset; most clusters retained a biphasic curve (59 / 61 out of 72 for RV / HR, respectively), but with considerably different peak times.

7.4.3 Variance Explained in the fMRI Data

The VE by each of the physiological noise models tested, averaged across GM and subjects, is shown in Figure 7.4, as a function of the level of specificity *(Group/Dataset/Cluster/Voxel)*.

A global statistical analysis on VE, averaged across GM, was performed in order to test for differences and interactions between model type *(Single-Lag, Dual-Lag, Standard IRF Convolution, GS-derived IRF Convolution)*, specificity level *(Group, Subject, Cluster k = 2, Cluster k = 3, Cluster k = 4, Cluster k = 5, Cluster k = 6)*, and physiological variable (RV/HR), using a 3-way repeated measures analysis of variance (ANOVA). In this analysis, the specificity level Voxel was not included since this level was considered only for two of the four model types. A significant main effect was found for the specificity level ($F = 113$, $\eta^2 = 0.926$, $p < 0.001$) and the model type ($F = 77$, $\eta^2 = 0.875$, $p < 0.001$), but not for the physiological variable ($F = 4.5$, $\eta^2 = 0.292$, $p > 0.05$). There was a significant interaction between specificity level and model type ($F = 25$, $\eta^2 = 0.697$, $p < 0.001$), with only marginally significant interactions of physiological variable with both level of specificity and model type ($F \sim 3$, $\eta^2 \sim 0.2$, $p > 0.01$). For this reason, further statistical analyses were performed separately for model type and

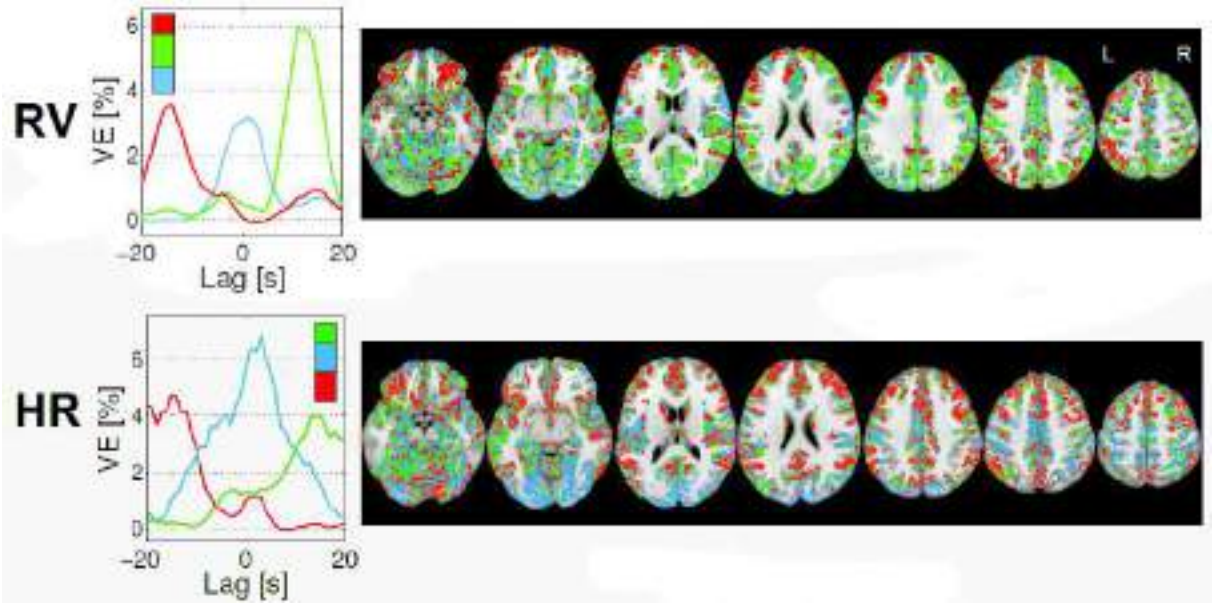

Figure 7.3: Illustrative example of the newly proposed GM spatial clustering approach based on each voxel's VE vs lag optimization curve, for both RV and HR physiological noise models: Left) Cluster average VE vs lag curves for the three clusters; and Right) spatial maps of the three clusters in seven representative axial slices.

specificity level.

Significant main effects of model type were found for each specificity level ($p < 0.001$). Post-hoc analysis yielded significant differences between *Single* and *Dual-Lag*, for specificity levels *Group, Subject, Cluster k = 2* and *Cluster k = 3*, and between *GS-derived IRF Convolution* and all other models, for all specificity levels, while no significant differences were found between *Dual-Lag* and *Standard IRF Convolution* models. At the *Voxel* level, no statistical main effect was found for model type ($F = 0.015$, $\eta^2 = 0.001$, $p = 0.905$).

Since the *Dual-Lag* model type generally outperformed the other model types, this was selected for subsequent analysis of specificity level; for consistency, for the *Voxel* level, the *single-lag* model was chosen (rather than *Standard IRF Convolution*). A significant main effect was found for specificity level, for all model types ($F = 31$, $\eta^2 = 0.739$, $p < 0.001$). Post-hoc analysis yielded significant differences between successive specificity levels up to *Cluster k = 3*; subsequent to this, only the *Voxel* level was significantly different from *Cluster k = 3*; furthermore, the *Voxel* level was significantly different from *Group, Subject, Cluster k = 2* and *Cluster k = 3* levels, but not from *Cluster k = 4, 5* or *6* levels. We therefore conclude that *k = 3* is the "optimum" number of clusters when using the *Cluster* specificity level.

The group average VE maps obtained with the deemed optimal models at each specificity level are shown in Figure 7.5. On average (across GM), 6.9 ± 1.1% of variance was explained by a model optimized at the group level, while nearly two times more variance (13.7 ± 0.9%) was explained when optimizing time lags at the voxel level. *Subject* and *cluster*–level optimized models explained 8.8 ± 1.1% and 10 ± 1.2% variance in the GM, respectively. Irrespective

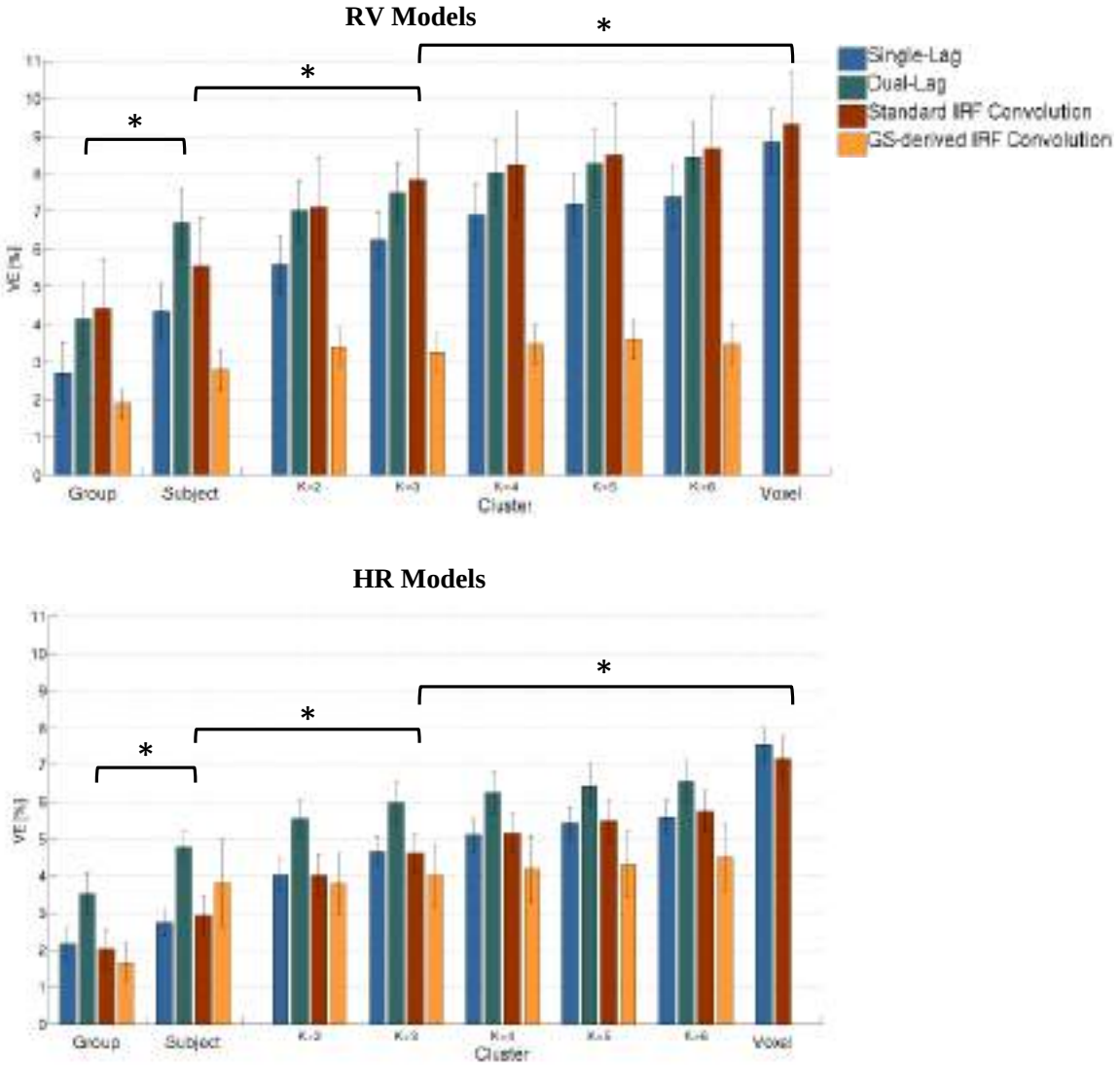

Figure 7.4: Group average VE in GM, for *RV* (top) and *HR* (bottom) physiological noise models, and for the different model types tested (*Single-Lag/Dual-Lag/Standard IRF Convolution/GS-derived IRF Convolution*), as a function of the specificity level (*Group/Subject/Cluster (k = 2, 3, 4, 5, and 6)/Voxel*) used for the model optimization. Statistically significant differences between different specificity levels are indicated.

of spatial specificity level, all models accounted for the most variance within the occipital and parietal lobes.

The VE results obtained using data smoothed with a larger kernel (FWHM = 5 mm) are shown in Figure C.2 (supplementary figure can be found in Appendix C). As expected, we found generally higher VE values for the physiological noise models in this case. Nevertheless, the increase of VE with specificity level was still observed.

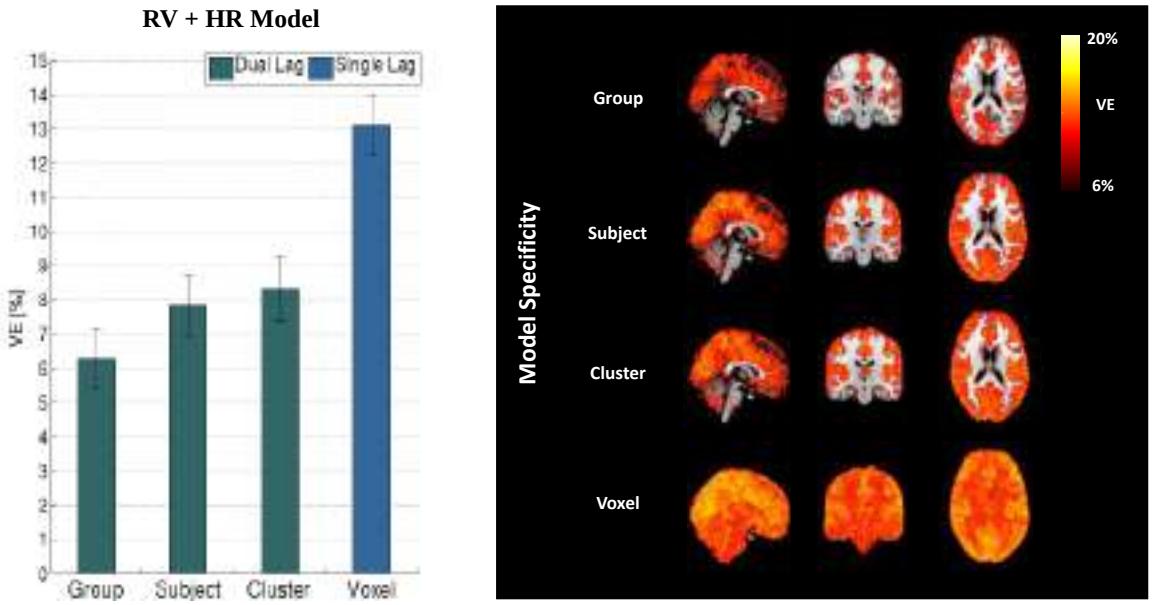

Figure 7.5: Group average VE results by the optimal *RV+HR* physiological noise model at each level of spatial specificity adopted for lag optimization (*Dual-Lag* for *Group, Subject and Cluster*, and *Single-Lag* for *Voxel*): GM mean values (bars represent group average and error bars the respective standard error) (left) and VE maps (right).

7.4.4 Impact on Functional Connectivity Measurements

The group results for the FCS measurements obtained inside the RSN, across the whole GM and across WM + CSF, using the different spatial specificity levels of the physiological correction model, are shown in Figure 7.6. A 3-way repeated measures ANOVA was performed on the FCS values with factors: spatial specificity (*Uncorrected, Group-, Subject-, Cluster-*, and *Voxel*-level correction), brain region (*RSN, GM, WM+CSF*); and RSN seed (*PCC/SMA/IPS*). A statistically significant main effect was found for spatial specificity level (but not brain region or RSN seed), reflecting a general decrease of temporal correlations with the seed as more temporal fluctuations are removed from the data with increasingly more specific physiological noise models. This general decrease was, however, relatively less accentuated inside the RSNs (i.e., in brain areas that are expected to exhibit true neuronal correlations with the seed), when compared with the whole GM or WM+CSF regions.

Accordingly, the ratio between the average FCS inside the RSN and average FCS in the whole GM generally increased with specificity level. Most importantly, however, this increase was significant only up to the subject level and a decrease was then observed at the voxel level (Figure 7.6, Right). A 2-way repeated measures ANOVA was performed on the FCS ratios with factors: spatial specificity (*Uncorrected, Group-, Subject-, Cluster-*, and *Voxel*-level correction) and RSN seed (*PCC/SMA/IPS*). A statistically significant main effect was found for the spatial

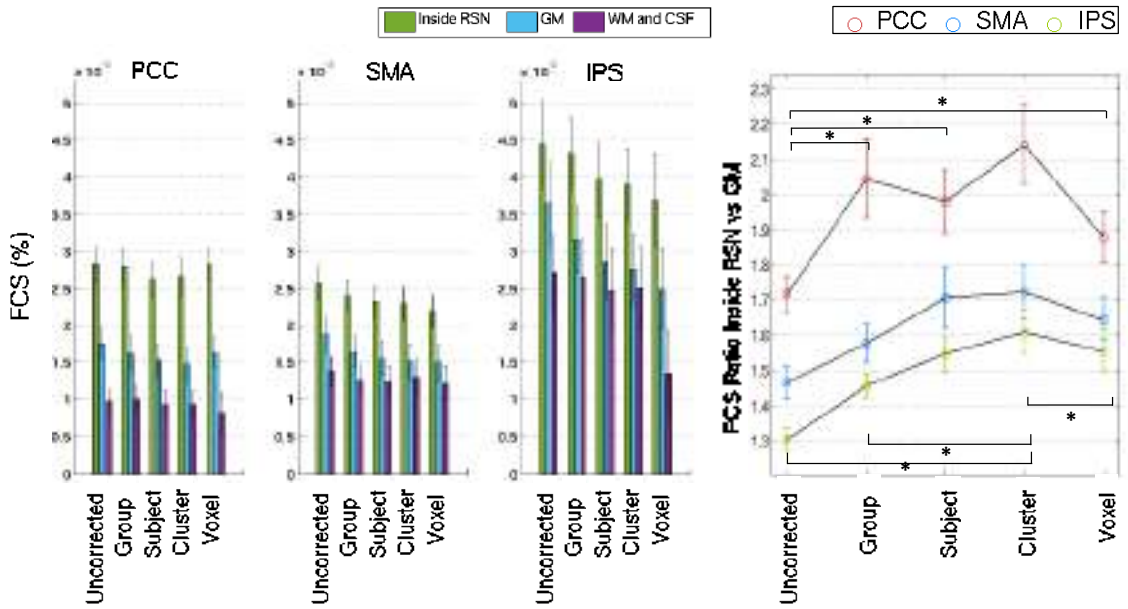

Figure 7.6: Group average FCS measurements for each seed (PCC, SMA, IPS), as a function of the spatial specificity level of the deemed optimal RV+HR physiological noise: Left) FCS averaged inside the RSN (defined by the suprathreshold group Fischer-Z maps), across the whole GM, and across WM and CSF; and Right) ratio between the average FCS inside the RSNs and the average FCS across the whole GM. Statistically significant differences ($p<0.05$, Bonferroni corrected) between spatial specificity levels are indicated.

specificity level ($F = 9.2$, $\eta^2 = 0.455$, $p < 0.001$), and for RSN seed ($F = 6.6$ η^2 =0.377, $p < 0.006$), with no interactions. Post-hoc comparisons showed significant improvements at all correction specificity levels relative to the *Uncorrected* condition ($p < 0.001$), and also between the *Cluster* level correction and the *Group* and *Voxel* levels ($p = 0.009$ and $p = 0.01$, respectively) (with no significant change relative to the *Subject* level). The functional connectivity maps obtained with the PCC seed at the group-level are shown in Figure 7.7, for each physiological noise correction condition. It may be observed that, consistently with the FCS ratio variation with correction level, FCS changes are slightly globally more pronounced outside the RSN, with no specific spatial distribution. We also computed FCS and corresponding ratios for all the numbers of clusters tested (k = 2, 3, 4, 5 and 6), and we verified there was no significant main effect in the FCS ratio of the different number of clusters ($F = 0.498$, η^2 =0.043, $p = 0.6$) (Figure C.3, supplementary figure can be found in Appendix C).

7.5 Discussion

We systematically compared different models of the RV and HR physiological noise contributions in whole-brain high spatial resolution rs-fMRI data collected at 7T. We found that the optimal time-lags of these models varied considerably between subjects and across the brain.

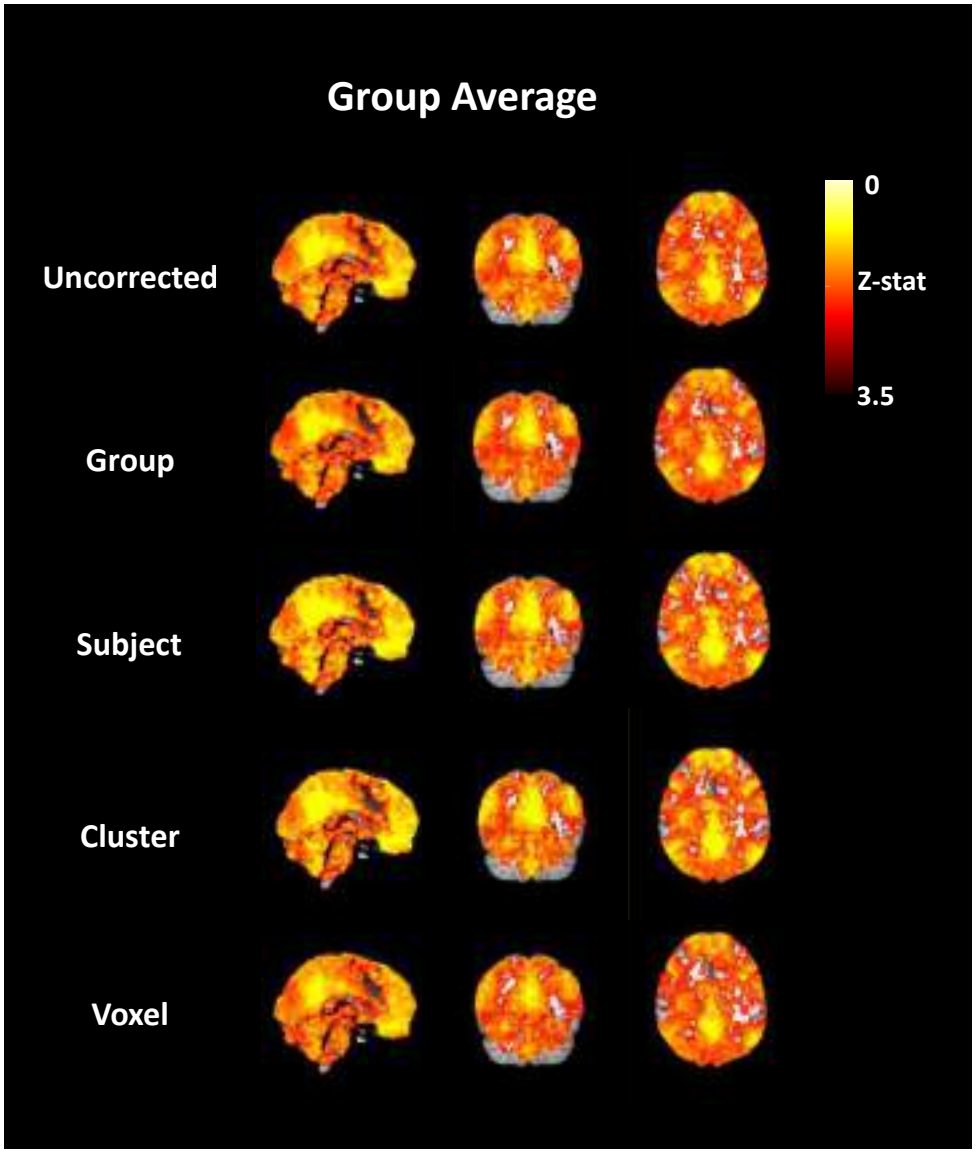

Figure 7.7: PCC-based functional connectivity maps (group-level Z-stat maps), obtained for each physiological noise correction condition.

Consistently, models optimized at greater degrees of spatial specificity, from group to subject, cluster and voxel levels, generally explained more signal variance, as expected. However, the accuracy of FCS measurements in three common RSNs improved with optimization specificity only up to the cluster level, and subsequently decreased at the voxel level, suggesting that the latter incurs in over-fitting to local fluctuations with no physiological meaning.

7.5.1 Lag Optimization Specificity

In our time-lag optimization, we identified two main peaks at approximately -7 / +11 s and -3 / +9 s for RV and HR, respectively, which closely matches the results in (Bianciardi et al., 2009a) (-9 / +9 s and at -3 / +9 s for RV and HR, respectively). The asymmetry in amplitude between the positive and negative peaks in the RV response, as well as the less defined biphasic

behavior for HR are also in agreement with (Bianciardi et al., 2009a). Moreover, we found high inter-subject variability in the optimal time-lags, which is also consistent with (Bianciardi et al., 2009a). In their case, the presence of a negative peak in the average GM VE curve was not apparent, and could only be detected based on the average t-statistic (Bianciardi et al., 2009a). Golestani and colleagues also reported a high inter-subject variability in the derived CRF response, with an oscillatory behavior observed after the 2^{nd} (negative) peak, further evidencing the difficulties in the identification of the negative peak in this case (Golestani et al., 2015).

Most importantly, we found that the optimal time-lags also showed important variations across the brain in each individual subject, which motivated the introduction of a further level of specificity by finding spatial clusters of the VE vs time-lag curves. These spatial variations may at least partially be explained by the fact that the contributions of both RV and HR to the fMRI signal are directly related with blood flow and thus with the brain's vasculature characteristics (e.g. location, geometry etc.). We tested different numbers of clusters, between 2 and 6, and found that using 3 clusters explained significantly more fMRI signal variance across GM than using 2 clusters, and only *voxel*-level optimization outperformed this. Also, 3 clusters provided the overall most favorable values of the silhouette criterion (Figure C.1, supplementary figure can be found in Appendix C). We have further verified that spatially smoothing the fMRI data with a larger kernel size (FWHM = 5 mm vs. 3 mm) did not significantly affect these findings. Splitting the brain voxels into three clusters based on their VE vs lag optimization curves resulted in comparable sized clusters presenting very different average VE curves. While most clusters preserved a biphasic behavior, confirming the validity of the more general, whole-brain strategies employing two time lags / biphasic IRFs, important differences were observed both in terms of peak amplitude and time-to-peak.

As expected, increasing the level of optimization specificity generally resulted in a greater fraction of fMRI signal variance being explained by the RV and HR models. The only exception occurred for the *GS-derived IRF convolution* models, which explained less variance after spatial clustering. This finding may be explained by the fact that the joint deconvolution of RRF and CRF underlying this type of model is not fully used in the clustering approach. Indeed, the RV and HR clusters are obtained independently based on their respective VE vs lag curves. Thus, each voxel is modeled by RV and HR responses that come from an independent deconvolution process (the RV/HR responses are respectively deconvolved from the RV/HR clusters' average signal to which each voxel pertains), not taking into account the relationship between the two. As a result, the performance of this model, which assumes dependency as it deconvolves both responses from the average signal simultaneously, is hindered.

7.5.2 Model Types

The *Dual-Lag* and *Standard IRF Convolution* models showed comparable performances and consistently explained a larger fraction of spurious variance than that by the *Single-Lag* models,

supporting the positive impact of modeling a second time-lag in addition to the main one. The exception to this trend was observed at the voxel level, where no statistically significant differences were observed between the *Single-Lag* and *Standard IRF Convolution* models. This observation most likely stems from the lack of sufficient SNR at this level to identify accurate timings of the RV and HR responses.

Regarding the *GS-derived IRF Convolution* models, one could expect that response functions derived from the data would account for the lag properly. However, these models produced generally lower VE values than the other model types, and did not improve with increasing levels of specificity, in contrast to all other models (as seen in Figure 7.4). This may be due to an insufficiently short TR (2.5 s) to accurately sample the response, as well as to the great sensitivity of the deconvolution procedure to the noise in the data, which increases with the level of specificity (due to less signal averaging across voxels). If the deconvolution does not perform well enough, then the *GS-derived IRF Convolution* models are at a disadvantage relative to all other models tested, for which time-lag optimization is performed; this may at least partly explain their relatively lower VE values. However, we should note that other papers employing similar approaches have reported responses that were also considerably different from the standard (Cordes et al., 2014; Falahpour et al., 2013). Falahpour used exactly the same technique as Chang's and reported a much earlier negative peak for both RRF and CRF ($\sim$ 10 s for both, relative to 16/12 s, respectively). By using a different strategy with the same purpose, Cordes et al. reported a negative peak between 11 and 14 s (with an earlier positive peak between 1.5 and 5 s) for CRF, and a negative peak between 4 and 9 s for RRF. Importantly, we observed that the estimated RRF was quite variable between subjects, more so than the CRF, which is in agreement with the findings in both of those studies, particularly when using longer temporal delays. In a related study, Golestani et al. used a similar approach to Chang's to simultaneously estimating three response functions, including not only RRF and CRF, but also the response to $PETCO_2$ changes (Cordes et al., 2014; Falahpour et al., 2013; Golestani et al., 2015). The estimated CRF was consistent to Chang's, but that the RRF was considerably different from previous studies, which can probably be explained by the simultaneous estimation of the $PETCO_2$ response; interestingly, they found slower RRF dynamics in this case.

We also investigated the sensitivity of the deconvolution algorithm to the three hyperparameters (l, σ_f^2, σ_e^2), by systematically testing the following values: σ_f (0.5, 1, 2, 3, 4), σ_e (0.1, 0.3, 0.5, 0.7, 0.9) and l (1, 2, 3, 4, 5, 6). We observed small differences in the IRF's obtained, as depicted in Figure C.4 (top) (supplementary figure can be found in Appendix C), for one illustrative subject, where average IRF's across subjects are also shown. When changing σ_f^2 and σ_e^2, only negligible changes were observed. The impact of changing the l parameter, related to the degree of smoothness, was higher: increasing l delayed the negative peak, making it more similar to the standard IRF's. However, when going for much higher l values, the shape of the RRF was smeared out, with the positive peak disappearing. Nevertheless, we further tested the impact of using the highest l value (l = 6) on the model VE, and we obtained a 28% increase in VE

associated with RV and a 34% decrease in VE associated with HR, relative to $l = 2$ (Figure C.4 - bottom, supplementary figure can be found in Appendix C). In any case, the overall changes in VE were not statistically significant, and for that for reason we kept the original value ($l = 2$).

7.5.3 Data-Driven Methods

Besides the model-based methods explored in our study, a plethora of data-driven methods have also been proposed for physiological noise correction, many of which address variability across subjects and brain regions by fitting multiple components to a given dataset (e.g., (Abreu et al., 2016; Behzadi et al., 2007; Bianciardi et al., 2009b; Jorge et al., 2013; Nunes et al., 2016; Tierney et al., 2016). In general, noise-related regions of interest (ROIs) are defined, multiple regressors are extracted, most often using principal component analysis, and a given number of selected components are then regressed out from the data. Behzadi and colleagues obtained the ROIs by thresholding the maps of temporal standard deviation (Behzadi et al., 2007). Alternatively, a biophysically-inspired measure of robust temporal signal-to-noise ratio has also been proposed (Tierney et al., 2016). In a different approach, Pamilo and colleagues applied principal component analysis to group fMRI data and extracted the signal components that correlate maximally in one subject's data but minimally in another subject's data (Pamilo et al., 2015), and found that this subject-specific physiological noise correction method outperformed methods operating at group level. Independent Component Analysis (ICA) is also commonly used for fMRI denoising by separating multiple signal sources, associated with processes such as scanner artifacts, physiological noise and brain activity (Beckmann and Smith, 2004; Brooks et al., 2008). Non-neuronal fluctuations are usually identified manually or resorting to automatic classification tools (Churchill et al., 2012; De Martino et al., 2007; Salimi-Khorshidi et al., 2014; Tohka et al., 2008).

7.5.4 Functional Connectivity

Analysis of three well-known RSNs revealed that increasing model specificity up to the cluster level reduced FCS within the networks, but to a smaller extent than it reduced FCS across the whole GM. Although the more specific models generally removed more correlated signal fluctuations, compared to the whole brain, they removed relatively less fluctuations within networks that were expected to display synchronous activity of neuronal origin (and not just physiological noise). These results indicate that increasingly specific optimizations of the RV and HR response time-lags indeed better modeled the associated spurious fMRI signal fluctuations and therefore helped improve the accuracy of subsequent functional connectivity measurements assumed to reflect neural sources. The inversion of this trend at the voxel level showed that, despite the improvement in model fitting apparent from the VE results alone, voxelwise optimization did not benefit the accurate measurement of functional connectivity. This behavior may be explained

by an over-fitting of the data with these models, which might in fact be adjusting to random, unstructured noise fluctuations and not strictly the RV/HR contributions to physiological noise. This has a direct impact on the specificity of fluctuations regressed out from the data, which makes the FCS ratio between network and global GM brain regions closer to 1.

Our results indicate that, even if individual or spatial variations are not taken into account, a group level model optimization still significantly improved the accuracy of functional connectivity measurements compared with no correction. Thus, if optimizing the models at the subject or cluster levels is not an option due to time or computational restraints, using a group-level optimization is still highly recommended. Future studies should investigate the nature of inter-individual and spatial variations in the RV and HR contributions to physiological noise in fMRI data, and propose more accurate methods of differentiating the shape and timings of the associated responses across the brain.

7.5.5 Limitations of the Current Work

The acquisition protocol used in this study was designed to achieve whole-brain coverage with high spatial resolution (1.1 mm isotropic), making the most of the improved sensitivity at ultrahigh field (7T) combined with an ultrafast SMS acquisition sequence. This protocol is therefore quite uncommon in the literature of resting-state studies, which are most often performed at 3T with larger voxel sizes, typically $\sim$ 3.5 mm cubic (e.g., (Birn et al., 2014)). These differences may limit the generalizability of our results, and are thus discussed here. Physiological noise fluctuations are known to increase with field strength (Krüger and Glover, 2001; Krüger et al., 2001; Triantafyllou et al., 2005). Therefore, using lower field strengths such as 3T should reduce the observed RV and HR contributions and possibly also the benefit of optimizing the respective models. On the other hand, 1.1 mm isotropic fMRI at 7T might have less physiologic noise contributions than 3.5 mm isotropic fMRI at 3T because it might be dominated by thermal noise. The exact voxel size below which thermal noise dominates over physiological noise, for a certain field strength, depends on several factors as investigated by Bodurka and colleagues (Bodurka et al., 2007). As a consequence, even at 7T, 1.1 mm isotropic fMRI data smoothed by a kernel with FWHM = 3 mm may have lower SNR, and thus be more likely to incur in model over-fitting, compared to the more commonly used $\sim$ 3.5 mm isotropic 3T data smoothed by a kernel with FWHM $\sim$ 6 mm (e.g., (Birn et al., 2014)). However, our analysis of a continuum of spatial scales for the model optimization, from the whole brain down to the voxel level through different numbers (sizes) of spatial clusters, suggests that over-fitting may in fact occur at larger parcel sizes than single $\sim$ 1 mm^3 voxels.

Although the relatively long sampling rate used in our study (TR = 2.5 s) does not alias slow physiological signals such as HR and RV (despite aliasing high-frequency cardiac and respiratory contributions such as the ones reflected in RETROICOR), it reduces the temporal resolution of the VE vs. lag curves potentially hindering their accurate spatiotemporal clustering across the brain. Finally, the relatively short duration (5 min) of the fMRI data runs in our study may

compromise the reliability of the functional connectivity measurements. Nevertheless, the fact that we were able to observe significant effects indicates that the data duration was sufficient for the proposed study. We are currently performing some preliminary tests of our proposed approach on a subset of fMRI data with longer duration (10 min) and, as expected, we can appreciate an increase in the sensitivity to detect seed-based correlations and hence the respective RSN's (results not shown because preliminary in nature as well as because obtained on a different data-set, thus preventing a formal comparison).

Finally, we acknowledge that the sample size of our study (N = 12 subjects) could yield relatively low statistical power. However, it was sufficient to identify the effects of interest in our study, as demonstrated by the effect sizes obtained for the respective statistical tests, usually laying within the large range according to (Cohen, 1988). Future studies using larger sample sizes should nevertheless be conducted in order to further validate the results.

7.6 Conclusions

In this work, we showed that increasing the spatial specificity level of the optimization of RV and HR physiological noise model contributions removes increasingly larger fractions of putative spurious variance from rs-fMRI data. Most critically, we also showed that the impact of the associated physiological noise correction on the ensuing RSN functional connectivity measurements improved from the group to the subject and to the cluster levels of optimization, but deteriorated at the voxel level. Thus, we conclude that, in order to maximize the accuracy of functional connectivity studies, physiological noise correction should account for the individual spatial variability in the time-lags of the RV and HR contributions.

Acknowledgements

The authors would like to thank C. Chang for providing us with the code to implement GS-derived models. This work was funded by FCT grants PTDC/EEI-ELC/3246/2012, PTDC/BBB-IMG/2137/2012, UID/EEA/50009/2013, and NIH grants NIBIB P41-RR014075 and NIBIB K01-EB019474.

8

Cerebral Haemodynamics in Small Vessel Disease

Contents

This chapter briefly describes the application of the methodologies developed in the previous chapters to the study of a group of patients with small vessel disease (SVD). The pathophysiology of the disease will first be overviewed and the methods and results obtained so far will be presented.

The work to be presented in this chapter was developed under the scope of FCT Project NeuroPhysIm, "Non-Invasive Quantitative Imaging of Cerebral Physiology" (PTDC/BBB-IMG/2137/2012, 2013-2015), a joint collaboration between *Instituto de Sistemas e Robótica* (ISR-Lisboa), *Hospital da Luz* and CEDOC - Chronic Diseases Research Center (FCM/UNL). The results presented here were obtained with the collaboration of other members of the Projects' team. This is an ongoing work and the final results are yet to be reached.

8.1 Introduction

8.1.1 Pathophysiology of Small Vessel Disease

Small Vessel Disease (SVD), a recently introduced term that includes all pathological processes that affect the small vessels of the brain regardless of the underlying pathogenesis, has been described as the most common vascular cause of dementia, and generally a major contributor to cognitive decline and age-related disability (Pantoni, 2010; Zwanenburg and van Osch, 2017). In fact, SVD currently accounts for about 20% of all strokes worldwide and 25% of ischaemic strokes, of which about 20% leave the patient disabled (Shi and Wardlaw, 2016). Furthermore, with the ageing of the population the prevalence of SVD is increasing and so are the costs associated with its consequences.

The proper functioning of cerebral small vessels is vital to the provision of oxygen and nutrients. SVD is characterized by a wide range of clinical manifestations from neuropsychological impairments such as depression, cognitive decline, and dementia to physical disabilities including motor and gait disturbances, urinary incontinence, and progressive loss of autonomy to perform daily activities. Nevertheless, since it is such a broad term, SVD encompasses and overlaps with many other well-known pathologies, increasing the interest and curiosity towards understanding the relationship and interaction between these concepts.

SVD includes both ischaemic and hemorrhagic events in small vessels, affecting blood supply and tissue of the deep white and gray matter (GM) areas of the brain (Blair et al., 2017; Pantoni, 2010). SVD can be sporadic (sSVD) or have an hereditary cause. Lesions thought to be instigated by these vessel changes have been assumed as the standard SVD biomarkers. Having those lesions as basis, SVD has been classified in 6 different subtypes (Pantoni, 2010)

- Type 1: Arteriolosclerosis (or age-related and vascular risk-factor-related SVD);
- Type 2: Sporadic and hereditary cerebral amyloid angiopathy (CAA);

- Type 3: Inherited or genetic SVD distinct from cerebral amyloid angiopathy (including Cerebral Autosomal Dominant Arteriopathy with Subcortical Ischaemic strokes and Leukoencephalopathy (CADASIL));
- Type 4: Inflammatory and immunologically mediated SVD;
- Type 5: Venous collagenosis;
- Type 6: Other SVD.

The most prevalent types of SVD are Type 1 and Type 2. Type 1 is characterized by loss of smooth muscle cells from the tunica media, deposits of fibro-hyaline material, thickening of the vessel wall, and narrowing of the lumen (Pantoni, 2010). This type of SVD is highly associated with ageing, diabetes and, in particular, hypertension.

Cerebral amyloid angiopathy (CAA) (Type 2) is characterized by the progressive accumulation of amyloid-peptide in the walls of arteries and arterioles, mainly located in the leptomeningeal space, the cortex and also, in the capillaries and veins.

Type 3, inherited or genetic SVD (distinct from CAA), including CADASIL, offers great opportunities for studies using genetic models as patients often present similar clinical phenotype, usually in the presence of minor age-related changes (Chabriat et al., 2009; O'Sullivan et al., 2001). CADASIL is thought to be an autosomal dominant condition triggered by mutations of the NOTCH3 gene which is the predominant NOTCH receptor in vascular smooth muscle cells, particularly in small brain arteries (Patel and Markus, 2011).

The other types of SVD are rarer. Inflammatory and immunologically mediated SVD (Type 4) is characterized by the presence of inflammatory cells in the vessel's walls. Venous collagenosis (Type 5) is described by the presence of veins and venules with increased thickness, mostly collagen, located next to the lateral ventricles. Type 6 contains other SVD variations such as non-amyloid changes seen in the capillaries and basal membrane in Alzheimer's disease patients and post-radiation angiopathy, a possible side-effect of cerebral irradiation therapy that mainly affects the small vessels of the white matter (WM) that show fibrinoid necrosis by thickening of the wall (Pantoni, 2010).

8.1.2 Cognition Profile in Small Vessel Disease

Studies have shown that SVD groups perform significantly worse than control groups on executive function and processing speed domains (Charlton et al., 2006; Lawrence et al., 2013). Longitudinal studies confirm this pattern, with significant cognitive decline in the executive function. Working memory and processing speed are also declined, but not significantly. Nevertheless, the superior performance of executive function composite measures suggests that it may not be appropriate to use a single domain to characterize the condition (Lawrence et al., 2013).

Furthermore, one cannot exclude the possible overlap between Alzheimer's disease and vascular changes of SVD. When differentiating cognitive profiles of mild cognitive impairment resulting

from SVD and Alzheimer's disease, multiple cognitive domains were impaired in the SVD group, while memory and executive functions were mainly impaired in the Alzheimer's disease group (Zhou and Jia, 2009). Furthermore, SVD group performed worse in processing speed measures. Nevertheless, the cognitive profile in SVD is less specific than in Alzheimer's disease patients (Zhou and Jia, 2009).

Overall, larger sample sizes are required to obtain stronger conclusions. Furthermore, the subjective nature of cognitive profiling in SVD only highlights the importance of alternative approaches to measure cognitive function such as MRI markers.

8.1.3 Imaging Biomarkers of Small Vessel Disease

As introduced previously, SVD is an age-related pathology that affects the small vessels of the brain, leading to progressive cognitive and physical decline (Pantoni, 2010). For that reason, it is of major importance to identify early physiological alterations prior to any irreversible damage. As small vessels are not easily visualized in vivo, neuroimaging biomarkers have focused on the indirect consequences of the pathology, namely in terms of the resulting macroscopic lesions. However, more advanced techniques for imaging cerebral haemodynamics have started to be investigated in order to probe more subtle, but potentially more precocious, alterations.

8.1.3.A Structural Imaging

Current neuroimaging SVD diagnosis is commonly performed by identifying structural lesions secondary to the pathology itself. Conventional image-based markers are retrieved from structural MRI scans such as fluid attenuated inversion recovery (FLAIR) images, double inversion recovery (DIR) images, T_2-weighted images, susceptibility-weighted imaging (SWI) and diffusion weighted imaging (DWI) as well as T_1-weighted images (Figure 8.1).

Common SVD lesions identified by these MRI techniques include recent small subcortical infarcts, white matter hyperintensities (WMH), lacunes, perivascular spaces and cerebral microbleeds (Wardlaw et al., 2013). In particular, WMH, also commonly know as leukoaraiosis or WM lesions, are the most distinctive type of SVD lesions. They are easily recognized as hyperintensities in the WM tissue when using FLAIR and T_2-weighted MRI. Lacunar infarcts are small ovoid infarcts with 3-15 mm in diameter in subcortical regions, consistent with previous small subcortical infarcts or haemorrhagic events in the territory of one perforating arterioles. These lesions can be recognized as hypointensities with hyperintense borders in FLAIR imaging, hyperintensities in T_2-weighted MRI and hypointensities in T_1-weighted imaging. Recent small subcortical infarcts are infarctions in the territory of one perforating arteriole, with imaging features or clinical symptoms consistent with a lesion that occurred a few weeks prior to image acquisition. Their diameter is usually below 20 mm. This type of lesion is best identified using DWI, although it can be also characterized by hyperintensities in FLAIR and T_2-weighted imaging and hypointensities in T_1-weighted imaging. Perivascular spaces are commonly not visible

on conventional neuroimaging, although, if enlarged, they can be recognized as hyperintense regions in T_2-weighted imaging and hypointense in FLAIR and T_1-weighted MRI. In contrast with lacunar infarcts, these lesions appear to not have an hyperintense border and have smaller diameter (usually below 3 mm). Cerebral microbleeds are small areas of signal void, with 2–5 mm in diameter. They are only visible using SWI or T_2^*-weighted gradient-echo sequences (Pantoni, 2010). Other structural image-based markers include a decrease in WM structural and functional integrity assessed by DWI (Croall et al., 2017; Lyoubi-Idrissi et al., 2017)

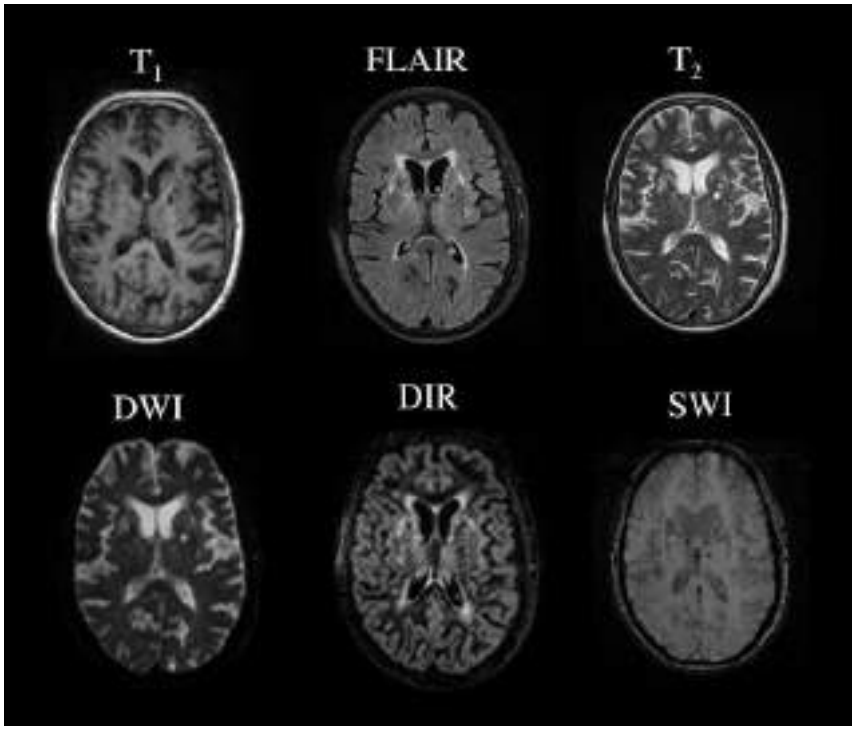

Figure 8.1: Illustrative examples of structural lesions in SVD, as visualized using different types of MRI sequences: FLAIR - fluid attenuated inversion recovery; DWI - diffusion weighted imaging; DIR - double inversion recovery; SWI - susceptibility-weighted imaging.

Several studies have assessed the relationship between structural SVD biomarkers and cognition, although no clear consensus has been reached so far. A review study concluded that the presence of WMH is significantly associated with concomitant cognitive deficits in memory, processing speed, attention, executive function, and perception/construction (Kloppenborg et al., 2014). Furthermore, the progression of WMH is associated with greater cognitive decline, most pronounced in executive functions and attention (Kloppenborg et al., 2014). Another study presented evidence that extensive WMH were associated with impairment in processing speed, memory, and social cognition, while small and moderate WMH barely affected cognition (Kynast et al., 2018). Also recently, it was observed that moderate to severe WMH and lacunar infarcts were associated with a mild impairment of processing speed and executive function in the elderly (Nylander et al., 2018). The correlation between WMH and working and episodic memory has been further investigated, in part because episodic memory is mainly related to areas that

are usually unaffected by WMH (van Leijsen et al., 2018). Although some studies explain this association by the apparent disruptions in WM connections created by WMH that might lead to hippocampal atrophy and subsequent memory decline (van Leijsen et al., 2018), others report no association and interaction between WMH and hippocampal volume with cognition (Legdeur et al., 2019).

Cognitive decline has been shown to be correlated with silent lacunar infarcts in a prospective study (Vermeer et al., 2003). In a multi-predictor analysis, independent predictors of processing speed were the number of lacunar infarcts and brain atrophy (Lawrence et al., 2013). Furthermore, the impact of the number of lacunes on cognition is thought to be region-dependent (Benisty et al., 2009). In particular, silent thalamic infarcts have been shown to be associated with a decline in memory performance, whereas non-thalamic infarcts were associated to a decrease in psychomotor speed (Vermeer et al., 2003). In contrast, another study observed that lacunes in the thalamus were associated with cognitive decline assessed by mini-mental state examination and speed, motor control, and executive functions testing, and lacunes in the putamen/pallidum were negatively associated with memory performance (Benisty et al., 2009). Furthermore, lacunes in the internal capsule, lobar WM, and caudate nucleus were not significantly negatively associated (Benisty et al., 2009).

Microinfarcts have also been correlated with cognitive impairment (Smith et al., 2012). Cortical microinfarcts are thought to be associated with episodic memory, semantic memory, and perceptual speed (Arvanitakis et al., 2011). In contrast, subcortical microinfarcts were not associated with poor cognitive performance (Arvanitakis et al., 2011).

Studies of perivascular space relationship with cognitive impairment in SVD have yielded inconsistent results. A study reported that enlarged perivascular spaces of basal ganglia are associated with a decrease in processing speed, independent of age and WM lesion burden. However, in the centrum semiovale no correlation was observed between enlarged perivascular spaces and cognitive state (Huijts et al., 2014). This different association between these two brain areas was also observed in another study (Hurford et al., 2014). Nevertheless, a more recent study verified that perivascular spaces are not a predictor of cognitive decline (Benjamin et al., 2018).

8.1.3.B Haemodynamic Imaging

Despite SVD diagnosis being commonly performed by identifying structural manifestations, the tissue and wall damage present in SVD disorders is expected to affect functional integrity and architecture of vessels even at an earlier stage. For that reason, recent advances in SVD imaging have been primary focused on haemodynamic imaging methodologies. These include blood-brain barrier leakage by dynamic contrast enhancement MRI as well as imaging of microvascular haemodynamics using fMRI (Blair et al., 2017; Pasi et al., 2016; Wardlaw et al., 2017). The focus of this thesis is on the latter.

Cerebral Blood Flow

In terms of perfusion, most of the studies associate this functional metric with structural biomarkers. In particular, studies have demonstrated a decrease in global, GM and WM cerebral blood flow (CBF) of subjects with severe WMH burden, but this relationship was mainly observed in cross-sectional studies; longitudinal studies yielded conflicting results, as highlighted in a recent systematic review (Shi and Wardlaw, 2016). Furthermore, this relationship was attenuated when excluding subjects with dementia and non-age-matched groups (Shi and Wardlaw, 2016). Nonetheless, while a large study found that high WMH burden predicted decreased CBF at follow-up but low CBF did not predict increased WMHs in the long term (van der Veen et al., 2015), another study observed that low CBF predicted progression of periventricular WMHs only (both phase-contrast MRI studies) (ten Dam et al., 2007). It has also been reported that CBF increases in some regions with WMH progression using positron emission tomography (PET) (Kraut et al., 2008), and that CBF is lower in regions where WMH develop at follow-up (dynamic susceptibility contrast study) (Bernbaum et al., 2015). An ASL study reported a decrease in mean global, subcortical and cortical GM CBF in subjects with diffuse confluent WMH in comparison with subjects with punctiform or beginning confluent WMH (Bastos-Leite et al., 2008), while another associated higher WMH lesion volume with lower GM CBF in adults with mild to severe lesion burden (Crane et al., 2015). More recently, it was observed that lower ASL-derived CBF in normal appearing white matter (NAWM) neighboring WMH regions is associated with expansion of WMH (Promjunyakul et al., 2015, 2016). Furthermore, the CBF values increase from the area immediately surrounding WMH to the outer layers of NAWM, suggesting that the development of WMH is somehow a continuous process (Promjunyakul et al., 2015). Nevertheless, the lower number of capillaries in WM regions than in GM, the slower dynamics of CBF, and the existence of watershed areas may in fact lead to greater sensitivity of WM to changes in CBF (Brown et al., 2018).

Cerebrovascular Reactivity

Cerebrovascular reactivity (CVR) has been studied in SVD patients using BOLD-fMRI in combination with different vascular challenges. Nevertheless, results are still insufficient to determine a clear relationship (Blair et al., 2017), perhaps due to the different types of patients studied, small sample sizes or the multitude of vasoactive stimuli and post-processing tools involved. Some studies show an association between decreased CVR and increased WMH, when using CO_2 challenge and hyperventilation as vasoactive stimuli (Hund-Georgiadis et al., 2003; Yezhuvath et al., 2012) and with the presence of microbleeds when using a breath-hold (BH) task (Conijn et al., 2012). However, others report no association between these structural markers and CVR assessed by CO_2 challenge and BH task (Conijn et al., 2012; Gauthier et al., 2015; Richiardi et al., 2015). A longitudinal study using acetazolamide demonstrated that impaired baseline CVR is associated with larger increase of WMH after several years, but not with larger

increase of lacunar infarcts or microbleeds (Liem et al., 2009). Studies using CO_2 manipulation as vasoactive stimulus reported lower CVR in areas of NAWM that became WMH in the follow-up (Sam et al., 2016b) and negative CVR being associated with lower CBF and microstructural damage (Sam et al., 2016a). One study used ASL and found that lower CVR was also associated with increased number of lacunes and brain atrophy in CADASIL patients (Moreton et al., 2018). In this same study, subjects with depressive symptoms, disability or delayed processing speed also displayed a trend towards lower CVR.

Studies using visual stimulus showed a decrease in the occipital lobe BOLD fMRI amplitude and timing response in CAA patients compared to healthy subjects, although baseline CBF remained similar between groups (Dumas et al., 2012). Interestingly, this impaired BOLD response occurred before the onset of clinical symptoms of the disease (van Opstal et al., 2017) and progressively declined over time (Switzer et al., 2016). Nevertheless, others report that, in contrast with CAA reports, the amplitude of BOLD response to the visual stimulus of CADASIL patients increases (Cheema et al., 2017), although this increase may reflect compensatory mechanisms for injury (Cheema et al., 2017).

Resting-State Haemodynamic Fluctuations

Some studies suggest that alterations of spontaneous BOLD fluctuations in SVD patients might be useful for the characterization of this pathology. Makedonov et al. investigated voxelwise fluctuations on the whole power spectrum of the fluctuations as well as on a specific frequency, the cardiac frequency (cardiac pulsatility). Statistically significant differences in NAWM measures between young controls, elderly controls and SVD patients, using both metrics, were observed, with the latter group yielding the highest values. Furthermore, within the SVD group, a significant reduction of the two metrics in WMH compared to NAWM was also found, with cardiac pulsatility presenting an increased sensitivity to differentiate WMH lesions from NAWM (Makedonov et al., 2016).

Another study focused on the BOLD low-frequency (0.01 - 0.8 Hz) fluctuations of CADASIL patients and a healthy control group (Wang et al., 2017). Results showed significantly reduced values of ALFF in the bilateral precuneus for the CADASIL group. Furthermore, several other areas revealed greater values of ALFF for the CADASIL group, including the bilateral anterior cingulate gyrus/corpus callosum, left insula/temporal pole and the bilateral midbrain/pons. No significant correlations were found between ALFF and normalized WMH volume (Wang et al., 2017).

Arterial Stiffness and Pulsatility

Arterial stiffness, SVD and cognitive impairment were investigated systematically by van Sloten and colleagues (van Sloten et al., 2015), using carotid-femoral pulse wave velocity (PWV), brachial-ankle PWV, local distensibility measurements of the carotid artery, and pulse pressure

as markers of arterial stiffness. There was an association between increasing arterial stiffness and SVD markers (WMH, cerebral microbleeds, and lacunar infarcts), although studies on cognitive impairment could not be pooled due to large heterogeneity. Nevertheless, some studies showed an association, although relatively weak, between greater stiffness and cognitive impairment. Indices of arterial stiffness (assessed by PWV) and atherosclerosis (as measured by carotid-intima media thickness load) were associated with more lacunes and atrophy in CADASIL patients (Moreton et al., 2018). Regarding blood pressure, the Discontinuation of ANti-hypertensive Treatment in the Elderly (DANTE) study, comprising 203 subjects (Foster-Dingley et al., 2015), demonstrated that there is no association between CBF (measured by ASL) and blood pressure in older cognitively impaired subjects, despite hypertension being one of the strongest risk factors for SVD.

It is thought that increased arterial stiffening reduces damping of the arterial waveform and hence will cause higher pulsatile energy transmission further down the vascular network, potentially damaging small vessels (Makedonov et al., 2013). Arterial pulsatility in SVD was reviewed by Shi and colleagues, summarizing results from 20 Doppler ultrasound and 7 phase-contrast MRI studies (Shi et al., 2018). Those studies only assessed pulsatility in larger arteries and there were substantial variations in the methodological aspects across them, including pulsatility metrics. Furthermore, most of the studies did not report or include potential confounders such as age in their analysis. Nevertheless, most of the studies supported an association between higher pulsatility in large intracranial arteries and SVD (Shi et al., 2018). It should be noted that it has been shown recently in rodents that the fluid flow through the glymphatic system, also known as perivascular pumping, is driven by arterial pulsatility from the cardiac cycle (Kiviniemi et al., 2016; Mestre et al., 2018). This pumping is reduced in hypertension, possibly due to changes in vessel dynamics, including increased backflow and changes in the arterial wall motion waveform, decreasing the CSF net flow in perivascular spaces (Mestre et al., 2018). More recently, a 2D phase-contrast MRI at 7T was also employed to assess CBF pulsatility in small cerebral perforating arteries. Despite the non-significant differences in CBF velocities, the pulsatility index in the SVD group was higher than in the control group for both regions (Geurts et al., 2019).

8.1.4 Objectives

Although a growing number of studies have started to explore advanced MRI techniques for probing cerebral haemodynamics in SVD, their value as disease biomarkers remains unclear. One of the limitations is the variability of methods used in the literature, while very few have simultaneously assessed more than one haemodynamic parameter.

In this study, we aim to evaluate the potential of completely non-invasive MRI techniques for imaging different aspects of cerebral haemodynamics to provide sensitive biomarkers of SVD. For this purpose, we studied a group of SVD patients using the following techniques: multiple-delay ASL for measuring baseline CBF; BOLD-fMRI combined with breath-holding for measuring CVR; and resting-state BOLD-fMRI for measuring spontaneous haemodynamic fluctuations

potentially related with arterial stiffness and pulsatility.

8.2 Materials and Methods

8.2.1 Data Acquisition

Demographic and Clinical Data

A group of SVD patients including eleven patients with sporadic SVD (sSVD) and six patients with a genetic form of SVD (CADASIL) was recruited from *Hospital Egas Moniz* Neurology Outpatient Clinic between 2015-2016. Twelve age-matched healthy volunteers, without relevant medical history, were also recruited for comparison purposes. All subjects provided informed consent and the study was approved by the local ethics committee.

During recruitment, SVD patients were clinically examined by a neurologist in order to verify all inclusion and exclusion criteria, and to register demographic and other relevant factors such as history of previous stroke, hypertension, blood pressure, hypercholesterolaemia, diabetes, and smoking.

Inclusion criteria included independence in daily activities as assessed by the Instrumental Activities of Daily Living (IADL) scale (Lawton and Brody, 1969) and absence of hemodynamic significant large vessel disease by Doppler ultrasound. Specifically for the sSVD group, criteria included presence of deep WMH lesions without any other plausible explanation, with moderate and severe degrees according to Fazekas scale (Fazekas et al., 1987). For the CADASIL group, patients had to be symptomatic with evidence of WMH lesions and molecular diagnosis confirmed by mutation on the NOTCH3 gene.

Exclusion criteria included contraindications for MRI acquisition, evidence of WMH lesions from other known aetiology, presence of concurrent chronic incapacitating disorders, stroke in the past three months, illiteracy and visual acuity compromise.

SVD patients also performed a comprehensive battery of neuropsychological assessments, testing four predefined cognitive domains of interest: executive function, processing speed, working memory and long-term memory. For each of the domains the corresponding tests were (Buffon et al., 2006; Zhou and Jia, 2009):

1. Executive function (EF) - Stroop interference (total interference score) and Trail making test part B (time to complete);
2. Processing speed (PS) - Trail making test Part A (time to complete);
3. Working memory (WM) - Wechsler Adult Intelligence Scale III (digit span);
4. Long-term memory (LTM) - Wechsler Memory Scale III (immediate recall learning (delayed recall) and percentage of retention).

Imaging Data

MRI acquisition was performed according to an optimized and standardized protocol. Whole-brain images were acquired on a 3T Siemens Verio scanner using a 12-channel radio-frequency receive coil in Hospital da Luz, including the following images (among others not considered for this study): T_1-weighted structural image collected using an MPRAGE sequence with TR/TE = 2250/2.26 ms and 1 mm^3 isotropic resolution; FLAIR image with TR/TE = 8500/97 ms and 0.69 × 0.69 × 3 mm^3 resolution; DIR with TR/TE = 7500/334 ms and 1.35 mm^3 isotropic resolution; SWI with TR/TE = 28/20 ms and 0.6 × 0.6 × 1.4 mm^3 resolution. Functional images were also acquired, including:

1. CVR imaging: BOLD-fMRI acquired using a 2D multi-slice gradient echo - echo planar imaging (GE-EPI) sequence during a BH task, with TR/TE = 2500/30 ms, 40 contiguous slices, 3.5 × 3.5 × 3.0 mm^3 resolution, 132 volumes;

   The optimized BH protocol consisted of 3 cycles of a 15 s BH after inspiration, alternated with normal breathing following inspiration/expiration auditory cues, as illustrated in Figure 8.2, delivered to the subject using MR-compatible NordicNeuroLAb AudioSystem (headphones, https://www.nordicneurolab.com).

Figure 8.2: Breath-Hold protocol applied during BOLD-fMRI acquisition: the instructions indicated in each box were provided to the subject using auditory cues.

2. rs-fMRI imaging: BOLD-fMRI acquired using a GE-EPI during resting-state with eyes open (∼ 6.5 min), with TR/TE = 2500/30 ms, 40 contiguous slices, 3.5 × 3.5 × 3.0 mm^3 resolution, 132 volumes;

3. Baseline CBF imaging: multiple inversion time (multiple-TI) PASL fMRI acquired using a PICORE-Q2TIPS (Luh et al., 1999) sequence, with 2D multi-slice GE-EPI readout and with TR/TE = 2500/11 ms, 28 contiguous slices, 3.5 × 3.5 × 5.0 mm^3 resolution. Data were sampled at 11 TI values (400 – 2400 ms in steps of 200 ms), with 8 control-label pairs for each TI value, and slice acquisition time of 36 ms. The Q2TIPS module allows limiting the labeling to a maximum of 750 ms by adjusting TI1 and TI1s for each TI: for TI < 1000 ms, TI1 = TI1s = TI-25 ms; and for TI > 1000 ms, TI1 = 750 ms and TI1s = 900 ms.

Pressure of End-Tidal Carbon Dioxide

During the imaging acquisition, $PETCO_2$ levels were recorded using a capnograph (Cap10 Capnograph, Medlab GmbH - Figure 8.3) connected to a nasal cannula as well as to a computer through an Arduino board. $PETCO_2$ traces were processed using MATLAB tools, in order to obtain $PETCO_2$ levels at each exhalation. The signal was interpolated, low-pass filtered, underwent peak detection and convolution with a canonical HRF. The time delay between imaging signal and the $PETCO_2$ timecourses was estimated by detecting the peak cross correlation between the two signals. The variation of $PETCO_2$ with BH, $\Delta PETCO_2$, was computed as the difference between the first $PETCO_2$ value after the BH period and the average across the baseline period (before the BH). For each subject, the average across the three BH cycles was computed.

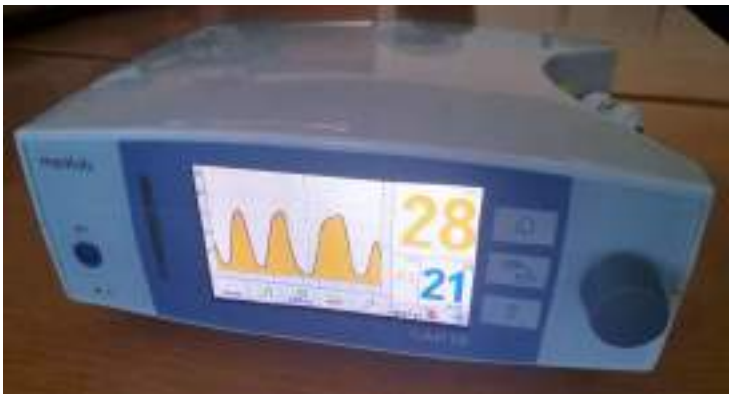

Figure 8.3: Capnograph monitor displaying $PETCO_2$ levels (CAP10 Capnograph; Medlab, Germany).

8.2.2 Data Analysis

Structural Imaging

Structural images were brain-extracted using the FSL brain extraction tool (BET) (Smith, 2002). In some of the subjects, center of the brain coordinates were set manually after careful visual inspection.

Co-registration of images and masks belonging to the same subject was performed using FSL's FLIRT (Jenkinson and Smith, 2001; Jenkinson et al., 2002). Co-registration between images or masks of different subjects was achieved using the non-linear registration of tools of the software ANTs (`http://stnava.github.io/ANTs/`).

The FLAIR images were manually segmented in order to obtain masks of WMH lesions. The WMH lesion load (NWMHLL) was subsequently estimated as the WMH lesion volume normalized by whole-brain volume in percentage. This normalized brain tissue volume (NBV), normalized for subject head size, was estimated by applying FSL's SIENAX tool on the MPRAGE images (Smith et al., 2002, 2004). The previously defined WMH lesion masks were also used as input in order to minimize GM misclassification. Total brain volume was computed as the sum

of GM and WM volumes. Furthermore, a experienced rater classified the number of microbleeds on the SWI images, following the Microbleed Anatomical Rating Scale (MARS) criteria (Gregoire et al., 2009). The same rater also classified the lacunes as areas of tissue lost with cavitation of 0.3-1.5 cm of diameter on T_1-weighted images. An illustrative example of the five tissue masks is shown in Figure 8.4.

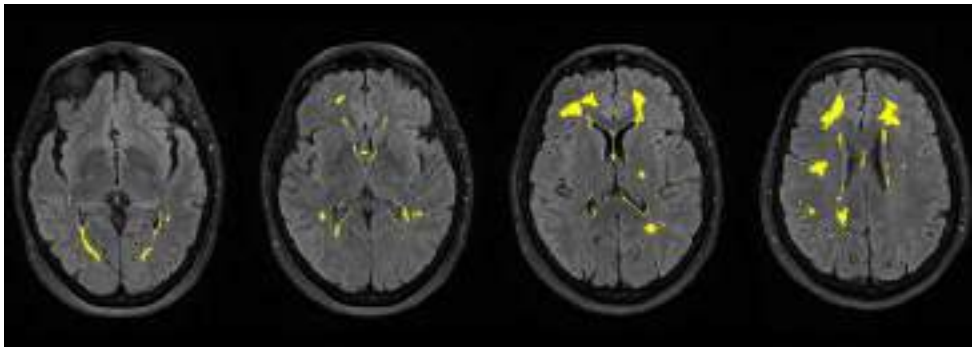

Figure 8.4: Four illustrative axial slices displaying the manual WMH segmentation (yellow) overlaid on corresponding the FLAIR images, for one subject.

Segmentation of brain tissue was performed on the MPRAGE images using FSL's FAST tool, yielding masks of GM, WM and CSF (Zhang et al., 2001). Subcortical structures were further segmented using FSL's FIRST (Patenaude et al., 2011).

Five brain regions masks were then obtained for each patient (Figure 8.5), including (i) lateral ventricles (LV) mask, obtained from the intersection between the CSF mask and a ventricles mask obtained from the MNI atlas; (ii) WM hyperintensities (WMH) mask, which resulted from the subtraction of the LV mask to the WM lesions segmented from the FLAIR image; (iii) subcortical GM (sGM) mask, which is the result of the output of FIRST segmentation without the brainstem, the CSF and the WMH mask; (iv) cortical GM (cGM) mask, obtained by subtracting from the GM segmented using FAST the CSF, all the subcortical structures and the WMHs; and (v) NAWM mask, which resulted from the subtraction of the brainstem and all the previously mentioned masks to the WM from FAST.

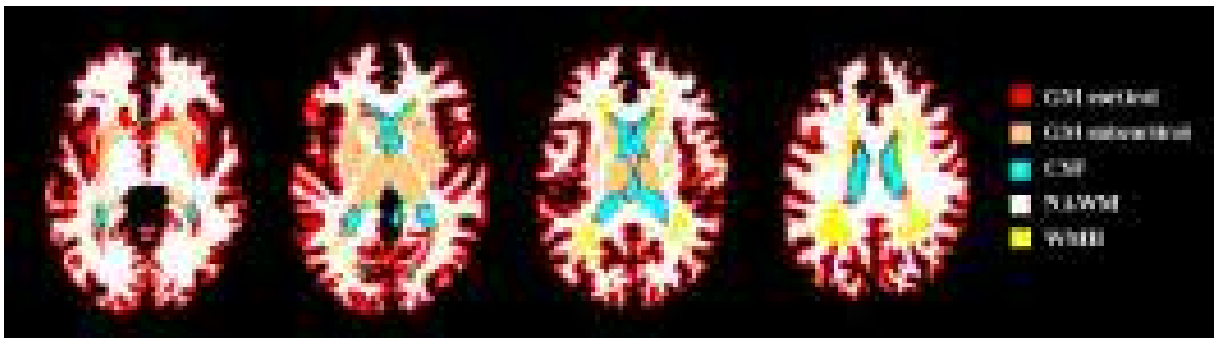

Figure 8.5: Illustrative example of tissue segmentation in the structural space.

Cerebral Blood Flow

The multiple-TI PASL images were aligned with each other by motion correction using FSL's MCFLIRT (Jenkinson et al., 2002). At each TI, the control images and the pairwise differences between control and label images were averaged across repetitions, yielding time series of mean control images and mean magnetization difference images as a function of TI. Additionally, off-resonance effects caused by imperfect inversion slice profile in 2D multi-slice imaging were corrected (Figueiredo et al., 2005). An extended kinetic model was fitted to difference images, yielding maps of relative CBF, aBV and ATT (Chappell et al., 2010). Since the Q2TIPS PASL acquisition sequence includes a presaturation pulse (Luh et al., 1999), derivation of the equilibrium magnetization of tissue (M_{0t}) map was achieved using the saturation recovery approach (Chapter 4 (asl_calib, https://fsl.fmrib.ox.ac.uk/fsl/fslwiki/BASIL/, also estimating presaturation efficiency)). Calibration was then performed voxelwise, deriving the equilibrium magnetization of arterial blood (M_{0a}) map by smoothing M_{0t} (Gaussian kernel, FWHM = 10.5 mm) and using a brain average brain-blood water partition coefficient (λ) (0.9). For each parameter, average values were computed across GM (sGM and cGM) and NAWM ROIs.

Cerebrovascular Reactivity

BH BOLD fMRI pre-processing steps included correction of EPI distortions due to magnetic field inhomogeneities using a B_0 field mapping approach (FSL's FUGUE, https://fsl.fmrib.ox.ac.uk/fsl/fslwiki/FUGUE/), removal of non-brain tissues using FSL's BET (Smith, 2002), head motion correction using FSL's MCFLIRT (Jenkinson et al., 2002), spatial smoothing using a Gaussian kernel of 5 mm FWHM and high-pass temporal filtering (frequency cutoff = 100 s). For response modeling, a general linear model (GLM) approach was used using FEAT (Woolrich et al., 2001), including as regressors of interest a sine and a cosine at the task frequency and corresponding 1^{st} harmonics as well as the motion regressors estimated with MCFLIRT (Figure 8.6).

Voxelwise maps were derived for two CVR metrics: amplitude (PSC), computed as the percent signal change normalized by the corresponding tissue mask baseline average period (the initial 25 s period was used as the baseline for temporal averaging, and the GM and WM ROIs were used as the tissue masks for spatial averaging) and the time-to-peak (TTP), defined as the difference between the first maximum timepoint after the BH period and beginning of the BH period. Both PSC and TTP were averaged across the GM (sGM and cGM) and NAWM regions.

Amplitude of Spontaneous Fluctuations

BOLD resting-state fMRI pre-processing steps were similar to the ones performed for CVR assessment: correction of EPI distortions using a field mapping approach (FSL's FUGUE, https://fsl.fmrib.ox.ac.uk/fsl/fslwiki/FUGUE/), removal of non-brain tissues using

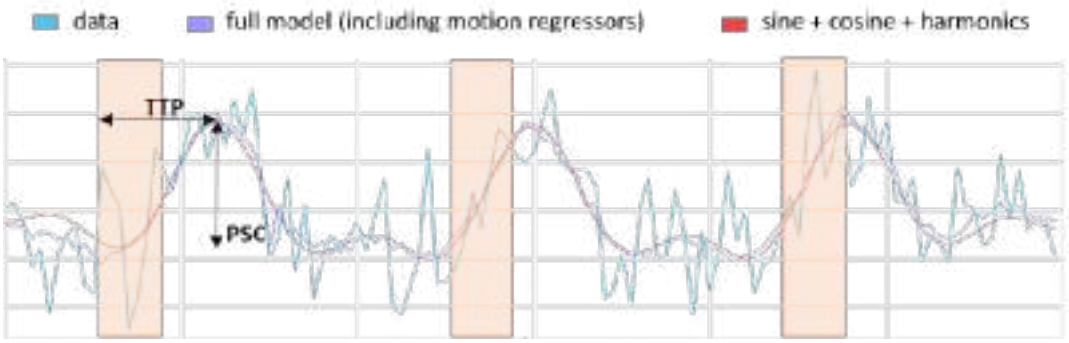

Figure 8.6: Illustrative time-courses depicting BOLD fMRI data and corresponding regressors, from one GM voxel of one illustrative subject. The orange boxes indicate the BH periods.

FSL's BET (Smith, 2002), head motion correction using FSL's MCFLIRT (Jenkinson et al., 2002) and spatial smoothing using a 5 mm Gaussian kernel. Additionally, motion outliers were detected using FSL tool Motion Outliers and subsequently, a GLM was fitted to the data (FEAT) (Woolrich et al., 2001), using as regressors the outliers previously detected as well as the six motion regressors estimated with MCFLIRT, and a second-order polynomial, removing low-frequency artifacts associated with scanner drifts.

The ALFF metric was then computed. Steps included the conversion of the BOLD fMRI to percent signal change through division by the average signal over time in each voxel, computation of the signal's fast fourier transform (FFT) and the computation of power spectrum as the square of the amplitude of each frequency component divided by the length of the signal. Consequently, ALFF was given by the calculation of the square root of the power spectrum for a specific frequency range. Voxelwise maps were derived and average values were calculated across the GM and NAWM masks.

8.3 Results

Demographic and Clinical Data

Demographic data of interest is summarized in Table 8.1, whereas relevant clinical information is depicted in Table 8.2. SVD patients were significantly less educated than healthy subjects ($p<0.001$); other demographic variables were not significantly different across groups. Moreover, the number of hypertensive sSVD patients was significantly higher than for the CADASIL group ($p=0.02$). Other clinical variables did not show significant differences between SVD groups.

Table 8.2: Summary of clinical data of SVD patients. Significant group comparisons are depicted with * ($p<0.05$).

	SVD (N = 15)	sSVD (N = 11)	CADASIL (N = 4)
Hypertension (# of subjects)*	10	9	1
Systolic BP (mmHg)	134 ± 20	133 ± 21	135 ± 22
Diastolic BP (mmHg)	79 ± 14	788 ± 16	79 ± 12
Diabetes Mellitus (# of subjects)	1	1	0
Hypercholesterolaemia (# of subjects)	9	7	2
Previous Stroke (# of subjects)	4	2	2
Smoker (# of subjects)	5	4	1
History of depression (# of subjects)	8	6	2

Table 8.1: Summary of demographic data of all subjects. Significant group comparisons are depicted by * ($p<0.05$).

	SVD (N = 17)	sSVD (N = 11)	CADASIL (N = 6)	Healthy Subjects (N=12)
Age (years)	50 ± 9	52 ± 7	47 ± 11	52 ± 6
Gender (# females)	13	9	4	6
Education (years) *	10 ± 6	11 ± 5	10 ± 6	17 ± 4

The cognitive profile of the SVD patients is summarized in Table 8.3. One patient was unable to perform the cognitive evaluation. All cognitive functions were significantly impaired compared to the expected performance for a healthy population, assessed using T-tests ($p<0.05$). In contrast with previous reports, where executive function and processing speed are described as the most impaired cognitive domains in SVD, in this cohort working-memory was the cognitive function yielding the worst results (Zhou and Jia, 2009). For each patient, the correspondent percentile score values were converted into z-scores considering normative data for the Portuguese population, except for the TMT (where an online interface was used for this purpose (Cavaco et al., 2013)). Furthermore, for both EF and LTM a composite score was computed, combining the z-scores of the corresponding tests.

Table 8.3: Cognitive profile analysis of SVD patients: average cognitive scores of executive function, processing speed, working memory, and long-term memory domains.

	Cognitive Domain			
	Executive Function	Processing Speed	Working Memory	Long-term Memory
Mean ± Standard Deviation	-0.47 ± 0.77	-0.83 ± 0.73	-1.08 ± 0.27	-0.26 ±0.46

Table 8.4: Neuroimaging features extracted from structural images: group mean values (± standard deviation) are presented for NBV and NWMHLL, while mean and range are presented for nCMB and nLac since the latter were not normally distributed. Significant differences between groups are depicted with * ($p<0.05$). NBV = Normalised brain volume; nCMB = Number of cerebral microbleeds; nLac = Number of lacunes; NWMHLL = Normalized white matter hyperintensities lesion load

	SVD (N=17)	**CADASIL (N=6)**	**sSVD (N=11)**	**Healthy Subjects (N=12)**
NBV (cm^3) *	1506 ± 72	1551 ± 50	1481 ±72	1451 ± 67
nCMB [range]	1.82 [0-20]	3.5 [0-20]	0.91 [0-4]	-
nLac [range]	0.53 [0-4]	1.5 [0-4]	0	-
NWMHLL (%) *	3 ± 2	4 ± 3	2 ± 1	0.05 ± 0.07

Structural Imaging

Table 8.4 summarizes the features extracted from the structural images. NBV was marginally but significantly higher in SVD patients compared to healthy subjects ($p=0.045$). As expected, SVD patients exhibited a higher WMH lesion load compared to controls ($p<0.001$). Moreover, CADASIL patients manifested a relatively higher lesion load compared to sSVD ($p=0.04$). Our patient cohort exhibited low number of nCMB and nLac compared to previous reports (Croall et al., 2017; Zeestraten et al., 2017). For this reason, further analyses did not include these features.

Pearson correlation analysis between the neuropsychological scores in each of the four cognitive domains and the structural imaging covariates considered (NBV and NWMHLL) as well as age was performed. Only NBV exhibited significant correlation with the executive function domain ($p = 0.016$).

Pressure of End-Tidal Carbon Dioxide

The average $\Delta PETCO_2$, across the three BH cycles, was 8.0 ± 1.8 for healthy subjects and 7.3 ± 2.7 for SVD patients. No statistical significant differences were observed between the two groups.

Cerebral Blood Flow

An illustrative example of the CBF, aBV, and ATT maps obtained for one patient is presented in Figure 8.7.

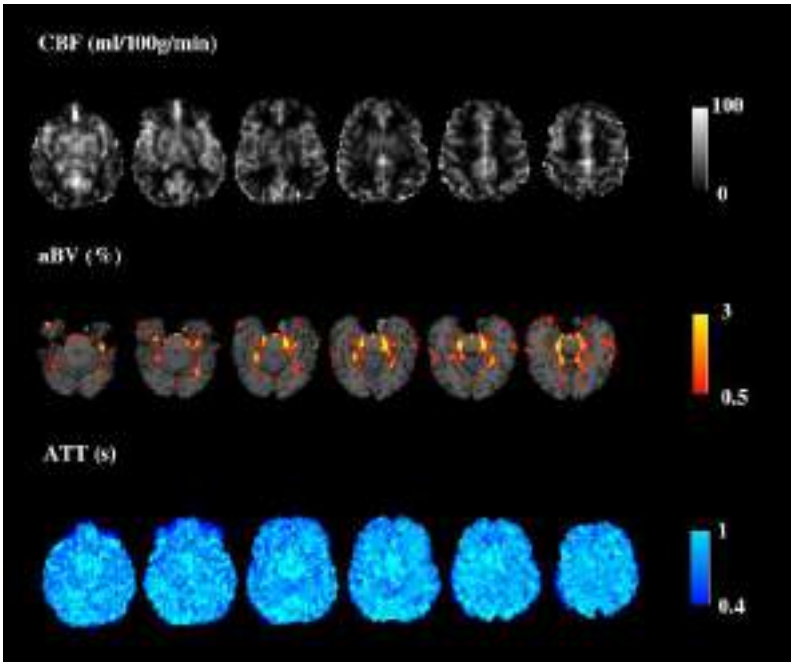

Figure 8.7: llustrative example of the CBF (top), aBV (middle) and ATT (bottom) maps obtained for one patient in the structural space. The aBV map overlays the corresponding T_1-weighted structural image. Illustrative slices covering the lower part of the brain with higher density of arterial component are shown for aBV.

Average maps of CBF, aBV and ATT for healthy subjects are depicted in Figure 8.8. The corresponding maps for SVD patients are displayed in Figure 8.9.

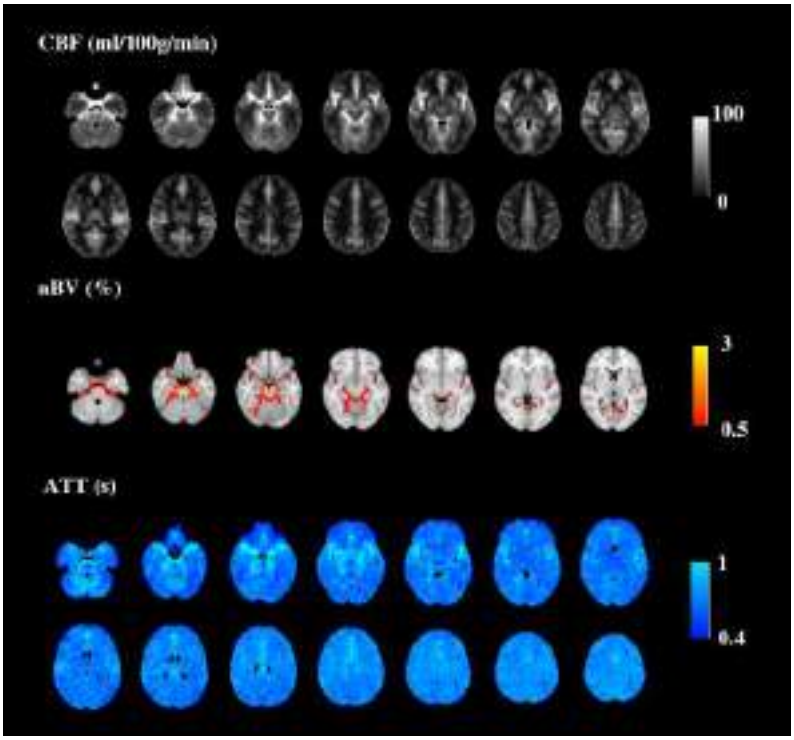

Figure 8.8: Average maps of CBF (top), aBV (middle) and ATT (bottom) for healthy subjects. The aBV map overlays the MNI152 image. Illustrative slices covering the lower part of the brain with higher density of arterial component are shown for aBV.

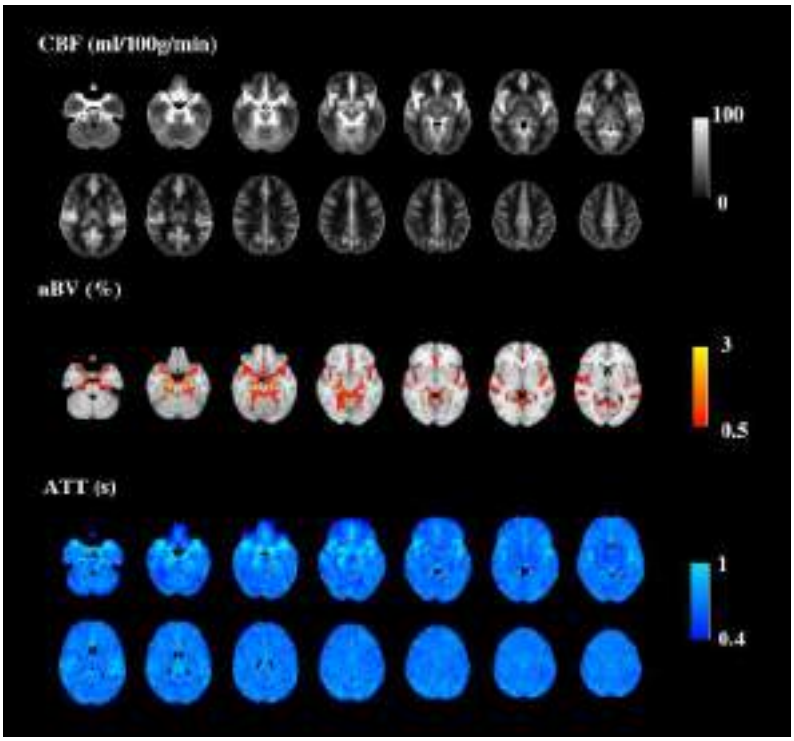

Figure 8.9: Average maps of CBF (top), aBV (middle) and ATT (bottom) for SVD patients. The aBV map overlays the MNI152 image. Illustrative slices covering the lower part of the brain with higher density of arterial component are shown for aBV

Figure 8.10 shows the boxplots representing the distributions of CBF and ATT values across GM and NAWM for healthy subjects and SVD patients. aBV average values are not displayed due the difficulty of defining an appropriate ROI. Statistical main effects were observed for the type of ROI (GM vs NAWM) (two-way ANOVA, with group as between subject factor, $p<0.001$) with GM regions having higher CBF and ATT than NAWM. No statistically significant differences were observed between groups.

Pearson correlation analysis between the scores in each of the four cognitive domains and each of the CBF metrics considered (CBF, aBV, and ATT in GM and NAWM) for SVD patients showed no statistically significant correlations.

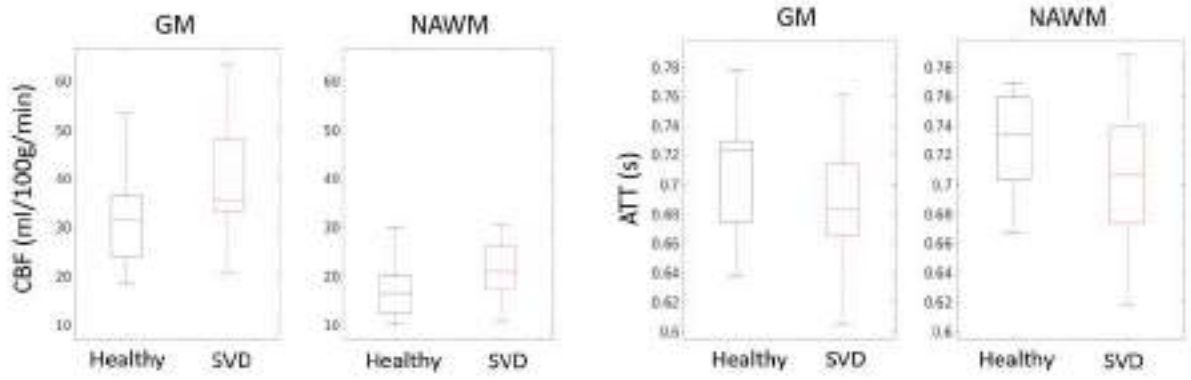

Figure 8.10: Boxplots representing the distributions of CBF and ATT values across GM and NAWM for healthy subjects and SVD patients. The central mark indicates the median; the upper and lower edges of the box correspond to the 25^{th} and 75^{th} percentiles, respectively; and the dots correspond to outliers.

Cerebrovascular Reactivity

An illustrative example of the CVR amplitude (PSC) and delay (TTP) maps for one patient is presented in Figure 8.11.

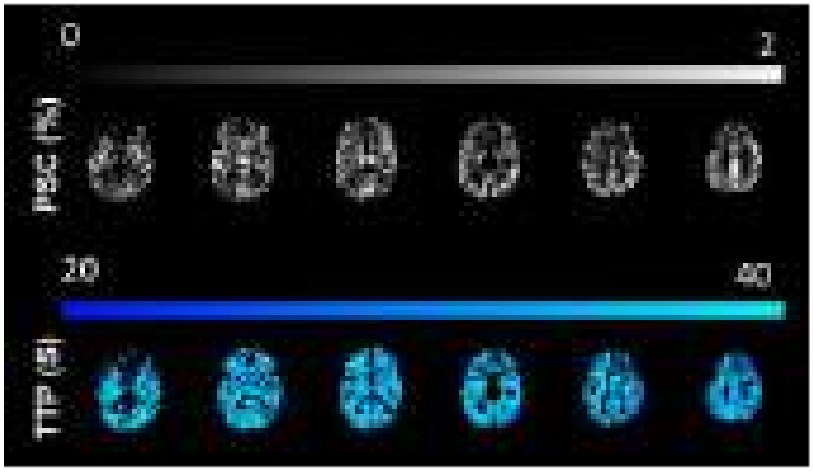

Figure 8.11: Illustrative example of the CVR PSC and TTP maps for one patient. PSC and TTP are only showed for voxels exhibiting significant BOLD-fMRI changes.

Average maps of CVR PSC and TTP for healthy subjects and SVD patients are depicted in Figures 8.12 and 8.13, respectively.

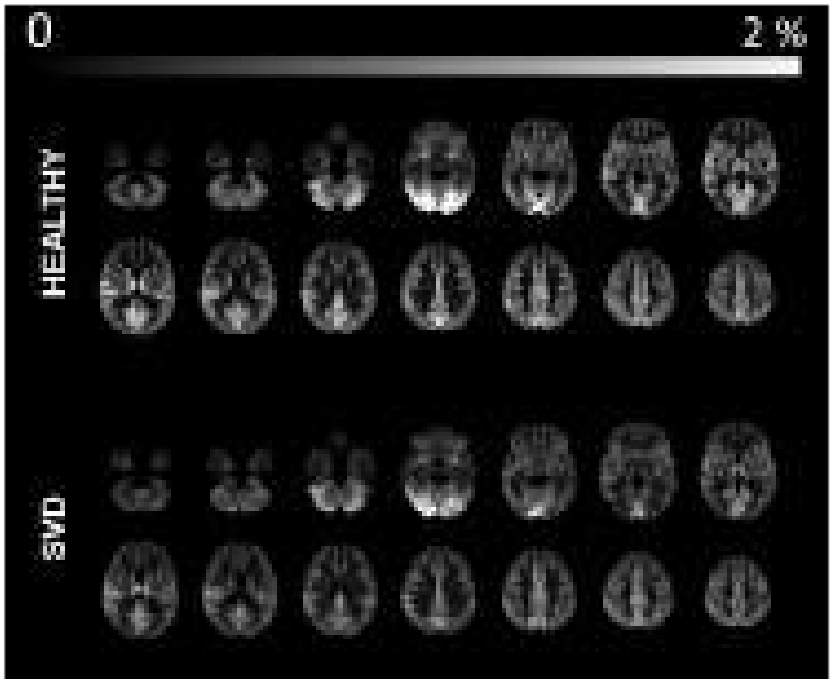

Figure 8.12: Average maps of CVR amplitude (PSC) (Healthy subjects - top and SVD patients - bottom).

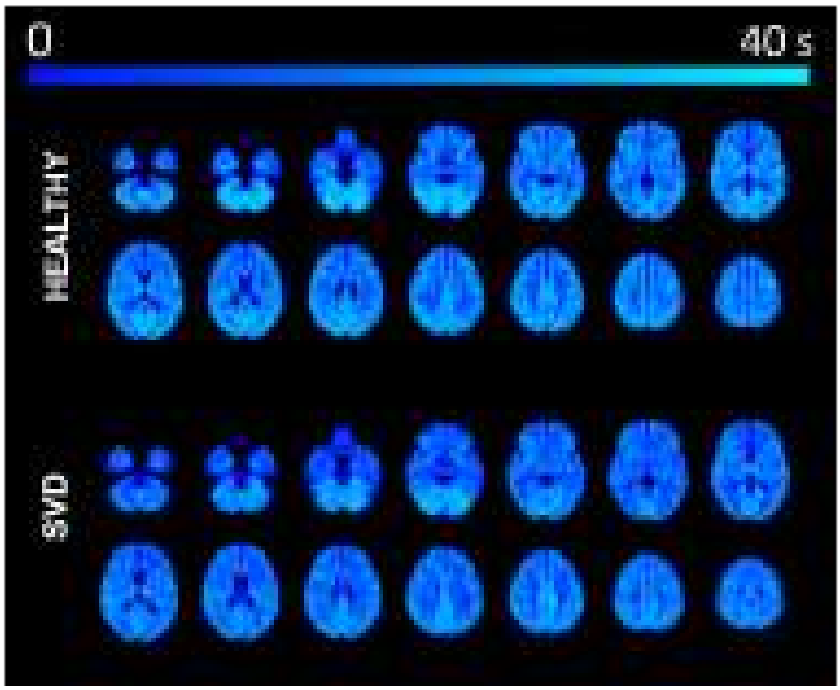

Figure 8.13: Average maps of CVR delay (TTP) (Healthy subjects - top; SVD patients - bottom).

Figure 8.14 shows the boxplots representing the distributions of CVR PSC and TTP values across GM and NAWM for healthy subjects and SVD patients. A statistically significant main effect was also observed for the type of ROI (GM vs NAWM) (two-way ANOVA, with group as between subject factor, $p<0.001$), with GM regions having higher PSC and lower TTP than NAWM regions. No statistically significant differences were observed between groups.

Pearson correlation analysis between the scores in each of the four cognitive domains and each of the CVR metrics considered (CVR and TTP in GM and NAWM) for SVD patients showed no statistically significant correlations.

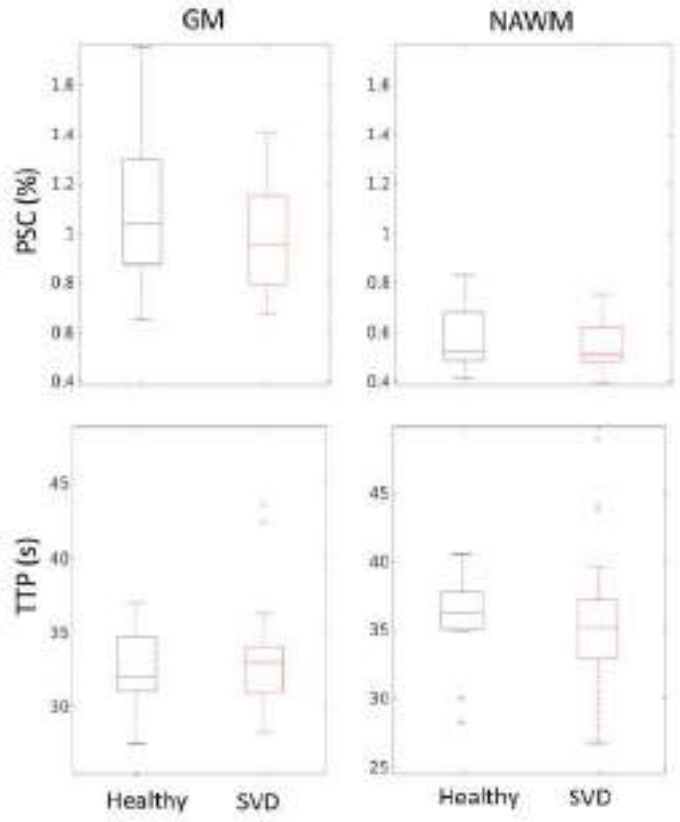

Figure 8.14: Boxplots representing the distributions of CVR amplitude (PSC, top) and delay (TTP, bottom) across GM and NAWM for healthy subjects and SVD patients. The central mark indicates the median; the upper and lower edges of the box correspond to the 25^{th} and 75^{th} percentiles, respectively; and the dots correspond to outliers.

Amplitude of Spontaneous Haemodynamic Fluctuations

The mean power spectrum (PS) of one illustrative subject was plotted and analyzed for several ROIs (GM, LV and NAWM) (Figure 8.15). Subsequently, a visual inspection was performed in order to confirm that the peaks were not intersected by frequency bands' limits imposed.

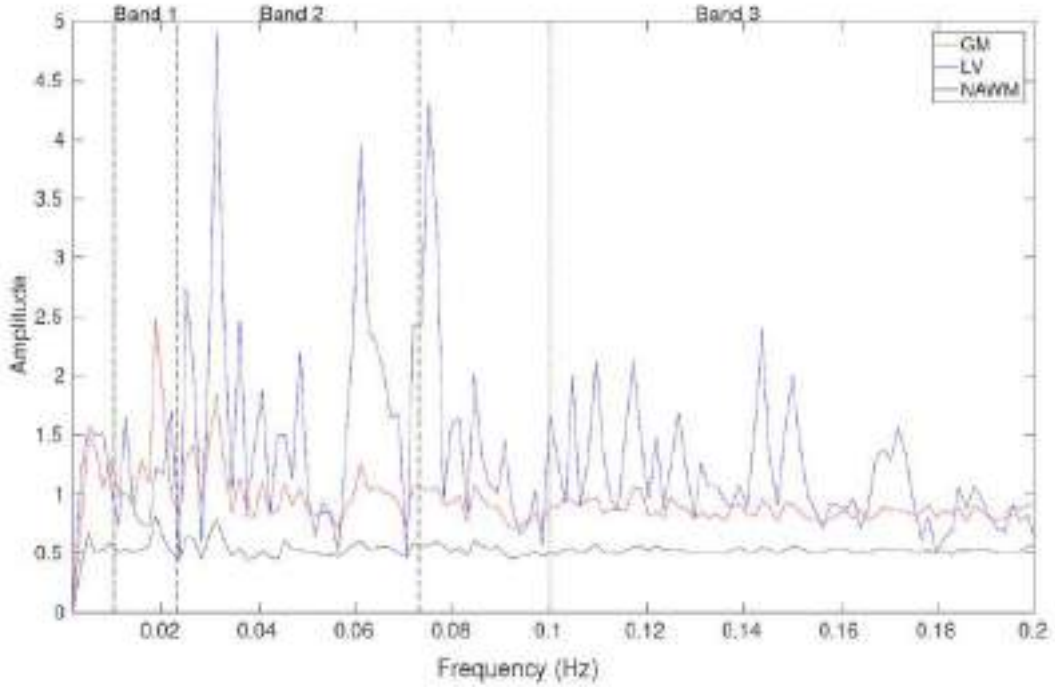

Figure 8.15: Mean power spectrum of rs-fMRI BOLD timecourses from GM, LV and NAWM from one illustrative subject. The red dashed line delimits the typical low-frequency range in rs-fMRI analysis, whereas the black dashed lines indicate the limits of the three frequency bands of interest.

The aforementioned figure shows that distinct regions of the brain display different dominant frequencies of spontaneous BOLD fluctuations. While GM regions are mainly dominated by low-frequency fluctuations, presumably mostly of neuronal origin, WM and the LV display mainly contributions arising from higher frequency fluctuations, presumably of physiological origin. In particular, GM is characterized by higher amplitudes within band 1, the lateral ventricles show higher amplitudes distributed across the entire frequency range but predominantly in bands 2 and 3 and the NAWM presents a distribution of power more constant across all frequency ranges, although with a slightly higher contribution from band 1. Results were generally consistent in all subjects.

An illustrative example of the ALFF maps for one patient is presented in Figure 8.16.

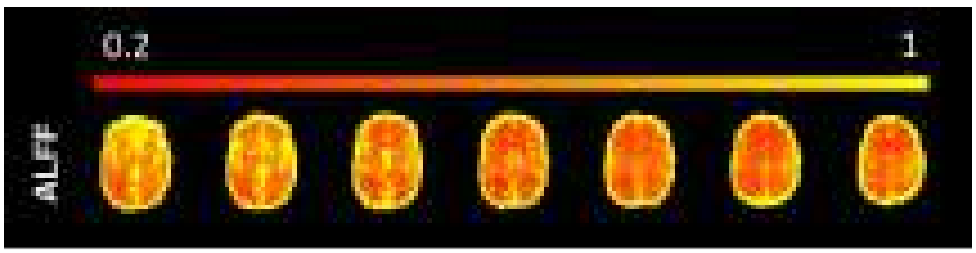

Figure 8.16: Illustrative example of the ALFF map for one patient.

Figure 8.17 shows the ALFF maps, averaged across all patients, displaying the distribution of each metric across the brain. No considerable differences are noted in ALFF's spatial dis-

tributions between the groups. To be noted that the total power of each voxel, corresponding to the ALFF metric applied to the entire frequency spectrum, includes physiologic fluctuations that arise from cardiac and respiratory sources, clearly noticeable around ventricles, brainstem and borders of the brain.

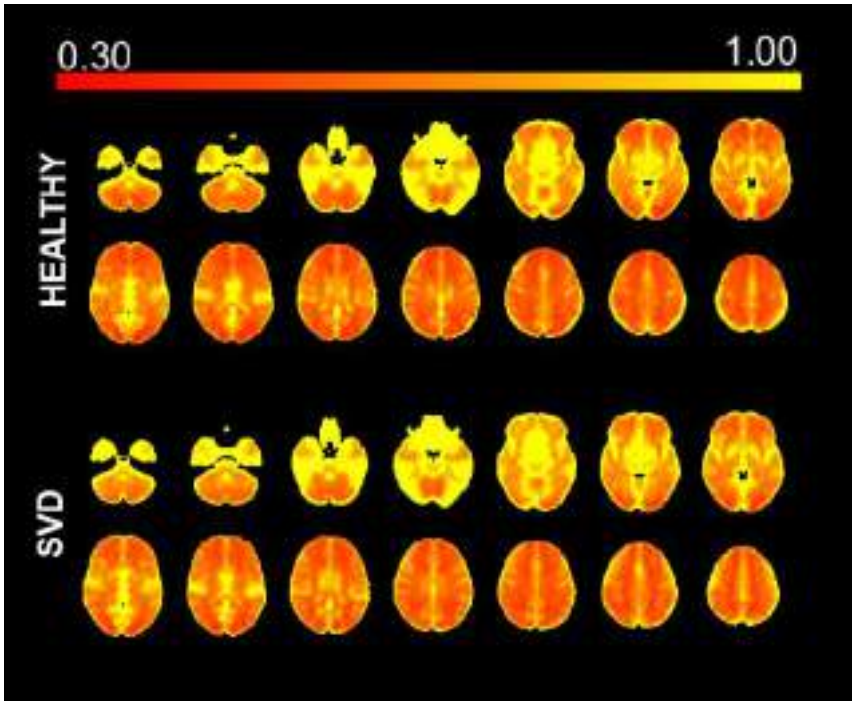

Figure 8.17: Average maps of ALFF (Healthy subjects - top and SVD patients - bottom).

Figure 8.18 shows the boxplots representing the distributions of ALFF values across GM and NAWM for healthy subjects and SVD patients.

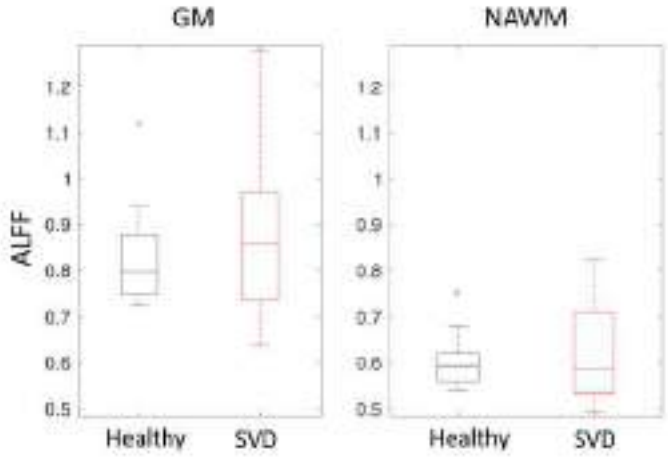

Figure 8.18: Boxplots representing the distributions of ALFF values in GM and NAWM for healthy controls and SVD patients. The central mark indicates the median; the upper and lower edges of the box correspond to the 25^{th} and 75^{th} percentiles, respectively; and the dots correspond to outliers.

A statistically significant main effect was observed for the type of ROI (GM vs NAWM) (two-way ANOVA, with group as between subject factor, $p<0.001$), with decreased ALFF values in NAWM regions when compared to GM regions. No statistically significant differences were observed between groups. Furthermore and similarly to Makedonov et al. (Makedonov et al., 2013), BOLD fluctuations (here evaluated through ALFF) were significantly decreased in WMH relative to NAWM ($p<0.001$) (Figure 8.19). Regarding the ALFF distributions, a wider distribution is found in the SVD group compared with the healthy subjects. The high variability present in ALFF measures for SVD patients could be related with variations across patients in terms of their cognitive function or covariates such as age or WM lesion burden.

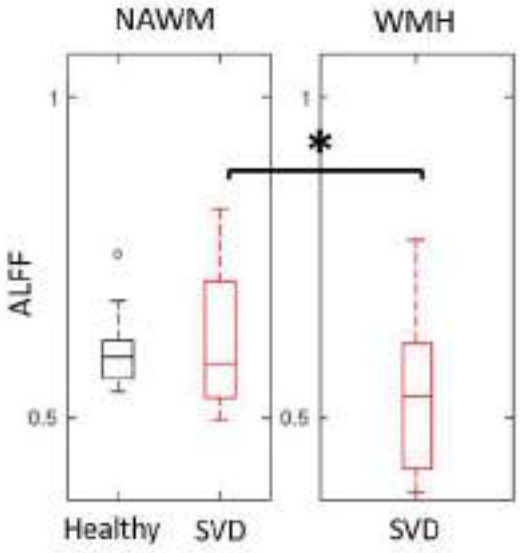

Figure 8.19: Boxplots representing the distributions of ALFF values in NAWM in WMH (only for the SVD group). The central mark indicates the median; the upper and lower edges of the box correspond to the 25^{th} and 75^{th} percentiles, respectively; and the dots correspond to outliers.

Fig. 8.20 represents the Pearson correlation analysis between the neuropsychological scores in each of the four cognitive domains and the ALFF metric in GM and NAWM regions. Interestingly, we found that processing speed was predicted with significance using ALFF in both GM and NAWM ($p = 0.014$ and $p = 0.017$, respectively).

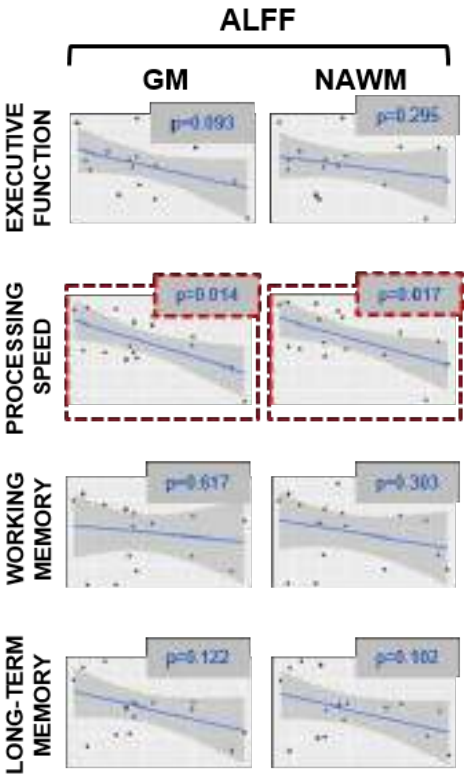

Figure 8.20: Pearson correlation plots between scores in each of the 4 cognitive domains (rows) and the ALFF metric in GM and NAWM (columns). Significant correlations were found between processing speed scores and ALFF in GM and NAWM ($p = 0.014$ and $p = 0.017$, respectively).

8.4 Discussion and Conclusion

The use of metrics sensitive to differences in cerebral haemodynamics can prove useful in the characterization of vascular pathologies such as SVD. Our preliminary work focused on the investigation of cerebral haemodynamics obtained using completely noninvasive fMRI metrics in the context of SVD. We employed multiple-delay ASL for the measurement of multiple perfusion parameters, including CBF as well as ATT and aBV, for the first time in SVD. We also employed a BH BOLD-fMRI protocol to assess both the amplitude and delay of CVR, also for the first time in SVD. Finally, we have extended a previous report on the study of spontaneous physiological fluctuations using rs-fMRI in SVD, by further showing that variations across patients are correlated with their performance in processing speed tests (Makedonov et al., 2013). Comparisons between healthy subjects and SVD patients, conducted through a region-based approach, did not yield statistically significant differences between groups. Moreover, due to the low number of subjects in sSVD and CADASIL subgroups no comparisons between these subgroups were performed. Future work will be done in order to investigate voxelwise differences as well as more specific regions related with the pathology. Moreover, we will also conduct

a multi-parametric analysis taking into account the various haemodynamic measures obtained here.

In fact, our results highlight the potential of fMRI metrics to predict cognitive decline in SVD, further supporting the hypothesis that these metrics might provide sensitive disease biomarkers. In particular, ALFF metrics obtained using resting-state BOLD-fMRI are significantly correlated with cognitive impairment in the processing speed domain, while the only structural covariate that exhibited significant correlation with cognition was NBV. Another interesting finding was the difference between ALFF in NAWM and WMH, already observed using other low-frequency fluctuations metric (Makedonov et al., 2013). In fact, it has been demonstrated that the amplitude of spontaneous BOLD fluctuations measured by rs-fMRI is increased in the NAWM of SVD patients compared with age-matched healthy subjects, which were consistent with increased cardiac pulsatility (Makedonov et al., 2013). Nevertheless, further work is necessary to fully understand the relationships between the different fMRI metrics and the physiological meaning behind them.

9

Conclusion

Contents

This thesis proposes and improves non-invasive functional magnetic resonance imagine (fMRI) methodologies for cerebral haemodynamic mapping and demonstrates their applicability, whether in healthy subjects or in diseased state.

In this chapter, the main contributions of this work are first described and some future directions are then outlined, concluding with some final remarks.

9.1 Summary of Main Contributions

The preservation and regulation of cerebral haemodynamics under a range of conditions is crucial, with the structure and function of brain vasculature playing a significant role in the maintenance of homeostasis. This is achieved through a complex cerebral circulatory system including bigger arteries such as the anterior cerebral artery, the middle cerebral artery and the posterior cerebral artery, their branches and corresponding arterioles penetrating into the cortex and deep structures, ultimately feeding an extensive network of capillaries.

Cerebral blood flow (CBF) regulation is achieved through the combination of several physiological effectors that work together to ensure optimal delivery of oxygen and nutrients. The main mechanisms for cerebral blood flow regulation were briefly described in Chapter 2, although to date, they remain poorly understood.

Furthermore, vessels have an intrinsic reactive mechanism that alters their caliber in response to vasoactive stimuli. This mechanism, known as cerebrovascular reactivity (CVR), can possibly be used to infer the functional integrity of vessels. This parameter was also extensively described in Chapter 2. Both CVR amplitude and timing parameters can reflect differences in cerebral vascular tone and response in healthy and pathological conditions. CVR assessment is usually performed by applying a challenge to brain vasculature and measuring the concomitant haemodynamic changes using an appropriate modality. For the former, several challenges have been used to elicit a robust vascular response, from the use of vasoactive drugs to respiratory challenges. These were extensively described in Chapter 5. Regarding the imaging methods used to assess these cerebral haemodynamics changes, these were introduced in Chapter 3, with blood oxygen level dependant (BOLD) fMRI remaining the most commonly used non-invasive method for whole-brain mapping. Nevertheless, this contrast represents the combined effect of several haemodynamic parameter and, for that reason, ASL might provide a more robust non-invasive MRI alternative, providing truly quantitative maps of CBF.

Having in mind all these factors and their interactions, this work aimed to overcome and improve some methodological aspects of cerebral haemodynamic assessment using MRI. In Chapter 4, a systematic comparison of several calibration methods and their corresponding processing pipelines and options was performed, in terms of their impact on perfusion quantification of two multiple post-labeling-delay arterial spin labeling (ASL) datasets. Our results highlight the great impact of the different pipeline options, with calibration based on cerebrospinal fluid (CSF) as reference tissue being the most sensitive to options. In contrast, voxelwise calibration

method was the least sensitive to the processing options supporting the current recommendation for ASL calibration. Other options such as the level of spatial smoothing as well as the value of brain-blood water partition coefficient had moderate to negligible impact. Importantly, some of the calibration methods tested in this study may not be appropriate to use in certain clinical populations. For example, in patients with white matter abnormalities such as in multiple sclerosis or small vessel disease the reference tissue methods based on CSF or gray matter may be preferable to reference tissue methods based on white matter. Regardless of the calibration method chosen, our findings clearly highlight the need for a complete description of the calibration procedure and corresponding pipeline options in ASL studies.

Regarding vasoactive challenges to elicit a robust vascular response, we overviewed the common methodological approaches used to evaluate CVR using magnetic resonance imaging (MRI), with special focus on non-invasive methods (Chapter 5). In particular, task-based and resting-state approaches were extensively discussed with regard to acquisition and data analysis strategies. Due to the complexity of the physiological mechanisms behind the haemodynamic responses, a deeper understanding is still required in order to draw plausible inferences between different mechanisms. In the future, validation studies are needed in order to standardize the methodological approaches and reach a consensus on the most suitable acquisition method and analysis strategy to derive a vascular health biomarker. Nevertheless, we further investigated and compared the use of Fourier models of the BOLD response to a breath-hold task in Chapter 6. Our results demonstrate that a Fourier series set consisting of a sine–cosine pair at the task frequency and its two harmonics is an appropriate model for BOLD-fMRI CVR measurements based on a breath-hold task with preparatory inspiration in terms of variance explained and reproducibility.

Resting-state fMRI metrics and their increased interest in the study of the brain's intrinsic functional connectivity has encouraged the use of these methodologies to understand brain haemodynamics. However, these time synchronous connections across the brain can not only be caused by neuronal activity but also by non-neuronal mechanisms. Several strategies have been proposed to model and remove these non-neuronal contributions, particularly at 7T, including contributions from respiratory volume rate (RV) and heart rate (HR) signal fluctuations. We investigated the impact of the degree of specificity in the optimization of RV and HR physiological noise model contributions on functional connectivity measures in high-spatial resolution resting-state fMRI at 7T. Our results indicate that functional connectivity measures in rs-fMRI studies at 7T may be improved by optimizing physiological noise correction at least at the cluster level. Nevertheless, the acquisition protocol used in this study is quite uncommon in the literature of resting-state studies, which are most often performed at 3T, with larger voxel resolution and longer duration. These differences may limit the generalization of our results and more studies should be performed in order to further validate our observations.

Finally, in Chapter 8 some of the developed methodologies were applied to a group of patients with small vessel disease (SVD). Our preliminary work demonstrates, for the first time,

the feasibility of employing multiple-delay ASL to measure CBF as well as arterial transit times and arterial blood volume. Moreover, we also extracted both magnitude and delay information from breath-hold BOLD-fMRI measurements of CVR. Finally, by analyzing resting-state BOLD-fMRI, we found evidence amplitude metrics based on baseline resting-state BOLD-fMRI fluctuations have the potential to predict cognitive decline in SVD. In particular, the amplitude of low-frequency fluctuations of BOLD rs-fMRI is significantly correlated with cognitive impairments in processing speed. Overall, these results indicate that measures of BOLD fluctuations, particularly in NAWM, may provide sensitive disease biomarkers. Nonetheless, further work is necessary to understand the physiological meaning of the relationship between fluctuations metrics in healthy and pathological conditions.

9.2 Future Work

As described previously, mapping of cerebral haemodynamics using fMRI techniques is a promising tool that might provide valuable and earlier disease biomarkers. Nevertheless, the work presented here has some limitations that could be addressed in future studies.

Despite ASL metrics yielding quantitative measurements of cerebral haemodynamics, the intrinsic low SNR hampers its applicability in clinical settings. In order to further validate our results, a new and larger study acquiring different ASL schemes on the same subjects should be conducted. Furthermore, the optimized multiple-delay protocols employed in this work may not be generalizable for all pathological conditions or baseline states. The Bayesian modeling approach used also employs *a priori* knowledge of the parameters averages and distributions. These might need to be adjusted in diseased conditions.

Regarding CVR metrics, due to the broad range of stimuli and analysis methods, it is extremely difficult to compare results across literature. A consensus work should be performed, exhibiting the potential pitfalls of the different approaches and highlighting the most appropriate methods for specific cases. One major pitfall of our work is the complex qualitative nature of BOLD signal, making quantitative perfusion imaging techniques such as ASL desirable. Furthermore, when dealing with potentially less cooperative patients, BH with preparatory inspiration tend to be easier to perform, although the preparatory inspiration leads to a more complex BOLD response. Studies using BH without preparatory inspiration, as well as using ASL acquisition schemes, should be performed in order to investigate whether Fourier series sets are also suitable models for these type of CVR measurements.

The protocol used in our 7T study is quite uncommon in resting-state literature, limiting the generalizability of our results. Lower field strengths such as 3T should reduce the observed physiological noise contributions. Nevertheless, investigation of different spatial scales for the model optimization should be performed.

Finally, regarding our clinical application, the SVD and CADASIL groups were relatively small. Longitudinal studies with a higher number of subjects should be conducted in the future

in order to evaluate disease progression and the sensitivity of fMRI biomarkers. On that matter, reproducibility studies could be of added value. Including other ROIs into the analysis such as regions of NAWM closer to WMH might provide additional information longitudinally. During BOLD acquisitions, shorter repetition times could allow a better investigation of the nature of cerebral haemodynamics, also avoiding aliasing of cardiac and respiratory cycles. An approach to overcome this limitation could include the use of simultaneous multi-slice acceleration, exploring the availability of multi-channel RF coil arrays with higher number channels. More interestingly, understanding the physiological relationships between the different fMRI methods and metrics is crucial. The next steps include performing a voxelwise analysis of the data and also combining and comparing the different MRI methods and metrics acquired in this SVD cohort.

Future research should also include multi-modal research, allowing a better interpretation of the physiological mechanisms and their relations. For example, integration of simultaneously recorded methodologies such as EEG (EEG-fMRI) could provide novel insights into the understanding of brain haemodynamics and their relation to the fMRI metrics.

9.3 Final considerations

This Thesis addresses a number of critical methodological challenges, developing robust quantitative fMRI techniques for evaluation of cerebral haemodynamics, hopefully bringing haemodynamic imaging MRI techniques closer to clinical practice. Our results evidence that the new and optimized processing strategies and the cerebral haemodynamic metrics derived from them seem promising when applied in either healthy subjects or in patients. Nevertheless, further work is necessary to fully understand the physiological meaning and relationships between methods and metrics. With these improved non-invasive methodologies and corresponding metrics, important steps were taken towards providing novel insights into the haemodynamics mechanisms, that might be impaired or abolished in pathological states.

Bibliography

Aalkjaer, C., Boedtkjer, D., and Matchkov, V. Vasomotion - what is currently thought? Acta Physiologica, 202(3):253–269, 2011.

Aalkjaer, C. and Nilsson, H. Vasomotion: cellular background for the oscillator and for the synchronization of smooth muscle cells. British Journal of Pharmacology, 144(5):605–616, 2005.

Aaslid, R., Lindegaard, K. F., Sorteberg, W., and Nornes, H. Cerebral autoregulation dynamics in humans. Stroke, 20(1):45–52, 1989.

Abbott, D. F., Opdam, H. I., Briellmann, R. S., and Jackson, G. D. Brief breath holding may confound functional magnetic resonance imaging studies. Human brain mapping, 24(4): 284–90, 2005.

Abhishek Raj, Alankrita, Akansha Srivastava, and Vikrant Bhateja. Computer Aided Detection of Brain Tumor in Magnetic Resonance Images. IACSIT International Journal of Engineering and Technology, 3(5):523–532, 2011.

Abreu, R., Leite, M., Jorge, J., Grouiller, F., van der Zwaag, W., Leal, A., and Figueiredo, P. Ballistocardiogram artifact correction taking into account physiological signal preservation in simultaneous EEG-fMRI. NeuroImage, 135:45–63, 2016.

Ainslie, P. N. and Duffin, J. Integration of cerebrovascular CO 2 reactivity and chemoreflex control of breathing : mechanisms of regulation , measurement , and interpretation. 2009.

Ainslie, P. N., Murrell, C., Peebles, K., Swart, M., Skinner, M. A., Williams, M. J. A., and Taylor, R. D. Early morning impairment in cerebral autoregulation and cerebrovascular CO2 reactivity in healthy humans: relation to endothelial function. Experimental physiology, 92 (4):769–77, 2007.

Ainslie, P. N. and Brassard, P. Why is the neural control of cerebral autoregulation so controversial? F1000prime reports, 6:14, 2014.

Alsop, D. C. and Detre, J. A. Reduced Transit-Time Sensitivity in Noninvasive Magnetic Resonance Imaging of Human Cerebral Blood Flow. Journal of Cerebral Blood Flow & Metabolism, 16(6):1236–1249, 1996.

Alsop, D. C., Detre, J. A., Golay, X., Günther, M., Hendrikse, J., Hernandez-Garcia, L., Lu, H., MacIntosh, B. J., Parkes, L. M., Smits, M., van Osch, M. J. P., Wang, D. J. J., Wong, E. C., and Zaharchuk, G. Recommended implementation of arterial spin-labeled perfusion MRI for clinical applications: A consensus of the ISMRM perfusion study group and the European consortium for ASL in dementia. Magnetic resonance in medicine, 73(1):spcone, 2015.

Andersson, J., Jenkinson, M., and Smith, S. Non-linear registration aka Spatial normalisation, FMRIB Technical Report TR07 JA2. Technical report, 2007.

Andrade, K. C., Pontes-Neto, O. M., Leite, J. P., Santos, A. C., Baffa, O., and de Araujo, D. B. Quantitative aspects of brain perfusion dynamic induced by BOLD fMRI. Arquivos de neuro-psiquiatria, 64(4):895–8, 2006.

Aron, A. R., Gluck, M. A., and Poldrack, R. A. Long-term test-retest reliability of functional MRI in a classification learning task. NeuroImage, 29(3):1000–6, 2006.

Arvanitakis, Z., Leurgans, S. E., Barnes, L. L., Bennett, D. A., and Schneider, J. A. Microinfarct Pathology, Dementia, and Cognitive Systems. Stroke, 42(3):722–727, 2011.

Asllani, I., Borogovac, A., and Brown, T. R. Regression algorithm correcting for partial volume effects in arterial spin labeling MRI. Magnetic Resonance in Medicine, 60(6):1362–1371, 2008.

Aso, K., Ogasawara, K., Sasaki, M., Kobayashi, M., Suga, Y., Chida, K., Otawara, Y., and Ogawa, A. Preoperative cerebrovascular reactivity to acetazolamide measured by brain perfusion SPECT predicts development of cerebral ischemic lesions caused by microemboli during carotid endarterectomy. European journal of nuclear medicine and molecular imaging, 36(2): 294–301, 2009.

Bandettini, P. A. and Wong, E. C. A Hypercapnia-Based Normalization Method for Improved Spatial Localization of Human Brain Activation with fMRI. NMR in Biomedicine, 10:197–203, 1997.

Banzett, R. B., Garcia, R. T., and Moosavi, S. H. Simple contrivance "clamps" end-tidal PCO(2) and PO(2) despite rapid changes in ventilation. Journal of applied physiology (Bethesda, Md. : 1985), 88(5):1597–600, 2000.

Bastos-Leite, A. J., Kuijer, J. P. A., Rombouts, S. A. R. B., Sanz-Arigita, E., van Straaten, E. C., Gouw, A. A., van der Flier, W. M., Scheltens, P., and Barkhof, F. Cerebral blood flow by using pulsed arterial spin-labeling in elderly subjects with white matter hyperintensities. AJNR. American journal of neuroradiology, 29(7):1296–301, 2008.

Bayliss, W. M. On the local reactions of the arterial wall to changes of internal pressure. The Journal of physiology, 28(3):220–31, 1902.

Beckmann, C. and Smith, S. Probabilistic Independent Component Analysis for Functional Magnetic Resonance Imaging. IEEE Transactions on Medical Imaging, 23(2):137–152, 2004.

Behzadi, Y., Restom, K., Liau, J., and Liu, T. T. A component based noise correction method (CompCor) for BOLD and perfusion based fMRI. NeuroImage, 37(1):90–101, 2007.

Benisty, S., Gouw, A. A., Porcher, R., Madureira, S., Hernandez, K., Poggesi, A., van der Flier, W. M., Van Straaten, E. C. W., Verdelho, A., Ferro, J., Pantoni, L., Inzitari, D., Barkhof, F., Fazekas, F., Chabriat, H., and LADIS Study group. Location of lacunar infarcts correlates with cognition in a sample of non-disabled subjects with age-related white-matter changes: the LADIS study. Journal of Neurology, Neurosurgery & Psychiatry, 80(5):478–483, 2009.

Benjamin, P., Trippier, S., Lawrence, A. J., Lambert, C., Zeestraten, E., Williams, O. A., Patel, B., Morris, R. G., Barrick, T. R., MacKinnon, A. D., and Markus, H. S. Lacunar Infarcts, but Not Perivascular Spaces, Are Predictors of Cognitive Decline in Cerebral Small-Vessel Disease. Stroke, 49(3):586–593, 2018.

Bernbaum, M., Menon, B. K., Fick, G., Smith, E. E., Goyal, M., Frayne, R., and Coutts, S. B. Reduced blood flow in normal white matter predicts development of leukoaraiosis. Journal of cerebral blood flow and metabolism : official journal of the International Society of Cerebral Blood Flow and Metabolism, 35(10):1610–5, 2015.

Bhattacharyya, P. K. and Lowe, M. J. Cardiac-induced physiologic noise in tissue is a direct observation of cardiac-induced fluctuations. Magnetic Resonance Imaging, 22(1):9–13, 2004.

Bianciardi, M., Fukunaga, M., van Gelderen, P., Horovitz, S. G., de Zwart, J. A., Shmueli, K., and Duyn, J. H. Sources of functional magnetic resonance imaging signal fluctuations in the human brain at rest: a 7 T study. Magnetic resonance imaging, 27(8):1019–29, 2009a.

Bianciardi, M., Vangelderen, P., Duyn, J., Fukunaga, M., and Dezwart, J. Making the most of fMRI at 7 T by suppressing spontaneous signal fluctuations. NeuroImage, 44(2):448–454, 2009b.

Birn, R. M., Diamond, J. B., Smith, M. A., and Bandettini, P. A. Separating respiratory-variation-related fluctuations from neuronal-activity-related fluctuations in fMRI. NeuroImage, 31(4):1536–48, 2006.

Birn, R. M., Smith, M. A., Jones, T. B., and Bandettini, P. A. The respiration response function: the temporal dynamics of fMRI signal fluctuations related to changes in respiration. NeuroImage, 40(2):644–54, 2008.

Birn, R. M., Smith, M. A., Jones, T. B., and Bandettini, P. A. NIH Public Access. Neurocritical care, 40(2):644–654, 2009.

Birn, R. M. The role of physiological noise in resting-state functional connectivity. NeuroImage, 62(2):864–870, 2012.

Birn, R. M., Cornejo, M. D., Molloy, E. K., Patriat, R., Meier, T. B., Kirk, G. R., Nair, V. a., Meyerand, M. E., and Prabhakaran, V. The influence of physiological noise correction on test-retest reliability of resting-state functional connectivity. Brain connectivity, 4(7):511–22, 2014.

Biswal, B., Yetkin, F. Z., Haughton, V. M., and Hyde, J. S. Functional connectivity in the motor cortex of resting human brain using echo-planar MRI. Magnetic resonance in medicine, 34(4):537–41, 1995.

Biswal, B., Hudetz, A. G., Yetkin, F. Z., Haughton, V. M., and Hyde, J. S. Hypercapnia Reversibly Suppresses Low-Frequency Fluctuations in the Human Motor Cortex during Rest Using Echo–Planar MRI. Journal of Cerebral Blood Flow & Metabolism, 17(3):301–308, 1997.

Biswal, B. B. and Kannurpatti, S. S. Resting-State Functional Connectivity in Animal Models: Modulations by Exsanguination. Dynamic Brain Imaging, pages 255–274, 2009.

Biswal, B. B., Kannurpatti, S. S., and Rypma, B. Hemodynamic scaling of fMRI-BOLD signal: validation of low-frequency spectral amplitude as a scalability factor. Magnetic resonance imaging, 25(10):1358–69, 2007.

Blair, G. W., Maria Valdez Hernandez, M., Thrippleton, M. J., Doubal, F. N., and Wardlaw, J. M. Advanced Neuroimaging of Cerebral Small Vessel Disease. Curr Treat Options Cardio Med, 19:56, 2017.

Bland, J. M. and Altman, D. G. Measurement error. Statistics Notes, BMJ, 312:1654, 1996.

Blockley, N. P., Driver, I. D., Francis, S., Fisher, J. A., and Gowland, P. An improved method for acquiring cerebrovascular reactivity maps. Magnetic resonance in medicine : official journal of the Society of Magnetic Resonance in Medicine / Society of Magnetic Resonance in Medicine, 65(5):1278–86, 2011.

Bodurka, J., Ye, F., Petridou, N., Murphy, K., and Bandettini, P. Mapping the MRI voxel volume in which thermal noise matches physiological noise—Implications for fMRI. NeuroImage, 34(2):542–549, 2007.

Bright, M. G. and Murphy, K. Reliable quantification of BOLD fMRI cerebrovascular reactivity despite poor breath-hold performance. NeuroImage, 83:559–68, 2013.

Bright, M. G., Bulte, D. P., Jezzard, P., and Duyn, J. Characterization of regional heterogeneity in cerebrovascular reactivity dynamics using novel hypocapnia task and BOLD fMRI. NeuroImage, 48(1):166–75, 2009.

Bright, M. G., Donahue, M., Duyn, J., Jezzard, P., and Bulte, D. P. The effect of basal vasodilation on hypercapnic and hypocapnic reactivity measured using magnetic resonance imaging. Journal of cerebral blood flow and metabolism : official journal of the International Society of Cerebral Blood Flow and Metabolism, 31(2):426–38, 2011.

Brooks, J. C. W., Faull, O. K., Pattinson, K. T. S., and Jenkinson, M. Physiological Noise in Brainstem fMRI. Frontiers in Human Neuroscience, 7:623, 2013.

Brooks, J. C., Beckmann, C. F., Miller, K. L., Wise, R. G., Porro, C. A., Tracey, I., and Jenkinson, M. Physiological noise modelling for spinal functional magnetic resonance imaging studies. NeuroImage, 39(2):680–692, 2008.

Brown, R., Benveniste, H., Black, S. E., Charpak, S., Dichgans, M., Joutel, A., Nedergaard, M., Smith, K. J., Zlokovic, B. V., and Wardlaw, J. M. Understanding the role of the perivascular space in cerebral small vessel disease. Cardiovascular Research, 114(11):1462–1473, 2018.

Buckner, R. L., Andrews-Hanna, J. R., and Schacter, D. L. The Brain's Default Network. Annals of the New York Academy of Sciences, 1124(1):1–38, 2008.

Buffon, F., Porcher, R., Hernandez, K., Kurtz, A., Pointeau, S., Vahedi, K., Bousser, M.-G., and Chabriat, H. Cognitive profile in CADASIL. Journal of neurology, neurosurgery, and psychiatry, 77(2):175–80, 2006.

Bulte, D. P., Chiarelli, P. A., Wise, R. G., and Jezzard, P. Cerebral perfusion response to hyperoxia. Journal of Cerebral Blood Flow & Metabolism, 27:69–75, 2007.

Bulte, D. P., Drescher, K., and Jezzard, P. Comparison of hypercapnia-based calibration techniques for measurement of cerebral oxygen metabolism with MRI. Magnetic resonance in medicine : official journal of the Society of Magnetic Resonance in Medicine / Society of Magnetic Resonance in Medicine, 61(2):391–8, 2009.

Buterbaugh, J., Wynstra, C., Provencio, N., Combs, D., Gilbert, M., and Parthasarathy, S. Cerebrovascular Reactivity in Young Subjects with Sleep Apnea. Sleep, 38(2):241–250, 2015.

Buxton, R. B., Frank, L. R., Wong, E. C., Siewert, B., Warach, S., and Edelman, R. R. A general kinetic model for quantitative perfusion imaging with arterial spin labeling. Magnetic resonance in medicine : official journal of the Society of Magnetic Resonance in Medicine / Society of Magnetic Resonance in Medicine, 40(3):383–96, 1998.

Buxton, R. B. Introduction to functional magnetic resonance imaging : principles and techniques. Cambridge University Press, 2009.

Buxton, R. B. Interpreting oxygenation-based neuroimaging signals: the importance and the challenge of understanding brain oxygen metabolism. Frontiers in neuroenergetics, 2:8, 2010.

Buzsaki, G. Neuronal Oscillations in Cortical Networks. Science, 304(5679):1926–1929, 2004.

Caballero-Gaudes, C. and Reynolds, R. C. Methods for cleaning the BOLD fMRI signal. NeuroImage, 154:128–149, 2017.

Cantin, S., Villien, M., Moreaud, O., Tropres, I., Keignart, S., Chipon, E., Le Bas, J.-F., Warnking, J., and Krainik, A. Impaired cerebral vasoreactivity to CO2 in Alzheimer's disease using BOLD fMRI. NeuroImage, 58(2):579–87, 2011.

Carroll, T. J., Teneggi, V., Jobin, M., Squassante, L., Treyer, V., Hany, T. F., Burger, C., Wang, L., Bye, A., von Schulthess, G. K., and Buck, A. Absolute Quantification of Cerebral Blood Flow with Magnetic Resonance, Reproductibility of the Method , and Comparison with H215O Positron Emission Tomography. Journal of Cerebral Blood Flow & Metabolism, (22): 1149–1156, 2002.

Cavaco, S., Goncalves, A., Pinto, C., Almeida, E., Gomes, F., Moreira, I., Fernandes, J., and Teixeira-Pinto, A. Trail Making Test: Regression-based Norms for the Portuguese Population. Archives of Clinical Neuropsychology, 28(2):189–198, 2013.

Cavuşoğlu, M., Pfeuffer, J., Uğurbil, K., and Uludağ, K. Comparison of pulsed arterial spin labeling encoding schemes and absolute perfusion quantification. Magnetic resonance imaging, 27(8):1039–45, 2009.

Chabriat, H., Joutel, A., Dichgans, M., Tournier-Lasserve, E., and Bousser, M.-G. Cadasil. The Lancet. Neurology, 8(7):643–53, 2009.

Chang, C. and Glover, G. H. Relationship between respiration, end-tidal CO2, and BOLD signals in resting-state fMRI. Neuroimage, 47(4):1381–1393, 2009a.

Chang, C. and Glover, G. H. Effects of model-based physiological noise correction on default mode network anti-correlations and correlations. NeuroImage, 47(4):1448–59, 2009b.

Chang, C., Thomason, M. E., and Glover, G. H. Mapping and correction of vascular hemodynamic latency in the BOLD signal. NeuroImage, 43(1):90–102, 2008.

Chang, C., Cunningham, J. P., and Glover, G. H. Influence of heart rate on the BOLD signal: The cardiac response function. NeuroImage, 44(3):857–869, 2009.

Chang, T.-Y., Kuan, W.-C., Huang, K.-L., Chang, C.-H., Chang, Y.-J., Wong, H.-F., Lee, T.-H., and Liu, H.-L. Heterogeneous cerebral vasoreactivity dynamics in patients with carotid stenosis. PloS one, 8(9):e76072, 2013.

Chapin, J. L. Relationship Between Lung Volume and Breath-Holding Breaking Point. J Appl Physiol, 8(1):88–90, 1955.

Chappell, M. A., MacIntosh, B. J., Donahue, M. J., Günther, M., Jezzard, P., and Woolrich, M. W. Separation of macrovascular signal in multi-inversion time arterial spin labelling MRI. Magnetic resonance in medicine : official journal of the Society of Magnetic Resonance in Medicine / Society of Magnetic Resonance in Medicine, 63(5):1357–65, 2010.

Chappell, M. A., Groves, A. R., MacIntosh, B. J., Donahue, M. J., Jezzard, P., and Woolrich, M. W. Partial volume correction of multiple inversion time arterial spin labeling MRI data. Magnetic Resonance in Medicine, 65(4):1173–1183, 2011.

Chappell, M., Groves, A., Whitcher, B., and Woolrich, M. Variational Bayesian Inference for a Nonlinear Forward Model. IEEE Transactions on Signal Processing, 57(1):223–236, 2009.

Charlton, R. A., Morris, R. G., Nitkunan, A., and Markus, H. S. The cognitive profiles of CADASIL and sporadic small vessel disease. Neurology, 66(10):1523–1526, 2006.

Cheema, I., Switzer, A. R., McCreary, C. R., Hill, M. D., Frayne, R., Goodyear, B. G., and Smith, E. E. Functional magnetic resonance imaging responses in CADASIL. Journal of the Neurological Sciences, 375:248–254, 2017.

Chen, Y., Wang, Z., and Detre, J. Impact of equilibrium magnetization of blood on ASL quantification. Proc. Intl. Soc. mag. Reson. Med. 19, page 300, 2011.

Choi, H., Yoo, M. Y., Cheon, G. J., Kang, K. W., Chung, J.-K., and Lee, D. S. Parametric Cerebrovascular Reserve Images Using Acetazolamide (99m)Tc-HMPAO SPECT: A Feasibility Study of Quantitative Assessment. Nuclear medicine and molecular imaging, 47(3):188–95, 2013.

Chu, W.-C., Hsu, Y.-Y., Lim, K.-E., and Liu, H.-L. Quantitative Evaluation of the Dynamic BOLD and CBF Responses to Breath Hold in Different Brain Territories. Proc. Intl. Soc. Mag. Reason. Med., 19:1644, 2011.

Churchill, N. W., Yourganov, G., Spring, R., Rasmussen, P. M., Lee, W., Ween, J. E., and Strother, S. C. PHYCAA: Data-driven measurement and removal of physiological noise in BOLD fMRI. NeuroImage, 59(2):1299–1314, 2012.

Cicchetti, D. V. Methodological Commentary The Precision of Reliability and Validity Estimates Re-Visited: Distinguishing Between Clinical and Statistical Significance of Sample Size Requirements. Journal of Clinical and Experimental Neuropsychology, 2010.

Cipolla, M. J. Anatomy and Ultrastructure, 2009.

Cohen, E. R., Ugurbil, K., and Kim, S.-G. Effect of basal conditions on the magnitude and dynamics of the blood oxygenation level-dependent fMRI response. Journal of cerebral blood flow and metabolism : official journal of the International Society of Cerebral Blood Flow and Metabolism, 22(9):1042–53, 2002.

Cohen, J. Statistical power analysis for the behavioral sciences. L. Erlbaum Associates, 1988.

Coleman, T. F. and Li, Y. An Interior Trust Region Approach for Nonlinear Minimization Subject to Bounds. SIAM Journal on Optimization, 2006.

Collins, D. L., Holmes, C. J., Peters, T. M., and Evans, A. C. Automatic 3-D model-based neuroanatomical segmentation. Human Brain Mapping, 3(3):190–208, 1995.

Comon, P. Independent component analysis, A new concept? Signal Processing, 36:287–314, 1994.

Conijn, M. M., Hoogduin, J. M., van der Graaf, Y., Hendrikse, J., Luijten, P. R., and Geerlings, M. I. Microbleeds, lacunar infarcts, white matter lesions and cerebrovascular reactivity — A 7 T study. NeuroImage, 59(2):950–956, 2012.

Conklin, J., Fierstra, J., Crawley, A. P., Han, J. S., Poublanc, J., Mandell, D. M., Silver, F. L., Tymianski, M., Fisher, J. A., and Mikulis, D. J. Impaired cerebrovascular reactivity with steal phenomenon is associated with increased diffusion in white matter of patients with Moyamoya disease. Stroke; a journal of cerebral circulation, 41(8):1610–6, 2010.

Cordes, D., Haughton, V. M., Arfanakis, K., Carew, J. D., Turski, P. A., Moritz, C. H., Quigley, M. A., and Meyerand, M. E. Frequencies contributing to functional connectivity in the cerebral cortex in "resting-state" data. AJNR. American journal of neuroradiology, 22(7):1326–33, 2001.

Cordes, D., Nandy, R. R., Schafer, S., and Wager, T. D. Characterization and reduction of cardiac- and respiratory-induced noise as a function of the sampling rate (TR) in fMRI. NeuroImage, 89:314–330, 2014.

Crane, D. E., Black, S. E., Ganda, A., Mikulis, D. J., Nestor, S. M., Donahue, M. J., and MacIntosh, B. J. Gray matter blood flow and volume are reduced in association with white matter hyperintensity lesion burden: a cross-sectional MRI study. Frontiers in Aging Neuroscience, 7:131, 2015.

Croall, I. D., Lohner, V., Moynihan, B., Khan, U., Hassan, A., O'Brien, J. T., Morris, R. G., Tozer, D. J., Cambridge, V. C., Harkness, K., Werring, D. J., Blamire, A. M., Ford, G. A., Barrick, T. R., and Markus, H. S. Using DTI to assess white matter microstructure in cerebral small vessel disease (SVD) in multicentre studies. Clinical Science, 131(12):1361–1373, 2017.

Dagli, M. S., Ingeholm, J. E., and Haxby, J. V. Localization of Cardiac-Induced Signal Change in fMRI. NeuroImage, 9(4):407–415, 1999.

Dahl, A., Russell, D., Rootwelt, K., Nyberg-Hansen, R., and Kerty, E. Cerebral vasoreactivity assessed with transcranial Doppler and regional cerebral blood flow measurements. Dose,

serum concentration, and time course of the response to acetazolamide. Stroke, 26(12):2302–6, 1995.

Dai, W., Garcia, D., de Bazelaire, C., and Alsop, D. C. Continuous flow-driven inversion for arterial spin labeling using pulsed radio frequency and gradient fields. Magnetic resonance in medicine : official journal of the Society of Magnetic Resonance in Medicine / Society of Magnetic Resonance in Medicine, 60(6):1488–97, 2008.

De Martino, F., Gentile, F., Esposito, F., Balsi, M., Di Salle, F., Goebel, R., and Formisano, E. Classification of fMRI independent components using IC-fingerprints and support vector machine classifiers. NeuroImage, 34(1):177–194, 2007.

de Munck, J., Gonçalves, S., Faes, T., Kuijer, J., Pouwels, P., Heethaar, R., and Lopes da Silva, F. A study of the brain's resting state based on alpha band power, heart rate and fMRI. NeuroImage, 42(1):112–121, 2008.

De Vis, J. B., Bhogal, A. A., Hendrikse, J., Petersen, E. T., and Siero, J. C. Effect sizes of BOLD CVR, resting-state signal fluctuations and time delay measures for the assessment of hemodynamic impairment in carotid occlusion patients. NeuroImage, 179:530–539, 2018.

Detre, J. A., Leigh, J. S., Williams, D. S., and Koretsky, A. P. Perfusion imaging. Magnetic resonance in medicine, 23(1):37–45, 1992.

Donahue, M., Stevens, R. D., de Boorder, M., Pekar, J. J., Hendrikse, J., and van Zijl, P. C. M. Hemodynamic changes after visual stimulation and breath holding provide evidence for an uncoupling of cerebral blood flow and volume from oxygen metabolism. Journal of cerebral blood flow and metabolism : official journal of the International Society of Cerebral Blood Flow and Metabolism, 29(1):176–85, 2009.

Donahue, M. J., Ayad, M., Moore, R., van Osch, M., Singer, R., Clemmons, P., and Strother, M. Relationships between hypercarbic reactivity, cerebral blood flow, and arterial circulation times in patients with moyamoya disease. Journal of Magnetic Resonance Imaging, 38(5): 1129–1139, 2013.

Donahue, M. J., Strother, M. K., Lindsey, K. P., Hocke, L. M., Tong, Y., and deB Frederick, B. Time delay processing of hypercapnic fMRI allows quantitative parameterization of cerebrovascular reactivity and blood flow delays. Journal of Cerebral Blood Flow & Metabolism, 36(10):1767–1779, 2016.

Draghici, A. E. and Taylor, J. A. The physiological basis and measurement of heart rate variability in humans. Journal of physiological anthropology, 35(1):22, 2016.

Duffin, J., Sobczyk, O., Crawley, A. P., Poublanc, J., Mikulis, D. J., and Fisher, J. A. The dynamics of cerebrovascular reactivity shown with transfer function analysis. NeuroImage, 114:207–16, 2015.

Dumas, A., Dierksen, G. A., Gurol, M. E., Halpin, A., Martinez-Ramirez, S., Schwab, K., Rosand, J., Viswanathan, A., Salat, D. H., Polimeni, J. R., and Greenberg, S. M. Functional magnetic resonance imaging detection of vascular reactivity in cerebral amyloid angiopathy. Annals of Neurology, 72(1):76–81, 2012.

Eaton, K. P., Szaflarski, J. P., Altaye, M., Ball, A. L., Kissela, B. M., Banks, C., and Holland, S. K. Reliability of fMRI for studies of language in post-stroke aphasia subjects. NeuroImage, 41(2):311–22, 2008.

Edelman, R. R., Siewert, B., Darby, D. G., Thangaraj, V., Nobre, A. C., Mesulam, M. M., and Warach, S. Qualitative mapping of cerebral blood flow and functional localization with echo-planar MR imaging and signal targeting with alternating radio frequency. Radiology, 192(2):513–520, 1994.

Edelstein, W. A., Glover, G. H., Hardy, C. J., and Redington, R. W. The intrinsic signal-to-noise ratio in NMR imaging. Magnetic Resonance in Medicine, 3(4):604–618, 1986.

Evans, A., Collins, D., Mills, S., Brown, E., Kelly, R., and Peters, T. 3D statistical neuroanatomical models from 305 MRI volumes. In IEEE Conference Record Nuclear Science Symposium and Medical Imaging Conference, pages 1813–1817. IEEE, 1993.

Falahpour, M., Refai, H., and Bodurka, J. Subject specific BOLD fMRI respiratory and cardiac response functions obtained from global signal. NeuroImage, 72:252–264, 2013.

Fazekas, F., Chawluk, J., Alavi, A., Hurtig, H., and Zimmerman, R. MR signal abnormalities at 1.5 T in Alzheimer's dementia and normal aging. American Journal of Roentgenology, 149 (2):351–356, 1987.

Fazlollahi, A., Bourgeat, P., Liang, X., Meriaudeau, F., Connelly, A., Salvado, O., and Calamante, F. Reproducibility of multiphase pseudo-continuous arterial spin labeling and the effect of post-processing analysis methods. NeuroImage, 117:191–201, 2015.

Fernández-Seara, M. A., Wang, Z., Wang, J., Rao, H.-Y., Guenther, M., Feinberg, D. A., and Detre, J. A. Continuous arterial spin labeling perfusion measurements using single shot 3D GRASE at 3 T. Magnetic Resonance in Medicine, 54(5):1241–1247, 2005.

Fierstra, J., Sobczyk, O., Battisti-Charbonney, A., Mandell, D. M., Poublanc, J., Crawley, A. P., Mikulis, D. J., Duffin, J., and Fisher, J. A. Measuring cerebrovascular reactivity: what stimulus to use? The Journal of physiology, 591(23):5809–21, 2013.

Fierstra, J., van Niftrik, B., Piccirelli, M., Burkhardt, J. K., Pangalu, A., Kocian, R., Valavanis, A., Weller, M., Regli, L., and Bozinov, O. Altered intraoperative cerebrovascular reactivity in brain areas of high-grade glioma recurrence. Magnetic Resonance Imaging, 34(6):803–808, 2016.

Figueiredo, P., Clare, S., and Jezzard, P. Quantitative perfusion measurements using pulsed arterial spin labeling: effects of large region-of-interest analysis. Journal of magnetic resonance imaging, 21(6):676–82, 2005.

Foster-Dingley, J. C., Moonen, J. E., de Craen, A. J., de Ruijter, W., van der Mast, R. C., and van der Grond, J. Blood Pressure Is Not Associated With Cerebral Blood Flow in Older Persons. Hypertension, 66(5):954–960, 2015.

Fox, M. D., Snyder, A. Z., Vincent, J. L., Corbetta, M., Van Essen, D. C., and Raichle, M. E. The human brain is intrinsically organized into dynamic, anticorrelated functional networks. Proceedings of the National Academy of Sciences of the United States of America, 102(27): 9673–8, 2005.

Friedman, L., Turner, J. A., Stern, H., Mathalon, D. H., Trondsen, L. C., and Potkin, S. G. Chronic smoking and the BOLD response to a visual activation task and a breath hold task in patients with schizophrenia and healthy controls. NeuroImage, 40(3):1181–94, 2008.

Friston, K., Holmes, A. P., Poline, J. B., Grasby, P. J., Williams, S. C., Frackowiak, R. S., and Turner, R. Analysis of fMRI Time-Series Revisited. NeuroImage, 2(1):45–53, 1995.

Friston, K. J., Williams, S., Howard, R., Frackowiak, R. S. J., and Turner, R. Movement-Related effects in fMRI time-series. Magnetic Resonance in Medicine, 35(3):346–355, 1996.

Friston, K., Fletcher, P., Josephs, O., Holmes, A., Rugg, M., and Turner, R. Event-Related fMRI: Characterizing Differential Responses. NeuroImage, 7(1):30–40, 1998.

Gati, J. S., Menon, R. S., Ugurbil, K., and Rutt, B. K. Experimental determination of the BOLD field strength dependence in vessels and tissue. Magnetic resonance in medicine, 38 (2):296–302, 1997.

Gauthier, C. J., Lefort, M., Mekary, S., Desjardins-Crépeau, L., Skimminge, A., Iversen, P., Madjar, C., Desjardins, M., Lesage, F., Garde, E., Frouin, F., Bherer, L., and Hoge, R. D. Hearts and minds: linking vascular rigidity and aerobic fitness with cognitive aging. Neurobiology of Aging, 36(1):304–314, 2015.

Geranmayeh, F., Wise, R. J., Leech, R., and Murphy, K. Measuring vascular reactivity with breath-holds after stroke: A method to aid interpretation of group-level BOLD signal changes in longitudinal fMRI studies. Human Brain Mapping, 36(5):1755–1771, 2015.

Geurts, L. J., Zwanenburg, J. J., Klijn, C. J., Luijten, P. R., and Biessels, G. J. Higher Pulsatility in Cerebral Perforating Arteries in Patients With Small Vessel Disease Related Stroke, a 7T MRI Study. Stroke, 50(1):62–68, 2019.

Gevers, S., van Osch, M. J., Bokkers, R. P. H., Kies, D. A., Teeuwisse, W. M., Majoie, C. B., Hendrikse, J., and Nederveen, A. J. Intra- and multicenter reproducibility of pulsed, continuous and pseudo-continuous arterial spin labeling methods for measuring cerebral perfusion.

Journal of cerebral blood flow and metabolism : official journal of the International Society of Cerebral Blood Flow and Metabolism, 31(8):1706–15, 2011.

Gil-Gouveia, R., Pinto, J., Figueiredo, P., Vilela, P. F., and Martins, I. P. An Arterial Spin Labeling MRI Perfusion Study of Migraine without Aura Attacks. Frontiers in neurology, 8: 280, 2017.

Glover, G. H., Li, T. Q., and Ress, D. Image-based method for retrospective correction of physiological motion effects in fMRI: RETROICOR. Magnetic resonance in medicine, 44(1): 162–7, 2000.

Golay, X., Petersen, E. T., Zimine, I., and Lim, T. C. C. Arterial Spin Labeling: a one-stop-shop for measurement of brain perfusion in the clinical settings. Conference proceedings: Annual International Conference of the IEEE Engineering in Medicine and Biology Society. IEEE Engineering in Medicine and Biology Society. Conference, 2007:4320–3, 2007.

Golay, X., Hendrikse, J., and Lim, T. C. C. Perfusion imaging using arterial spin labeling. Topics in magnetic resonance imaging : TMRI, 15(1):10–27, 2004.

Golestani, A. M., Chang, C., Kwinta, J. B., Khatamian, Y. B., and Jean Chen, J. Mapping the end-tidal CO2 response function in the resting-state BOLD fMRI signal: Spatial specificity, test–retest reliability and effect of fMRI sampling rate. NeuroImage, 104:266–277, 2015.

Golestani, A. M., Wei, L. L., and Chen, J. J. Quantitative mapping of cerebrovascular reactivity using resting-state BOLD fMRI: Validation in healthy adults. NeuroImage, 138:147–163, 2016.

Gonzales, M. M., Tarumi, T., Mumford, J. A., Ellis, R. C., Hungate, J. R., Pyron, M., Tanaka, H., and Haley, A. P. Greater BOLD response to working memory in endurance-trained adults revealed by breath-hold calibration. Human Brain Mapping, 35(7):2898–2910, 2014.

Gonzalez-At, J. B., Alsop, D. C., and Detre, J. A. Cerebral perfusion and arterial transit time changes during task activation determined with continuous arterial spin labeling. Magnetic Resonance in Medicine, 43(5):739–746, 2000.

Goode, S. D., Altaf, N., Auer, D. P., and MacSweeney, S. T. R. Carotid endarterectomy improves cerebrovascular reserve capacity preferentially in patients with preoperative impairment as indicated by asymmetric BOLD response to hypercapnia. European journal of vascular and endovascular surgery : the official journal of the European Society for Vascular Surgery, 38 (5):546–51, 2009.

Gregoire, S. M., Chaudhary, U. J., Brown, M. M., Yousry, T. A., Kallis, C., Jager, H. R., and Werring, D. J. The Microbleed Anatomical Rating Scale (MARS): Reliability of a tool to map brain microbleeds. Neurology, 73(21):1759–1766, 2009.

Greicius, M. D., Krasnow, B., Reiss, A. L., and Menon, V. Functional connectivity in the resting brain: A network analysis of the default mode hypothesis. Proceedings of the National Academy of Sciences, 100(1):253–258, 2003.

Greitz, D., Franck, A., and Nordell, B. On the pulsatile nature of intracranial and spinal CSF-circulation demonstrated by MR imaging. Acta radiologica (Stockholm, Sweden : 1987), 34 (4):321–8, 1993.

Greve, D. N. and Fischl, B. Accurate and robust brain image alignment using boundary-based registration. NeuroImage, 48(1):63–72, 2009.

Griffanti, L., Salimi-Khorshidi, G., Beckmann, C. F., Auerbach, E. J., Douaud, G., Sexton, C. E., Zsoldos, E., Ebmeier, K. P., Filippini, N., Mackay, C. E., Moeller, S., Xu, J., Yacoub, E., Baselli, G., Ugurbil, K., Miller, K. L., and Smith, S. M. ICA-based artefact removal and accelerated fMRI acquisition for improved resting state network imaging. NeuroImage, 95: 232–247, 2014.

Griswold, M. A., Jakob, P. M., Heidemann, R. M., Nittka, M., Jellus, V., Wang, J., Kiefer, B., and Haase, A. Generalized autocalibrating partially parallel acquisitions (GRAPPA). Magnetic Resonance in Medicine, 47(6):1202–1210, 2002.

Haight, T. J., Bryan, R. N., Erus, G., Davatzikos, C., Jacobs, D. R., D'Esposito, M., Lewis, C. E., and Launer, L. J. Vascular risk factors, cerebrovascular reactivity, and the default-mode brain network. NeuroImage, 115:7–16, 2015.

Hajjar, I., Zhao, P., Alsop, D., and Novak, V. Hypertension and Cerebral Vasoreactivity: A Continuous Arterial Spin Labeling Magnetic Resonance Imaging Study. Hypertension, 56(5): 859–864, 2010.

Halani, S., Kwinta, J. B., Golestani, A. M., Khatamian, Y. B., and Chen, J. J. Comparing cerebrovascular reactivity measured using BOLD and cerebral blood flow MRI: The effect of basal vascular tension on vasodilatory and vasoconstrictive reactivity. NeuroImage, 110: 110–123, 2015.

Hall, C. N., Reynell, C., Gesslein, B., Hamilton, N. B., Mishra, A., Sutherland, B. A., O'Farrell, F. M., Buchan, A. M., Lauritzen, M., and Attwell, D. Capillary pericytes regulate cerebral blood flow in health and disease. Nature, 508(7494):55–60, 2014.

Handwerker, D., Gazzaley, A., Inglis, B. A., and D'Esposito, M. Reducing vascular variability of fMRI data across aging populations using a breath holding task. Human brain mapping, 28(9):846–59, 2007.

Harvey, A. K., Pattinson, K. T., Brooks, J. C., Mayhew, S. D., Jenkinson, M., and Wise, R. G. Brainstem functional magnetic resonance imaging: Disentangling signal from physiological noise. Journal of Magnetic Resonance Imaging, 28(6):1337–1344, 2008.

Haussen, D. C., Katsnelson, M., Rodriguez, A., Campo, N., Campo-Bustillo, I., Romano, J. G., and Koch, S. Moderate correlation between breath-holding and CO(2) inhalation/hyperventilation methods for transcranial doppler evaluation of cerebral vasoreactivity. Journal of clinical ultrasound : JCU, 40(9):554–8, 2012.

Heyn, C., Poublanc, J., Crawley, A., Mandell, D., Han, J., Tymianski, M., TerBrugge, K., Fisher, J. A., and Mikulis, D. J. Quantification of cerebrovascular reactivity by blood oxygen level-dependent MR imaging and correlation with conventional angiography in patients with Moyamoya disease. American Journal of Neuroradiology, 31(5):862–7, 2010.

Hsu, Y.-Y., Chang, C.-N., Jung, S.-M., Lim, K.-E., Huang, J.-C., Fang, S.-Y., and Liu, H.-L. Blood oxygenation level-dependent MRI of cerebral gliomas during breath holding. Journal of magnetic resonance imaging : JMRI, 19(2):160–7, 2004.

Hu, X., Le, T. H., Parrish, T., and Erhard, P. Retrospective estimation and correction of physiological fluctuation in functional MRI. Magnetic Resonance in Medicine, 34(2):201–212, 1995.

Hudetz, A. G., Biswal, B. B., Shen, H., Lauer, K. K., and Kampine, J. P. Spontaneous Fluctuations in Cerebral Oxygen Supply. pages 551–559. 1998.

Huijts, M., Duits, A., Staals, J., Kroon, A. A., de Leeuw, P. W., and van Oostenbrugge, R. J. Basal ganglia enlarged perivascular spaces are linked to cognitive function in patients with cerebral small vessel disease. Current neurovascular research, 11(2):136–41, 2014.

Hund-Georgiadis, M., Zysset, S., Naganawa, S., Norris, D. G., and von Cramon, D. Y. Determination of Cerebrovascular Reactivity by Means of fMRI Signal Changes in Cerebral Microangiopathy: A Correlation with Morphological Abnormalities. Cerebrovascular Diseases, 16(2): 158–165, 2003.

Hurford, R., Charidimou, A., Fox, Z., Cipolotti, L., Jager, R., and Werring, D. J. MRI-visible perivascular spaces: relationship to cognition and small vessel disease MRI markers in ischaemic stroke and TIA. Journal of neurology, neurosurgery, and psychiatry, 85(5):522–5, 2014.

Hyvärinen, A. and Oja, E. Independent Component Analysis: Algorithms and Applications. Technical Report 5, 2000.

Iadecola, C. The Neurovascular Unit Coming of Age: A Journey through Neurovascular Coupling in Health and Disease. Neuron, 96(1):17–42, 2017.

Iranmahboob, A., Peck, K. K., Brennan, N. P., Karimi, S., Fisicaro, R., Hou, B., and Holodny, A. I. Vascular Reactivity Maps in Patients with Gliomas Using Breath-Holding BOLD fMRI. Journal of Neuroimaging, 26(2):232–239, 2016.

Ito, H., Kanno, I., Iida, H., Hatazawa, J., Shimosegawa, E., Tamura, H., and Okudera, T. Arterial fraction of cerebral blood volume in humans measured by positron emission tomography. Annals of nuclear medicine, 15(2):111–6, 2001.

Ito, H., Kanno, I., Kato, C., Sasaki, T., Ishii, K., Ouchi, Y., Iida, A., Okazawa, H., Hayashida, K., Tsuyuguchi, N., Kuwabara, Y., and Senda, M. Database of normal human cerebral blood flow, cerebral blood volume, cerebral oxygen extraction fraction and cerebral metabolic rate of oxygen measured by positron emission tomography with 15O-labelled carbon dioxide or water, carbon monoxide a. European Journal of Nuclear Medicine and Molecular Imaging, 31 (5):635–643, 2004.

Ito, S., Mardimae, A., Han, J., Duffin, J., Wells, G., Fedorko, L., Minkovich, L., Katznelson, R., Meineri, M., Arenovich, T., Kessler, C., and Fisher, J. A. Non-invasive prospective targeting of arterial P CO 2 in subjects at rest. The Journal of Physiology, 586(15):3675–3682, 2008.

Jackson, W. F. Potassium Channels in the Peripheral Microcirculation. Microcirculation, 12 (1):113–127, 2005.

Jahanian, H., Ni, W. W., Christen, T., Moseley, M. E., Tamura, M. K., and Zaharchuk, G. Spontaneous BOLD Signal Fluctuataions in Young Healthy Subjects and Elderly Patients with Chronic Kidney Disease. PLoS ONE, 9(3):e92539, 2014.

Jahanian, H., Christen, T., Moseley, M. E., Pajewski, N. M., Wright, C. B., Tamura, M. K., Zaharchuk, G., and Group, f. t. S. S. R. Measuring vascular reactivity with resting-state blood oxygenation level-dependent (BOLD) signal fluctuations: A potential alternative to the breath-holding challenge? Journal of Cerebral Blood Flow & Metabolism, page 0271678X1667092, 2016.

Jenkinson, M. and Smith, S. A global optimisation method for robust affine registration of brain images. Medical image analysis, 5(2):143–56, 2001.

Jenkinson, M., Bannister, P., Brady, M., and Smith, S. Improved Optimization for the Robust and Accurate Linear Registration and Motion Correction of Brain Images. NeuroImage, 17 (2):825–841, 2002.

Jenkinson, M., Beckmann, C. F., Behrens, T. E., Woolrich, M. W., and Smith, S. M. FSL. NeuroImage, 62(2):782–790, 2012.

Jessen, N. A., Munk, A. S. F., Lundgaard, I., and Nedergaard, M. The Glymphatic System: A Beginner's Guide. Neurochemical research, 40(12):2583–99, 2015.

Jo, H. J., Saad, Z. S., Simmons, W. K., Milbury, L. A., and Cox, R. W. Mapping sources of correlation in resting state FMRI, with artifact detection and removal. NeuroImage, 52(2): 571–582, 2010.

Johnson, N. L. and Welch, B. L. Applications of the Non-Central t-Distribution. Biometrika, 31(3/4):362, 1940.

Jones, N. L., Robertson, D. G., and Kane, J. W. Difference between end-tidal and arterial PCO2 in exercise. Journal of applied physiology: respiratory, environmental and exercise physiology, 47(5):954–60, 1979.

Jones, T. W. Discovery That the Veins of the Bat's Wing (Which Are Furnished with Valves) Are Endowed with Rhythmical Contractility, and That the Onward Flow of Blood Is Accelerated by Such Contraction. Edinburgh Medical and Surgical Journal, 79(195):367, 1853.

Jorge, J., Figueiredo, P., van der Zwaag, W., and Marques, J. P. Signal fluctuations in fMRI data acquired with 2D-EPI and 3D-EPI at 7 Tesla. Magnetic resonance imaging, 31(2):212–20, 2013.

Josephs, O., Turner, R., and Friston, K. Even-Related fMRI. Human Brain Mapping, 5:243–248, 1997.

Julian Seifter, David Sloane, and Austin Ratner. Concepts in Medical Physiology. Lippincott Williams and Wilkins, 2005.

Julien, C. The enigma of Mayer waves: Facts and models. Cardiovascular Research, 70(1): 12–21, 2006.

Kalcher, K., Boubela, R. N., Huf, W., Biswal, B. B., Baldinger, P., Sailer, U., Filzmoser, P., Kasper, S., Lamm, C., Lanzenberger, R., Moser, E., and Windischberger, C. RESCALE: Voxel-specific task-fMRI scaling using resting state fluctuation amplitude. NeuroImage, 70: 80–8, 2013.

Kannurpatti, S. S. and Biswal, B. B. Detection and scaling of task-induced fMRI-BOLD response using resting state fluctuations. NeuroImage, 40(4):1567–1574, 2008.

Kannurpatti, S. S., Motes, M. A., Rypma, B., and Biswal, B. B. Neural and vascular variability and the fMRI-BOLD response in normal aging. Magnetic Resonance Imaging, 28(4):466–476, 2010.

Kannurpatti, S. S., Motes, M. A., Rypma, B., and Biswal, B. B. Increasing measurement accuracy of age-related BOLD signal change: Minimizing vascular contributions by resting-state-fluctuation-of-amplitude scaling. Human Brain Mapping, 32(7):1125–1140, 2011.

Kannurpatti, S. S., Motes, M. A., Biswal, B. B., and Rypma, B. Assessment of unconstrained cerebrovascular reactivity marker for large age-range FMRI studies. PloS one, 9(2):e88751, 2014.

Kao, Y.-H., Guo, W.-Y., Liou, A. J.-K., Hsiao, Y.-H., and Chou, C.-C. The respiratory modulation of intracranial cerebrospinal fluid pulsation observed on dynamic echo planar images. Magnetic Resonance Imaging, 26(2):198–205, 2008.

Kassner, A., Winter, J. D., Poublanc, J., Mikulis, D. J., and Crawley, A. Blood-oxygen level dependent MRI measures of cerebrovascular reactivity using a controlled respiratory challenge: reproducibility and gender differences. Journal of magnetic Resonance Imaging, 31(2):298–304, 2010.

Kastrup, A., Dichgans, J., Niemeier, M., and Schabet, M. Changes of Cerebrovascular CO2 Reactivity During Normal Aging. Stroke, 29(7):1311–1314, 1998.

Kastrup, A., Krüger, G., Glover, G. H., Neumann-Haefelin, T., and Moseley, M. E. Regional variability of cerebral blood oxygenation response to hypercapnia. NeuroImage, 10(6):675–81, 1999.

Kastrup, A., Krüger, G., Neumann-Haefelin, T., and Moseley, M. E. Assessment of cerebrovascular reactivity with functional magnetic resonance imaging: comparison of CO(2) and breath holding. Journal of magnetic Resonance Imaging, 19(1):13–20, 2001.

Katura, T., Tanaka, N., Obata, A., Sato, H., and Maki, A. Quantitative evaluation of interrelations between spontaneous low-frequency oscillations in cerebral hemodynamics and systemic cardiovascular dynamics. NeuroImage, 31(4):1592–1600, 2006.

Kaufman, L. and Rousseeuw, P. J., editors. Finding Groups in Data. Wiley Series in Probability and Statistics. John Wiley & Sons, Inc., Hoboken, 1990.

Kazan, S. M., Mohammadi, S., Callaghan, M. F., Flandin, G., Huber, L., Leech, R., Kennerley, A., Windischberger, C., and Weiskopf, N. Vascular autorescaling of fMRI (VasA fMRI) improves sensitivity of population studies: A pilot study. NeuroImage, 124:794–805, 2016.

Kety, S. S. and Schmidt, C. F. THE DETERMINATION OF CEREBRAL BLOOD FLOW IN MAN BY THE -USE OF NITROIJS OXIDE IN LOW CONCENTRATIONS. Am J Physiol, 143:53–66, 1945.

Kim, J. S., Moon, D. H., Kim, G. E., Cho, Y. P., Ryu, J. S., and Lee, H. K. Acetazolamide stress brain-perfusion SPECT predicts the need for carotid shunting during carotid endarterectomy. Journal of nuclear medicine : official publication, Society of Nuclear Medicine, 41(11):1836–41, 2000.

Kim, S. G. Quantification of relative cerebral blood flow change by flow-sensitive alternating inversion recovery (FAIR) technique: application to functional mapping. Magnetic resonance in medicine, 34(3):293–301, 1995.

Kiviniemi, V., Wang, X., Korhonen, V., Keinänen, T., Tuovinen, T., Autio, J., Levan, P., Keilholz, S., Zang, Y.-F., Rgen Hennig, J., and Nedergaard, M. Ultra-fast magnetic resonance encephalography of physiological brain activity-Glymphatic pulsation mechanisms? 2016.

Kloppenborg, R. P., Nederkoorn, P. J., Geerlings, M. I., and van den Berg, E. Presence and progression of white matter hyperintensities and cognition. Neurology, 82(23):2127–2138, 2014.

Ko, E. A., Han, J., Jung, I. D., and Park, W. S. Physiological roles of K+ channels in vascular smooth muscle cells. Journal of smooth muscle research = Nihon Heikatsukin Gakkai kikanshi, 44(2):65–81, 2008.

Koehle, M. S., Giles, L., Curtis, A. N., Walsh, M. L., and White, M. D. Performance of a compact end-tidal forcing system. Respiratory physiology & neurobiology, 167(2):155–61, 2009.

Kong, Y., Jenkinson, M., Andersson, J., Tracey, I., and Brooks, J. C. Assessment of physiological noise modelling methods for functional imaging of the spinal cord. NeuroImage, 60(2):1538–1549, 2012.

Krainik, A., Hund-Georgiadis, M., Zysset, S., and von Cramon, D. Y. Regional impairment of cerebrovascular reactivity and BOLD signal in adults after stroke. Stroke; a journal of cerebral circulation, 36(6):1146–52, 2005.

Kraut, M. A., Beason-Held, L. L., Elkins, W. D., and Resnick, S. M. The Impact of Magnetic Resonance Imaging-Detected White Matter Hyperintensities on Longitudinal Changes in Regional Cerebral Blood Flow. Journal of Cerebral Blood Flow & Metabolism, 28(1):190–197, 2008.

Krüger, G. and Glover, G. H. Physiological noise in oxygenation-sensitive magnetic resonance imaging. Magnetic resonance in medicine, 46(4):631–7, 2001.

Krüger, G., Kastrup, A., and Glover, G. H. Neuroimaging at 1.5 T and 3.0 T: comparison of oxygenation-sensitive magnetic resonance imaging. Magnetic resonance in medicine, 45(4): 595–604, 2001.

Kuroda, S., Houkin, K., Kamiyama, H., Mitsumori, K., Iwasaki, Y., Abe, H., Yonas, H., Wechsler, L. R., Nemoto, E., and Pindzola, R. Long-Term Prognosis of Medically Treated Patients With Internal Carotid or Middle Cerebral Artery Occlusion: Can Acetazolamide Test Predict It? Editorial Comment: Can Acetazolamide Test Predict It? Stroke, 32(9):2110–2116, 2001.

Kwee, R. M. and Kwee, T. C. Virchow-Robin Spaces at MR Imaging. RadioGraphics, 27(4): 1071–1086, 2007.

Kwong, K. K., Belliveau, J. W., Chesler, D. A., Goldberg, I. E., Weisskoff, R. M., Poncelet, B. P., Kennedy, D. N., Hoppel, B. E., Cohen, M. S., and Turner, R. Dynamic magnetic resonance imaging of human brain activity during primary sensory stimulation. Proceedings of the National Academy of Sciences of the United States of America, 89(12):5675–9, 1992.

Kynast, J., Lampe, L., Luck, T., Frisch, S., Arelin, K., Hoffmann, K.-T., Loeffler, M., Riedel-Heller, S. G., Villringer, A., and Schroeter, M. L. White matter hyperintensities associated with small vessel disease impair social cognition beside attention and memory. Journal of Cerebral Blood Flow & Metabolism, 38(6):996–1009, 2018.

Lassen, N. A. Cerebral Blood Flow and Oxygen Consumption in Man. Physiological Reviews, 39(2):183–238, 1959.

Lawrence, A. J., Patel, B., Morris, R. G., MacKinnon, A. D., Rich, P. M., Barrick, T. R., and Markus, H. S. Mechanisms of Cognitive Impairment in Cerebral Small Vessel Disease: Multimodal MRI Results from the St George's Cognition and Neuroimaging in Stroke (SCANS) Study. PLoS ONE, 8(4):e61014, 2013.

Lawton, M. P. and Brody, E. M. Assessment of Older People: Self-Maintaining and Instrumental Activities of Daily Living. The Gerontologist, 9(3 Part 1):179–186, 1969.

Legdeur, N., Greenia, D., Woodworth, D., Fletcher, E., DeCarli, C., Kawas, C., and Corrada, M. White Matter Hyperintensities and Hippocampal Atrophy in Relation to Cognition: The 90+ Study (S34.005). Neurology, 92(15 Supplement), 2019.

Leoni, R. F., Mazzetto-Betti, K. C., Andrade, K. C., and de Araujo, D. B. Quantitative evaluation of hemodynamic response after hypercapnia among different brain territories by fMRI. NeuroImage, 41(4):1192–8, 2008.

Leoni, R. F., Mazzetto-Betti, K. C., Silva, A. C., Dos Santos, A. C., de Araujo, D. B., Leite, J. P., and Pontes-Neto, O. M. Assessing Cerebrovascular Reactivity in Carotid Steno-Occlusive Disease Using MRI BOLD and ASL Techniques. Radiology research and practice, 2012:268483, 2012.

Leontiev, O. and Buxton, R. B. Reproducibility of BOLD, perfusion, and CMRO2 measurements with calibrated-BOLD fMRI. NeuroImage, 35(1):175–184, 2007.

Li, T.-Q., Kastrup, A., Takahashi, A. M., and Moseley, M. E. Functional MRI of human brain during breath holding by BOLD and FAIR techniques. NeuroImage, 9(2):243–9, 1999.

Liem, M. K., Lesnik Oberstein, S., Haan, J., Boom, R. V. D., Ferrari, M. D., Buchem, M., and Grond, J. D. Cerebrovascular reactivity is a main determinant of white matter hyperintensity progression in CADASIL. AJNR. American journal of neuroradiology, 30(6):1244–7, 2009.

Lipp, I., Murphy, K., Wise, R., and Caseras, X. Understanding the contribution of neural and physiological signal variation to the low repeatability of emotion-induced BOLD responses. NeuroImage, 86:335–342, 2014.

Lipp, I., Murphy, K., Caseras, X., and Wise, R. G. Agreement and repeatability of vascular reactivity estimates based on a breath-hold task and a resting state scan. NeuroImage, 113: 387–96, 2015.

Liu, H.-L., Huang, J.-C., Wu, C.-T., and Hsu, Y.-Y. Detectability of blood oxygenation level-dependent signal changes during short breath hold duration. Magnetic resonance imaging, 20 (9):643–8, 2002.

Liu, P., Welch, B. G., King, D., Li, Y., Pinho, M., and Lu, H. Can resting state fMRI be used to map cerebrovascular reactivity? In Proc. Intl. Soc. Mag. Reson. Med. 23 (2015), page 50, 2015.

Liu, P., Li, Y., Pinho, M., Park, D. C., Welch, B. G., and Lu, H. Cerebrovascular reactivity mapping without gas challenges. NeuroImage, 146:320–326, 2017.

Liu, T. T. Neurovascular factors in resting-state functional MRI. NeuroImage, 80:339–348, 2013.

Lu, H., Golay, X., Pekar, J. J., and van Zijl, P. C. Functional magnetic resonance imaging based on changes in vascular space occupancy. Magnetic Resonance in Medicine, 50(2):263–274, 2003.

Luh, W. M., Wong, E. C., Bandettini, P. A., and Hyde, J. S. QUIPSS II with thin-slice TI1 periodic saturation: a method for improving accuracy of quantitative perfusion imaging using pulsed arterial spin labeling. Magnetic resonance in medicine : official journal of the Society of Magnetic Resonance in Medicine / Society of Magnetic Resonance in Medicine, 41(6):1246–54, 1999.

Lyoubi-Idrissi, A., Jouvent, E., Poupon, C., and Chabriat, H. Diffusion magnetic resonance imaging in cerebral small vessel disease. Revue Neurologique, 173(4):201–210, 2017.

MacIntosh, B. J., Klassen, L. M., and Menon, R. S. Transient hemodynamics during a breath hold challenge in a two part functional imaging study with simultaneous near-infrared spectroscopy in adult humans. NeuroImage, 20(2):1246–52, 2003.

MacIntosh, B. J., Lindsay, A. C., Kylintireas, I., Kuker, W., Gunther, M., Robson, M. D., Kennedy, J., Choudhury, R. P., and Jezzard, P. Multiple Inflow Pulsed Arterial Spin-Labeling Reveals Delays in the Arterial Arrival Time in Minor Stroke and Transient Ischemic Attack. American Journal of Neuroradiology, 31(10):1892–1894, 2010.

Magon, S., Basso, G., Farace, P., Ricciardi, G. K., Beltramello, A., and Sbarbati, A. Reproducibility of BOLD signal change induced by breath holding. NeuroImage, 45(3):702–12, 2009.

Makedonov, I., Black, S. E., Macintosh, B. J., and Chao, L. BOLD fMRI in the White Matter as a Marker of Aging and Small Vessel Disease. 2013.

Makedonov, I., Chen, J. J., Masellis, M., MacIntosh, B. J., and Alzheimer's Disease Neuroimaging Initiative. Physiological fluctuations in white matter are increased in Alzheimer's disease and correlate with neuroimaging and cognitive biomarkers. Neurobiology of Aging, 37:12–18, 2016.

Mäkiranta, M. J., Ruohonen, J., Suominen, K., Sonkajärvi, E., Salomäki, T., Kiviniemi, V., Seppänen, T., Alahuhta, S., Jäntti, V., and Tervonen, O. BOLD-contrast functional MRI signal changes related to intermittent rhythmic delta activity in EEG during voluntary hyperventilation—simultaneous EEG and fMRI study. NeuroImage, 22(1):222–231, 2004.

Mandell, D., Han, J., Poublanc, J., Crawley, A., Stainsby, J. A., Fisher, J. A., and Mikulis, D. J. Mapping cerebrovascular reactivity using blood oxygen level-dependent MRI in Patients with arterial steno-occlusive disease: comparison with arterial spin labeling MRI. Stroke, 39(7): 2021–8, 2008a.

Mandell, D. M., Han, J. S., Poublanc, J., Crawley, A. P., Kassner, A., Fisher, J. A., and Mikulis, D. J. Selective reduction of blood flow to white matter during hypercapnia corresponds with leukoaraiosis. Stroke; a journal of cerebral circulation, 39(7):1993–8, 2008b.

Margulies, D. S., Kelly, A. C., Uddin, L. Q., Biswal, B. B., Castellanos, F. X., and Milham, M. P. Mapping the functional connectivity of anterior cingulate cortex. NeuroImage, 37(2): 579–588, 2007.

Mark, C., Slessarev, M., Ito, S., Han, J., Fisher, J. A., and Pike, G. B. Precise control of end-tidal carbon dioxide and oxygen improves BOLD and ASL cerebrovascular reactivity measures. Magnetic resonance in medicine : official journal of the Society of Magnetic Resonance in Medicine / Society of Magnetic Resonance in Medicine, 64(3):749–56, 2010.

Mark, C. I., Fisher, J. A., and Pike, G. B. Improved fMRI calibration: precisely controlled hyperoxic versus hypercapnic stimuli. NeuroImage, 54(2):1102–11, 2011.

Mark, C. I., Mazerolle, E. L., and Chen, J. J. Metabolic and vascular origins of the BOLD effect: Implications for imaging pathology and resting-state brain function. Journal of magnetic resonance imaging : JMRI, 42(2):231–46, 2015.

Markus, H. and Cullinane, M. Severely impaired cerebrovascular reactivity predicts stroke and TIA risk in patients with carotid artery stenosis and occlusion. Brain : a journal of neurology, 124(Pt 3):457–67, 2001.

Markus, H. S., Lythgoe, D. J., Ostegaard, L., O'Sullivan, M., and Williams, S. C. Reduced cerebral blood flow in white matter in ischaemic leukoaraiosis demonstrated using quantitative

exogenous contrast based perfusion MRI. Journal of neurology, neurosurgery, and psychiatry, 69(1):48–53, 2000.

Mazziotta, J., Toga, A., Evans, A., Fox, P., Lancaster, J., Zilles, K., Woods, R., Paus, T., Simpson, G., Pike, B., Holmes, C., Collins, L., Thompson, P., MacDonald, D., Iacoboni, M., Schormann, T., Amunts, K., Palomero-Gallagher, N., Geyer, S., Parsons, L., Narr, K., Kabani, N., Le Goualher, G., Boomsma, D., Cannon, T., Kawashima, R., and Mazoyer, B. A probabilistic atlas and reference system for the human brain: International Consortium for Brain Mapping (ICBM). Philosophical transactions of the Royal Society of London. Series B, Biological sciences, 356(1412):1293–322, 2001.

Meadows, G. E., Dunroy, H. M. A., Morrell, M. J., and Corfield, D. R. Hypercapnic cerebral vascular reactivity is decreased, in humans, during sleep compared with wakefulness. Journal of Applied Physiology, 94(6):2197–2202, 2003.

Mestre, H., Tithof, J., Du, T., Song, W., Peng, W., Sweeney, A. M., Olveda, G., Thomas, J. H., Nedergaard, M., and Kelley, D. H. Flow of cerebrospinal fluid is driven by arterial pulsations and is reduced in hypertension. Nature Communications, 9(1):4878, 2018.

Mezue, M., Segerdahl, A. R., Okell, T. W., Chappell, M. A., Kelly, M. E., and Tracey, I. Optimization and reliability of multiple postlabeling delay pseudo-continuous arterial spin labeling during rest and stimulus-induced functional task activation. Journal of cerebral blood flow and metabolism : official journal of the International Society of Cerebral Blood Flow and Metabolism, 34(12):1919–27, 2014.

Mitsis, G. D., Poulin, M. J., Robbins, P. A., and Marmarelis, V. Z. Nonlinear Modeling of the Dynamic Effects of Arterial Pressure and CO 2 Variations on Cerebral Blood Flow in Healthy Humans. IEEE TRANSACTIONS ON BIOMEDICAL ENGINEERING, 51(11), 2004.

Momjian-Mayor, I. and Baron, J.-C. The Pathophysiology of Watershed Infarction in Internal Carotid Artery Disease Review of Cerebral Perfusion Studies. 2005.

Moreton, F. C., Dani, K. A., Goutcher, C., O'Hare, K., and Muir, K. W. Respiratory challenge MRI: Practical aspects. NeuroImage: Clinical, 11:667–677, 2016.

Moreton, F. C., Cullen, B., Delles, C., Santosh, C., Gonzalez, R. L., Dani, K., and Muir, K. W. Vasoreactivity in CADASIL: Comparison to structural MRI and neuropsychology. Journal of Cerebral Blood Flow & Metabolism, 38(6):1085–1095, 2018.

Mukherjee, B., Houston, G. C., Papadakis, N. G., Carpenter, T. A., Hall, L. D., and Huang, C. L.-H. Mapping of the cerebral response to acetazolamide using graded asymmetric spin echo EPI. Magnetic Resonance Imaging, 23(9):907–920, 2005.

Müller, M., Voges, M., Piepgras, U., and Schimrigk, K. Assessment of cerebral vasomotor reactivity by transcranial Doppler ultrasound and breath-holding. A comparison with acetazolamide as vasodilatory stimulus. Stroke, 26(1):96–100, 1995.

Murphy, K., Coulson, J., Harris, A. D., Fjodorova, M., and Wise, R. G. The association between pulse wave velocity, as a marker of sympathetic tone, and resting state BOLD signals. Technical report, 2011a.

Murphy, K., Harris, A. D., and Wise, R. G. Robustly measuring vascular reactivity differences with breath-hold: normalising stimulus-evoked and resting state BOLD fMRI data. NeuroImage, 54(1):369–79, 2011b.

Murphy, K., Birn, R. M., Handwerker, D. A., Jones, T. B., and Bandettini, P. A. The impact of global signal regression on resting state correlations: Are anti-correlated networks introduced? NeuroImage, 44(3):893–905, 2009.

Murphy, K., Birn, R. M., and Bandettini, P. A. Resting-state fMRI confounds and cleanup. NeuroImage, 80:349–359, 2013.

Mutsaerts, H. J., van Osch, M. J., Zelaya, F. O., Wang, D. J., Nordhøy, W., Wang, Y., Wastling, S., Fernandez-Seara, M. A., Petersen, E., Pizzini, F. B., Fallatah, S., Hendrikse, J., Geier, O., Günther, M., Golay, X., Nederveen, A. J., Bjørnerud, A., and Groote, I. R. Multi-vendor reliability of arterial spin labeling perfusion MRI using a near-identical sequence: Implications for multi-center studies. NeuroImage, 113:143–152, 2015.

Muxworthy, J. F. Breath holding studies: Relationship to lung volume. U.S.A.F. Technical Reports, Wright-Patterson Air Force Base, Dayton,, 6528:452–456, 1951.

Naganawa, S., Norris, D. G., Zysset, S., and Mildner, T. Regional Differences of fMR Signal Changes Induced by Hyperventilation : Comparison Between SE-EPI and GE-EPI at 3-T. 30:23–30, 2002.

Nakada, K., Yoshida, D., Fukumoto, M., and Yoshida, S. Chronological analysis of physiological T2* signal change in the cerebrum during breath holding. Journal of magnetic resonance imaging : JMRI, 13(3):344–51, 2001.

Nilsson, H. and Aalkjaer, C. Vasomotion: Mechanisms and Physiological Importance. Molecular Interventions, 3(2):79–89, 2003.

Nolte, J. The human brain: an introduction to its functional anatomy. Mosby/Elsevier, 2009.

Noth, U., Kotajima, F., Deichmann, R., Turner, R., and Corfield, D. R. Mapping of the cerebral vascular response to hypoxia and hypercapnia using quantitative perfusion MRI at 3T. NMR in Biomedicine, 21(5):464–472, 2008.

Novack, P., SHENKIN, H. A., BORTIN, L., GOLUBOFF, B., SOFFE, A. M., Batson, P., and Golden, D. The effects of carbon dioxide inhalation upon the cerebral blood flow and cerebral oxygen consumption in vascular disease. The Journal of clinical investigation, 32(8):696–702, 1953.

Nunes, S., Bianciardi, M., Dias, A., Abreu, R., Rodrigues, J., Silveira, L. M., Wald, L. L., and Figueiredo, P. Subject-specific modeling of physiological noise in resting-state fMRI at 7T. In International Society of Magnetic Resonance in Medicine (ISMRM), page 23, 2015.

Nunes, S., Bianciardi, M., Dias, A., Silveira, L. M., and Lawrence, L. Physiological Noise Model Comparison for Resting-State Fmri At 7 T. pages 1001–1004, 2016.

Nylander, R., Kilander, L., Ahlström, H., Lind, L., and Larsson, E.-M. Small Vessel Disease on Neuroimaging in a 75-Year-Old Cohort (PIVUS): Comparison With Cognitive and Executive Tests. Frontiers in Aging Neuroscience, 10:217, 2018.

Obrig, H., Neufang, M., Wenzel, R., Kohl, M., Steinbrink, J., Einhäupl, K., and Villringer, A. Spontaneous Low Frequency Oscillations of Cerebral Hemodynamics and Metabolism in Human Adults. NeuroImage, 12(6):623–639, 2000.

Ogawa, S., Lee, T. M., Kay, A. R., and Tank, D. W. Brain magnetic resonance imaging with contrast dependent on blood oxygenation. Proceedings of the National Academy of Sciences of the United States of America, 87(24):9868–72, 1990.

Ogawa, S., Tank, D. W., Menon, R., Ellermann, J. M., Kim, S. G., Merkle, H., and Ugurbil, K. Intrinsic signal changes accompanying sensory stimulation: functional brain mapping with magnetic resonance imaging. Proceedings of the National Academy of Sciences of the United States of America, 89(13):5951–5, 1992.

Okell, T. W., Chappell, M. A., Kelly, M. E., and Jezzard, P. Cerebral blood flow quantification using vessel-encoded arterial spin labeling. Journal of cerebral blood flow and metabolism : official journal of the International Society of Cerebral Blood Flow and Metabolism, 33(11): 1716–24, 2013.

O'Sullivan, M., Jarosz, J. M., Martin, R. J., Deasy, N., Powell, J. F., and Markus, H. S. MRI hyperintensities of the temporal lobe and external capsule in patients with CADASIL. Neurology, 56(5):628–34, 2001.

Pamilo, S., Malinen, S., Hotta, J., and Seppä, M. A correlation-based method for extracting subject-specific components and artifacts from group-fMRI data. European Journal of Neuroscience, 42(9):2726–2741, 2015.

Pantoni, L. Cerebral small vessel disease: from pathogenesis and clinical characteristics to therapeutic challenges. The Lancet. Neurology, 9(7):689–701, 2010.

Papantchev, V., Stoinova, V., Aleksandrov, A., Todorova-Papantcheva, D., Hristov, S., Petkov, D., Nachev, G., and Ovtscharoff, W. The role of Willis circle variations during unilateral selective cerebral perfusion: a study of 500 circles†. European Journal of Cardio-Thoracic Surgery, 44(4):743–753, 2013.

Pasi, M., van Uden, I. W., Tuladhar, A. M., de Leeuw, F.-E., and Pantoni, L. White Matter Microstructural Damage on Diffusion Tensor Imaging in Cerebral Small Vessel Disease. Stroke, 47(6):1679–1684, 2016.

Patel, B. and Markus, H. S. Magnetic resonance imaging in cerebral small vessel disease and its use as a surrogate disease marker. International journal of stroke : official journal of the International Stroke Society, 6(1):47–59, 2011.

Patenaude, B., Smith, S. M., Kennedy, D. N., and Jenkinson, M. A Bayesian model of shape and appearance for subcortical brain segmentation. NeuroImage, 56(3):907–922, 2011.

Pauling, L. and Coryell, C. The magnetic properties and structure of hemoglobin, oxyhemoglobin adn carbonmonoxyhemoglobin. pages 210–216, 1936.

Payne, S. Cerebral autoregulation : control of blood flow in the brain. 2016.

Peacock, J., Black, D., DeLone, D., and Welker, K. Use of a Simple Breath-Holding Task for Cerebrovascular Reactivity Scans in Clinical Functional MR Imaging. Neurographics, 6(4): 213–218, 2016.

Peebles, K., Celi, L., McGrattan, K., Murrell, C., Thomas, K., and Ainslie, P. N. Human cerebrovascular and ventilatory CO2 reactivity to end-tidal, arterial and internal jugular vein PCO2. The Journal of physiology, 584(Pt 1):347–57, 2007.

Petersen, E. T., Mouridsen, K., and Golay, X. The QUASAR reproducibility study, Part II: Results from a multi-center Arterial Spin Labeling test-retest study. NeuroImage, 49(1): 104–13, 2010.

Peterson, E. C., Wang, Z., and Britz, G. Regulation of cerebral blood flow. International journal of vascular medicine, 2011:823525, 2011.

Petrica, L., Petrica, M., Vlad, A., Bob, F., Gluhovschi, C., Gluhovschi, G., Jianu, C. D., Ursoniu, S., Schiller, A., Velciov, S., Trandafirescu, V., and Bozdog, G. Cerebrovascular reactivity is impaired in patients with non-insulin-dependent diabetes mellitus and microangiopathy. Wiener klinische Wochenschrift, 119(11-12):365–71, 2007.

Pillai, J. J. and Mikulis, D. J. Cerebrovascular Reactivity Mapping : An Evolving Standard for Clinical Functional Imaging. AJNR. American journal of neuroradiology, pages 1–7, 2014.

Pillai, J. J. and Zacá, D. Clinical utility of cerebrovascular reactivity mapping in patients with low grade gliomas. World journal of clinical oncology, 2(12):397–403, 2011.

Pimentel, M. A. F., Vilela, P., Sousa, I., and Figueiredo, P. Localization of the hand motor area by arterial spin labeling and blood oxygen level-dependent functional magnetic resonance imaging. Human Brain Mapping, 34(1):96–108, 2013.

Pindzola, R. R., Balzer, J. R., Nemoto, E. M., Goldstein, S., and Yonas, H. Cerebrovascular Reserve in Patients with Carotid Occlusive Disease Assessed by Stable Xenon-Enhanced CT Cerebral Blood Flow and Transcranial Doppler. Stroke, 32:1811–1817, 2001.

Pinto, J., Jorge, J., Sousa, I., Vilela, P., and Figueiredo, P. Fourier modeling of the BOLD response to a breath-hold task: Optimization and reproducibility. NeuroImage, 135:223–231, 2016.

Pinto, J., Nunes, S., Bianciardi, M., Dias, A., Silveira, L. M., Wald, L. L., and Figueiredo, P. Improved 7 Tesla resting-state fMRI connectivity measurements by cluster-based modeling of respiratory volume and heart rate effects. NeuroImage, 153:262–272, 2017.

Ponsaing, L. B., Lindberg, U., Rostrup, E., Iversen, H. K., Larsson, H. B., and Jennum, P. Impaired cerebrovascular reactivity in obstructive sleep apnea: a case-control study. Sleep Medicine, 43:7–13, 2018.

Posse, S., Olthoff, U., Weckesser, M., Jäncke, L., Müller-Gärtner, H. W., and Dager, S. R. Regional dynamic signal changes during controlled hyperventilation assessed with blood oxygen level-dependent functional MR imaging. AJNR. American journal of neuroradiology, 18(9): 1763–70, 1997.

Pradhan, R. K. and Chakravarthy, V. S. Informational dynamics of vasomotion in microvascular networks: a review. Acta Physiologica, 201(2):193–218, 2011.

Prilipko, O., Huynh, N., Thomason, M. E., Kushida, C. A., and Guilleminault, C. An fMRI study of cerebrovascular reactivity and perfusion in obstructive sleep apnea patients before and after CPAP treatment. Sleep Medicine, 15(8):892–898, 2014.

Prisman, E., Slessarev, M., Han, J., Poublanc, J., Mardimae, A., Crawley, A., Fisher, J. A., and Mikulis, D. J. Comparison of the effects of independently-controlled end-tidal PCO(2) and PO(2) on blood oxygen level-dependent (BOLD) MRI. Journal of magnetic resonance imaging : JMRI, 27(1):185–91, 2008.

Promjunyakul, N., Lahna, D., Kaye, J., Dodge, H., Erten-Lyons, D., Rooney, W., and Silbert, L. Characterizing the white matter hyperintensity penumbra with cerebral blood flow measures. NeuroImage: Clinical, 8:224–229, 2015.

Promjunyakul, N.-o., Lahna, D. L., Kaye, J. A., Dodge, H. H., Erten-Lyons, D., Rooney, W. D., and Silbert, L. C. Comparison of cerebral blood flow and structural penumbras in relation to white matter hyperintensities: A multi-modal magnetic resonance imaging study. Journal of Cerebral Blood Flow & Metabolism, 36(9):1528–1536, 2016.

Purdon, P. L. and Weisskoff, R. M. Effect of temporal autocorrelation due to physiological noise and stimulus paradigm on voxel-level false-positive rates in fMRI. Human brain mapping, 6 (4):239–49, 1998.

Raichle, M. E., MacLeod, A. M., Snyder, A. Z., Powers, W. J., Gusnard, D. A., and Shulman, G. L. A default mode of brain function. Proceedings of the National Academy of Sciences of the United States of America, 98(2):676–82, 2001.

Raj, D., Anderson, A. W., and Gore, J. C. Respiratory effects in human functional magnetic resonance imaging due to bulk susceptibility changes. Physics in medicine and biology, 46 (12):3331–40, 2001.

Rasmussen, P., Stie, H., Nielsen, B., and Nybo, L. Enhanced cerebral CO2 reactivity during strenuous exercise in man. European Journal of Applied Physiology, 96(3):299–304, 2005.

Ratnatunga, C. and Adiseshiah, M. Increase in middle cerebral artery velocity on breath holding: A simplified test of cerebral perfusion reserve. European Journal of Vascular Surgery, 4(5): 519–523, 1990.

Raut, R. V., Nair, V. A., Sattin, J. A., and Prabhakaran, V. Hypercapnic evaluation of vascular reactivity in healthy aging and acute stroke via functional MRI. NeuroImage: Clinical, 12: 173–179, 2016.

Reivich, M. ARTERIAL PCO2 AND CEREBRAL HEMODYNAMICS. The American journal of physiology, 206:25–35, 1964.

Richiardi, J., Monsch, A. U., Haas, T., Barkhof, F., Van de Ville, D., Radü, E. W., Kressig, R. W., and Haller, S. Altered cerebrovascular reactivity velocity in mild cognitive impairment and Alzheimer's disease. Neurobiology of Aging, 36(1):33–41, 2015.

Riecker, A., Grodd, W., Klose, U., Schulz, J. B., Gröschel, K., Erb, M., Ackermann, H., and Kastrup, A. Relation between regional functional MRI activation and vascular reactivity to carbon dioxide during normal aging. Journal of cerebral blood flow and metabolism : official journal of the International Society of Cerebral Blood Flow and Metabolism, 23(5):565–73, 2003.

Robbins, P. A., Swanson, G. D., and Howson, M. G. A prediction-correction scheme for forcing alveolar gases along certain time courses. J Appl Physiol, 52(5):1353–1357, 1982.

Roberts, T., Jezzard, P., and Bulte, D. P. Comparison of Breath Holding Techniques for the Calibration of FMRI Measurements of Oxygen Metabolism. In Proc. Intl. Soc. Mag. Reason. Med., page 1, 2009.

Rostrup, E., Law, I., Blinkenberg, M., Larsson, H., Born, A. P., Holm, S., and Paulson, O. Regional differences in the CBF and BOLD responses to hypercapnia: a combined PET and fMRI study. NeuroImage, 11(2):87–97, 2000.

Rostrup, E., Knudsen, G., Law, I., Holm, S., Larsson, H., and Paulson, O. The relationship between cerebral blood flow and volume in humans. NeuroImage, 24(1):1–11, 2005.

Roy, C. S. and Sherrington, C. S. On the Regulation of the Blood-supply of the Brain. The Journal of physiology, 11(1-2):85–158.17, 1890.

Saad, Z. S., Gotts, S. J., Murphy, K., Chen, G., Jo, H. J., Martin, A., and Cox, R. W. Trouble at Rest: How Correlation Patterns and Group Differences Become Distorted After Global Signal Regression. Brain Connectivity, 2(1):25–32, 2012.

Saito, H., Ogasawara, K., Suzuki, T., Kuroda, H., Kobayashi, M., Yoshida, K., Kubo, Y., and Ogawa, A. Adverse effects of intravenous acetazolamide administration for evaluation of cerebrovascular reactivity using brain perfusion single-photon emission computed tomography in patients with major cerebral artery steno-occlusive diseases. Neurologia medico-chirurgica, 51(7):479–83, 2011.

Salimi-Khorshidi, G., Douaud, G., Beckmann, C. F., Glasser, M. F., Griffanti, L., and Smith, S. M. Automatic denoising of functional MRI data: Combining independent component analysis and hierarchical fusion of classifiers. NeuroImage, 90:449–468, 2014.

Sam, K., Conklin, J., Holmes, K. R., Sobczyk, O., Poublanc, J., Crawley, A. P., Mandell, D. M., Venkatraghavan, L., Duffin, J., Fisher, J. A., Black, S. E., and Mikulis, D. J. Impaired dynamic cerebrovascular response to hypercapnia predicts development of white matter hyperintensities. NeuroImage. Clinical, 11:796–801, 2016a.

Sam, K., Crawley, A. P., Conklin, J., Poublanc, J., Sobczyk, O., Mandell, D. M., Venkatraghavan, L., Duffin, J., Fisher, J. A., Black, S. E., and Mikulis, D. J. Development of White Matter Hyperintensity Is Preceded by Reduced Cerebrovascular Reactivity. Annals of Neurology, 80 (2):277–285, 2016b.

Sam, K., Peltenburg, B., Conklin, J., Sobczyk, O., Poublanc, J., Crawley, A. P., Mandell, D. M., Venkatraghavan, L., Duffin, J., Fisher, J. A., Black, S. E., and Mikulis, D. J. Cerebrovascular reactivity and white matter integrity. Neurology, 87(22):2333–2339, 2016c.

Sandrone, S., Bacigaluppi, M., Galloni, M. R., Cappa, S. F., Moro, A., Catani, M., Filippi, M., Monti, M. M., Perani, D., and Martino, G. Weighing brain activity with the balance: Angelo Mosso's original manuscripts come to light. Brain, 137(2):621–633, 2014.

Sato, Y., Ogasawara, K., Kuroda, H., Suzuki, T., Chida, K., Fujiwara, S., Aso, K., Kobayashi, M., Yoshida, K., Terasaki, K., and Ogawa, A. Preoperative Central Benzodiazepine Receptor Binding Potential and Cerebral Blood Flow Images on SPECT Predict Development of New Cerebral Ischemic Events and Cerebral Hyperperfusion After Carotid Endarterectomy. Journal of Nuclear Medicine, 52(9):1400–1407, 2011.

Schubert, T., Santini, F., Stalder, A., Bock, J., Meckel, S., Bonati, L., Markl, M., and Wetzel, S. Dampening of Blood-Flow Pulsatility along the Carotid Siphon: Does Form Follow Function? American Journal of Neuroradiology, 32(6):1107–1112, 2011.

Schwertfeger, N., Neu, P., Schlattmann, P., Lemke, H., Heuser, I., and Bajbouj, M. Cerebrovascular reactivity over time course in healthy subjects. Journal of the neurological sciences, 249 (2):135–9, 2006.

Scouten, A. and Schwarzbauer, C. Paced respiration with end-expiration technique offers superior BOLD signal repeatability for breath-hold studies. NeuroImage, 43(2):250–7, 2008.

Secher, N. H., Seifert, T., and Van Lieshout, J. J. Cerebral blood flow and metabolism during exercise: implications for fatigue. Journal of Applied Physiology, 104(1):306–314, 2008.

Shehzad, Z., Kelly, A. M. C., Reiss, P. T., Gee, D. G., Gotimer, K., Uddin, L. Q., Lee, S. H., Margulies, D. S., Roy, A. K., Biswal, B. B., Petkova, E., Castellanos, F. X., and Milham, M. P. The Resting Brain: Unconstrained yet Reliable. Cerebral Cortex, 19(10):2209–2229, 2009.

Shi, Y. and Wardlaw, J. M. Update on cerebral small vessel disease: a dynamic whole-brain disease. Stroke and Vascular Neurology, 2016.

Shi, Y., Thrippleton, M. J., Marshall, I., and Wardlaw, J. M. Intracranial pulsatility in patients with cerebral small vessel disease: a systematic review. Clinical science (London, England : 1979), 132(1):157–171, 2018.

Shiino, A., Morita, Y., Tsuji, A., Maeda, K., Ito, R., Furukawa, A., Matsuda, M., and Inubushi, T. Estimation of Cerebral Perfusion Reserve by Blood Oxygenation Level-Dependent Imaging: Comparison with Single Photon Emission Computed Tomography. Journal of Cerebral Blood Flow & Metabolism, 23:121–135, 2003.

Shin, K., Ahn, K., Choi, H., Jung, S., Kim, B., Jeon, S., and Hong, Y. DCE and DSC MR perfusion imaging in the differentiation of recurrent tumour from treatment-related changes in patients with glioma. Clinical Radiology, 69(6):e264–e272, 2014.

Shmueli, K., van Gelderen, P., de Zwart, J., Horovitz, S., Fukunaga, M., Jansma, J., and Duyn, J. Low-frequency fluctuations in the cardiac rate as a source of variance in the resting-state fMRI BOLD signal. NeuroImage, 38(2):306–20, 2007.

Shrout, P. E. and Fleiss, J. L. Intraclass Correlations: Uses in Assessing Rater Reliability. Psychological Bulletin, 86(2):420–428, 1979.

Silva, A. C. and Kim, S.-G. Perfusion-based functional magnetic resonance imaging. Concepts in Magnetic Resonance, 16A(1):16–27, 2003.

Silvestrini, M., Vernieri, F., Troisi, E., Passarelli, F., Matteis, M., Pasqualetti, P., Rossini, P. M., and Caltagirone, C. Cerebrovascular reactivity in carotid artery occlusion: possible implications for surgical management of selected groups of patients. Acta neurologica Scandinavica, 99(3):187–91, 1999.

Skow, R. J., Day, T. A., Fuller, J. E., Bruce, C. D., and Steinback, C. D. The ins and outs of breath holding: simple demonstrations of complex respiratory physiology. Advances in physiology education, 39(3):223–31, 2015.

Slessarev, M., Han, J., Mardimae, A., Prisman, E., Preiss, D., Volgyesi, G., Ansel, C., Duffin, J., and Fisher, J. A. Prospective targeting and control of end-tidal CO2 and O2 concentrations. The Journal of physiology, 581(Pt 3):1207–19, 2007.

Smith, E. E., Schneider, J. A., Wardlaw, J. M., and Greenberg, S. M. Cerebral microinfarcts: the invisible lesions. The Lancet Neurology, 11(3):272–282, 2012.

Smith, S. Fast robust automated brain extraction. Human Brain Mapping, 17:143–155, 2002.

Smith, S. M., Zhang, Y., Jenkinson, M., Chen, J., Matthews, P. M., Federico, A., and De Stefano, N. Accurate, robust, and automated longitudinal and cross-sectional brain change analysis. NeuroImage, 17(1):479–89, 2002.

Smith, S. M., Jenkinson, M., Woolrich, M. W., Beckmann, C. F., Behrens, T. E., Johansen-Berg, H., Bannister, P. R., De Luca, M., Drobnjak, I., Flitney, D. E., Niazy, R. K., Saunders, J., Vickers, J., Zhang, Y., De Stefano, N., Brady, J. M., and Matthews, P. M. Advances in functional and structural MR image analysis and implementation as FSL. NeuroImage, 23: S208–S219, 2004.

Smith, S. M., Fox, P. T., Miller, K. L., Glahn, D. C., Fox, P. M., Mackay, C. E., Filippini, N., Watkins, K. E., Toro, R., Laird, A. R., and Beckmann, C. F. Correspondence of the brain's functional architecture during activation and rest. Proceedings of the National Academy of Sciences of the United States of America, 106(31):13040–5, 2009.

Sommer, L. Z., Iscoe, S., Robicsek, A., Kruger, J., Silverman, J., Rucker, J., Dickstein, J., Volgyesi, G., and Fisher, J. A simple breathing circuit minimizing changes in alveolar ventilation during hyperpnoea. European Respiratory Journal, 12(3):698–701, 1998.

Somogyi, R. B., Vesely, A. E., Preiss, D., Prisman, E., Volgyesi, G., Azami, T., Iscoe, S., Fisher, J. A., and Sasano, H. Precise control of end-tidal carbon dioxide levels using sequential rebreathing circuits. Anaesthesia and intensive care, 33(6):726–32, 2005.

Sousa, I., Santos, N., Sanches, J., and Figueiredo, P. Challenges for non-invasive brain perfusion quantification using arterial spin labeling. The neuroradiology journal, 24(1):77–83, 2011.

Sousa, I., Vilela, P., and Figueiredo, P. Reproducibility of hypocapnic cerebrovascular reactivity measurements using BOLD fMRI in combination with a paced deep breathing task. NeuroImage, 98:31–41, 2014a.

Sousa, I., Vilela, P., and Figueiredo, P. Reproducibility of the quantification of arterial and tissue contributions in multiple postlabeling delay arterial spin labeling. Journal of magnetic resonance imaging : JMRI, 40(6):1453–62, 2014b.

Spano, V., Mandell, D., Sam, K., Battisti-charbonney, A., Pucci, O., Han, J., Crawley, A., Fisher, J. A., and Mikulis, D. J. CO2 Blood Oxygen Level-dependent MR Mapping of Cerebrovascular Reserve in a Clinical Population : Safety, Tolerability, and Technical Feasibility. Radiology, 266(2), 2013.

Svaldi, D. O., Joshi, C., Robinson, M. E., Shenk, T. E., Abbas, K., Nauman, E. A., Leverenz, L. J., and Talavage, T. M. Cerebrovascular Reactivity Alterations in Asymptomatic High School Football Players. Developmental Neuropsychology, 40(2):80–84, 2015.

Swanson, G. D. and Bellville, J. W. Step changes in end-tidal CO2: methods and implications. J Appl Physiol, 39(3):377–385, 1975.

Switzer, A. R., McCreary, C., Batool, S., Stafford, R. B., Frayne, R., Goodyear, B. G., and Smith, E. E. Longitudinal decrease in blood oxygenation level dependent response in cerebral amyloid angiopathy. NeuroImage: Clinical, 11:461–467, 2016.

Taccone, F. S., Scolletta, S., Franchi, F., Donadello, K., and Oddo, M. Brain perfusion in sepsis. Current vascular pharmacology, 11(2):170–86, 2013.

Tameem, A. and Krovvidi, H. Cerebral physiology. Continuing Education in Anaesthesia Critical Care & Pain, 13(4):113–118, 2013.

Tancredi, F. B. and Hoge, R. D. Comparison of cerebral vascular reactivity measures obtained using breath-holding and CO2 inhalation. Journal of cerebral blood flow and metabolism : official journal of the International Society of Cerebral Blood Flow and Metabolism, 33(7): 1066–74, 2013.

Tancredi, F. B., Gauthier, C. J., Madjar, C., Bolar, D. S., Fisher, J. A., Wang, D. J. J., and Hoge, R. D. Comparison of pulsed and pseudocontinuous arterial spin-labeling for measuring CO2 -induced cerebrovascular reactivity. Journal of magnetic resonance imaging : JMRI, 36 (2):312–21, 2012.

Tchistiakova, E., Anderson, N. D., Greenwood, C. E., and MacIntosh, B. J. Combined effects of type 2 diabetes and hypertension associated with cortical thinning and impaired cerebrovascular reactivity relative to hypertension alone in older adults. NeuroImage: Clinical, 5:36–41, 2014.

Tchistiakova, E., Crane, D. E., Mikulis, D. J., Anderson, N. D., Greenwood, C. E., Black, S. E., and MacIntosh, B. J. Vascular risk factor burden correlates with cerebrovascular reactivity but not resting state coactivation in the default mode network. Journal of Magnetic Resonance Imaging, 42(5):1369–1376, 2015.

ten Dam, V. H., van den Heuvel, D. M. J., de Craen, A. J. M., Bollen, E. L. E. M., Murray, H. M., Westendorp, R. G. J., Blauw, G. J., and van Buchem, M. A. Decline in Total Cerebral Blood Flow Is Linked with Increase in Periventricular but Not Deep White Matter Hyperintensities. Radiology, 243(1):198–203, 2007.

Thomas, B., Logan, W., Donner, E. J., and Shroff, M. Assessment of cerebrovascular reactivity using real-time BOLD fMRI in children with moyamoya disease: a pilot study. Child's nervous system : ChNS : official journal of the International Society for Pediatric Neurosurgery, 29 (3):457–63, 2013.

Thomason, M. E. and Glover, G. H. Controlled inspiration depth reduces variance in breath-holding-induced BOLD signal. NeuroImage, 39(1):206–14, 2008.

Thomason, M. E., Burrows, B., Gabrieli, J. D. E., and Glover, G. H. Breath holding reveals differences in fMRI BOLD signal in children and adults. NeuroImage, 25(3):824–37, 2005.

Thomason, M. E., Foland, L. C., and Glover, G. H. Calibration of BOLD fMRI using breath holding reduces group variance during a cognitive task. Human brain mapping, 28(1):59–68, 2007.

Thulborn, K. R., Waterton, J. C., Matthews, P. M., and Radda, G. K. Oxygenation dependence of the transverse relaxation time of water protons in whole blood at high field. Biochimica et Biophysica Acta (BBA) - General Subjects, 714(2):265–270, 1982.

Tierney, T. M., Weiss-Croft, L. J., Centeno, M., Shamshiri, E. A., Perani, S., Baldeweg, T., Clark, C. A., and Carmichael, D. W. FIACH: A biophysical model for automatic retrospective noise control in fMRI. NeuroImage, 124(Pt A):1009–1020, 2016.

Tjandra, T., Brooks, J. C. W., Figueiredo, P., Wise, R. G., Matthews, P. M., and Tracey, I. Quantitative assessment of the reproducibility of functional activation measured with BOLD and MR perfusion imaging: implications for clinical trial design. NeuroImage, 27(2):393–401, 2005.

Tohka, J., Foerde, K., Aron, A. R., Tom, S. M., Toga, A. W., and Poldrack, R. A. Automatic independent component labeling for artifact removal in fMRI. NeuroImage, 39(3):1227–45, 2008.

Tong, Y., Bergethon, P. R., and Frederick, B. D. An improved method for mapping cerebrovascular reserve using concurrent fMRI and near-infrared spectroscopy with Regressor Interpolation at Progressive Time Delays (RIPTiDe). Neuroimage, 56(4):2047–2057, 2011.

Tong, Y. and deB. Frederick, B. Time lag dependent multimodal processing of concurrent fMRI and near-infrared spectroscopy (NIRS) data suggests a global circulatory origin for low-frequency oscillation signals in human brain. NeuroImage, 53(2):553–564, 2010.

Toro, R., Fox, P. T., and Paus, T. Functional coactivation map of the human brain. Cerebral cortex (New York, N.Y. : 1991), 18(11):2553–9, 2008.

Triantafyllou, C., Hoge, R., Krueger, G., Wiggins, C., Potthast, A., Wiggins, G., and Wald, L. Comparison of physiological noise at 1.5 T, 3 T and 7 T and optimization of fMRI acquisition parameters. NeuroImage, 26(1):243–250, 2005.

Tsvetanov, K. A., Henson, R. N. A., Tyler, L. K., Davis, S. W., Shafto, M. A., Taylor, J. R., Williams, N., Cam-CAN, and Rowe, J. B. The effect of ageing on fMRI: Correction for the confounding effects of vascular reactivity evaluated by joint fMRI and MEG in 335 adults. Human Brain Mapping, 36(6):2248–2269, 2015.

Turner, R., Jezzard, P., Wen, H., Kwong, K. K., Le Bihan, D., Zeffiro, T., and Balaban, R. S. Functional mapping of the human visual cortex at 4 and 1.5 tesla using deoxygenation contrast EPI. Magnetic resonance in medicine, 29(2):277–9, 1993.

Urback, A. L., MacIntosh, B. J., and Goldstein, B. I. Cerebrovascular reactivity measured by functional magnetic resonance imaging during breath-hold challenge: A systematic review. Neuroscience & Biobehavioral Reviews, 79:27–47, 2017.

van der Kouwe, A. J., Benner, T., Salat, D. H., and Fischl, B. Brain morphometry with multiecho MPRAGE. NeuroImage, 40(2):559–569, 2008.

van der Veen, P. H., Muller, M., Vincken, K. L., Hendrikse, J., Mali, W. P. T. M., van der Graaf, Y., Geerlings, M. I., and SMART Study Group. Longitudinal Relationship Between Cerebral Small-Vessel Disease and Cerebral Blood Flow: The Second Manifestations of Arterial Disease-Magnetic Resonance Study. Stroke, 46(5):1233–1238, 2015.

van der Zande, F., Hofman, P., and Backes, W. Mapping hypercapnia-induced cerebrovascular reactivity using BOLD MRI. Neuroradiology, 47(2):114–20, 2005.

van der Zwaag, W., Francis, S., Head, K., Peters, A., Gowland, P., Morris, P., and Bowtell, R. fMRI at 1.5, 3 and 7 T: Characterising BOLD signal changes. NeuroImage, 47(4):1425–1434, 2009.

Van Dijk, K. R., Sabuncu, M. R., and Buckner, R. L. The influence of head motion on intrinsic functional connectivity MRI. NeuroImage, 59(1):431–438, 2012.

van Leijsen, E. M. C., Tay, J., van Uden, I. W. M., Kooijmans, E. C. M., Bergkamp, M. I., van der Holst, H. M., Ghafoorian, M., Platel, B., Norris, D. G., Kessels, R. P. C., Markus, H. S., Tuladhar, A. M., and de Leeuw, F.-E. Memory decline in elderly with cerebral small

vessel disease explained by temporal interactions between white matter hyperintensities and hippocampal atrophy. Hippocampus, 2018.

van Niftrik, C. H. B., Piccirelli, M., Bozinov, O., Pangalu, A., Valavanis, A., Regli, L., and Fierstra, J. Fine tuning breath-hold-based cerebrovascular reactivity analysis models. Brain and Behavior, 6(2):n/a–n/a, 2016.

van Niftrik, C. H. B., Piccirelli, M., Bozinov, O., Maldaner, N., Strittmatter, C., Pangalu, A., Valavanis, A., Regli, L., and Fierstra, J. Impact of baseline CO 2 on Blood-Oxygenation-Level-Dependent MRI measurements of cerebrovascular reactivity and task-evoked signal activation. Magnetic Resonance Imaging, 49:123–130, 2018.

Van Oers, C. A. M. M., Vink, M., Van Zandvoort, M. J. E., Van Der Worp, H. B., De Haan, E. H. F., Jaap Kappelle, L., Ramsey, N. F., and Dijkhuizen, R. M. Contribution of the left and right inferior frontal gyrus in recovery from aphasia. A functional MRI study in stroke patients with preserved hemodynamic responsiveness. NeuroImage, 49:885–893, 2010.

van Oers, C. A. M. M., van der Worp, H. B., Kappelle, L. J., Raemaekers, M. A. H., Otte, W. M., and Dijkhuizen, R. M. Etiology of language network changes during recovery of aphasia after stroke. Scientific Reports, 8(1):856, 2018.

van Opstal, A. M., van Rooden, S., van Harten, T., Ghariq, E., Labadie, G., Fotiadis, P., Gurol, M. E., Terwindt, G. M., Wermer, M. J. H., van Buchem, M. A., Greenberg, S. M., and van der Grond, J. Cerebrovascular function in presymptomatic and symptomatic individuals with hereditary cerebral amyloid angiopathy: a case-control study. The Lancet Neurology, 16(2):115–122, 2017.

van Osch, M. J., Teeuwisse, W. M., Chen, Z., Suzuki, Y., Helle, M., and Schmid, S. Advances in arterial spin labelling MRI methods for measuring perfusion and collateral flow. Journal of Cerebral Blood Flow & Metabolism, 38(9):1461–1480, 2018.

van Sloten, T. T., Protogerou, A. D., Henry, R. M., Schram, M. T., Launer, L. J., and Stehouwer, C. D. Association between arterial stiffness, cerebral small vessel disease and cognitive impairment: A systematic review and meta-analysis. Neuroscience & Biobehavioral Reviews, 53:121–130, 2015.

Vermeer, S. E., Prins, N. D., den Heijer, T., Hofman, A., Koudstaal, P. J., and Breteler, M. M. Silent Brain Infarcts and the Risk of Dementia and Cognitive Decline. New England Journal of Medicine, 348(13):1215–1222, 2003.

Vesely, A., Sasano, H., Volgyesi, G., Somogyi, R., Tesler, J., Fedorko, L., Grynspan, J., Crawley, A., Fisher, J. A., and Mikulis, D. J. MRI mapping of cerebrovascular reactivity using square wave changes in end-tidal PCO2. Magnetic resonance in medicine : official journal of the

Society of Magnetic Resonance in Medicine / Society of Magnetic Resonance in Medicine, 45 (6):1011–3, 2001.

Vestergaard, M. B. and Larsson, H. B. Cerebral metabolism and vascular reactivity during breath-hold and hypoxic challenge in freedivers and healthy controls. Journal of Cerebral Blood Flow & Metabolism, 0(00):1–15, 2017.

Vidorreta, M., Wang, Z., Rodríguez, I., Pastor, M. A., Detre, J. A., and Fernández-Seara, M. A. Comparison of 2D and 3D single-shot ASL perfusion fMRI sequences. NeuroImage, 66:662–71, 2013.

Villien, M., Wey, H.-Y., Mandeville, J. B., Catana, C., Polimeni, J. R., Sander, C. Y., Zürcher, N. R., Chonde, D. B., Fowler, J. S., Rosen, B. R., and Hooker, J. M. Dynamic Functional Imaging of Brain Glucose Utilization using fPET-FDG. NeuroImage, 100:192, 2014.

Vogt, K. M., Ibinson, J. W., Schmalbrock, P., and Small, R. H. Comparison between end-tidal CO2 and respiration volume per time for detecting BOLD signal fluctuations during paced hyperventilation. Magnetic resonance imaging, 29(9):1186–94, 2011.

Vorstrup, S., Henriksen, L., and Paulson, O. B. Effect of acetazolamide on cerebral blood flow and cerebral metabolic rate for oxygen. The Journal of clinical investigation, 74(5):1634–9, 1984.

Wang, M., Su, J., Zhang, J., Zhang, H., Liu, J.-r., and Du, X. A preliminary study on the amplitude of low frequency fluctuations in CADASIL. In Proceedings of the 25th International Society for Magnetic Resonance in Medicine Conference, 2017.

Wang, P., Hou, P., Kesler, S., Colen, R., Kumar, A., Prabhu, S., and Liu, H. Resting-State Fluctuation of BOLD Signal Amplitude for Mapping Cerebrovascular Reactivity in Presurgical Functional MRI. Medical Physics, 43(6):3646–3647, 2016.

Wang, Y., Saykin, A. J., Pfeuffer, J., Lin, C., Mosier, K. M., Shen, L., and Kim, S.Hutchins, G. D. Regional reproducibility of pulsed arterial spin labeling perfusion imaging at 3T. Neuroimage, 54(2):1188–1195, 2011.

Wardlaw, J. M., Smith, E. E., Biessels, G. J., Cordonnier, C., Fazekas, F., Frayne, R., Lindley, R. I., O'Brien, J. T., Barkhof, F., Benavente, O. R., Black, S. E., Brayne, C., Breteler, M., Chabriat, H., Decarli, C., de Leeuw, F.-E., Doubal, F., Duering, M., Fox, N. C., Greenberg, S., Hachinski, V., Kilimann, I., Mok, V., van Oostenbrugge, R., Pantoni, L., Speck, O., Stephan, B. C. M., Teipel, S., Viswanathan, A., Werring, D., Chen, C., Smith, C., van Buchem, M., Norrving, B., Gorelick, P. B., Dichgans, M., and STandards for ReportIng Vascular changes on nEuroimaging (STRIVE v1), S. f. R. V. c. o. n. S. Neuroimaging standards for research into small vessel disease and its contribution to ageing and neurodegeneration. The Lancet. Neurology, 12(8):822–38, 2013.

Wardlaw, J. M., Makin, S. J., Valdés Hernández, M. C., Armitage, P. A., Heye, A. K., Chappell, F. M., Muñoz-Maniega, S., Sakka, E., Shuler, K., Dennis, M. S., and Thrippleton, M. J. Blood-brain barrier failure as a core mechanism in cerebral small vessel disease and dementia: evidence from a cohort study. Alzheimer's & Dementia, 13(6):634–643, 2017.

Weckesser, M., Posse, S., Olthoff, U., Kemna, L., Dager, S., and Muller-Gartner, H.-W. Functional imaging of the visual cortex with bold-contrast MRI: Hyperventilation decreases signal response. Magnetic Resonance in Medicine, 41(1):213–216, 1999.

Wei, E. P., Kontos, H. A., and Patterson, J. L. Dependence of pial arteriolar response to hypercapnia on vessel size. The American journal of physiology, 238(5):697–703, 1980.

Weissenbacher, A., Kasess, C., Gerstl, F., Lanzenberger, R., Moser, E., and Windischberger, C. Correlations and anticorrelations in resting-state functional connectivity MRI: A quantitative comparison of preprocessing strategies. NeuroImage, 47(4):1408–1416, 2009.

Williams, D. S., Detre, J. A., Leigh, J. S., and Koretsky, A. P. Magnetic resonance imaging of perfusion using spin inversion of arterial water. Proceedings of the National Academy of Sciences of the United States of America, 89(1):212–6, 1992.

Willie, C. K., Tzeng, Y.-C., Fisher, J. A., and Ainslie, P. N. Integrative regulation of human brain blood flow. The Journal of Physiology, 592:841–859, 2014.

Wintermark, M., Sesay, M., Barbier, E., Borbély, K., Dillon, W. P., Eastwood, J. D., Glenn, T. C., Grandin, C. B., Pedraza, S., Soustiel, J.-F., Nariai, T., Zaharchuk, G., Caillé, J.-M., Dousset, V., and Yonas, H. Comparative overview of brain perfusion imaging techniques. Stroke; a journal of cerebral circulation, 36(9):e83–99, 2005.

Wise, R. G., Pattinson, K. T. S., Bulte, D. P., Chiarelli, P. A., Mayhew, S. D., Balanos, G. M., O'Connor, D. F., Pragnell, T. R., Robbins, P. A., Tracey, I., and Jezzard, P. Dynamic forcing of end-tidal carbon dioxide and oxygen applied to functional magnetic resonance imaging. Journal of cerebral blood flow and metabolism : official journal of the International Society of Cerebral Blood Flow and Metabolism, 27(8):1521–32, 2007.

Wise, R. G., Ide, K., Poulin, M. J., and Tracey, I. Resting fluctuations in arterial carbon dioxide induce significant low frequency variations in BOLD signal. NeuroImage, 21(4):1652–1664, 2004.

Wong, E. C., Buxton, R. B., and Frank, L. R. Implementation of quantitative perfusion imaging techniques for functional brain mapping using pulsed arterial spin labeling. NMR in biomedicine, 10(4-5):237–49, 1997.

Wong, E. C., Buxton, R. B., and Frank, L. R. Quantitative imaging of perfusion using a single subtraction (QUIPSS and QUIPSS II). Magnetic resonance in medicine : official journal of

the Society of Magnetic Resonance in Medicine / Society of Magnetic Resonance in Medicine, 39(5):702–8, 1998.

Wong, E. C. Vessel-encoded arterial spin-labeling using pseudocontinuous tagging. Magnetic Resonance in Medicine, 58(6):1086–1091, 2007.

Wong, E. C., Cronin, M., Wu, W.-C., Inglis, B., Frank, L. R., and Liu, T. T. Velocity-selective arterial spin labeling. Magnetic Resonance in Medicine, 55(6):1334–1341, 2006.

Woolrich, M. W., Ripley, B. D., Brady, M., and Smith, S. M. Temporal Autocorrelation in Univariate Linear Modeling of FMRI Data. NeuroImage, 14(6):1370–1386, 2001.

Worsley, K. and Friston, K. Analysis of fMRI Time-Series Revisited—Again. NeuroImage, 2(3): 173–181, 1995.

Worsley, K., Liao, C., Aston, J., Petre, V., Duncan, G., Morales, F., and Evans, A. A General Statistical Analysis for fMRI Data. NeuroImage, 15(1):1–15, 2002.

Wu, B., Lou, X., Wu, X., and Ma, L. Intra- and interscanner reliability and reproducibility of 3D whole-brain pseudo-continuous arterial spin-labeling MR perfusion at 3T. Journal of Magnetic Resonance Imaging, 39(2):402–409, 2014.

Wu, P., Bandettini, P. A., Harper, R. M., and Handwerker, D. A. Effects of Thoracic Pressure Changes on MRI Signals in the Brain. Journal of Cerebral Blood Flow & Metabolism, 35(6): 1024–1032, 2015.

Wu, W.-C. C., St Lawrence, K. S., Licht, D. J., and Wang, D. J. Quantification issues in arterial spin labeling perfusion magnetic resonance imaging. Topics in magnetic resonance imaging : TMRI, 21(2):65–73, 2010.

Yacoub, E., Shmuel, A., Pfeuffer, J., Van De Moortele, P. F., Adriany, G., Andersen, P., Vaughan, J. T., Merkle, H., Ugurbil, K., and Hu, X. Imaging brain function in humans at 7 Tesla. Magnetic resonance in medicine, 45(4):588–94, 2001.

Yan, X., Zhang, J., Gong, Q., and Weng, X. Cerebrovascular reactivity among native-raised high altitude residents: an fMRI study. BMC neuroscience, 12(1):94, 2011.

Yezhuvath, U., Lewis-Amezcua, K., Varghese, R., Xiao, G., and Lu, H. On the assessment of cerebrovascular reactivity using hypercapnia BOLD MRI. NMR in biomedicine, 22(7):779–86, 2009.

Yezhuvath, U. S., Uh, J., Cheng, Y., Martin-Cook, K., Weiner, M., Diaz-Arrastia, R., van Osch, M., and Lu, H. Forebrain-dominant deficit in cerebrovascular reactivity in Alzheimer's disease. Neurobiology of Aging, 33(1):75–82, 2012.

Yu-Feng, Z., Yong, H., Chao-Zhe, Z., Qing-Jiu, C., Man-Qiu, S., Meng, L., Li-Xia, T., Tian-Zi, J., and Yu-Feng, W. Altered baseline brain activity in children with ADHD revealed by resting-state functional MRI. Brain and Development, 29(2):83–91, 2007.

Yuan, R., Di, X., Kim, E. H., Barik, S., Rypma, B., and Biswal, B. B. Regional homogeneity of resting-state fMRI contributes to both neurovascular and task activation variations. Magnetic Resonance Imaging, 31:1492–1500, 2013.

Zacà, D., Jovicich, J., Nadar, S. R., Voyvodic, J. T., and Pillai, J. J. Cerebrovascular reactivity mapping in patients with low grade gliomas undergoing presurgical sensorimotor mapping with BOLD fMRI. Journal of magnetic resonance imaging : JMRI, 40(2):383–90, 2014.

Zauner, A. and Muizelaar, J. P. Measuring Cerebral Blood Flow and Metabolism. Chapman & Hall, London, 1997.

Zeestraten, E. A., Lawrence, A. J., Lambert, C., Benjamin, P., Brookes, R. L., Mackinnon, A. D., Morris, R. G., Barrick, T. R., and Markus, H. S. Change in multimodal MRI markers predicts dementia risk in cerebral small vessel disease. Neurology, 89(18):1869–1876, 2017.

Zhang, Y., Brady, M., and Smith, S. Segmentation of brain MR images through a hidden Markov random field model and the expectation-maximization algorithm. IEEE transactions on medical imaging, 20(1):45–57, 2001.

Zhang, Z., Liao, W., Chen, H., Mantini, D., Ding, J.-R., Xu, Q., Wang, Z., Yuan, C., Chen, G., Jiao, Q., and Lu, G. Altered functional-structural coupling of large-scale brain networks in idiopathic generalized epilepsy. Brain, 134(10):2912–2928, 2011.

Zhao, P., Alsop, D. C., AbdulJalil, A., Selim, M., Lipsitz, L., Novak, P., Caplan, L., Hu, K., and Novak, V. Vasoreactivity and peri-infarct hyperintensities in stroke. Neurology, 72(7): 643–649, 2009.

Zhou, A. and Jia, J. Different cognitive profiles between mild cognitive impairment due to cerebral small vessel disease and mild cognitive impairment of Alzheimer's disease origin. Journal of the International Neuropsychological Society, 15(6):898–905, 2009.

Zhou, Y., Rodgers, Z. B., and Kuo, A. H. Cerebrovascular reactivity measured with arterial spin labeling and blood oxygen level dependent techniques. Magnetic resonance imaging, 33 (5):566–76, 2015.

Ziyeh, S., Rick, J., Reinhard, M., Hetzel, A., Mader, I., and Speck, O. Blood oxygen level-dependent MRI of cerebral CO2 reactivity in severe carotid stenosis and occlusion. Stroke, 36(4):751–756, 2005.

Zou, Q.-H., Zhu, C.-Z., Yang, Y., Zuo, X.-N., Long, X.-Y., Cao, Q.-J., Wang, Y.-F., and Zang, Y.-F. An improved approach to detection of amplitude of low-frequency fluctuation (ALFF)

for resting-state fMRI: fractional ALFF. Journal of neuroscience methods, 172(1):137–41, 2008.

Zuo, X.-N., Di Martino, A., Kelly, C., Shehzad, Z. E., Gee, D. G., Klein, D. F., Castellanos, F. X., Biswal, B. B., and Milham, M. P. The oscillating brain: Complex and reliable. 2010.

Zwanenburg, J. J. and van Osch, M. J. Targeting Cerebral Small Vessel Disease With MRI. Stroke, 48(11):3175–3182, 2017.

A

Chapter 2 - Vasoactive Challenges for CVR Assessment

In this appendix, supplementary information about the most commonly used techniques that induce a variation in cerebral blood flow (CBF) will be provided. This section is divided into two main topics, invasive methods and non-invasive methods, although a more in depth discussion of the latter was provided in Chapter 5.

A.1 Invasive Methods

A.1.1 Acetazolamide

The most common approach to induce a vascular response in clinical settings is the use of acetazolamide. This component is a selective inhibitor of the enzyme carbonic anhydrase that decreases the conversion rate of CO_2 to bicarbonate (Equation 2.5), causing hypercapnia and hence vasodilation and increased CBF (Aso et al., 2009; Müller et al., 1995; Vorstrup et al., 1984). The acetazolamide (ACZ) method does not require patient cooperation and its administration does not alter systemic blood pressure (Kuroda et al., 2001; Mukherjee et al., 2005). However, ACZ is injected intravenously making it an invasive method and does not allow evaluation of

the vasoconstrictor capability of the cerebrovasculature. Furthermore ACZ injection can lead to variable responses across subjects (Fierstra et al., 2013), and may result in adverse reactions, including dizziness, nausea, vomiting and headache (Dahl et al., 1995; Saito et al., 2011).

A.1.2 Respiratory Gas Manipulation Techniques

A.1.2.A Fixed Inspired Challenge

Another way to induce a variation in arterial pressure of gases is the direct inhalation of a gas mixture with fixed composition that is modified compared with air. Even though this requires an additional apparatus, it is a passive task, being less dependent on the subjects cooperation. CO_2 concentrations from 3 to 10% have been generally used and even though no adverse effects were observed in such studies, CO_2 concentrations greater than 7% were reported to be exhausting (Rostrup et al., 2000). Traditionally, subjects breathe via a non-rebreathing valve, inhaling a gas mixture from a reservoir. A concern with this method is the variability and unpredictability of the attained $PaCO_2$ values reached, mainly because they are also determined by the subject's ventilator response to CO_2 and minute ventilation (Wise et al., 2007). Furthermore, there is a significant interaction between changes in $PaCO_2$ and PaO_2, since increasing the concentration of inspired CO_2 may stimulate an increase in minute ventilation, reducing $PaCO_2$ and increasing PaO_2. Even though studies have demonstrated that BOLD and CBF reactivity to PaO_2 is much smaller than to $PaCO_2$, CVR can also be significantly distorted by these changes in PaO_2, particularly in BOLD signal (Mark et al., 2010; Prisman et al., 2008).

In order to overcome some of these issues, different techniques have been developed and improved along the years and these include Dynamic End-Tidal Forcing (Robbins et al., 1982; Wise et al., 2007); Sequential Gas Delivery (Kassner et al., 2010; Mandell et al., 2008b; van der Zande et al., 2005; Vesely et al., 2001); and Prospective End-Tidal Targeting (Mark et al., 2010; Prisman et al., 2008; Slessarev et al., 2007; Spano et al., 2013).

A.1.2.B Dynamic End-Tidal Forcing

The Dynamic End-Tidal Forcing (DEF) technique uses computer feedback control of inspired CO_2 and O_2 to rapidly and independently correct the supplied gas. This way is possible to achieve specified target levels of CO_2 and O_2 on a breath-by-breath basis, independently of minute-ventilation (Wise et al., 2007). The technique was developed originally using fast-acting solenoid valves to control gas flows (Robbins et al., 1982; Swanson and Bellville, 1975) but, since then, mass flow controllers have been introduced and more compact and portable end-tidal forcing have been developed (Koehle et al., 2009). DEF provides an accurate, target-controlled, repeatable respiratory challenge and is able to force rapid and sharp changes in arterial gases allowing more complex respiratory challenges to be implemented (Wise et al., 2007). However, some issues remain. Feedback mechanisms can be hampered by the time delay of the exhaled gas to reach the gas sensors. Furthermore, the DEF requires a very sophisticated

prediction–correction scheme, requiring very high gas flows to attain peak inspiratory flows (Slessarev et al., 2007). Contrarily to the fixed-inspiration approach previously described, the DEF approach can be used in conjunction with hyperventilation to maintain a normal O_2 and a steady but below normal $PETCO_2$.

A.1.2.C Sequential Gas Delivery

In 1998, Sommer and colleagues developed and tested a simple breathing circuit that minimizes the effect of minute ventilation on alveolar ventilation independently from the breathing pattern (Sommer et al., 1998). The circuit comprised a non-rebreathing valve connected to two gas reservoirs, one for gas without CO_2 (fresh gas) and another with a gas reserve with a CO_2 approximately equal to that in mixed venous blood. The flow of fresh gas was set to just match the minute ventilation of the subject during resting conditions. This flow was identified by observing that the reservoir collapsed at the end of each breath. When the subject's minute ventilation exceeded the fresh gas flow, the circuit passively added the reserve gas at a rate proportional to the increase in ventilation and, because the CO_2 in the reserve gas had a CO_2 level approximately equal to that in mixed venous blood, it does not contribute to pulmonary CO_2 exchange, maintaining arterial concentration of CO_2 constant (Sommer et al., 1998). However, in this circuit the reserve gas is only an approximation of alveolar gas composition. Alternatively, CO_2 can be supplied from actual alveolar gas expired on the previous breath, thus providing more precise regulation (Banzett et al., 2000). This was done by Banzett et al., using a large tube as the alveolar gas reservoir and calling this new method Sequential Gas Delivery (SGD) circuit. In their study they demonstrated the "clamping" properties of SGD, adjusting differences in end-tidal gases but also making intentional large changes in CO_2 and O_2 and holding each level constant, independently from minute ventilation (Banzett et al., 2000). In contrast with DEF, the SGD method is self-regulating, not requiring complex feedback protocols. Furthermore, the response of the SGD's device is essentially instantaneous (Banzett et al., 2000; Somogyi et al., 2005), optimizing the efficiency of the experimental procedure (Vesely et al., 2001). Nevertheless, the major limitation of this method remains the inability to precisely target desired end-tidal CO_2 and O_2 concentrations and to control them independently (Slessarev et al., 2007).

A.1.2.D Prospective End-Tidal Targeting

The Prospective End-Tidal Targeting method is an adaptation of the SGD method that allows precise targeting and independent control of the end-tidal CO_2 and O_2 concentrations and independent of minute ventilation (Prisman et al., 2008). In contrast with the SGD method, that only targets and maintains the level of one of the end-tidal gases, resulting in concomitant changes on the other gas confounding results, the prospective end-tidal targeting method targets and maintains the end-tidal values independently and independent of ventilation (Slessarev et al., 2007). This is achieved by delivering a specific volume of fresh gas into alveoli on each

breath, with concentrations computed *a priori*, using specific relations that were described in (Slessarev et al., 2007), in order to adjust the composition and flow rates of source gases based on the subject's CO_2 production and O_2 consumption (Slessarev et al., 2007). The system itself consists of a feed-forward, low gas flow system, that adjusts the composition and flow of the fresh gas needed, and a sequential gas delivery re-breathing circuit that controls the presentation of gases into the subject's lungs (Ito et al., 2008; Slessarev et al., 2007). Slessarev at al. illustrated the suitability of the method by using it to produce rapid cyclic step-changes in both $PETCO_2$ and $PETO_2$ with short duration steady states and the end-tidal values closely followed the target values despite large inter and intrasubject variability in minute ventilation. Ito further demonstrated that with this method it is possible to have a consistent and close agreement between $PETCO_2$ and arterial CO_2 values (Ito et al., 2008). Relative to the DEF method, that uses advanced prediction-correction schemes to target and control end-tidal values, this is a simpler, safer, faster and more compact alternative.

A.2 Non-Invasive Methods

Despite the previous methods being less dependent on subject's cooperation and allowing precise targeting of the gas inspired/expired, the use of complex experimental setups, including uncomfortable breathing masks, and not being well tolerated by some clinical populations, hinders the applicability of these methods in clinical settings. Furthermore, medical ethical concerns and availability of the gas modulation devices may pose additional difficulties to its applicability. Non-invasive strategies might offer a new opportunity for the application of CVR assessment as a useful clinical tool. In fact, it has been shown that non-invasive methods are well tolerated by healthy volunteers as well as patients and yield results comparable to those obtained with invasive methods (Golestani et al., 2016; Kastrup et al., 2001; Magon et al., 2009).

A.2.1 Breath-hold Task

The use of a breath-hold task (BH) for CVR mapping was first described by Ratnatunga and Adiseshiah in 1990 (Ratnatunga and Adiseshiah, 1990). BH protocols generally consist of alternating periods of self or computer-paced breathing and breath-hold. Arterial CO_2 levels increase during the breath-holding period, leading to an hypercapnic condition and consequently to a CBF increase. BH is a simple method for evaluating haemodynamic response, since it does not require an exogenous source of gas or the intravenous injection of a drug, making it a good non-invasive alternative (Andrade et al., 2006). Nevertheless, the haemodynamic response to this method depends on several factors, including the length of the BH period and the starting volume (i.e, breath-hold performed after expiration or inspiration). In addition, it is also dependent on the subject's ventilatory response to CO_2 and this is highly variable across subjects. This high intersubject variability results in unpredictable $PETO_2$ and $PETCO_2$ values. The BH task does not allow monitoring of gases during the BH period and just the simple BH act

can induce unwanted physiological changes, possibly confounding results. Moreover, this task is more prone to motion artifacts and its use may be limited in patients who have an impaired respiratory function (Leoni et al., 2012).

A.2.2 Hyperventilation

An hypocapnic state can be achieved voluntarily, without the need of any external gas sources, simply by increasing the breathing rate and/or depth (hyperventilation). Hyperventilation results in an increase in arterial O_2 level and a decrease in arterial CO_2 levels, consequently leading to vasoconstriction and a reduction in CBF (Vogt et al., 2011). The rates of change in arterial pressures are more rapid than with BH (Prisman et al., 2008). Nevertheless, this task also has some disadvantages, including the ones previously described in the BH task: unwanted motion, inter- and intrasubject variability in minute ventilation and ventilatory response to CO_2 and concomitant changes in O_2 levels.

A.2.3 Cued Deep Breathing

In order to overcome some of the disadvantages of hyperventilation, another respiratory task named Cued Deep Breathing (CDB) has been developed. CDB causes transient mild hypocapnia (decrease in $PaCO_2$) and consequently vasoconstriction and reduction in CBF. The CDB task is not as challenging to perform as other methods, such as BH (Bright et al., 2009), and since this mild hyperventilation is cued, is also less prone to unwanted motion. This new paradigm was extensively studied by Bright et al. and also employed in Sousa et al. (Bright et al., 2009, 2011; Sousa et al., 2014a). An example of a CDB paradigm can be seen in Figure 5.1, where cues of short duration are displayed consecutively. Bright et al. compared this approach with other methods, including the Fixed Inspiratory Challenge and the BH task, obtaining comparable CVR maps. The CDB task was generally felt to be less challenging than the BH and may allow a more precise temporal characterization due to the smaller delay of signal change and quicker return to baseline (Bright et al., 2009). Bright et al. also explored the effect of baseline dilation in cerebral vasculature, which is often present in pathological states, using hypocapnic CVR assessment. CDB reactivity was assessed during a simulated altered baseline condition, using prolonged inhalation of 4% CO_2 gas mixture, observing that the vasoconstrictive reactivity was significantly enhanced. The authors state that hypocapnia challenges, such as the CDB, may be more helpful for the identification of the level of vascular compliance in stroke patients (Bright et al., 2011).

B

Chapter 4 - Supplementary Material

B.1 Kinetic Modeling

The tissue component ΔM_{tiss} was described by the general kinetic model (Buxton et al., 1998)

PASL

$$\Delta M_{tiss}(t) = \alpha M_{0a} \frac{2f}{k} \begin{cases} 0 & \text{if } t < ATT \\ e^{\frac{-t}{T_{1a}}}(e^{k(t-ATT)} - 1) & \text{if } ATT \leq t < ATT + \tau \\ e^{\frac{-t}{T_{1a}}}(e^{k(t-ATT)} - e^{k(t-ATT-\tau)}) & \text{if } t \geq ATT + \tau \end{cases} \tag{B.1}$$

pCASL

$$\Delta M_{tiss}(t) = \alpha M_{0a} 2f T_1^{'} \begin{cases} 0 & \text{if } t < ATT \\ e^{\frac{-ATT}{T_{1a}}}(1 - e^{\frac{(t-ATT)}{T_1^{'}}}) & \text{if } ATT \leq t < ATT + \tau \\ e^{\frac{-ATT}{T_{1a}}}(e^{\frac{-(t-\tau-ATT)}{T_1^{'}}} - e^{\frac{-(t-ATT)}{T_1^{'}}}) & \text{if } t \geq ATT + \tau \end{cases} \tag{B.2}$$

with $k = \frac{1}{T_{1a}} - \frac{1}{T_1^{'}}$,$\frac{1}{T_1^{'}} = \frac{1}{T_1} + \frac{f}{\lambda}$, where ΔM_{tiss} is the control-label magnetization difference measured from the tissue compartment; M_{0a} is the equilibrium magnetization of the arterial

blood; τ is the bolus duration; T_{1a} is the longitudinal relaxation time of arterial blood; T_1' is the longitudinal relaxation time of brain tissue; λ is the blood-brain water partition coefficient; α is the labeling (inversion) efficiency; and t corresponds to TI for PASL and $\tau + PLD$ for pCASL. The intravascular arterial component (ΔM_{art}) was added as (Chappell et al., 2010, 2009):

PASL

$$\Delta M_{art}(t) = \alpha M_{0a} 2aBV \begin{cases} 0 & \text{if } t < ATTa \\ e^{\frac{-t}{T_{1a}}} & \text{if } ATTa \leq t < ATTa + \tau \\ 0 & \text{if } t \geq ATTa + \tau \end{cases} \tag{B.3}$$

pCASL

$$\Delta M_{art}(t) = \alpha M_{0a} 2aBV \begin{cases} 0 & \text{if } t < ATTa \\ e^{\frac{-ATTa}{T_{1a}}} & \text{if } ATTa \leq t < ATTa + \tau \\ 0 & \text{if } t \geq ATTa + \tau \end{cases} \tag{B.4}$$

where $ATTa$ is the intravascular arterial transit time; and τ_a is the intravascular bolus duration. Finally, the total magnetization difference $\Delta M_{total}(t) = \Delta M_{tiss}(t) + \Delta M_{art}(t)$ was fitted to the time series measured in each voxel using BASIL (Chappell et al., 2010, 2009).

B.2 Coefficients of Variation

CV_{inter} was computed for each session as:

$$\mathrm{CV_{inter}} = \frac{\mathrm{SD}}{\mu} \times 100[\%] \tag{B.5}$$

where μ and SD are the mean and standard deviation (SD) of the parameter across subjects (Bland and Altman, 1996). The final CV_{inter} was computed as the mean of the CV_{inter} of the two sessions. CV_{intra} was computed as:

$$\mathrm{CV_{intra}} = \frac{\mathrm{SD_{ws}}}{\mu} \times 100[\%] \tag{B.6}$$

where μ is the mean value of the parameter across subjects and sessions (Bland and Altman, 1996). SD_{ws} is the standard deviation of repeated measurements within-subject, computed as:

$$SD_{ws} = \sqrt{\left(\frac{\sum_{i=1}^{k} \left(a_{R_i S_1} - a_{R_i S_2} \right)^2}{2 \times k} \right)} \tag{B.7}$$

where k is the number of subjects and $a_{R_i S_1}$ and $a_{R_i S_2}$ are the measurements of subject i on session 1 and 2, respectively.

B.3 Registration and Tissue Segmentation

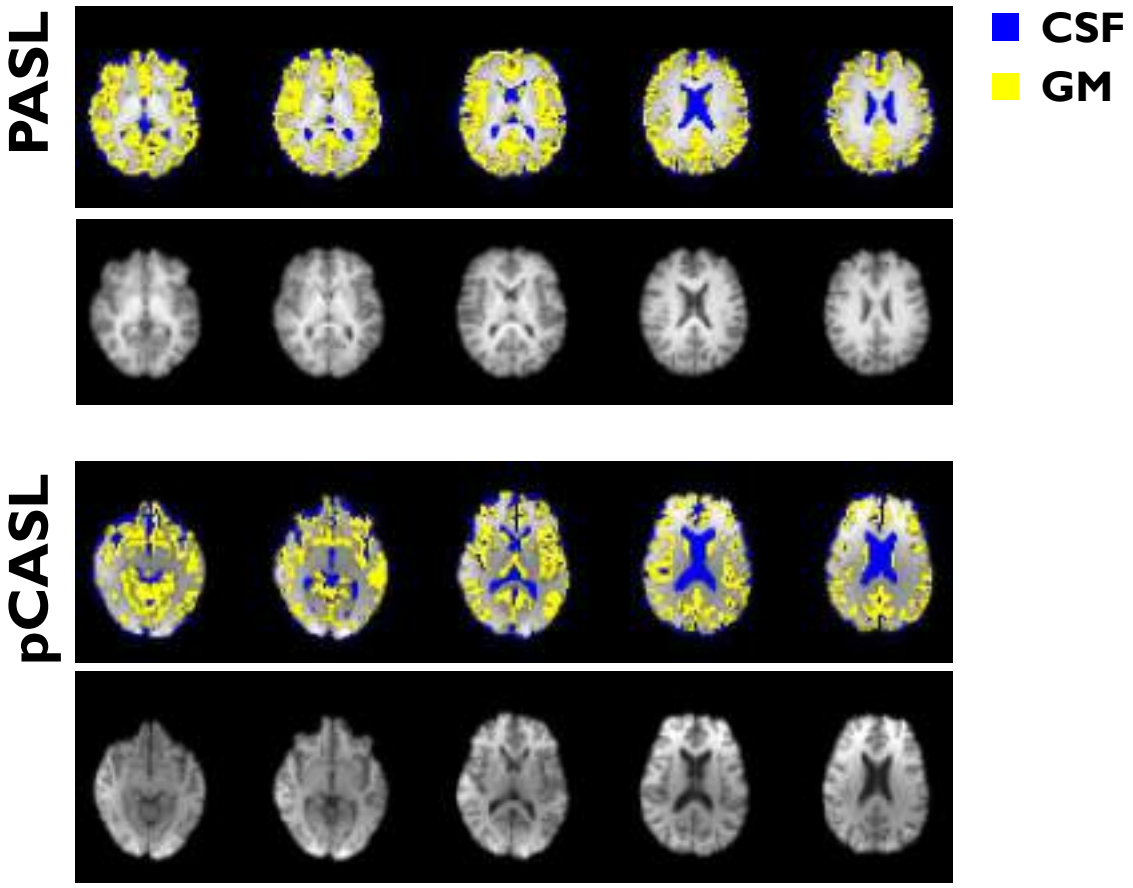

Figure B.1: Illustrative examples of MPRAGE images registered to ASL space (bottom) and respective CSF (blue) and GM (yellow) masks retrieved from MPRAGE image segmentation (top), for the PASL and pCASL data sets.

C

Chapter 7 - Supplementary Material

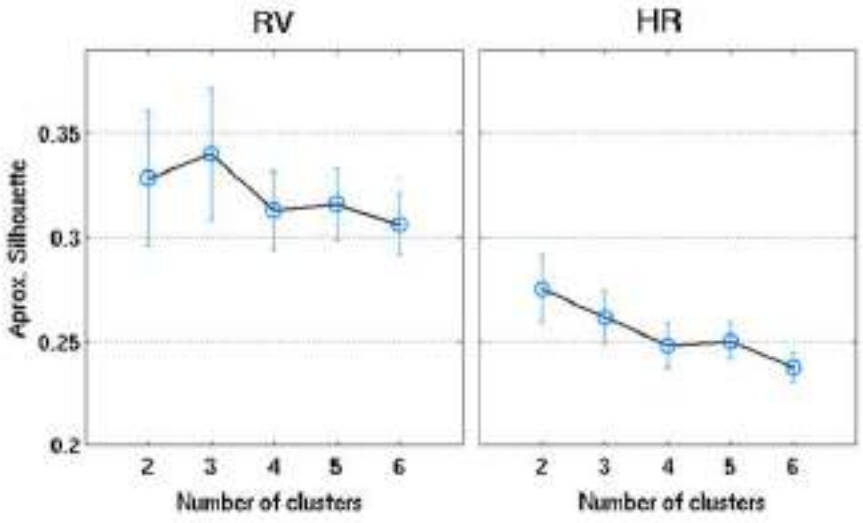

Figure C.1: Group average k-means silhouette values as a function of the number of clusters, k, for RV and HR. A high silhouette value indicates that each point is well-matched to its own cluster, and poorly-matched to neighboring clusters. Error bars represent standard error across subjects.

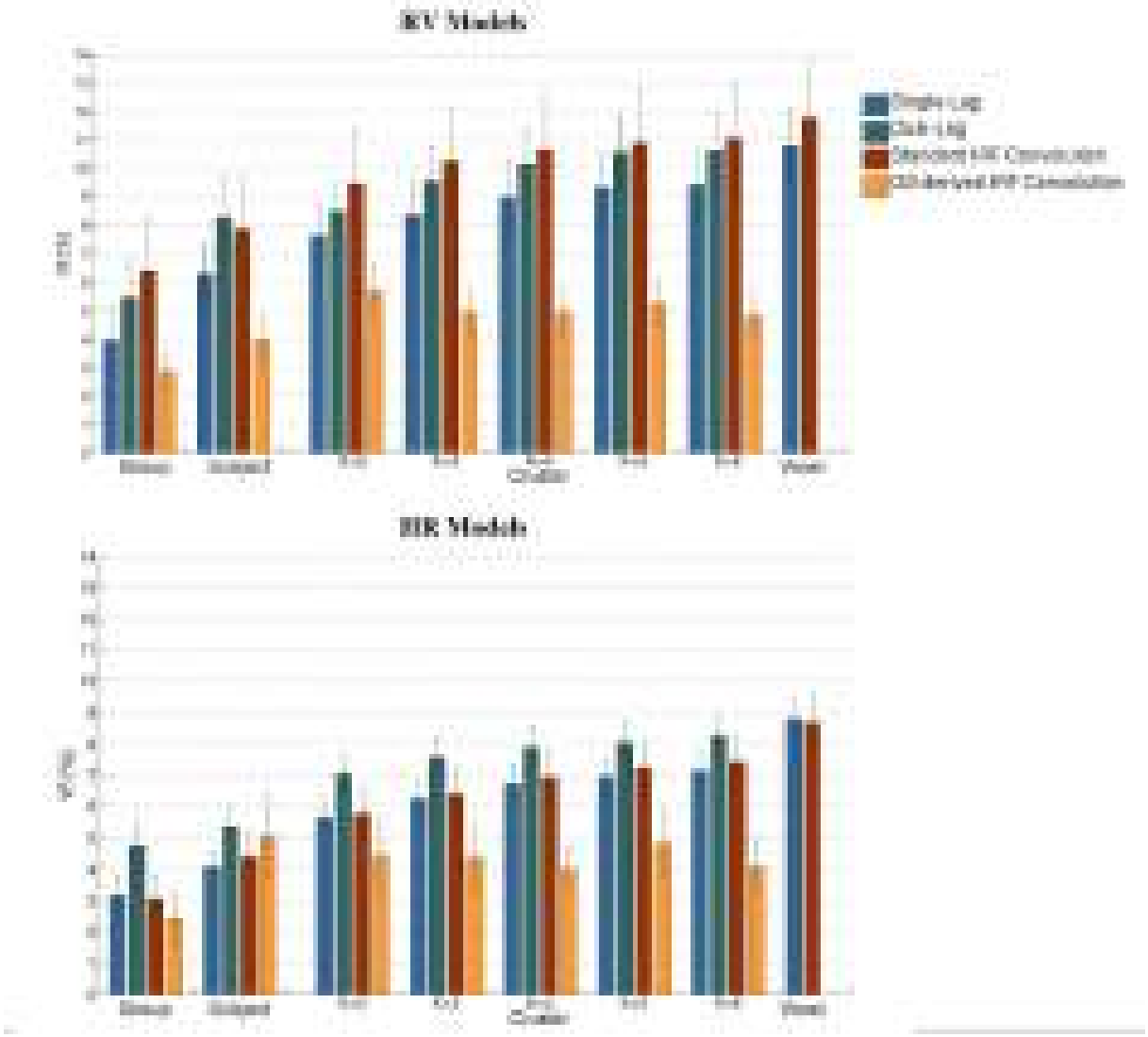

Figure C.2: Results obtained with data pre-processing using a spatial smoothing kernel with FWHM = 5 mm. Group average VE in GM, for RV (top) and HR (bottom) physiological noise models, and for the different model types tested (Single-Lag/Dual-Lag/Standard IRF Convolution/GS-derived IRF Convolution), as a function of the specificity level (Group/Subject/Cluster (k = 2, 3, 4, 5, and 6) /Voxel) used for the model optimization. Statistically significant differences between different specificity levels are indicated.

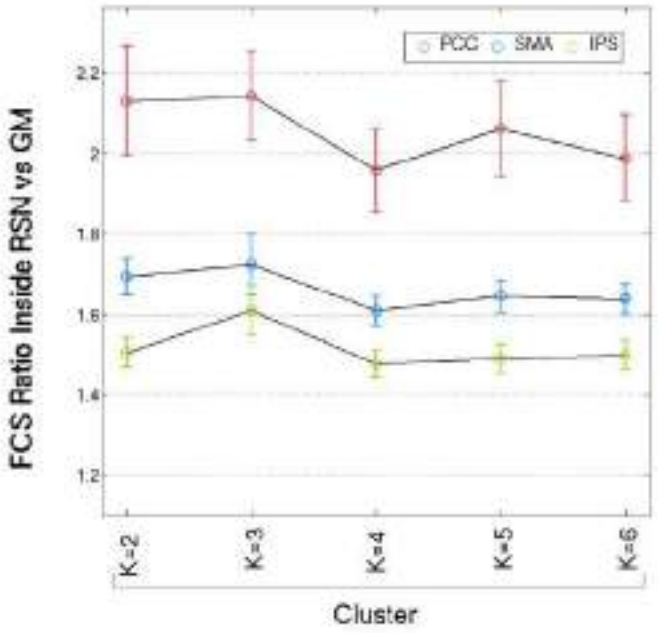

Figure C.3: Ratio between the average FCS inside the RSNs (PCC, SMA and IPS) and the average FCS across the whole GM for the different Cluster levels of specificity (k = 2, 3, 4, 5 and 6). No significanct main effect was found for the number of clusters.

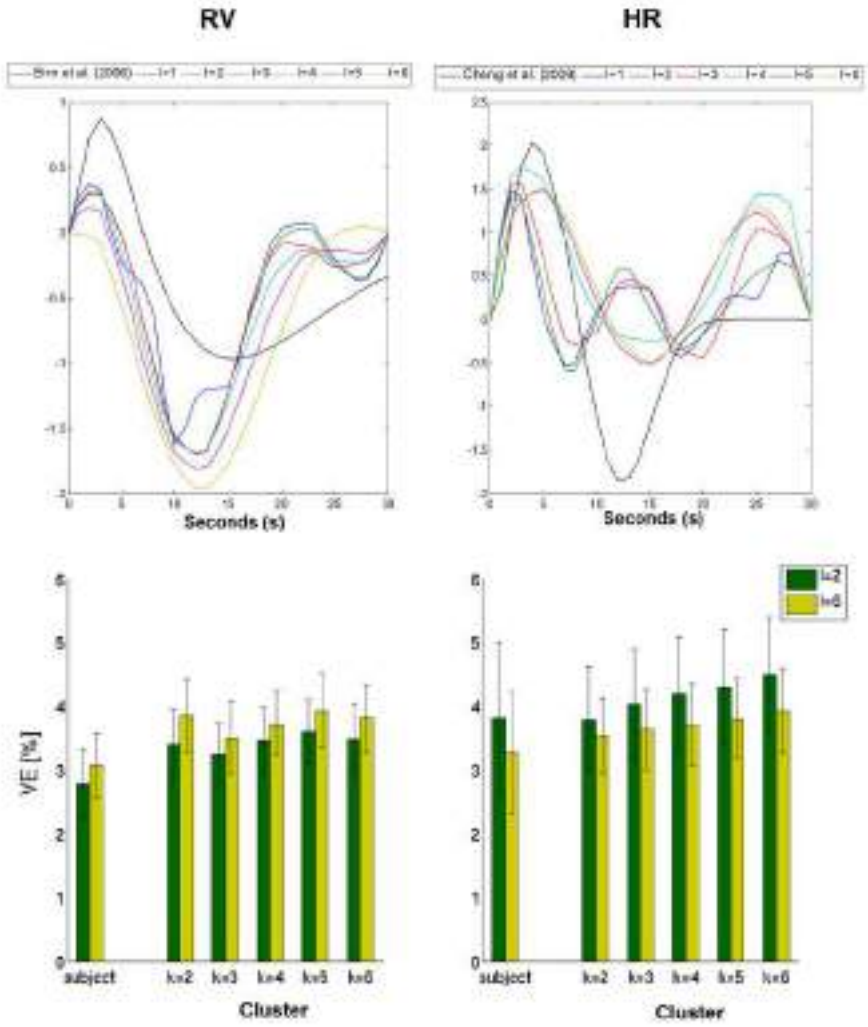

Figure C.4: Sensitivity of the IRF deconvolution model type to the hyperparameter l. Top) Deconvolved IRF's for RV and HR, obtained using $l = 1$, 2, 3, 4, 5 and 6, for an illustrative subject, compared with the respective standard IRF's; and Bottom) Group average VE of the RV and HR models obtained by Cluster-level optimization (k = 3), using $l = 2$ (default) and $l = 6$, compared with Subject-level optimization.